

## Dynamics of Excitons in Conjugated Molecules and Organic Semiconductor Systems

Oleg P. Dimitriev\*

Cite This: *Chem. Rev.* 2022, 122, 8487–8593

Read Online

ACCESS |

Metrics &amp; More

Article Recommendations

Supporting Information

**ABSTRACT:** The exciton, an excited electron–hole pair bound by Coulomb attraction, plays a key role in photophysics of organic molecules and drives practically important phenomena such as photoinduced mechanical motions of a molecule, photochemical conversions, energy transfer, generation of free charge carriers, etc. Its behavior in extended  $\pi$ -conjugated molecules and disordered organic films is very different and very rich compared with exciton behavior in inorganic semiconductor crystals. Due to the high degree of variability of organic systems themselves, the exciton not only exerts changes on molecules that carry it but undergoes its own changes during all phases of its lifetime, that is, birth, conversion and transport, and decay. The goal of this review is to give a systematic and comprehensive view on exciton behavior in  $\pi$ -conjugated molecules and molecular assemblies at all phases of exciton evolution with emphasis on rates typical for this dynamic picture and various consequences of the above dynamics. To uncover the rich variety of exciton behavior, details of exciton formation, exciton transport, exciton energy conversion, direct and reverse intersystem crossing, and radiative and nonradiative decay are considered in different systems, where these processes lead to or are influenced by static and dynamic disorder, charge distribution symmetry breaking, photoinduced reactions, electron and proton transfer, structural rearrangements, exciton coupling with vibrations and intermediate particles, and exciton dissociation and annihilation as well.



### CONTENTS

1. Introduction	8488	3.4.1. Exciton Localization	8514
2. The Excitonic “Zoo” in Organic Materials	8490	3.4.2. Shift of Exciton Energy	8514
2.1. Singlet and Triplet Excitons	8490	4. Transport of Excitons	8515
2.2. Localized and Delocalized Excitons	8490	4.1. Energy Funneling through the Manifold of Hot States	8515
2.3. Coherent and Incoherent Excitons	8491	4.2. Factors Controlling Different Regimes of Exciton Energy Transfer in Multichromophoric Systems	8517
2.4. Cold and Hot Excitons	8492	4.2.1. <u>Exciton–Phonon Coupling</u>	8517
2.5. Charge-Transfer Excitons	8492	4.2.2. <u>Donor–Acceptor Coupling</u>	8518
2.6. Dark Excitons	8493	4.3. Coherent Exciton Delocalization	8519
3. Birth of Excitons	8493	4.4. Exciton Diffusion	8520
3.1. Dynamics of Exciton Localization	8493	4.4.1. General Characteristics of the Exciton Diffusion Process	8520
3.1.1. Polymers with Torsional Degree of Freedom	8495	4.4.2. Driving Forces for Exciton Diffusion	8521
3.1.2. Polyenes	8495	4.4.3. The Role of Dynamic Disorder	8525
3.1.3. Rigid Molecular Systems	8496	4.5. <u>Coherent Energy Transfer</u>	8525
3.1.4. Molecular Assemblies	8498	4.5.1. Exciton Transport Driven by Torsional Dynamics in a Polymer Chain	8525
3.2. <u>Exciton-Induced Chemical Dynamics</u>	8501	4.5.2. Quantum Coherent Transport of Excitons in Natural Photosynthetic Systems	8526
3.2.1. Intramolecular Electron Transfer	8501		
3.2.2. Excited-State Proton Transfer	8503		
3.2.3. Symmetry Breaking	8505		
3.2.4. Photolysis and Photoinduced Fusion	8507		
3.3. Exciton-Induced Structural Reorganization	8511		
3.3.1. Exciton-Induced Conformational Changes of Polymer Chains	8511		
3.3.2. Exciton-Induced Structural Reorganization of Molecular Assemblies	8512		
3.4. Effect of Specific Static Conformations on Exciton Formation in Conjugated Molecules	8514		

Received: July 22, 2021

Published: March 17, 2022



4.5.3. Quantum Coherent Transport of Excitons in the Network of Protein Structures (Microtubules)	8527
<b>4.6. The Preferred Pathways and Control of Exciton Energy Transfer</b>	<b>8528</b>
4.6.1. Intrachain versus Interchain Energy Transfer in Conjugated Polymers	8528
4.6.2. Control of the Exciton Energy Transfer by Conformational Changes	8529
4.6.3. Energy Transfer via the Dark States in Large Multichromophoric Assemblies	8532
4.6.4. Enhancement of Exciton Energy Transfer by Using Floquet Engineering	8533
4.6.5. Mediation of the Exciton Energy Transfer by a Third Particle	8534
<b>5. Conversion and Decay of Excitons</b>	<b>8536</b>
5.1. Conversion Dynamics via Intersystem Crossing	8536
5.1.1. Rates of Intersystem Crossing	8536
5.1.2. Intersystem Crossing Facilitated by Nonplanar Conformation	8537
5.1.3. Reverse Intersystem Crossing via Thermal Activation Leading to Delayed Fluorescence	8539
5.2. Upconversion Dynamics of Excitons	8540
5.2.1. Multiphoton Upconversion	8541
5.2.2. Single-Photon Upconversion	8543
5.3. Down-Conversion Dynamics of Excitons	8544
5.3.1. Exciton Down-Shifting	8544
5.3.2. Exciton Fission	8546
5.3.3. Multiple Exciton Generation	8549
5.4. Dynamics of Direct Decay of Singlet Excitons	8549
5.4.1. Decay via Radiative Recombination	8549
5.4.2. Decay via Nonradiative Recombination	8555
5.4.3. Decay via Exciton Dissociation	8558
<b>6. Current Challenges and Future Directions</b>	<b>8561</b>
6.1. Light-Driven Molecular Machines	8561
6.2. Supramolecular Photochemistry	8563
6.3. Light Harvesting and Photovoltaics	8564
6.4. Supertransport of Excitons	8566
6.5. Excitonic Circuits	8567
6.6. Quantum Computing	8569
<b>7. Conclusions</b>	<b>8570</b>
<b>Associated Content</b>	<b>8570</b>
Supporting Information	8570
<b>Author Information</b>	<b>8570</b>
Corresponding Author	8570
Notes	8570
Biography	8570
<b>Acknowledgments</b>	<b>8571</b>
<b>List of Abbreviations</b>	<b>8571</b>
<b>References</b>	<b>8572</b>

## 1. INTRODUCTION

Absorption of light is a fundamental process leading to conversion of the energy of the excitation source to the inner energy of the material in the form of electronic or vibrational excitations or both. When a material has a relatively low dielectric constant, which is typical for organic materials, the Coulomb attraction between the excited electron and the positively charged vacancy (i.e., the hole) binds them to energy that is an order of magnitude higher than the thermal energy at

room temperature and thus does not allow the electron–hole pair to be completely separated and gives rise to an atomic quasiparticle called an exciton. The exciton can then relax, transform, be transported over some distance, and decay. All these stages of its lifetime have specific time scales that are influenced both by the molecule that carries the exciton (i.e., by molecular structure and properties) and by the environmental conditions.

At birth, exciton formation time scales span at least 4 orders of magnitude (Figure 1). If excitation induces some photochemical reactions, these can be considered as a part of the exciton formation too, which leads to even longer apparent times of the exciton formation. The actual excitation energy of  $\pi$ -conjugated organic molecules that yields the excitons falls in the UV–vis region of electromagnetic spectrum. Since the time scale of electronic excitation matches the period of the excitation wavelength in this spectral range, it takes about few femtoseconds. Thus, femtosecond excitation is the fastest process triggering exciton formation. Since organic materials are often soft systems with relatively weak intermolecular interactions and therefore a rather loose structure that can be rearranged easily, the electronic excitation can be accompanied by a number of processes, such as mechanical interatomic and intersegment motion, redox reactions, breaking and restoring of chemical bonds, photoisomerization, and inter- and intramolecular rearrangement; all these processes influence exciton formation as well. Therefore, the exciton formation in organic molecules is a process that is self-consistent with the system in which it is located, with a noticeable influence of the exciton on the system and the system on the exciton. Particularly, an exciton experiences localization and delocalization processes in the sub-picosecond and picosecond time ranges due to coupling with molecular vibrational modes caused by high-frequency interatomic stretching and low-frequency torsional dynamics, respectively.<sup>1,2</sup> If the molecule is composed of electron donor and electron acceptor moieties or if it is located in an inhomogeneous environment, the excitation is accompanied by ultrafast charge transfer resulting in localization of electrons on the acceptor and holes on the donor part, that is, in formation of the charge-transfer state.<sup>3</sup> Formation of the coherent charge-transfer excitons occurs immediately upon photoexcitation within 20–30 fs.<sup>4</sup>

A subsequent step that accompanies the exciton lifetime is exciton conversion or transport. Since the excited electron–hole pair stores energy, the change in exciton location or exciton transport is associated with energy transfer. Here, there are various pathways for this process, beginning from relaxation of a hot exciton through energy funneling to the lowest excited state to long-range intermolecular transfer. The rate of this process is largely dependent on exciton vibrational coupling and coupling between the donor and the acceptor of energy. The ultrafast energy transfer begins from tens<sup>5</sup> and hundreds<sup>6</sup> of femtoseconds in molecular wires, whereas relatively slow energy transfer with time constants of the order of microseconds can be found in donor–bridge–acceptor dinuclear metal complexes where the bulky substituents hamper energy transfer via increasing tilt angle between the bridge units.<sup>7,8</sup> Conversion of the exciton during its lifetime also includes various processes, such as exciton fission and fusion and up- and down-conversion of exciton energy, where the rates vary greatly. The ultrafast singlet fission starts from the sub-picosecond time scale,<sup>9</sup> whereas triplet–triplet fusion can be slowed by triplet exciton diffusion with delay to the sub-millisecond time range.<sup>10</sup> A singlet exciton can be converted to a triplet one through

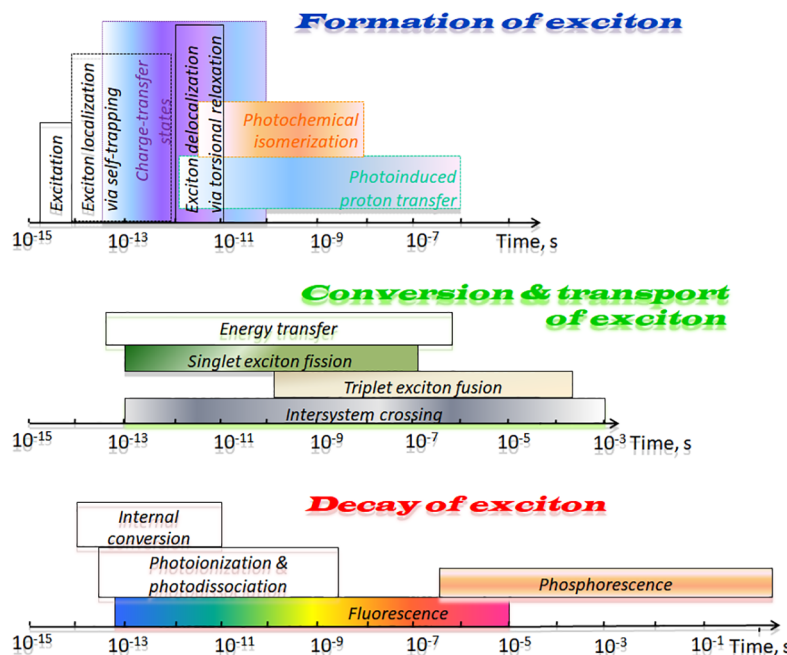


**Figure 1.** Time scales of the different phases of the exciton dynamics. The box widths indicate the time ranges of the processes.

**intersystem crossing (ISC).** Compared to the other processes, the time scale of ISC varies greatly, up to 10 orders of magnitude (Figure 1). Since photophysical processes with spin flip are usually forbidden, ISC in many cases occurs as a slow process in the micro- to millisecond time domains.<sup>11</sup> However, time constants of ISC can be significantly decreased to nano- and picoseconds if the spin-flip is mediated by an intermediate molecular structure appearing as a result of exciton evolution,<sup>12</sup> by molecular vibrations,<sup>13</sup> by charge transfer states,<sup>14,15</sup> and by the presence of heavy atoms.<sup>16,17</sup>

Finally, the exciton decay is triggered by different processes the rates of which span more than 10 orders of magnitude (Figure 1). The fastest process is internal conversion, which transfers electronic energy into molecular vibrations and heat within the sub-picosecond time scale. Exciton dissociation due to electron–hole separation which was proved to be effective in polymer solar cells, is another fast process with time constants that can be as small as tens of femtoseconds.<sup>18,19</sup> However, this rate can also be substantially reduced to  $\sim 10^{-9} \text{ s}^{-1}$  in such a system as a polymer non-fullerene acceptor via intermediate photoinduced charge-transfer states localized on the acceptor, which then transfer the photoinduced hole to the donor at a delayed time.<sup>20</sup> In addition, the lifetime of the charge-transfer states can be strongly extended due to an increased activation barrier against the decay generated, for example, by metal-to-ligand charge-transfer-type excited states in pseudo-octahedral iron(II) coordination complexes.<sup>21</sup>

The other decay channel for an exciton, radiative recombination, is controlled by different factors, such as the spatial dimensionality  $D$  of the system, rigidity and conformational change of the conjugated molecule, its band gap, exciton vibrational coupling, oscillator strength of the first excited singlet state, the extent of exciton delocalization over emitting chromophores coupled in a multichromophoric system, and energetic disorder of the system as well. Thus, the lifetime of the thermalized singlet exciton that undergoes radiative recombination typically ranges in the order of  $10^{-10}$  to  $10^{-7} \text{ s}$ . However,

some aromatic molecules, such as benzpyrene, thiocoumarin, or metalloporphyrins, demonstrate radiative decay from vibrationally hot unrelaxed excited states with lifetimes that often fall to the sub-picosecond time range;<sup>22,23</sup> otherwise, it would compete with intersystem crossing, which quenches the excitation. On the other hand, fluorophores with fluorescence lifetimes as long as  $\sim 10 \mu\text{s}$  have been developed recently.<sup>24,25</sup> The mechanism of this abnormal fluorescence lifetime for these fluorophores is unclear; however, it was shown recently that single-wall carbon nanotubes in liquid suspension, whose intrinsic radiative lifetime (free of nonradiative processes) is of the order of 1–10 ns, have a delayed, microsecond-scale fluorescence arising from upconverted triplet excitons that are directly created through energy transfer from singlet oxygen molecules ( ${}^1\text{O}_2$ ) in the presence of a photosensitizer in the solution.<sup>26</sup> Even longer room-temperature lifetimes, up to seconds, can be observed for phosphorescence due to the forbidden spin-flip of the excited electron relaxing to the ground state.<sup>27–31</sup>

This short overview of time scales of the exciton evolution indicates the richness of the photophysical processes at all stages of the exciton lifetime. As can be seen, exciton dynamics is characterized by multiple and overlapping time scales, where intrinsic intrachain (vibronic relaxation, etc.), interchain (e.g., donor–acceptor coupling), and extrinsic processes (e.g., molecule–solvent interactions) play significant roles. In this review, this short history of exciton evolution dynamics is given in more detail. The structure of the article is as follows. In section 2, the exciton classification is given as a glossary for nonspecialists. In section 3, the different aspects that accompany exciton formation are considered, which include exciton localization and conformational dynamics in systems of different rigidity and degrees of freedom, exciton-induced chemical reactions, such as photoinduced intramolecular electron and proton transfers, photolysis and photoinduced fusion, symmetry breaking, exciton-induced structural reorganization, and effects of structural configuration of the system to assist reaching certain excitation states. Section 4 describes the different aspects

of exciton transport, from intramolecular energy funneling to different regimes of energy transfer in multichromophoric systems, with emphasis on driving forces and preferred pathways of the excitation energy transfer. Conversion dynamics of the exciton via intersystem crossing, up- and down-conversion of excitation energy, and exciton fission and fusion, as well as different pathways of decay dynamics of singlet excitons, are given in section 5. Finally, modern trends and future directions of excitonic devices from light-driven machines to quantum computing are outlined in section 6.

The amount of publications in the field of exciton dynamics have increased significantly in the past 10 years, so there is no guarantee to include all of them in this review. A separate summary of the selected recent review articles, tutorials, and perspectives focused on specific or related topics in the field that have not been included in the main text is given in *Supporting Information*. These articles reflect the high level of activity in the field of exciton dynamics and can be used for an in-depth analysis of the particular topics within the field. Additionally, some recent books and special journal issues covering various aspects of exciton physics of organic semiconductors, materials design, spectroscopy, and device performance are available and can be referred to as a background material.<sup>32–42</sup>

## 2. THE EXCITONIC “ZOO” IN ORGANIC MATERIALS

### 2.1. Singlet and Triplet Excitons

Excitons can differ in spin multiplicity (i.e., orientation of the excited electron spin with respect to the spin of the hole counterpart). Quantum mechanics prohibits the presence of two electrons with the same spin orientation on the same energy level; therefore, the two spins on the ground-state (i.e., HOMO level) must be antiparallel. According to the spin conservation rule, electronic transitions between terms of different multiplicity are spin-forbidden, but these are spin-allowed between terms of the same multiplicity;<sup>43</sup> therefore, electronic excitations of molecules usually result in formation of a singlet exciton (i.e., an exciton with unchanged total spin zero, where spins of the excited electron and hole are antiparallel and thus compensate each other). This rule, however, can be relaxed due to certain factors, such as spin-orbit coupling, where the change in orbital angular momentum can assist in spin-flip while keeping the total angular momentum of the system conserved. Spin-orbit coupling is stronger in systems that contain heavy atoms with higher atomic number, which give rise to triplet excitons, where the spins of the excited electron and hole are parallel. Therefore, triplet excitons often take place in platinum(II) and transition metal complexes or in polymers and small molecules containing atoms, such as Se, Te, I, or Br.<sup>44</sup> Due to the forbidden character, the spin-flip is a relatively slow process with time constants  $>10^{-13}$  s (see Figure 1); therefore, triplet excitons cannot be directly generated by absorption of a photon, which occurs on the femtosecond time scale, but appear due to ISC, which occurs from relatively long-lived exciting single states (Figure 2). However, if a system does not have substantial spin-orbit coupling, triplet excitons can be generated by other means, for example, by spin–spin coupling or hyperfine interaction,<sup>45</sup> by energy or charge transfer from the triplet sensitizer,<sup>46</sup> or by injection of electrons to the triplet level due to applied electric field as well.<sup>47</sup>

A triplet exciton is more spatially localized compared to a singlet exciton because electrons with parallel spins in the triplet state are better correlated via the exchange interaction than the

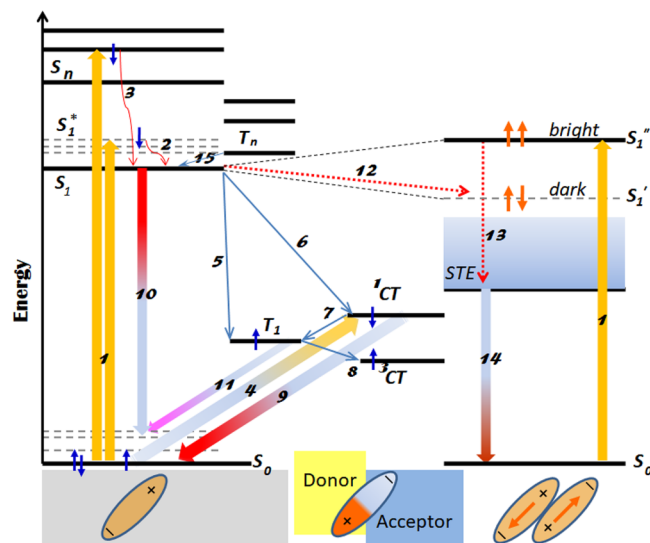


**Figure 2.** Jablonski diagram of the excitonic zoo for the monomer (left), interface (middle), and molecular ensemble (right); the bottom part schematically illustrates the exciton(s) generated in respective media. The energy levels correspond to  $S_0$  (the ground state),  $S_1\dots S_n$  (the manifold of singlet excitons),  $S_1$  and  $S_1^*$  (cold and hot singlet excitons, respectively),  $T_1\dots T_n$  (the manifold of triplet excitons),  ${}^1\text{CT}$  and  ${}^3\text{CT}$  (singlet and triplet charge-transfer excitons, respectively). STE (self-trapped (localized) exciton), and  $S_1''$  and  $S_1'$  (splitting energy levels due to molecular interaction corresponding to the bright and dark excitons, respectively). The arrows correspond to the following photophysical processes: (1) photoexcitation of the singlet exciton(s), (2) vibronic relaxation (thermalization), (3) internal conversion, (4) photoexcitation to the charge-transfer state, (5) intersystem crossing, (6) singlet exciton predissociation to the charge-transfer state, (7) intersystem crossing, (8) triplet exciton predissociation to the charge-transfer state, (9) recombination of the charge-transfer exciton, (10) recombination (fluorescence) of the cold singlet excitons, (11) recombination (phosphorescence) of the triplet exciton, (12) energy transfer to the dark exciton, (13) exciton self-trapping, (14) recombination of the self-trapped exciton, (15) reverse intersystem crossing. Small blue arrows indicate electron spin orientations, and the orange arrows indicate transition dipole orientation in a molecular dimer.

antiparallel ones in the singlet state.<sup>48</sup> The energy separation between the lowest singlet and triplet excited states is usually large and size-dependent for small molecules and short oligomers, but it saturates for long  $\pi$ -conjugated molecules at around 0.7 eV.<sup>49</sup> However, a singlet–triplet splitting as small as 49 meV was found in azulene molecules,<sup>50</sup> and even inverted gaps between first excited singlet and triplet states have been recently discovered in emergent molecules.<sup>51</sup>

### 2.2. Localized and Delocalized Excitons

The excitons in  $\pi$ -conjugated molecules are Frenkel excitons, the size of which is usually confined by size of the molecule that generates it. When an exciton is generated in an ensemble of chromophores that have close contacts and tight interaction to each other, for example, in a crystal or in an ordered aggregate or polymer molecule, which can be considered as a one-dimensional lattice, then it is reasonable to raise questions concerning the exciton size in such a system. In this case, the exciton size can be controlled by such factors as ordering of exciton dipoles on the neighboring sites, system dimensions, and exciton interaction with the vibrational modes. In crystals or ordered polymer chains, excitons interact with phonons (i.e., the

lattice vibrations). In the case of weak coupling, the excitons are scattered by phonons. However, when the coupling is strong, excitons became localized or self-trapped.<sup>52</sup> Self-trapping results in dressing excitons with a dense cloud of virtual phonons, which strongly suppress the exciton mobility, because a local deformation of the crystal lattice moves along with the exciton and thus increases its effective mass significantly. The energetic criterion for self-trapping states is that the latter can be achieved when the energy of lattice deformation can compete with the width of the exciton band, which is about an electronvolt.<sup>53</sup> The features of a self-trapped exciton (STE) are as follows. First, STE states always have a small radius, on the order of the lattice constant. A STE can be described as a bound electron–hole pair, where at least one carrier of the pair (electron or hole) has a strong coupling to the crystal lattice, in which a carrier may be self-trapped as a small polaron in its own lattice distortion field. Second, in order to be localized the free exciton should overcome a self-trapping barrier separating free and self-trapped states, whereas the presence of such a barrier allows coexistence of the free and self-trapped excitons.<sup>54</sup> The barrier width is about  $r_0 \approx \gamma^2 m / \omega^2$ , and the barrier height is  $W \approx \omega^4 / (\gamma^4 m^3)$ , where  $m$  is the exciton effective mass,  $\gamma$  is the exciton–phonon coupling constant, and  $\omega$  is the characteristic frequency of optical phonons.<sup>42</sup> Thus, large values of  $m$  and  $\gamma$  give rise to exciton self-trapping. In low-dimensional systems, the barrier height approaches zero, and therefore free excitons can be seen only in pure samples and at low temperatures.

Exciton delocalization in molecular systems is largely dependent on both static and dynamic disorder. In most amorphous materials, the molecular energy levels vary across the same molecules in the system, are described by a Gaussian distribution, and are referred to as global energy disorder.<sup>55</sup> The Gaussian distribution is dependent on local interactions and the potential well in which the molecule is sitting, which is determined by factors such as individual equilibrium size and conformation, flexibility, degree of crystallinity, and the presence of possible additives such as dopants, etc., and is referred to as static disorder.<sup>56</sup> Exciton vibrational interactions lead to thermal vibrations, which cause fluctuations and a spread of energy levels in time. These fluctuations, which are driven by a number of molecular motions, such as methyl rotations, pedal motions, resonances in hydrogen bonds, and dipole orientational changes, are referred to as dynamic disorder.<sup>57,58</sup> The exciton delocalization behavior in polymers is determined by the intrachain configurational disorder, including the transfer integral disorder, which determines the electron transfer between the nearest-neighbor sites along the chain, and on-site energy disorder, such as chain conformations; both of them influence the exciton binding energy and thus can facilitate exciton delocalization and even exciton dissociation into oppositely charged polarons driven by the intrinsically existing internal electric field in the chain, if the above disorder parameters are beyond a critical strength.<sup>59</sup> Excitons in large dye aggregates can be delocalized across many fluorophores owing to collective interactions, which, in turn, facilitate suppression of the exciton scattering by molecular vibrations. This delocalization over  $N$  fluorophores leads to the enhanced emission with the rate proportional to  $N^2$ , also called super-radiance. Super-radiance occurs when a group of  $N$  emitters interact with a common light field possessing a wavelength much greater than the separation of the emitters; then the emitters interact with the light in a collective and coherent fashion, which causes this ensemble to emit light of high intensity.<sup>60</sup>

### 2.3. Coherent and Incoherent Excitons

An exciton in a many-body system can be considered with respect to the extent of correlation between the excitations contributing from the different sites. A laser pulse that induces a homogeneous excitation defines a coherent exciton with a coherent-limit many-body wave function  $|h\rho_{coh}\rangle$ , which represents a superposition of the electron and hole excited states.<sup>61</sup> At the same time, this superposition yields a nonzero polarization due to the coherent dipole orientations of the excited states. The exciton coherence can be understood in terms of the joint dynamics of both carrier density (electrons and holes) and polarization, where the coherent exciton state is determined by synchronous carrier density dynamics and polarization dynamics, which are driven by the field and meet the following coherent-limit state relation:<sup>62</sup>

$$(f_k - 1/2)^2 + |P_k|^2 = 1/4 \quad (1)$$

where  $f_k$  is the carrier density and  $P_k$  is the polarization.

For a coherent exciton, the dynamics of its carrier density and polarization are identical, while the dephasing of these processes leads to break of coherence (Figure 3). Incoherence arises due to

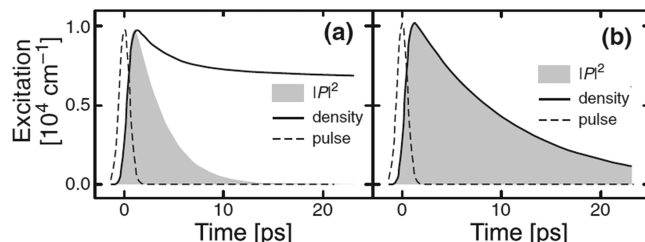


**Figure 3.** (a) Incoherent and (b) coherent decay dynamics of carrier density (solid line) and polarization (shaded region) in a resonantly excited quantum wire. Dynamics of the excitation pulse is shown by the dashed line. Reprinted from ref 61 with permission from Elsevier. Copyright 2006 Elsevier.

excitation- and phonon-induced scattering, which breaks superposition of excited electron and hole states into a strongly correlated two-particle electron–hole pair state. Incoherent excitons can survive the polarization decay and may exist longer after the coherences have decayed (Figure 3). Therefore, the exciton dynamics in general are characterized by two rate constants, the excited state depopulation rate  $\Gamma$  due to radiative and nonradiative recombination processes, which is inversely proportional to the population decay time  $\tau_1$ , and the dephasing rate  $\gamma$  that interrupts phase coherence between the molecular ground  $|0\rangle$  and excited  $|1\rangle$  states, which is inversely proportional to the coherence time  $\tau_2$  and is due to elastic exciton–exciton and exciton–phonon scattering.<sup>63</sup> The latter defines the homogeneous line width of an exciton resonance, whereas the former defines the inhomogeneous broadening due to a varying local potential landscape, which acts differently on the different excitons and masks the intrinsic homogeneous line width in most optical spectroscopy experiments.

The exciton coherence has generated much interest in quantum biology owing to discovery of coherent oscillations in exciton-transfer complexes, which led to an assumption that quantum coherence drives an energy transfer in natural photosynthetic complexes, making them extremely efficient.<sup>64–68</sup>

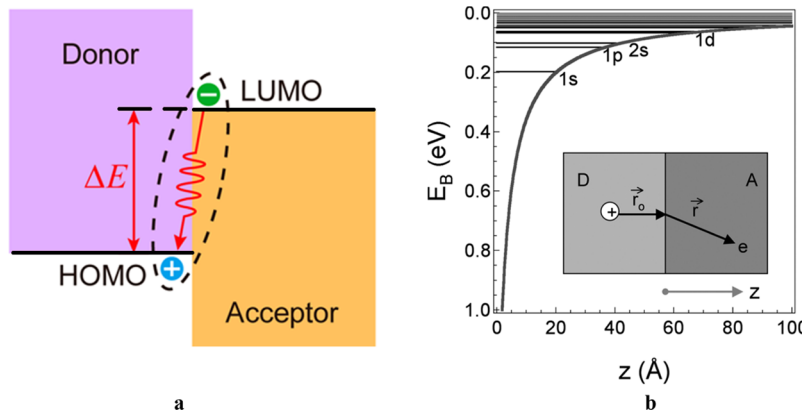


**Figure 4.** (a) Spatial distribution of charges in a CT exciton and (b) binding energy of a CT exciton versus its size. Eigenvalues for the CT exciton are shown in the H atom model. The potential shown is along  $z$ . The binding energy ( $E_B$ ) is referenced to the conduction band minimum. Part b reproduced from ref 75. Copyright 2009 American Chemical Society.

## 2.4. Cold and Hot Excitons

An excitation that lifts an electron above the lowest excitation level of the same multiplet and is not relaxed via vibronic relaxation during the first picoseconds to this level is called a hot exciton. Therefore, hot excitons are excitons that are dressed with vibrational energy. They cool down predominantly via vibrational relaxation to the lowest singlet excitation level, a process that is also called thermalization, resulting in formation of a cold exciton. The hot and cold excitons are accompanied by different degrees of chain distortion and different lengths of exciton localization on the chain. Whereas the mean electron–hole separation due to transitions between  $\pi$  and  $\pi^*$  orbitals, which are both delocalized along the conjugated polymer chain and have similar spatial overlap, can be the same, the extent of exciton delocalization determined by the effective conjugation length that the electron–hole wave packet explores may vary for some polymers. The latter differs for hot and cold excitons, reflecting their different dynamics. Usually the hot excitons with higher energy are more delocalized compared to relaxed cold excitons, which possess smaller coherent size.<sup>69</sup> For example, in poly(*para*-phenylene vinylene) (PPV) oligomers, delocalization of the hot exciton occurs over the whole chain with length of up to 14-mer, whereas excitation distribution for the cold exciton after the vibrational relaxation of the hot one is about four repeat units.<sup>70</sup> Hot excitons, since they are more energetically active compared to the cold exciton, play an important role in photochemical reactions and exciton dissociation at the heterointerfaces, normally accelerating these processes.<sup>71</sup>

Hot excitons can be both singlet and triplet. According to Kasha's rule, hot singlet excitons usually have little effect on fluorescence emission, since their thermalization to the cold exciton state occurs at a much higher rate than the fluorescence itself. On the other hand, hot triplet excitons can contribute to the photophysical properties by using so-called "hot exciton" materials.<sup>72</sup> These materials can effectively harvest the hot nonradiative triplet excitons in organic electroluminescent devices via reverse intersystem crossing from high-lying triplet states  $T_n$  to singlet states  $S_m$  ( $T_n \rightarrow S_m; n \geq 2, m \geq 1$ , Figure 2).

Hot excitons can arise due to the coherent nuclear wavepacket motion of the  $S_1$  state where oscillatory pattern follows almost the same amplitude and phase across the absorption peak, so the modulation of the transition intensity gives rise to quantum beating. Here, the intensity of the quantum beat is coordinate dependent on the  $S_n \leftarrow S_1$  transition moment, that is, the non-

Condon effect, where the vibronic coupling of the  $S_n$  state with other electronic states is significantly large and can be associated with the Herzberg–Teller coupling contribution to the intensity of the quantum beat.<sup>73</sup>

## 2.5. Charge-Transfer Excitons

The concept of the charge-transfer (CT) exciton is normally applied to inhomogeneous media with spatially separated donor and acceptor regions, where charge transfer (electron or hole) occurs across a material interface, such as the donor/acceptor interface in an organic heterojunction solar cell, between different atomic sites of the lattice, or between different molecules, one of them being the donor and the other being the acceptor, while the transferred charge is still electrostatically bound to its counterpart charge, spreading the wave function over a larger distance compared to that of a Frenkel exciton. A typical Frenkel exciton consists of an electron and a hole located in the same spatial region and possesses no dipole moment, whereas the CT exciton represents an intermediate case between Frenkel and Wannier excitons; however, unlike Frenkel and Wannier excitons, CT excitons display a static electric dipole moment.

One can estimate the binding energy of a CT exciton across a donor/acceptor interface which, accounting for the typical low values of dielectric constants of organic semiconductors and the sizes of conjugated molecules, is smaller than the lower limit of the binding energy of a Frenkel exciton,  $E_b = 0.3$  eV<sup>74</sup> but greater by about 1 order of magnitude than the thermal energy,  $k_B T$ , at room temperature (Figure 4). Thus, the CT exciton in organic semiconductors has a relatively low probability of dissociation but can be considered as a predissociation state corresponding to the so-called geminate pairs. In order to provide full charge separation in organic heterojunction solar cells, usually higher excitation level, that is, a hot CT exciton, which is more weakly bound by the Coulomb potential and more easily dissociated, is used.<sup>75</sup>

The hot CT exciton can be regarded as the "dynamic exciton" where a nonadiabatic CT process is driven by coherent vibronic oscillations, which can be observed when energy matching between the vibronic levels for the CT results in the hot exciton. In this case, both electronic coupling between donor and acceptor and entropy are time-dependent by the non-Condon effect due to changing coordinates through conformation dynamics and thermally activated collective movements including the spin–orbit coupling.<sup>76</sup>

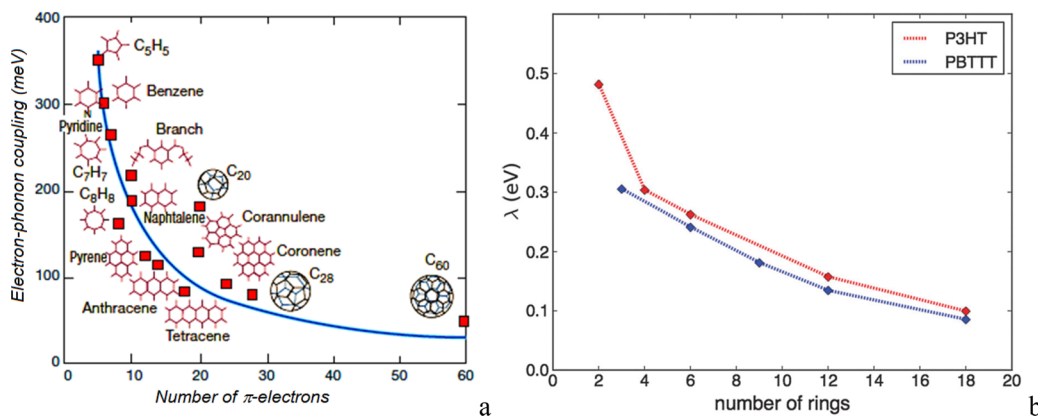


**Figure 5.** (a) Calculated  $\pi$  electron number dependence of the full electron–phonon coupling per molecule. Reproduced with permission from ref 86. Copyright 1998 by the American Physical Society; (b) Reorganization energy of P3HT and PBTTT oligomers as a function of the ring number in the molecular backbone. Republished with permission of the Royal Society of Chemistry from ref 87. Copyright 2015 Royal Society of Chemistry.

The size of the CT exciton generally increases for high-energy CT states, and it also depends on the orientation of the excitation with respect to the interface. Larger excitons are produced by delocalization of the electrons perpendicularly to the interface, whereas smaller electron–hole distances occur for excitations that are delocalized parallel to the interface yielding also a denser spectrum of low-energy CT states.<sup>77</sup>

## 2.6. Dark Excitons

The dark exciton is an optically forbidden electronic excitation in which the direct electronic transition is prohibited by conservation rules. Dark states can be dipole, spin or momentum forbidden. Spin forbidden dark states can be realized in single molecules. For example, the triplet states play the role of dark states as electronic transitions between terms of different multiplicity are spin-forbidden according to the spin conservation rule. In a multichromophoric system, the excited level is formed due to superposition of transition dipoles of interacting chromophores; therefore, photon absorption is allowed if the excited level corresponds to a net nonzero dipole transition moment; otherwise, it would be dark. Different orientation of transition dipoles in an ensemble such as H- and J-aggregates can result in an emergent bright level possessing different energy. In momentum-forbidden dark excitons, the electrons have a different momentum from the holes to which they are bound, which prevents them from absorbing light. The momentum forbidden dark states can be observed in crystalline semiconductors with the band structure like that of transition metal dichalcogenides, due to the shift of the minimum of the conduction band with respect to the maximum of the valence band. The direct electronic transition between these states is forbidden and requires participation of the intervalley phonon.<sup>78</sup>

The optically inactive excitations live orders of magnitude longer than the corresponding optically active excitation, the bright exciton, in which the electron–hole pair has antiparallel spins of the counterparts.<sup>79</sup> Dark excitons can participate in energy transfer through a nonradiative mechanism; however, their observation is difficult. A special class of chromophores, so-called dark quenchers, that primarily relax from the excited state to the ground state nonradiatively (i.e., the dark excitons) can be used as acceptors for Förster resonance energy transfer without contributing significantly to background in the donor-emission channel, even at high concentrations of the quencher.<sup>80</sup>

## 3. BIRTH OF EXCITONS

### 3.1. Dynamics of Exciton Localization

**3.1.1. Polymers with Torsional Degree of Freedom.** Absorption of a light quantum by the conjugated molecule leads to formation of excitation, which encompasses a certain amount of atoms on the conjugated molecular backbone due to the fast delocalization of the exciton followed by its localization. The processes of delocalization and localization of the exciton are dynamic, that is, they are time dependent from the moment of excitation. It should be noted that the localization–delocalization dynamics is applicable only to long conjugated molecules whose length is greater than the exciton radius.

Overall, the localization–delocalization dynamics is mainly dictated by two factors, the spatial dimensionality  $D$  of the system and the electron–phonon coupling. First, the excitation process differs greatly in 1D and 3D systems. In bulk 3D semiconductors, an exciton due to the excited electron–hole pair has a weak Coulomb interaction on the order of a few millielectronvolts. Since this binding energy is comparable to or smaller than  $kT$  ( $T$  = room temperature), such excitons are mostly dissociated after the excitation. In conjugated chains, which are typical quasi-1D semiconductors, exciton binding energies are 1–2 orders of magnitude larger; therefore, 1D excitons are bound tightly, and they have small radius and easily recombine. These properties can be obtained by solving the simple hydrogenic Schrödinger equation in fractional dimensional space,<sup>81</sup> which yields the exciton radius,  $r_e$ , and the binding energy,  $E_b$ , of the 1s exciton as a function of  $D$ :

$$r_e = ((D - 1)/2)^2 r_b \quad (2)$$

$$E_b = (2/(D - 1))^2 E_e \quad (3)$$

where  $r_b$  is the Bohr radius and  $E_e$  is the effective Rydberg constant. It follows from eqs 2 and 3 that in an ideal one-dimensional system the exciton is confined to negligibly small radius and bound by infinitely large Coulomb energy.

Second, a remarkable feature of a 1D electronic system consists in its strong electron–phonon coupling, which is responsible for the dynamic torsional disorder along the 1D chain. The measurement of the electron–phonon coupling is the total relaxation energy,  $E_{rel}$ , which can be expressed via the Huang–Rhys factor,  $S_{ij}$ ; the latter is proportional to the squared displacement of the potential energy minima between the state

$S_i$  and the excited state  $S_j$  as a function of the configuration coordinate, which has the following relation with the former:<sup>82</sup>

$$E_{\text{rel}} = \sum_q S_{ijq} h\nu_q \quad (4)$$

The electron–phonon coupling was found to be a function of length for 1D conjugated oligomers and molecules. It was reported that electron–phonon coupling increases in molecules with a smaller amount of  $\pi$ -conjugated bonds (Figure 5a), and for the linear aromatic acenes it increases linearly as a function of the inverse number of carbon atoms in the molecule.<sup>83</sup> Also, a linear increase of the Huang–Rhys factor versus  $1/m$  (where  $m$  is the number of monomers in the oligomer chain) was reported for *para*-phenylene vinylene<sup>84</sup> and thiophene<sup>85</sup> oligomers with lengths up to 5-mer and 16-mer, respectively, being  $S = 1.44$  for 8-mer,  $S = 1.37$  for 12-mer, and  $S = 1.25$  for 16-mer oligothiophenes. The reorganization energy, which is also a measure of electron–phonon coupling, reflects the difference in vibronic (torsional) relaxations of the excited and ground states, and causes the Stokes shift, decreases with increasing oligomer length (Figure 5b).

However, for the long polymer chain of regioregular poly(3-octylthiophene) (RR P3OT) the Huang–Rhys factor becomes 1.79, larger than that in oligothiophenes. This phenomenon was explained by the stereoregular head-to-tail folding of RR P3OT leading to chain distortion.<sup>85</sup> Thus, the primary factor that increases the electron–phonon coupling is a kind of disorder in long polymer chains or reduced molecular length in oligomers, which both restrict the effective conjugation length.

The dynamics of exciton localization and delocalization in conjugated oligomers of PPV of different length was studied by Tretiak et al.<sup>70</sup> Tretiak and coauthors found that only for long oligomers ( $\text{PPV}_{10}$  to  $\text{PPV}_{14}$ ) the process of exciton relaxation from the hot to the cold state is accompanied by exciton localization in the center of the chain, which suggests exciton self-trapping at the center of the chain by vibrational relaxation. STE may dramatically influence energy transport and radiative recombination of the exciton, showing a broad excimer-like band on the low-energy side of the resonant emission.<sup>88</sup> The self-trapping of the exciton takes place only if the chain is deformable and the constant of exciton–lattice coupling is strong enough; then the exciton creates a chain distortion that produces a new polaronic state below the exciton band bottom.<sup>89</sup>

Self-trapping depends strongly on the exciton motion dimension, and the excitons characterized by one-dimensional motion should always be self-trapped according to the theory developed by Rashba and Toyozawa,<sup>90,91</sup> because there is no any energy barrier that separates free and self-trapped excitonic states, while self-trapping minimum lies lower (Figure 6).

The rate of self-trapping is amazingly fast, and for poly[2-(2'-ethylhexyloxy)-5-methoxy-1,4-phenylenevinylene] (MEH-PPV) films, it was found that exciton localization (self-trapping) occurs with a time constant of  $<120$  fs, which was attributed to coherent dynamics of localization of the initially delocalized excitons driven by structural relaxation of the excited segments.<sup>92</sup>

A similar dynamics of the exciton was found in P3HT polymer chains. First, the primary photoexcitation in P3HT single molecules generates a singlet Frenkel exciton that is initially delocalized over  $\sim 15$  monomer units. At this stage, such an excitation was proposed to be better considered as the exciton delocalized precursor,<sup>93</sup> that is, a kind of CT exciton with quasi-

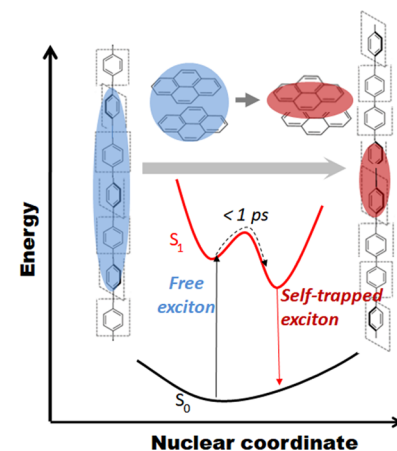


**Figure 6.** Schematic illustration of the exciton self-trapping process in a pyrene dimer and PPP chain: a free exciton (blue spot) may be self-trapped (red spot) due to distortion of intermolecular distance or torsional angle, causing a reduction in exciton energy and mobility.

free electrons and holes capable of ultrafast coherent charge transfer of the primary photoexcited carriers by a quantum mechanical mechanism. This can also be considered as an exciton–polaron formation within tens of femtoseconds from photoexcitation.<sup>94</sup> Second, localization of the above charge carriers to the “true” bound exciton takes place within  $\sim 100$  fs and is associated with local structural chain distortion, which facilitates self-trapping of the exciton to less than 10 monomer units. This ultrafast process gives rise to the initial Stokes shift. This process is not the result of random dynamics due to incoherent hopping of energy by the Förster mechanism, but it can be considered as a quantum coherent process, in the sense that no random dephasing due to electron–phonon interactions is introduced in the scattering wave functions,<sup>95</sup> and therefore it is driven by coherent low-frequency torsional excited-state dynamics, which reorganizes the polymer to lower its free energy so that the exciton drops to a local minimum, or trap, on the excited-state potential energy surface<sup>96</sup> (Figure 6). Third, in addition to the ultrafast ( $< 1$  ps) relaxation, which proceeds within nonequilibrium localized inter-ring torsional motion, there is a slower relaxation ( $> 1$  ps) of the exciton that proceeds on a macromolecular scale and encompasses large-scale planarization of the polymer chain through C=C stretching and torsional twisting.<sup>97</sup> The latter slow relaxation process is due to chain reorganization resulting from stochastic relaxation of the nonequilibrium planarized structure toward a thermally occupied distribution of conformations of the excited state (Figure 7). Such a delayed full geometric relaxation of the distorted molecule can be hindered by intermolecular collisions with the solvent environment and occurs on a time scale of several picoseconds, dependent on the solvent viscosity. Lenderink et al. reported that this process in tetraphenylethylene molecules can be accompanied by the formation of a charge-separated state, so the equilibrium includes a transition between this charge-separated state and the nonpolar excited state.<sup>98</sup>

A clear distinction between the effects of C–C stretch and those of inter-ring torsional relaxation on the exciton localization and delocalization processes was shown by Chang et al. for a set of conjugated zinc porphyrin oligomers.<sup>99</sup> The molecules represented zinc porphyrin macrocycles linked through butadiyne bridges into conjugated oligomers, which displayed degrees of freedom either for only C–C stretch or for both C–C

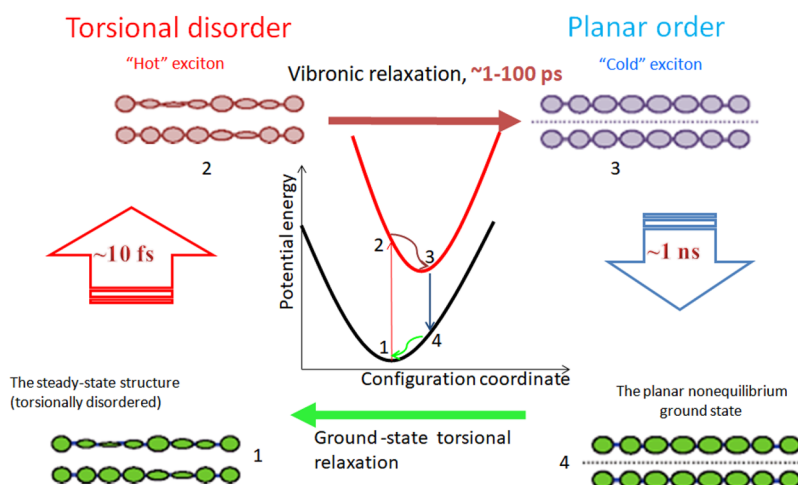


**Figure 7.** Excitation-induced torsional changes in conjugated chains with ring moieties: (1) equilibrium ground-state polymer chain; (2) formation of hot exciton; (3) exciton thermalization; (4) nonequilibrium ground-state polymer chain just after exciton recombination.

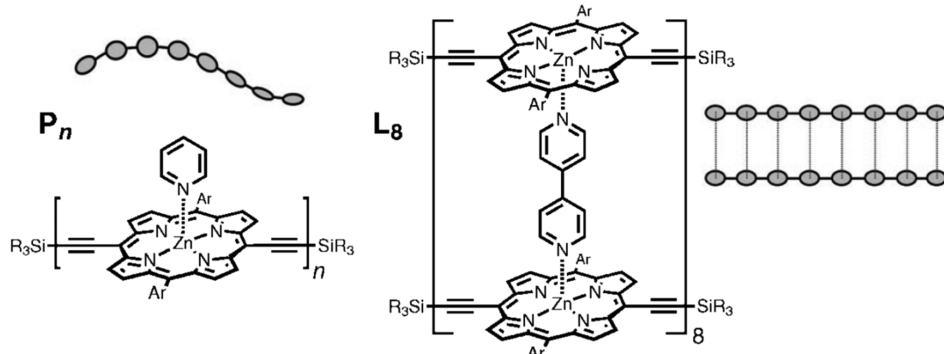


**Figure 8.** Chemical structure and equivalent scheme of the butadiyne-linked zinc porphyrin assemblies in the form of wormlike single-stranded porphyrin oligomers with  $n = 4, 6$ , and  $8$  ( $P_n$ ) and rigid double-stranded ladder octamer ( $L_8$ ), which have degrees of freedom either for both C–C stretch and inter-ring torsional vibrations or for C–C stretch only, respectively. Adapted from ref 99. Copyright 2008 American Chemical Society.

stretch and inter-ring torsional vibrations (Figure 8). These vibrations have a different time scale. Whereas the period of C–C stretch is  $\sim 25$  fs for a typical phonon energy of  $1400\text{--}1600\text{ cm}^{-1}$ , the torsional relaxation can proceed at time scales on the order of one to hundreds of picoseconds. Chang et al. found that photoexcitation generates first an excited state that is initially strongly delocalized along the oligomer but contracts rapidly following vibrational relaxation of the nuclei along C–C stretch coordinates of the porphyrin units and the linking bridges and results in excitonic self-localization on a sub-picosecond time scale. A subsequent torsional relaxation, which proceeds over  $\sim 100$  ps and leads to increased emission intensity and red-shift in the emission band, was associated with growth in the oscillator strength and increasing electronic delocalization of the excited state as a result of chain planarization and enhanced conjugation, respectively. Thus, oscillation of the extent of the excitonic delocalization was shown, when the initially highly delocalized excited-state wave function first contracts and then expands again along the conjugated backbone in accordance with the time scales of the vibrational modes coupled to the electronic transition.

Rather interesting feedback of torsional relaxation on the character of exciton behavior in donor– $\pi$ -bridge–acceptor copolymers, which can play the role of a trap for exciton localization, was revealed by Roy et al.<sup>100</sup> Roy and coauthors demonstrated the gating role of bridge torsions in charge

transfer between the donor and acceptor moieties. Specifically, rich vibrational dynamics of the bridge modes upon photoexcitation leads to backbone planarization within 400 fs, which facilitates hot intramolecular charge transfer state formation, while subsequent cooling vibrational dynamics of the bridge locks the charge transfer state preventing charge recombination and thus resulting in localization of the CT exciton (Figure 9).

Although the torsional relaxation, which plays such an important role in governing the exciton dynamics, can range within time scales between several picoseconds and several hundreds of picoseconds, depending critically on chain length, solvent viscosity, and temperature,<sup>101</sup> Clark et al. showed that in oligofluorene solutions, the torsional relaxation can speed up from  $\sim 10$  ps to  $<0.1$  ps by excitation to a specific higher-lying excited state denoted as  $S_n$ , followed by driving of the excess kinetic energy through nonadiabatic transitions during internal conversion from  $S_n$  to the lowest-lying excited state,  $S_1$ , which causes momentum redistribution so that electronic energy is efficiently dumped into the torsional modes.<sup>102</sup>

**3.1.2. Polyenes.** In polyenes, there are no ring units in the conjugated molecular backbone and therefore an exciton cannot be self-trapped through ring twisting relaxation. This imposes some features on exciton localization and relaxation processes in such chains. In particular, it is widely accepted that *trans*-polyacetylene (*trans*-PA) is a nonluminescent polymer due to the fast relaxation of the photoexcited state into soliton pairs

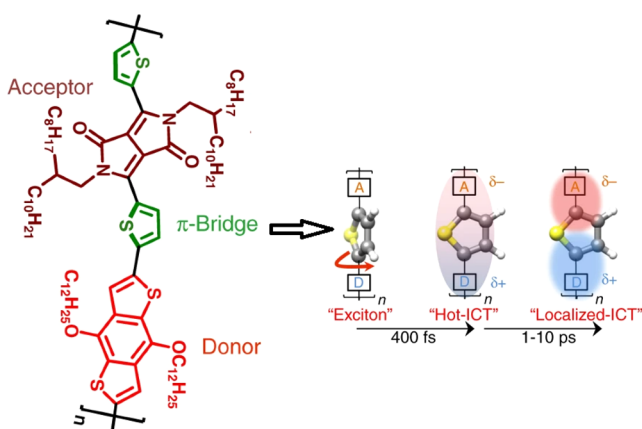


**Figure 9.** Structure of the donor– $\pi$ -bridge–acceptor copolymer and scheme of exciton relaxation via thiophene bridge planarization leading to hot delocalized intramolecular charge transfer (ICT) character and its subsequent cooling dynamics. Adapted with permission from ref 100. Copyright 2017 The Authors under a Creative Commons Attribution 4.0 International License; <https://creativecommons.org/licenses/by/4.0/>.

(Figure 10) instead of localization and radiative recombination of the exciton.<sup>103</sup> It should be noted that solitons can be available

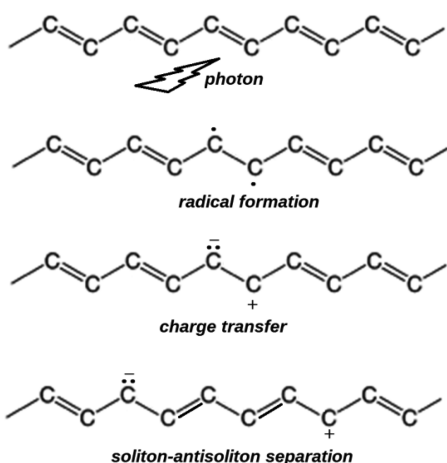


**Figure 10.** Scheme of the excitation dynamics in a polyene chain resulting in soliton–antisoliton pair formation. Not shown is the bond-length deformation in the vicinity of each soliton, which can affect several neighboring monomer units.

in polymers with twisting rings as well, such as pernigraniline (PNB); however, they are confined to two neighboring rings in contrast to *trans*-PA in which the soliton extends over  $\sim 14$  repeat units.<sup>104</sup> Moreover, the intrachain hopping rate ( $\sim 10^8 \text{ s}^{-1}$ ) and the intrachain diffusion coefficient ( $< 10^{-6} \text{ cm}^2 \text{ s}^{-1}$ ) in PNB are much lower compared to those of *trans*-PA, in which these are  $> 10^{13} \text{ s}^{-1}$  and  $\sim 10^{-4} \text{ cm}^2 \text{ s}^{-1}$ , respectively,<sup>105–107</sup> indicating a much more important role of the soliton in excitation dynamics of the polyenes.

Strong electron–phonon interaction also governs exciton dynamics in polyenes, so thermalization of the hot exciton in the PA chain is accompanied by a process where a fraction of the photogenerated  $B_u$  excitons undergo a phonon-assisted transition to the covalent  $2A_g$  state, which then decomposes into two neutral soliton–antisoliton pairs that are subject to ultrafast recombination or dissociation into stable neutral

solitons.<sup>108</sup> Bishop et al. predicted that formation of a soliton–antisoliton pair in PA is accompanied by a persistent, spatially localized, time-periodic nonlinear oscillation (i.e., a “breather”).<sup>109,110</sup> Takimoto et al. noted that soliton, antisoliton, and the first breather in the PA chain can be considered as three components of the triplet exciton.<sup>111</sup> Wang and Martino found that if the system energy is higher than some critical value, photogenerated soliton–antisoliton pairs are free to separate, leaving behind a central breather mode. If the system energy is lower than the critical value, then the soliton–antisoliton pairs are bound and form a different central oscillation called an exciton breather.<sup>112</sup>

The nature of breathers as a result of the ultrafast exciton localization–delocalization dynamics was investigated in more detail by Tretiak et al. through simulation of polyene oligomer molecules.<sup>113</sup> Tretiak and coauthors found an ultrafast variation of bond-length alternation (BLA),  $r_n$ , and lattice compression,  $s_n$ , in *cis*-PA 60-mer along the molecular backbone. While in the ground state, the molecule has a constant bond dimerization and lattice distortion is vanishing along the whole backbone; the exciton formation results in rapid distortion of the lattice in the middle of the chain at a time interval of 16 fs from the photoexcitation impulse and local reduction of the BLA, respectively, which leads to exciton localization in this region on a time scale of  $\sim 20$  fs (Figure 11). In response to the lattice distortion, dynamic vibrational excitations (phonons) are created that propagate in opposite directions, reflect from the chain ends, and meet in the middle of the chain again, pulling an exciton out of its well and leading to its delocalization. The exciton, in turn, attempts to localize again, creating more phonons, that is, energy is exchanging between electronic and vibrational degrees of freedom, thus inducing waves in both BLA and lattice compression (Figure 11). The subsequent breathing dynamics of exciton formation was qualitatively identified as phonon “waves”.<sup>113</sup>

It should be noted that the introduction of side chains to the polyene backbone can induce main-chain bond twisting, which confines excitons in the main-chain segments and results in bright photoluminescence (PL) of the substituted polyacetylene like poly(diphenylacetylene) (PDPA). In this case, the observed PL of pure PDPA-*n*Bu was interpreted through different dynamics of an exciton that relaxes to a lower energy through lattice/vibrational relaxation by the multiphonon process and then recombines from this lower energy radiatively as PL emission. The relaxation energy of this exciton was estimated to be about 0.4 eV, which corresponded to a large Stokes shift in PL of PDPA-*n*Bu and is much larger compared to that of the other conjugated polymers. These observations allow association of this exciton with strong lattice/vibrational relaxation, so that the exciton can be considered as a self-trapped exciton because a stabilized exciton of lower energy on the main chain cannot be easily transported to neighboring chains.<sup>114</sup>

**3.1.3. Rigid Molecular Systems.** In rigid molecules, such as polydiacetylene, ladder-type polymers, cyclic systems, or single-wall carbon nanotubes (SWCNTs), where torsional twisting is inhibited or absent and the electron–phonon coupling is weak, the mechanism of exciton self-trapping is different from that observed in flexible polymers. In SWCNTs, Zhu et al. attributed this process to subdiffusive trapping of dark excitons.<sup>115</sup> Styers-Barnett et al. suggested based on analysis of the transient absorption spectra of SWCNTs that self-trapping can originate from the nonlinear optical response due to the sequential two-photon excitation of biexcitons, giving rise to two

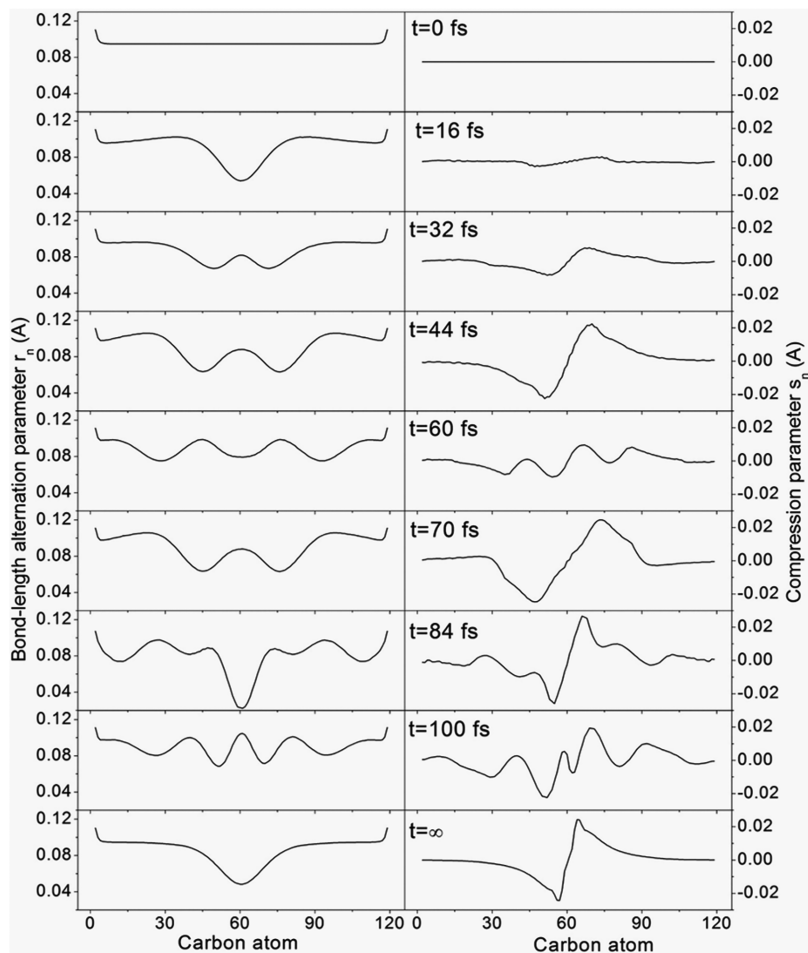


**Figure 11.** Variation of BLA [ $r_n$  ( $\text{\AA}$ )] and compression [ $s_n$  ( $\text{\AA}$ )] parameters in *cis*-PA 60-mer along the polymer's backbone at the indicated time intervals after photoexcitation.  $t = \infty$  corresponds to absorption (fluorescence) events for the molecule being at the ground (excited)-state equilibrium geometry. Reproduced with permission from ref 113. Copyright 2003 National Academy of Sciences, U.S.A.

closely spaced electron–hole pairs, and due to excited biexcitons. In this process, the excitons produced by the pump pulse act as perturbation centers, modifying susceptibility of the SWCNTs and thus changing localization conditions for subsequent electronic excitations in their local vicinity.<sup>116</sup>

Knupfer et al. reported that in the ladder-type phenylene-based (LPPP) polymers in addition to the delocalized exciton with dispersion expected for the  $\pi-\pi^*$  singlet excitonic excitations there exists also a highly localized exciton with a negligible dispersion. It was argued that the mechanism of localization of the latter can be due to the presence of charge-carrier traps slightly above the valence-band edge that have a very narrow energy distribution and are induced by local variations of the electronic structure due to the mutual arrangement of neighboring LPPP chains.<sup>117</sup>

Kraabel et al. emphasized that exciton self-trapping is an open question for single polydiacetylene chains and suggested that it can be a minor component of the  $B_u$  singlet exciton relaxation at best.<sup>118</sup> Despite the fact that electronic states of the polydiacetylene chain, as well as its double- and triple-bond stretching vibrations, are strictly 1D, the authors did not observe instantaneous self-trapping of the exciton as should be expected for ideal 1D models of isolated chains.<sup>62</sup> Kobayashi et al. found that  ${}^1B_u$  free excitons in polydiacetylene films (which of course are not a strict 1D isolated system) relax to the self-trapped state with time constants of  $150 \pm 50$  fs, which is 2 times slower than

in poly(3-methyl thiophene) films<sup>119</sup> which is comparable to the  ${}^1B_u$  exciton lifetime itself in isolated polydiacetylene chains, being 130–135 fs at 20 K.<sup>120</sup> The later studies by Lécuiller et al. showed that the temperature dependence of radiative lifetime of polydiacetylene is proportional to  $\sqrt{T}$  in a wide temperature range, which implies that the exciton behaves as a purely 1D system without localization.<sup>121</sup>

Curved molecular geometries yield specific excited-state dynamics. Ondarse-Alvarez et al. showed that in a bichromophore molecular polygon with bent chromophore chains the bending strain induces exciton localization on individual chromophore units of the conjugated chains and such localization is also very sensitive to molecular conformational distortions induced by thermal fluctuations; thus, both strain and thermal fluctuations lead to exciton localization at different parts of the chains for each excitation event, which makes the polygon a highly unpolarized absorber and emitter.<sup>122</sup> Thiessen et al. compared exciton localization dynamics in model  $\pi$ -conjugated materials possessing structurally the same emissive units but different molecular shape and rigidity, that is, oligomers and cyclic structures of carbazole-bridged phenylene-ethynylene butadiynylene,<sup>123</sup> which have either significant or inhibited twisting degrees of freedom, respectively (Figure 12). While both systems demonstrated a high degree of exciton localization, the localization targets were different. In the linear dimer structure, localization was accompanied by a significant

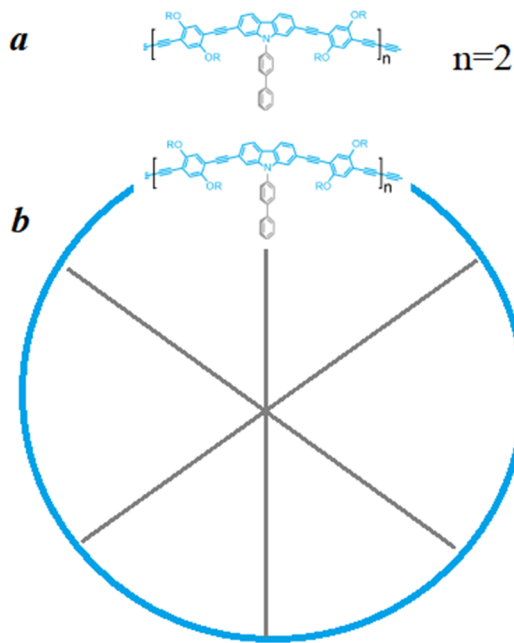


**Figure 12.** Scheme of (a) linear dimer and (b) closed ring structures with the same chromophore unit but with different extent of torsional motion. Adapted from ref 123. Copyright 2015 American Chemical Society.

spectral red-shift within  $\sim 100$  ps after photoexcitation, which was attributed to torsional relaxation, and it resulted in a deterministic exciton position with luminescence characteristics of a dipole. The structurally rigid macrocyclic analogue, where the relaxation mechanism was inhibited, behaved almost like an isotropic emitter because the exciton localized dynamically on different parts of the ring.

Thus, based on this overview of the excitation behavior in rigid molecular systems, one can conclude that exciton self-trapping is hardly possible there.

**3.1.4. Molecular Assemblies.** Whereas in single  $\pi$ -conjugated molecules an exciton can be formally considered as a linear combination of the single-excitation configurations of the chromophore subunits,<sup>124</sup> an exciton in an assembly of interacting chromophores is due to collective electronic excitation of several chromophore units. Interaction of two or more identical molecules in a dimer or in a multichromophoric system (an aggregate) occurs via an oscillating electronic transition dipole moment  $\mu$  between the ground  $|G\rangle$  and excited  $|E\rangle$  states and results in splitting of the degenerate energy levels of the molecules into two levels separated by a quantity,  $2V_{12}$ , called Davydov splitting, which leads to formation of the upper and lower excitonic states.<sup>125</sup> The nearest-neighbor dipole-dipole coupling energy,  $V_{12}$ , can be approximated by a Coulomb dipole–dipole interaction in the excited states:<sup>126</sup>

$$V_{12} = \frac{3\kappa c^3(1 - 3 \cos^2 \theta_{12})}{4\omega_0^3 r_{12}^3} \quad (5)$$

where  $\kappa$  is the spontaneous emission rate for an isolated monomer,  $\omega_0$  is the optical transition frequency,  $\theta_{12}$  is an equilibrium angle between the molecular dipole moment and the aggregate axis, and  $r_{12}$  is the equilibrium nearest-neighbor distance.

Depending on the mutual orientation of the transition dipole moments in an aggregate, these excitonic states can be populated

differently. The extreme cases correspond to the so-called J-aggregate (where transition dipoles of the neighboring chromophores are oriented in a head-to-tail fashion) and H-aggregate (with transition dipoles of the nearest-neighbor chromophores are oriented in a stack, side-by-side manner), when either upper or lower excitonic states, respectively, cannot be populated directly from the ground state and therefore are dark (dipole-forbidden) due to the vanishing resulting dipole moment of the electronic transition (Figure 13). The splitting

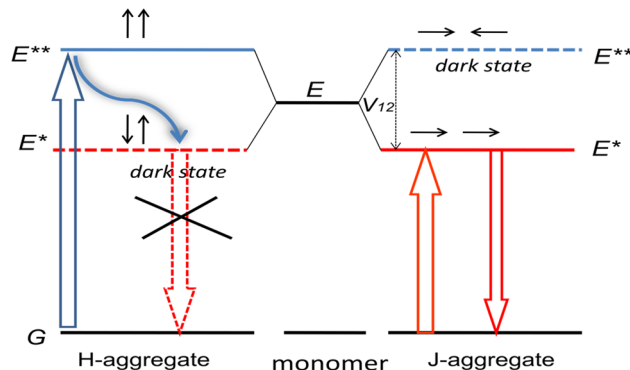


**Figure 13.** Schematic energy diagram of splitting of the excited states of two degenerate exciton-coupled chromophores. Solid straight arrows indicate allowed transitions, the dotted arrow indicates forbidden transition, and the waved arrow indicates the internal conversion.

and different population of the excitonic states has a profound effect on the photophysical properties of the aggregates: the excitation energy is red-shifted in a J-aggregate and blue-shifted in an H-aggregate compared to the spectrum of an isolated monomer, while J-aggregates possess a radiative transition and H-aggregates are essentially nonluminescent, since luminescence should proceed from the lowest excited level of energy multiplicity according to the Kasha rule.<sup>127</sup>

In contrast to the sign of the long-range Coulomb coupling, which changes only once, short-range coupling can render a nontrivial effect on photophysical properties of molecular aggregates due to extreme sensitivity of the short-range coupling to small (subangstrom) transverse displacements between neighboring molecules. On the example of perylene aggregates, Spano et al. demonstrated that the high sensitivity allows J- to H-aggregate interconversions over distances several times smaller than those predicted by Kasha's theory, because the sign of the short-range coupling changes several times as two molecules are "slipped" from a "side-by-side" to "head-to-tail" configuration.<sup>128</sup> Particularly, interference of both short- and long-range Coulomb couplings provides a more complex picture of aggregate formation, which gives rise to new aggregate types, referred to as HH, HJ, JH, and JJ aggregates, possessing distinct photophysical properties. For example, in "null" HJ-aggregates, total destructive interference leads to absorption line shapes practically identical to uncoupled molecules.

Nuclear dynamics of the molecules have a strong influence on the delocalization of an exciton in molecular assemblies, so that the internal interatomic conformation of the molecules forming an aggregate depends critically on the delocalization of the exciton state in the aggregate and vice versa. Beenken et al. considered a dimer as an elementary molecular assembly and showed that electronic excitation of the lower exciton state in a dimer is always localizing, but excitation to the upper exciton state can be delocalizing followed by its subsequent time

evolution governed by the nuclear dynamics.<sup>129</sup> Particularly, it was shown that for the upper exciton state the delocalization length first increases according to the exciton-delocalizing tendency of the nuclear dynamics and later decreases due to non-adiabatic coupling between the two excitonic states, which causes relaxation from the upper to the lower excitonic state and limits the maximum reachable exciton delocalization.

In molecular assemblies, particularly J-aggregates, a high degree of ordering and strong dipole–dipole interaction between molecules forming the J-aggregate leads to extended delocalization of an electronic excitation within a molecular chain. This implies collective electronic excitations in J-aggregates, when excitation of molecules in an assembly proceeds in a resonance manner, that is, coherently. The amount of molecules that participate in such a collective resonant excitation constitutes a coherence length,  $N_{coh}$ , of the aggregate and can be considered as a single absorber or a superradiant emitter. Thus, the excited states of J-aggregate molecular systems are Frenkel excitons that are delocalized over a coherence length that can range from several to several tens of molecules in an aggregate.

The self-trapping states of the exciton in J-aggregates originate from the free delocalized exciton obtained upon photoexcitation of the quasi-one-dimensional molecular assembly. However, the free exciton does not convert to the self-trapped (polaronic) state immediately as is expected for the ideal 1D systems, but both delocalized and self-trapped excitons coexist.<sup>130</sup> Such a phenomenon was explained by the fact that a J-aggregate is not an ideal 1D system and in order to get self-trapping the free exciton must overcome an energy barrier that appears for quasi-1D systems as a result of combination of one-dimensional exciton motion and three-dimension lattice deformation. Therefore, exciton–phonon coupling and aggregate disorder are the main driving forces that cause disturbance of the 1D system and formation of the exciton self-localization in J-aggregates.<sup>131,132</sup>

Both exciton–phonon coupling and disorder, which govern the exciton localization effect, display specific features in molecular assemblies. First, the exciton–phonon coupling results in well-pronounced vibronic progressions in the absorption and PL spectra of isolated chromophores, whereas such a progression is distorted and dependent on mutual orientation of the transition dipole moments in an assembly of the chromophores, and the relative peak intensities of the vibronic sidebands do not follow the Poissonian distribution characteristic of an isolated chromophore.<sup>133</sup> Furthermore, the vibronic line strengths are dependent on the exciton bandwidth, the nature of disorder, and the exciton coherence length. As was shown by Spano, the ratio of the oscillator strengths of the first two vibronic peaks in the absorption spectrum, that is,  $A(S_0 \rightarrow S_1^{0-0})/A(S_0 \rightarrow S_1^{0-1})$ , increases in J-aggregates and decreases in H-aggregates with the increasing exciton bandwidth.<sup>134</sup> In linear J-aggregates with no disorder and periodic boundary conditions, the intensity ratio of the main electronic transition to the first vibronic sideband in the low-temperature PL spectrum is

$$\text{PL}(S_1 \rightarrow S_0^{0-0})/\text{PL}(S_1 \rightarrow S_0^{0-1}) = N_{coh}/S^2 \quad (6)$$

where  $N_{coh}$  is the coherence length of the exciton and  $S^2$  is the squared Huang–Rhys factor of the coupled vibrational mode. With increasing temperature or increasing disorder, the above intensity ratio of the first two vibronic peaks (eq 6) decreases in J-aggregates and increases in H-aggregates. Because increasing disorder or temperature facilitates exciton localization, the PL

ratio in J-aggregates can be used to determine the exciton coherence length, which scales linearly with the ratio of PL vibronic peaks.<sup>135</sup> In H-aggregates, on the other hand, the PL ratio decreases with increasing exciton coherence length because of the more efficient destructive interference among the emitting chromophores.<sup>136</sup> Thus, the exciton–phonon coupling in molecular assemblies leads to redistribution of the vibronic peak intensity both in absorption spectra, depending on the exciton bandwidth, and in PL spectra, depending on the exciton coherence length.

Second, there are two types of disorder in molecular aggregates, the diagonal disorder due to inhomogeneous distribution of site energies and off-diagonal disorder due to variation of intermolecular coupling energies originating from the disorder in intermolecular distances and mutual angles of transition dipoles. These types of disorder can be referred to as static (topological) disorder. In addition, one can distinguish a dynamic disorder that can be described in terms of the temporal dependence of both diagonal and off-diagonal disorder as a result of exciton dynamics, that is, a phonon-assisted exciton hopping due to exciton–phonon coupling. The dynamic disorder implies deformation of an aggregate structure in response to the formation or migration of the exciton.<sup>137</sup> Self-trapping of the exciton proceeds due to dynamic, rather than static, disorder and can be achieved only if the energy of the aggregate structure deformation is comparable to the width of the exciton band and the exciton is able to overcome a self-trapping barrier separating free and self-trapped states, which is just created as a result of exciton-induced deformation of the aggregate structure. The height of the barrier can be estimated as  $W \approx \omega^4/(\gamma^4 m^3)$ , where  $m$  is the effective mass of the exciton,  $\gamma$  is the exciton–phonon coupling constant, and  $\omega$  is the characteristic frequency of optical phonons. Because both  $m$  and  $\gamma$  should be large enough for the exciton to become self-trapped, the barriers  $W$  are basically low. On the other hand, the spatial scale of the barrier is about  $r_b \sim m\gamma^2/\omega^2$ , which is typically much larger than the exciton radius of a monomer molecule. However, owing to the collective nature of a free exciton in J-aggregates, its coherence length can be as high as 50–100 molecules at low temperatures;<sup>138</sup> therefore, there is no problem for a free exciton to overcome this spatial scale as well.

The static disorder can be described as diagonal disorder in an aggregate, which is characterized by random distribution of site energies that obey a Gaussian distribution. It is interesting that for the Lévy type energetic disorder, Eisfeld et al. predicted two types of localization of the collective electronic excitations in molecular aggregates.<sup>139</sup> Whereas for Gaussian disorder only one mechanism of exciton localization exists, namely, localization of states in effective potential wells created by random site energies, in the case of the heavy-tailed Lévy distribution a second localization mechanism appears. This mechanism is owing to the long tails of Lévy distribution, which give rise to sites with relatively high energy. The energy of these outliers can be so large that they overcome the energy of interaction and break up the chain in segments of length  $N_{seg}$  capped by two outliers, which determine the intervals over which the excitons may delocalize. Eisfeld and coauthors discussed that the existence of two localization mechanisms with their own length scales is directly responsible for the observed nonuniversality of the localization length distribution and that the interplay between both mechanisms is also responsible for the disorder scaling of the exchange broadening of the absorption band.

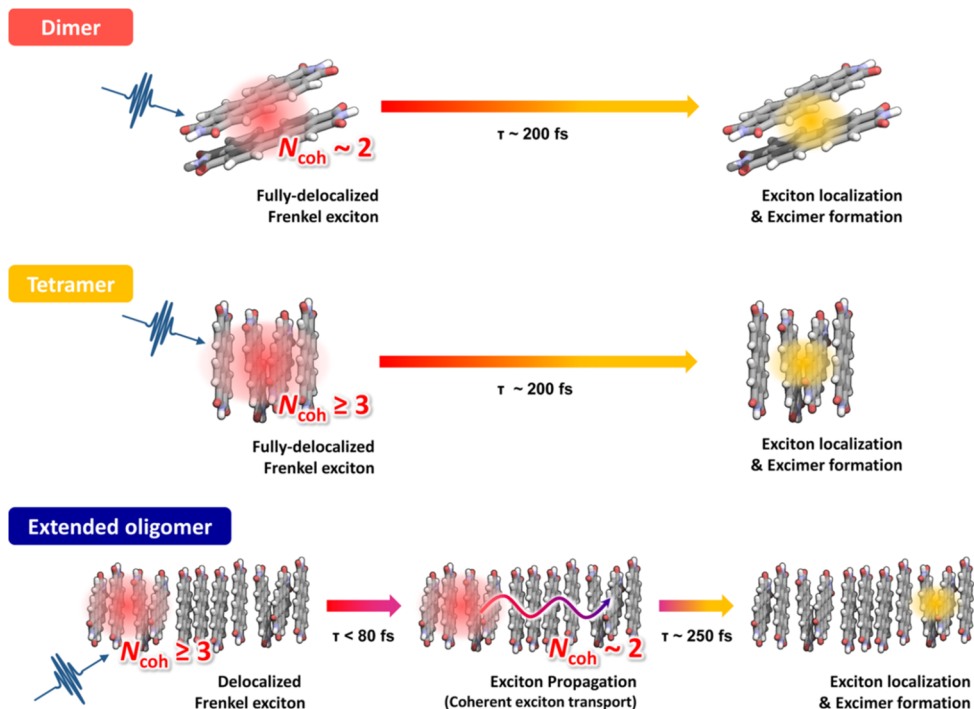


**Figure 14.** Schematic illustration of Frenkel exciton relaxation and excimer formation dynamics in PBI dimer, tetramer, and extended oligomeric H-aggregates. Reproduced from ref 147. Copyright 2018 American Chemical Society.

Excitons in two-dimensional excitonic systems, such as  $\pi$ -stacks of polymer chains with electronic excitations delocalized both along the polymer chain and between the chains, possess a dual nature.<sup>133</sup> On one hand, photoexcited electron–hole pairs within polymer chains are well delocalized over several repeat units and can be considered as excitons of the Wannier–Mott type. On the other hand, delocalization is limited at most to neighboring chains across the chains; therefore, the excitons in this case are of the Frenkel type. Thus, these excitations can be described as those related to both J- and H-aggregates.

In molecular assemblies, that is, molecular crystals, dimers of aromatic molecules such as pyrene, and J-aggregates of dyes such as cyanines, there is a particular case of exciton localization or self-trapping. Such localization is particularly associated with the deep self-trapping exciton state<sup>140</sup> originating from a free exciton that is relaxed on the same aggregate through interaction with molecular vibrational modes and can be classified in terms of excimer formation.<sup>141,142</sup> An excimer is normally referred to as an unstable complex composed of a pair of an excited molecule and a ground state molecule that exists due to attraction of the molecules as long as one of them is in the electronic excited state and dissociates after photon emission of the pair has occurred.<sup>143</sup> Excimers in the solid state (i.e., crystals, aggregates, films) possess some specificity, because the interacting species cannot literally dissociate being in the ground state, due to the rigid environment. Nevertheless, the luminescent emission of dimers with significant intermolecular interactions due to van der Waals forces or  $\pi$ – $\pi$  stacking like noble gas or aromatic pyrene crystals, respectively, has been recognized as being excimeric in nature as well. In inorganic crystals composed of metal halides or noble atoms a strong exciton–lattice coupling is responsible for the formation of the covalent bond in the excited state of adjacent atoms that do not have such bonding in their ground state. In molecular crystals or aggregates, it was discussed that the excimer configuration can be achieved with further

approach of two molecules that were already adjacent.<sup>144</sup> In other words, a preassociated dimer is needed to provide the formation of the molecular excimer.<sup>145</sup>

Although the term excimer or, in other words, excited state dimer is traditionally limited to cases where a true dimer is formed, a special interest is extended to larger complexes, that is, those composed of a large amount of molecules, that exist in the excited state. In the extended systems, first, the Frenkel exciton can be delocalized over more than one molecule, and second, the excimer formation normally requires significant diffusion of the electronic excitation to specific sites where the exciton becomes localized in the form of an excimer. Also, there is some difference depending on whether the excimer is formed in J- or H-aggregates.

Würthner et al. compared localization dynamics of the Frenkel exciton toward the excimer state in discrete  $\pi$ -stacks of perylene bisimide (PBI) depending on their size, that is, in dimeric, tetrameric, and oligomeric H-aggregates.<sup>146,147</sup> In dimers and tetramers of PBI, since the coherence length of a free Frenkel exciton ( $N_{coh} \geq 3$ ) is comparable to or confined by the aggregate size, there is the only option for the photoexcitation to relax to the excimer state with ultrafast exciton localization on a selected molecule of the aggregate during  $\sim 200$  fs. In the extended H-aggregate, on the other hand, the free exciton is able to propagate some distance for  $\sim 80$  fs, followed by its localization and formation of an excimer state similar to the process in the short aggregates (Figure 14). It is interesting that the exciton starts the localization process being in its coherent propagation along the long one-dimensional aggregate, so that its  $N_{coh}$  experiences an ultrafast decay to the value of  $\sim 2$ .

Slower dynamics of excimer formation was observed in crystalline pyrene. Pensack et al. found that the excimer formation in crystalline pyrene nanoparticles occurs in two stages on a picosecond time scale: first, the primary exciton converts to the intermediate thermally excited excimer during

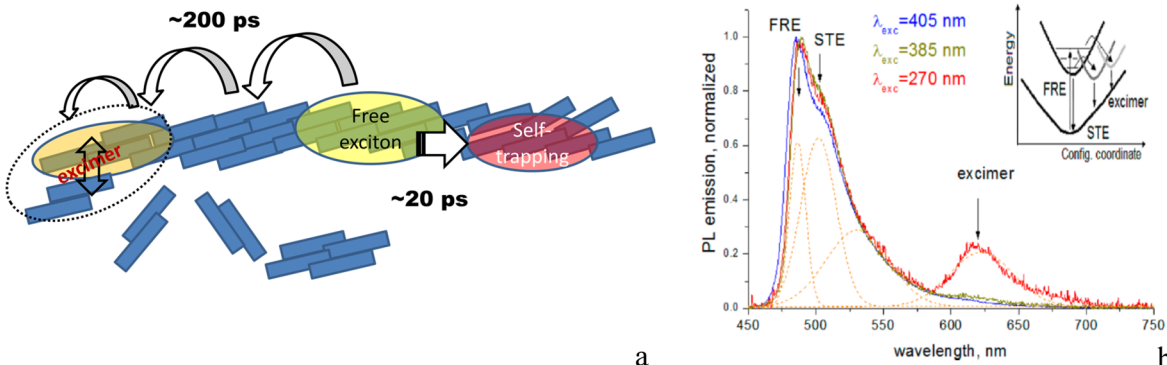


**Figure 15.** (a) Scheme of free exciton localization processes to self-trapping and excimer-forming sites and (b) signature of excimers in PL spectra of solution of mixed J-aggregates and dimers of thiamonomethinecyanine dye. Abbreviations: FRE, free resonance exciton; STE, self-trapped exciton. Reproduced from ref 148. Copyright 2018 American Chemical Society.

~4 ps, followed by the full structural relaxation of the hot excimer excitation in the next ~17 ps.<sup>142</sup> The authors discussed that excimer formation is a relatively straightforward process that can be simply viewed as the relaxation of a singlet exciton into excimer geometry, but a change in the mutual displacement of pyrene molecules with excimer relaxation takes place as well.

In more extended molecular assemblies such as J-aggregates of thiamonomethinecyanine dyes, which are in thermodynamic equilibrium in the solution with their building dimer blocks, specific excimers can arise due to intermolecular off-diagonal interactions of a free exciton of the J-aggregate and the dimers.<sup>148</sup> These excimers originate due to dynamics of free delocalized excitons possessing a coherence length of four molecules, which migrate to the excimer formation site during 100–200 ps, where they interact with a guest dimer in the ground state (Figure 15). Since formation of such excimers is competitive with exciton self-trapping and is also sensitive to the excitation energy, it was proposed that the original exciton should be hot in order to overcome the necessary barrier for the excimer formation (Figure 15).

### 3.2. Exciton-Induced Chemical Dynamics

Photoinduced transformations of the chemical structure of a molecule can be displayed via different intramolecular chemical reactions, such as exciton-induced intramolecular electron transfer, excited-state proton transfer, photocyclization, hydrogen bonding, molecule–metal ion–molecular anion release, photolysis, etc. Some of the above processes are reversible and some are not. Below we consider the most important cases of exciton-induced dynamics of molecular chemical state.

**3.2.1. Intramolecular Electron Transfer.** Excitations that promote changes in charge distribution and structural rearrangement of a molecule potentially influence its chemical reactivity and the course of chemical reactions it may encounter. Particularly, charge redistribution in the excited state may change molecule–molecule interaction and, therefore, molecular chemical reactivity. Exciton-induced intramolecular charge transfer (ICT) is one such option.

An exciton in conjugated molecules is often considered as a Frenkel exciton, when an electron–hole pair has small size on the order of a few conjugated bonds. However, in molecules whose different parts have different electron/hole affinities, the exciton tends to adopt a CT character, where the electron and holes become separated on these different molecular parts. The charge transfer character of the first excitation band of cyanine dyes, that is, the molecules that contain an odd number of

methine groups bound together by alternating single and double bonds, is well-known. However, this phenomenon is largely dependent on the conjugated chain length due to the change in the bond alternation character, which is a function of the chain length.

Relatively short cyanine dyes possess two dominant resonance forms with respect to the position of double bonds on a polymethine chain; the interchange of the single and double bonds in the chain does not change its energy, leading to an average “bond and a half” representation, that is, nonalternating, structure (Figure 16). Such a structure represents an ideal

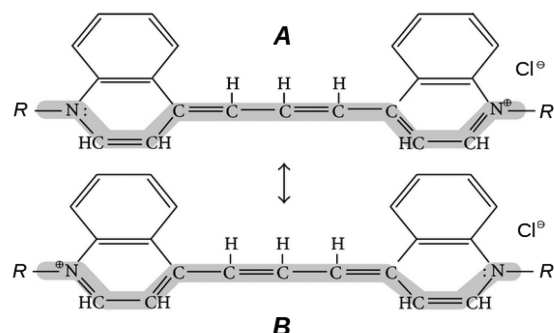


**Figure 16.** Two resonant forms of carbocyanine chloride dye. The A and B structures are equivalent in terms of energy.

molecular wire with  $\pi$ -electrons delocalized over the chain. However, at sufficient length the two forms are no longer equivalent due to Peierls transition leading to the bond localization (bond-length dimerization) in the chain, when single and double bonds cannot freely interchange anymore. In this case, cyanine dyes and related linear systems undergo symmetry collapse, leading to the electron density being locked at the electron-accepting end of the polymethine chain, while the chain ends cannot communicate in the ground state because the molecule is not a “molecular wire” anymore due to bond-length dimerization. Thus, the properties of these systems do not extrapolate from their shorter counterparts, demonstrating, for example, deviation from a linear dependence of the band gap on the reverse value of the effective conjugation length,  $N_{\text{eff}}$ , according to eq 7:<sup>149</sup>

$$\Delta E = hc/\lambda = E_\infty + k/N_{\text{eff}} \quad (7)$$

Here,  $N_{\text{eff}} = k/(N_\pi + C)$ , where  $N_\pi$  is the number of  $\pi$ -electrons involved in the conjugation,  $C$  is a constant that depends on the

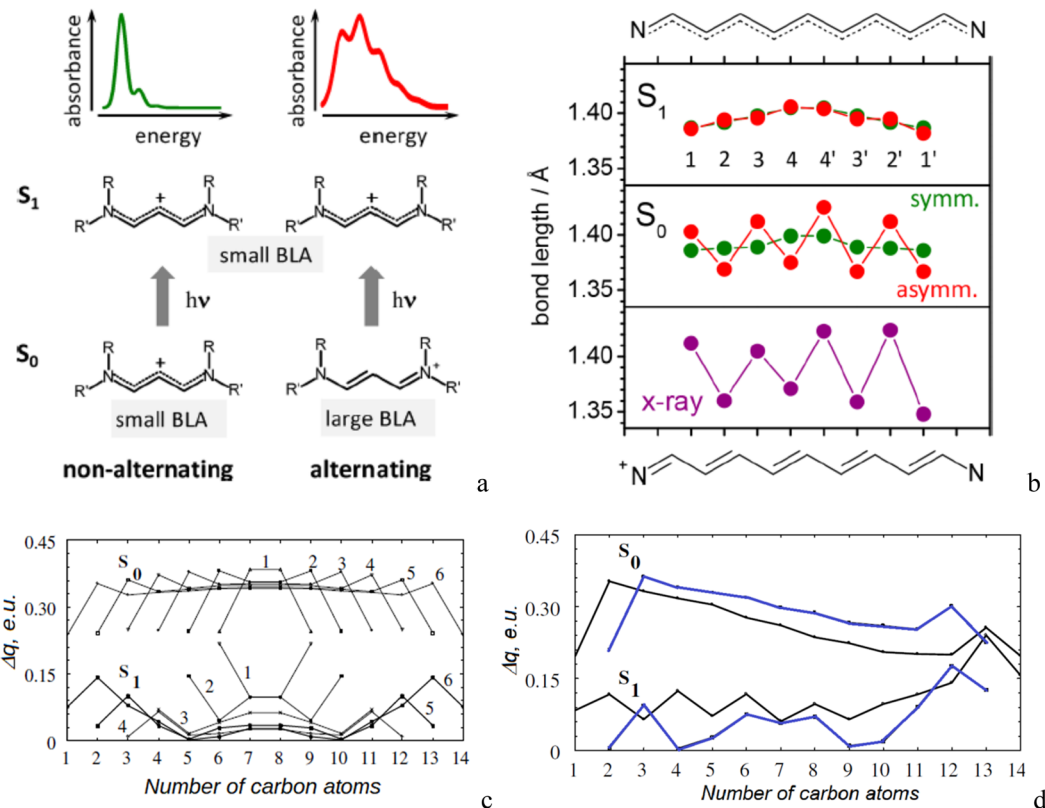


**Figure 17.** (a) Ground- and excited-state geometries of nonalternating and alternating cyanines and the impact on the absorption spectrum. (b) (TD)DFT calculations of bond lengths of the carbon–carbon bonds ( $n, n'$ ) of the ground-state (center) and excited-state (top) optimized states for the symmetric (green) and asymmetric (red) cases of the indicated cyanine dye salt and the bond lengths along the conjugated path according to the crystal structure (bottom). (c, d) Charge variation for the ground state ( $S_0$ ) and excited-state ( $S_1$ ) as a function of carbon atom and chain length for thiacarbocyanines of (c) symmetric mono- to hexa-carbocyanine (3–13 carbon atoms in the merocyanine chain) and (d) asymmetric penta- (blue curves) and hexa-carbocyanine (black curves) forms. Parts a and b reproduced from ref 157. Copyright 2020 American Chemical Society. Parts c and d reproduced with permission from ref 154. Copyright 2004 Elsevier B.V.

terminal groups, and  $E_\infty$  corresponds to the band gap at infinite chain length. It has been shown that while the absorption and fluorescence bands of polymethines with nonalternating structure can be significantly shifted from the visible to the IR-region up to 1600 nm by lengthening of the polymethine chain (according to eq 7) or by introduction of specific terminal groups with their own large  $\pi$ -electron systems,<sup>150</sup> the related neutral polyenes, which possess an alternating structure of the CC double and single bond lengths, undergo a substantial change of CC bond lengths upon photoexcitation, while the atomic charges remain practically unchanged, which results in their chain lengthening being accompanied by a much smaller red shift of the corresponding spectral bands as compared to polymethines, with their spectral limit of ~700–800 nm, which depends slightly on the constitution of the terminal groups.<sup>151</sup>

Kuhn determined that symmetry collapse as a function of the chain length takes place for simple cyanines at chain dimension of 30 carbon atoms,<sup>152</sup> whereas Tolbert et al. observed this limit for dipyridyl cyanine cation dyes to be 13 carbon atoms,<sup>153</sup> and Lepkowicz et al. reported that the symmetry breaking for thiacarbocyanines occurs for chain length as short as 11 carbon atoms.<sup>154</sup>

Formation of an exciton in symmetry-collapsed cyanines is associated with intervalence electron transfer absorption, demonstrating broad absorption bandwidth,  $\Delta$ :

$$\Delta = (2310E_{\text{CT}})^{1/2} \quad (8)$$

where  $E_{\text{CT}}$  is the energy of the intervalence absorption band in  $\text{cm}^{-1}$ . In this case, while the positive charge is localized at one end in the ground state, it clearly migrates to the other end in the first excited state. Thus, symmetry breaking leads to dramatic changes in the absorption spectrum, such as band broadening and a decrease in the intensity of the transition (Figure 17a). The band broadening due to the intramolecular charge transfer from one side of the dye molecule to the other was confirmed experimentally for a series of thiacarbocyanines (from monomethine to hexamethine) by Tolmachov et al.<sup>155</sup>

However, in addition to the asymmetrical form of the charge distribution in long polymethine chromophores, a symmetric charge distribution was predicted as well.<sup>154</sup> The latter was explained by a specific property of a linear conjugated polymethine chain, which experiences a symmetry collapse and becomes similar to a polyene chain, to produce solitons (see Figure 10). Then, if the width of the solitonic wave (15–17 carbon atoms) exceeds the dimensions of the dye molecule, the molecule can adopt only the symmetric charge distribution. In this case, polymethines possess a narrow and intense absorption band and nonpolar solvatochromism, a large red shift of the band with the increasing chain length. If the width of the soliton becomes comparable to the length of the polymethine chain then both symmetrical and asymmetrical charge distributions can be detected depending on the polarity of the solvent used (Figure 17b). For example, it was observed that the less polar solvent *o*-dichlorobenzene stabilizes the symmetric form only,

whereas the more polar acetonitrile leads to the coexistence of both symmetric and asymmetric forms of thiapentacarbocyanine iodide dye with the ratio of 5 to 1.<sup>154</sup>

It should be noted that the exciton formation in polymethine dyes is accompanied by different degrees of charge transfer in symmetric and asymmetric forms. In the symmetric forms, which possess equal lengths of the single and double bond and substantial alternation of the positive and negative charges at the carbon atoms, the  $S_0 \rightarrow S_1$  transition is accompanied by considerable  $\pi$ -electron density transfer from the carbon atoms in odd positions to ones in the even positions (Figure 17c). Since excitation leads to a substantial change of the atomic charges while the CC bond lengths remain practically unchanged, this leads to relatively strong first electronic transition  $S_0 \rightarrow S_1$ . The nature of the same transition for the asymmetric form is different; due to charge localization it is connected mostly with the transfer process from one part of the chromophore to another (Figure 17d), and these dyes show limitations in the peak absorption positions.

Excitation of conjugated molecules that consist of repeat units with conjugated rings is normally associated with the benzenoid-to-quinoid bond-order reversal.<sup>158</sup> However, such a dynamical change in the chemical structure has certain specific consequences for the different conjugated polymers. In polymers whose structure consists of equivalent ring moieties, such as PPP, P3HT, etc., benzenoid-to-quinoid bond-order exchange does not require charge transfer between the rings (Figure 18). The emeraldine base (EB) form of polyaniline

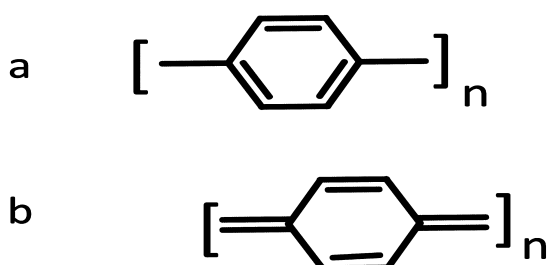


**Figure 18.** (a) Aromatic benzenoid and (b) quinoid structures as elements of the conjugated molecular backbone.

(PANI) represents the other structure, where the rings are two basic groups possessing different electron affinities, namely, the electron-rich benzenoid group and the electron-deficient quinoid group, connected either via amine or imine nitrogens (Figure 19a) and where the benzenoid-to-quinoid bond-order exchange requires charge (proton) transfer. On the other hand, the ratio of benzenoid-to-quinoid groups in the PANI backbone determines the chemical properties of the polymer itself.

Menšík et al. reported that the excitation of the EB form of PANI by a pump pulse (700 nm) in the absorption tail of the quinoid Q-band leads to break of the polymer initial symmetry via formation of a charge transfer state within 50 fs.<sup>159</sup> Since the PANI backbone consists of two basic groups possessing different electron affinities, then, the electron transfer is expected to proceed from the benzenoid to the quinoid units (Figure 19a). Addition of an electron to the quinoid ring and removal of it from the benzenoid one does not lead to benzenoid-to-quinoid bond-order reversal but to formation of a localized CT exciton. In case of doping of PANI with protonic acids, which converts quinoid moieties to the benzenoid ones, the absorption band associated with ICT cannot be observed in the protonated

PANI. On the other hand, blocking of some benzenoid units on the PANI backbone by oxidation with the strong electron acceptor tetracyanoquinodimethane (TCNQ) does not substantially affect the ICT, since the quinoid Q-band intensity remains almost the same<sup>160</sup> (Figure 19b), which means that the size of the CT exciton is very small and seizes only neighboring rings.

Copolymers possessing more than two building blocks with different electron-donating and electron-accepting properties in the backbone provide an interesting opportunity for observation of different types of CT excitons. Formation of more than a single CT exciton was suggested in a copolymer of aniline with 3-methylthiophene (PANIMT).<sup>161</sup> The two excitons are due to the presence of two reduced (aniline and 3-methylthiophene) and two oxidized (quinoid) groups on the polymer chain (inset in Figure 20). The exciton that arises due to absorption at 360 nm was assigned due to a shift of the electron density from the aniline to the 3-methylthiophene unit during the electronic excitation, whereas the exciton observed at  $\sim$ 530 nm was assigned to CT excitation in longer structural units of the copolymer chain, which involves oxidized units (Figure 20).

**3.2.2. Excited-State Proton Transfer.** Excited-state proton transfer is a chemical reaction that belongs to processes of photoinduced transformations of the chemical structure of a molecule. Excited-state proton transfer can be intramolecular or intermolecular. Excited-state intramolecular proton transfer (ESIPT) was reported for different compounds, such as benzoquinolines, naphthols, dihydroxydibenzophenazines, and hydroxyflavones.<sup>162</sup> Usually in these compounds, hydrogen bonding is present in the  $S_0$  state, but upon excitation the intramolecular hydrogen bonds are strengthened in the  $S_1$  state, for example, between the  $-\text{OH}$  group and the pyridine-type nitrogen atom in 1,8-dihydroxydibenzo[*a,h*]phenazine,<sup>163</sup> which can facilitate the proton transfer process effectively. However, ESIPT from the higher excited electronic states ( $S_n$ ,  $n > 1$ ) was reported as well.<sup>164</sup>

The ESIPT phenomenon can be presented with potential energy surfaces that possess two minima for both the ground and excited state (Figure 21), which correspond to the initially excited form and proton transferred form of the molecule. The two minima are often separated by a barrier. For example, an energy barrier of 1.93 kcal/mol was found in 1-morpholinylmethyl-2-naphthol. Upon optical excitation of the ground-state enol to the first excited state, proton transfer occurs along the route  $\text{O}_{17}-\text{H}\cdots\text{N}$ , which generates the keto tautomer (Figure 21). However, the low energy barrier (0.26 kcal/mol) for proton back-transfer facilitates the conformation transition from the keto to enol form.<sup>165</sup>

In some cases, three stable structures of corresponding tautomers can be found in the  $S_1$  state, which are separated by relatively low barriers and which therefore can initiate a double proton transfer.<sup>166</sup> Processes with small or zero barriers were observed for *o*-hydroxyl benzaldehyde, salicylic acid, and hydroxybenzoquinoline, to mention just a few. In this case, ESIPT is ultrafast and unidirectional. In 9,10-dihydroxybenzo-[*h*]quinoline (9,10-HBQ), ESIPT occurs in the  $S_1$  state that has no potential energy barrier along with hydrogen bond  $\text{O}_3-\text{H}_4\cdots\text{N}_5$  forming one proton-transfer molecular structure, whereas the second proton transfer via another intramolecular hydrogen bonded wire  $\text{O}_1-\text{H}_2\cdots\text{N}_3$  with a low potential energy barrier (about 7.69 kcal/mol) in the  $S_1$  state results in the other proton-transfer molecular configuration. After completing the excited

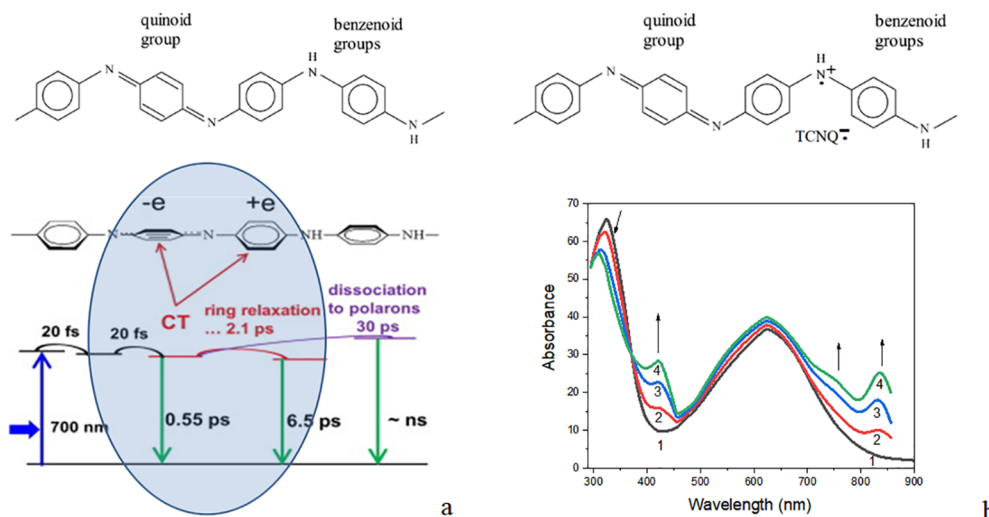


**Figure 19.** (a) Ground-state molecular structure and scheme of exciton dynamics in EB of PANI. CT exciton can recombine nonradiatively from either hot or relaxed CT energy states with time constants of 0.55 and 6.5 ps, respectively, or dissociate into polaron pairs. Time constants denote energy funneling through the manifold of hot states (20 fs), transition of the hot exciton to the ground state (0.55 ps), phenyl relaxation (2.1 ps), transition of the cold exciton to the ground state (6.5 ps), and polaron state formation (30 ps). Adapted with permission from ref 159. Copyright 2015 Elsevier. (b) Molecular structure of the oxidized form of PANI and electronic absorption spectra of the C<sub>15</sub>TCNQ-EB mixed solutions, corrected for the spectrum of the neutral C<sub>15</sub>TCNQ, with the following molar ratios of C<sub>15</sub>TCNQ to EB tetramer: (1) 0:1.0, (2) 0.03:1.0, (3) 0.07:1.0; (4) 0.10:1.0. The increasing band at 417 nm corresponds to the cation-radical of EB, while peaks at 758 and 856 nm correspond to the anion-radical of TCNQ. Reprinted from ref 160 with permission from Elsevier. Copyright 1997 Elsevier.

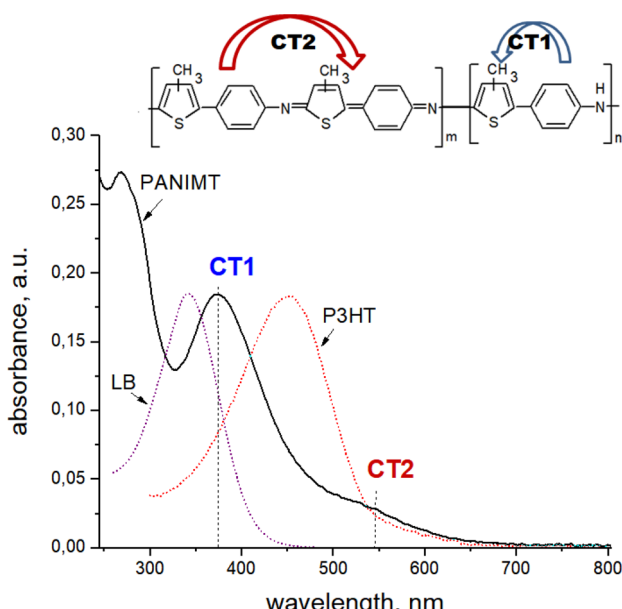


**Figure 20.** Molecular structure and electronic absorption spectrum of PANIMT in acetonitrile solution (0.001 wt %) compared with molecular spectra of leucoemeraldine base (LB) of PANI and P3HT. Adapted from ref 161. Copyright 2008 American Chemical Society.

state dynamical process, the S<sub>1</sub>-state proceeds back to the S<sub>0</sub> state resuming the initial 9,10-HBQ structure.<sup>167</sup>

The rate of ESIPT can vary greatly, from sub-picosecond<sup>168</sup> to microsecond<sup>169</sup> time scales, depending on the molecular structure, length of the hydrogen bond, and environmental media polarization.<sup>170</sup> Particularly, it was reported that stronger intramolecular N–H···N hydrogen bonding leads to faster and more exergonic ESIPT in amines,<sup>171</sup> whereas longer hydrogen

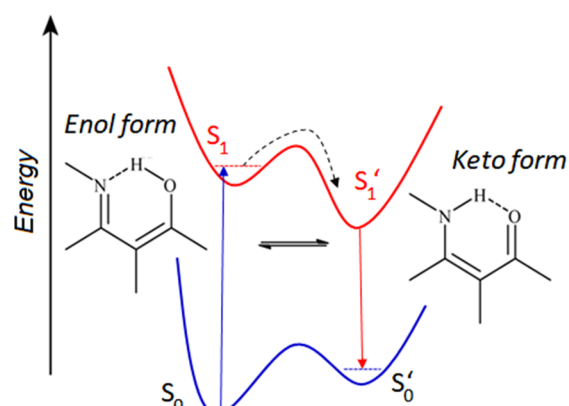


**Figure 21.** Illustration of ESIPT between enol and keto forms of *o*-hydroxy Schiff bases.

bonds lead to slower ESIPT rates among related indole derivatives.<sup>172</sup>

ESIPT can influence exciton delocalization as well. Guo et al. revealed by steady-state spectroscopy and theoretical calculations that ultrafast ESIPT in a novel 2-[3-(benzo[*d*]thiazol-2-yl)-2-hydroxy-5-methylstyryl]-3-ethylbenzo[*d*]thiazol-3-ium iodide NIR-emitting molecule leads to the efficient extension of  $\pi$ -conjugation in the molecular backbone in its excited states, which leads to a large Stokes shift and high quantum yield of fluorescence emission.<sup>173</sup>

Recently, a role of nuclear quantum effects in the ESIPT process was theoretically predicted by Zhao et al.<sup>174</sup> Their simulations reveal that nuclear quantum effects influence the proton transfer reaction rates and kinetic isotope effects due to the intrinsic delocalized nature of the quantum nuclear wave function. Yoneda et al. showed that ESIPT can be dynamically modulated by a nuclear wavepacket motion via Hertzberg–Teller type oscillations in 2,2'-dihydroxy-azobenzene. The

observed vibration was assigned to the mode that modulates the distance between oxygen and hydrogen atoms and the origin of the non-Condon effect was attributed to a dynamical change of configuration interaction between enol and keto characters along the vibrational coordinate, indicating that this vibration is strongly related to the reaction coordinate of ESIPT.<sup>175</sup>

Intermolecular excited-state proton transfer (ESPT) takes place due to a change in acidity or basicity of molecules upon photoexcitation because electronically excited states usually possess stronger acidic and stronger basic properties, respectively, compared to the corresponding acids and bases in the ground state.<sup>176,177</sup> In these cases, a proton release from the excited state is more facilitated, followed by immediate proton uptake upon exciton recombination to the ground state. This can be considered with the example of a phenol molecule, which is known to be a weak acid in its ground state but attains much stronger acidity in the excited state. Upon photoexcitation, ICT from the oxygen atom to the aromatic ring system takes place,<sup>178</sup> which reduces the electron density on the hydroxyl group and thus weakens the OH bond, making proton dissociation more facile. By this mechanism organic acids become more acidic in their electronically excited states. This phenomenon is called photoacidity and is displayed as significant changes in  $pK_a$  values for many phenols upon photoexcitation. 7-Amino-2-naphthol, for example, has a ground state  $pK_a$  of 9.6 but an excited state  $pK_a^*$  of 1.1.<sup>179</sup> Excitation of photoacids also causes redistribution of the hydrogen bonding network in the solvent environment, strengthening H-bonding between the hydrogen atom of the acid and oxygen of the solvent and weakening H-bonding between its oxygen atom and hydrogen atoms of the solvent molecules (Figure 22).

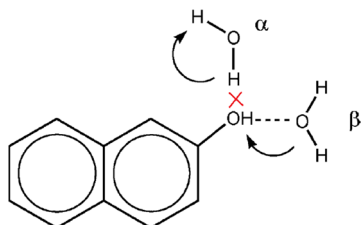


**Figure 22.** Upon photoexcitation,  $\alpha$  configuration breaks and  $\beta$  configuration becomes stronger due to the shift of electronic density from the hydroxyl to the aromatic core. Adapted from ref 183. Copyright 2005 American Chemical Society.

Organic bases also attain stronger basicity upon photoexcitation.<sup>180</sup> These properties lead to enhanced reactivity in mixtures of weak acids and bases and to the possibility of proton transfer between acidic and basic groups in the excited state in cases where such proton transfer is not possible in the ground state.<sup>181</sup> In this case, ESPT is a bimolecular process; however, it can proceed also as a pseudo-unimolecular one in case of the proton transfer from photoacid to solvent.<sup>182</sup>

The rate of ESPT reactions can span 8 decades in time scale, from sub-femtosecond to sub-microsecond, which includes the following processes: electronic redistribution upon excitation (sub-femtosecond), hydrogen-bond rearrangements near the OH group (femtosecond), proton dissociation followed by proton solvation and mobility (picosecond), and geminate recombination of the dissociated proton with the conjugate photobase, quenching, and excitation decay (nanosecond).<sup>183</sup> It is interesting to note that ESPT proceeds at a rate several orders of magnitude faster than the corresponding deprotonation in the

ground state. For example, the excited-state reaction rate in anthocyanins is on the order of  $10^{10} \text{ s}^{-1}$ , whereas the ground-state deprotonation rate constant, which is controlled by diffusion, is  $\sim 10^6 \text{ s}^{-1}$ .<sup>184</sup>

**3.2.3. Symmetry Breaking.** Molecular symmetry breaking upon photoexcitation can be observed in terms of substantial charge density redistribution or charge transfer, on one hand, and configurational rearrangement of a molecular structure, on the other hand. Many ICT effects have been considered in more detail in preceding sections. Here we emphasize changes in symmetry of both charge redistribution and molecular structure in the excited state.

Many quadrupolar D- $\pi$ -A- $\pi$ -D, A- $\pi$ -D- $\pi$ -A, and A-D-A molecules, where D and A are electron donating and accepting units, can behave as dipolar molecules in the  $S_1$  electronic excited state.<sup>185–187</sup> Dereka and coauthors showed that symmetry breaking in such molecules is governed by solvent fluctuations and solvent polarity, that is, in nonpolar solvents the molecule remains symmetric and quadrupolar but in weakly polar solvents a weakly asymmetric  $S_1$  state appears with one arm of the molecule bearing more excitation than the other and in highly polar media the excited state results in a purely dipolar  $S_1$  state with the excitation localized entirely on one arm.<sup>185</sup> For the other type of linear A- $\pi$ -D- $\pi$ -A quadrupolar molecules, possessing CN groups, it was shown that quadrupole symmetry breaking in the excited state can be significantly amplified in protic solvents by formation of H-bonding asymmetric interactions, which are the strongest at the CN group with the highest basicity and result in significant reduction in the  $S_1$  state lifetime.<sup>188</sup> Furthermore, Easwaramoorthi et al. showed that not only quadrupolar but also octupolar cyano triphenylamines display symmetry breaking upon photoexcitation as illustrated in Figure 23a, resulting in a dipolar charge transfer state, whose stability can be controlled by the rotation of the N-C bond of the amino and phenylene moiety. The symmetry broken ICT state possesses emissive long-lived properties.<sup>189</sup> Availability of a spacer between D and A moieties in quadrupolar molecules leads to higher asymmetry of the CT exciton distribution (Figure 23b).

Stahl et al. revealed unexpected behavior of amino substituted triarylborationes in the lowest excited state due to a dipole inversion upon photoexcitation, where the excitation energy is transferred from one subchromophore to another within the lifetime of the excited state. Such a symmetry break of the excited state led to negative solvatochromism of the CT absorption band and positive solvatochromism of the emission band, respectively.<sup>190</sup> Piet et al. emphasized the role of solvent in symmetry breaking of the excited state of 9,9'-bianthryls, where the density and structural fluctuations in the solvent environment caused flip-flop dipole reversal via a neutral excitonic state. The dipole relaxation times were determined to vary from 2 to 14 ps depending on the solvent polarity.<sup>191</sup>

When an excited molecule is able to overcome a barrier that separates its two structural forms, then the molecule can change its structural symmetry. Such a phenomenon is normally not due to the electron-coupling interaction only but requires temporal or permanent disruption of chemical bonds; that is, it is related to true intramolecular chemical reactions.

Symmetry breaking of molecular structure in the excited state can be observed already in small planar molecules like benzene and ethylene. Broken symmetry in these molecules, which yields nonplanar geometry in the core excited state, was explained by the local rehybridization of the bonding orbitals on the excited

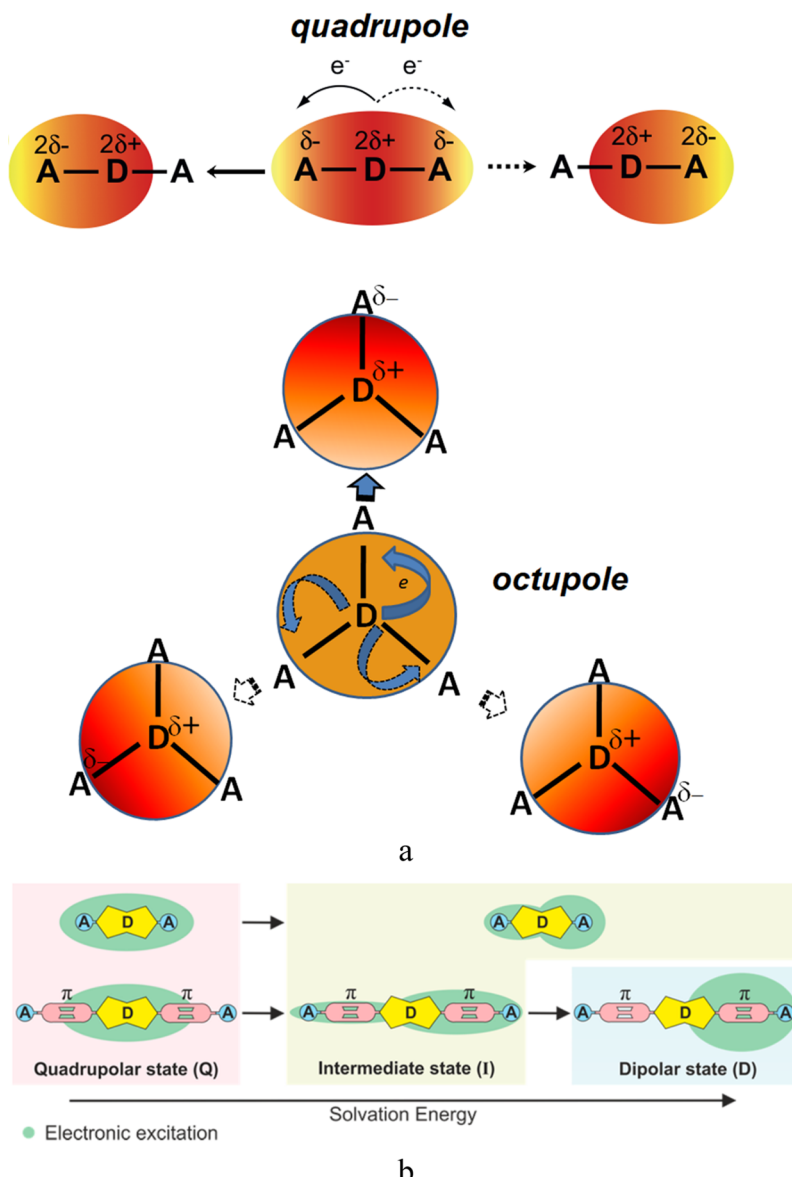


**Figure 23.** (a) Scheme of multipole ground-state symmetry (central part) breaking upon photoexcitation of a CT exciton resulting in a dipolar structure (peripheral parts) for the quadrupole and octupole. In a quadrupole molecule, CT occurs among two options, and in an octupole CT occurs among three options. (b) Schematic representation of the excited-state symmetry breaking and excitation distribution in A-D-A and A- $\pi$ -D- $\pi$ -A analogs. Part b reproduced from ref 186. Copyright 2017 American Chemical Society.

carbon atom.<sup>192</sup> Schalk et al. showed that cyclohexene experiences a two-stage structural transformation upon photoexcitation;<sup>193</sup> first, the exciton state leads to different options, such as hydrogen shift, carbene formation, bond cleavage, and ring puckering; second, further structural changes occur in the hot ground state of the molecule (Figure 24).

Reversible and nonreversible *cis*-*trans* photoisomerization is a well-known phenomenon, leading to a structural symmetry breaking in azobenzenes,<sup>194</sup> stilbenes,<sup>195</sup> cyanine dyes,<sup>196</sup> and other compounds (Figure 25). The barrier for the reversible isomerization is on the order of 1 eV for azobenzenes<sup>197</sup> and  $\sim 0.1$  eV for stilbenes;<sup>198</sup> therefore, such relatively large barriers ( $\gg kT$ ) separate the *cis* and *trans* isomers in the ground-state at room temperatures but not in the excited state. For example, in stilbene, isomerization can start from either the *cis* or the *trans* geometry; however, the starting conditions are energetically different. In the isolated molecule, the energy barrier is  $\sim 0.15$  eV

for the *trans*-to-*cis* and about 0.05 eV for the *cis*-to-*trans* reaction.<sup>199</sup> Both *cis* and *trans* conformations allow the molecule to rotate about its ethylene bond after electronic excitation because the central double bond in the excited state is weakened until the rotation reaches a minimum of potential energy at the twisting angle of 90°, called the phantom state.<sup>200</sup> This minimum of the excited state coincides with the maximum of the ground state geometry creating a conical intersection type situation, which facilitates nonradiative deactivation of the excited state to the *cis* or *trans* ground state. Consequent with the barrier heights, photoisomerization in stilbenes proceeds much faster from the *cis* than from the *trans* conformation (Figure 26).

Isomerization can proceed via two different mechanisms owing to the different groups of the molecule that are able to rotate. In a slow photoisomerization mechanism, called one bond flip (OBF), the substituents (i.e., phenyl group, Figure 27) rotate around the double bond and leave the molecular plane to

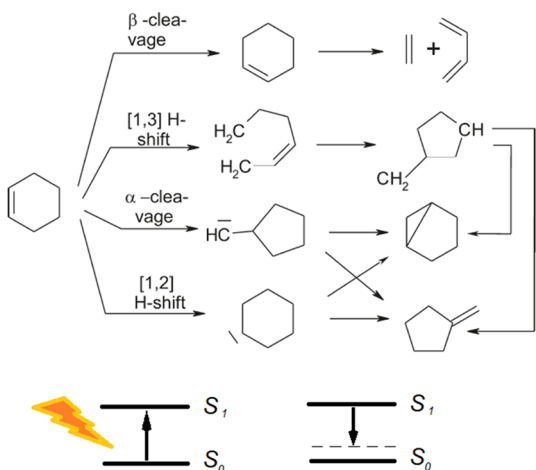


**Figure 24.** Two-stage photoreaction dynamics of cyclohexene with intermediate hydrogen shift, carbene formation, bond cleavage, and ring puckering options, followed by structural changes occurring in the hot ground state of the molecule. Adapted from ref 193. Copyright 2011 American Chemical Society.

circumscribe a cone. Such restructuring of the molecular geometry requires a wide free space and therefore is suppressed in confined media, such as solid solutions in the glassy state. The fast mechanism involves the rotation around both the double bond and the adjacent single bond, where only one CH group leaves the plane and turns by 180° from one to the other side of the molecule, whereas phenyl rings do not rotate (Figure 27). The latter mechanism is called the hula-twist (HuT), since it resembles the well-known dance.<sup>206</sup> It does not require large space and can be observed in frozen glasses. Both OBF and HuT isomerization mechanisms yield the same final isomer but different conformers (rotamers) (Figure 27).

Another related effect of photoexcitation is a reversible symmetry breaking leading to formation of a completely new molecule. Photocyclization is such a process, where the *cis* isomer forms an exciton-induced closed structure that is not an isomer but a new chemical compound. In this sense, photocyclization is a true photochemical reaction. Again, stilbene can be considered here as an example, where its closed chemical structure originates from the excited *cis* conformer via an intermediate pericyclic form (peri), where the benzene rings approach each other and two hydrogen atoms bend to different sides of the molecular plane (Figure 26a); however, it was proposed that the same result can be obtained from the phantom state, which involves the synchronous rotation around the central bond so that the benzene rings approach each other, while the hydrogen atoms deviate from the plane to yield the intermediate pericyclic form.<sup>205</sup> Examples of other compounds that demonstrate photocyclization are given in Figure 25b.

The effect of symmetry breaking upon photoexcitation on the emergent optical properties of the system in the excited state is highly important. For example, photoisomerization of the stilbenes leads to dramatic changes in emission of the different isomers, with much lower quantum yield of emission (~3 orders of magnitude) along with the broader emission spectrum for the *cis* excited state compared to the *trans* one.<sup>208</sup> Adamska et al. showed a breaking in optical selection rules upon photoexcitation of large molecules with curved geometry, that is, cycloparaphenylenes.<sup>209</sup> Specifically, in contrast to the linear chain, the circular geometries possess an optically forbidden first excited state  $S_1$ , so that the excitation is only possible to higher

energy levels,  $S_2$  and  $S_3$ , which are strongly optically allowed with perpendicular polarization emerging from the orthogonal transition dipole moments, making the cycloparaphenylenes good absorbers. The photoexcitation leads then to internal conversion to the lowest exciting state, amazingly fast self-trapping of the exciton within 100 fs, conformational distortion and bending strain of the chain, and an emergent transition dipole, which is not consistent with the Condon approximation stating that the dipole should be independent of the vibrational coordinates<sup>210</sup> (Figure 28). Adamska and coauthors concluded that the relatively large cycloparaphenylenes structure allows it to become a superior fluorophore with quantum yields well exceeding 50% in contrast to the small cycloparaphenylenes systems ( $n < 8$ ,  $n$  is the number of phenyl rings), which remain inefficient emitters, because the wave function remains always delocalized there.<sup>209</sup>

**3.2.4. Photolysis and Photoinduced Fusion.** Photolysis or photodissociation is a chemical reaction in which a chemical compound is broken down by photoexcitation. Photolysis is normally considered to be a harmful effect with respect to conjugated molecules since it causes their degradation. Poor stability against photolysis in the presence of oxygen or other catalysts is a well-known phenomenon for many organic dyes, such as triarylmethanes, azo-dyes, rhodamines, and thiazine.<sup>211</sup> In this process, a photoexcited electron of the dye molecule is easily accepted by molecular oxygen and the photoexcited hole is accepted by a water molecule, leading to breaking of the corresponding intramolecular bonds and chromophore cleavage.<sup>212</sup> Usually the necessary energies are produced by light wavelengths that lie in the ultraviolet (UV) region. For example, UV photolysis of imidazole, pyrrole, and phenol in the gas phase due to the  ${}^1\pi\sigma^*$  excited states has been reported.<sup>213</sup> However, some bonds are sensitive to the visible range as well. The average bond enthalpy for the C=C double bond in conjugated molecules is 614 kJ/mol, whereas the enthalpy for the C–C bond is 348 kJ/mol,<sup>214</sup> from which one can estimate the enthalpy contribution of the  $\pi-\pi$  interaction to be 266 kJ/mol. This estimated energy of the  $\pi-\pi$  bond is vulnerable to excitation by light at wavelengths up to 450 nm (2.75 eV). This estimate is corroborated by the recent report on photolysis, albeit with a small quantum yield of  $\varphi \approx 2.7 \times 10^{-5}$ , of benzoyl peroxide upon irradiation at  $\lambda = 480$ –365 nm, which leads to the direct photodissociation of the O–O peroxide bonds and C–H bonds of benzene rings to form benzyloxy radicals and atomic hydrogen.<sup>215</sup>

BODIPY derivatives represent a unique example of photo-cleavable compounds, whose photolysis associated with a single photon  $S_0 \rightarrow S_1$  photoexcitation of the chromophore can be tuned in a wide region of light wavelengths, from green to near-infrared (above 700 nm) depending on the derivative used.<sup>216–218</sup> A one-photon upconversion-like photolysis of boron-dipyrromethene (BODIPY)-based prodrug was demonstrated, which was achieved at longer wavelength of  $\lambda = 625$  nm than the direct photoexcitation ( $\lambda = 530$  nm) through triplet–triplet energy transfer (TTET) from a photosensitizer, platinum(II) tetraphenyltetrazenoporphyrin, with a photolysis quantum yield even higher than the photolysis by direct excitation.<sup>219</sup>

Photocleavage reactions can be driven by different mechanisms. One mechanism is due to generation of singlet oxygen through photosensitization of dissolved molecular oxygen, which is different from the photodynamic action mechanism in that the generated singlet oxygen reacts with an electron-rich

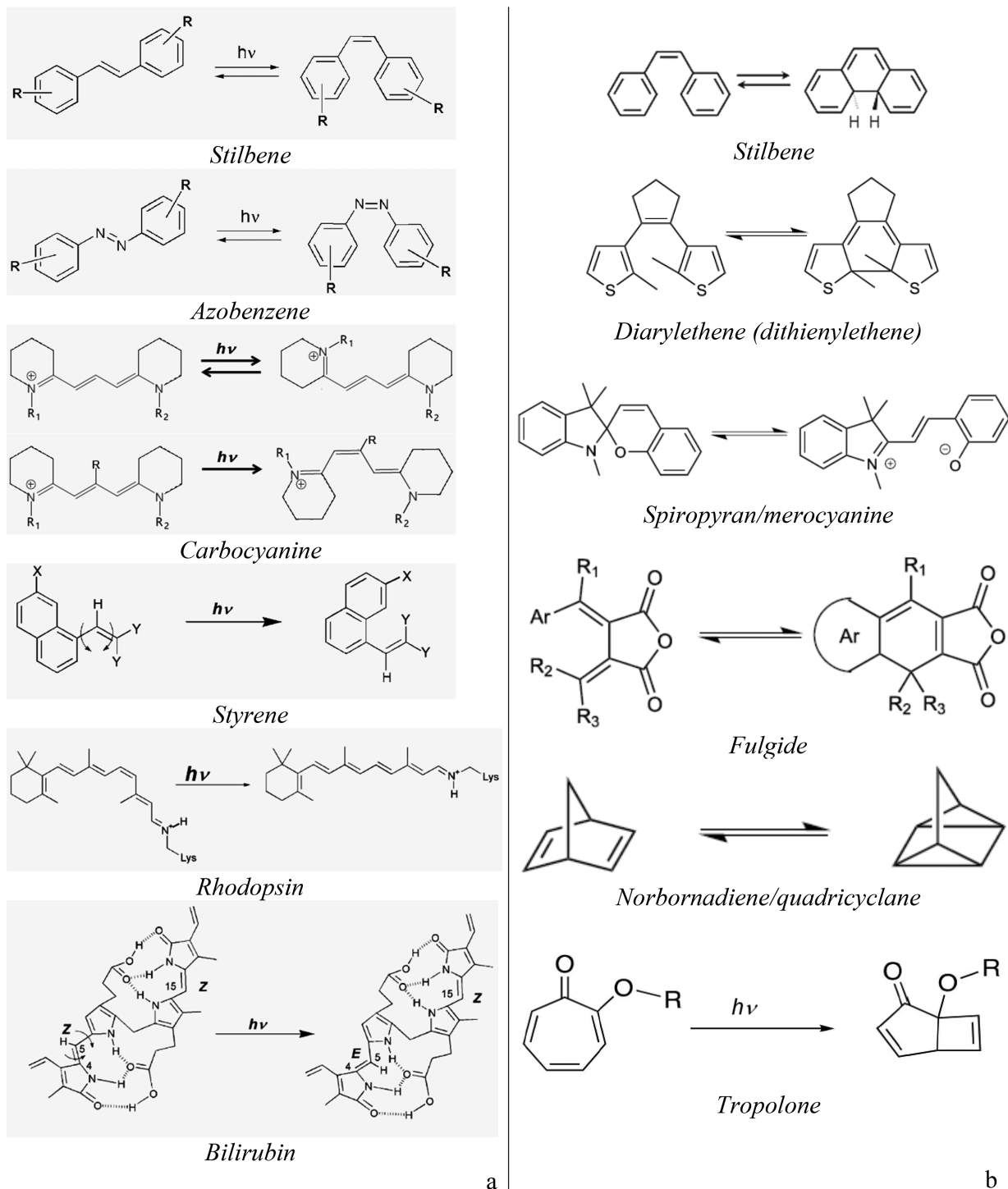


**Figure 25.** Examples of photochromic molecules that demonstrate (a) isomerization and (b) cyclization upon photoexcitation. Whereas stilbenes, azobenzenes, and unsubstituted carbocyanines are able to undergo reversible photoisomerization, meso-substituted carbocyanine,<sup>201</sup> styrene,<sup>202</sup> rhodopsin,<sup>203</sup> and bilirubin<sup>204</sup> undergo irreversible photoisomerization with only one preferred isomer.

alkene of the molecule, resulting in its cleavage into two fragments at the site of the electron-rich alkene.<sup>220</sup> The other mechanisms include involvement of triplet states and photo-induced charge separation. Offenbacht-Stiegert et al. showed that photolysis of coumarin photocages in water proceeds via charge-separated states, while the pathway in organic solvents proceeds via a triplet state. In both cases, the photolysis rate constants were determined to be on the order of  $10^2 \text{ s}^{-1}$ .<sup>221</sup> The photolysis through the triplet states proceeds with specific reactivity with

respect to dissociation of different bonds.<sup>222</sup> For example, aromatic ketones with  $n,\pi^*$  lowest triplet states are known to undergo much faster  $\alpha$ -cleavage and have shorter triplet lifetimes than ketones with  $\pi,\pi^*$  states.<sup>223</sup> A correlation of a long triplet lifetime with a high photolysis quantum yield was reported.<sup>221</sup>

One of the purposes of the controlled photolysis is to get residuals that possess emerging properties that are not present in the mother compound. Recent efforts were directed to synthesize photocages, also called photoremoveable protecting

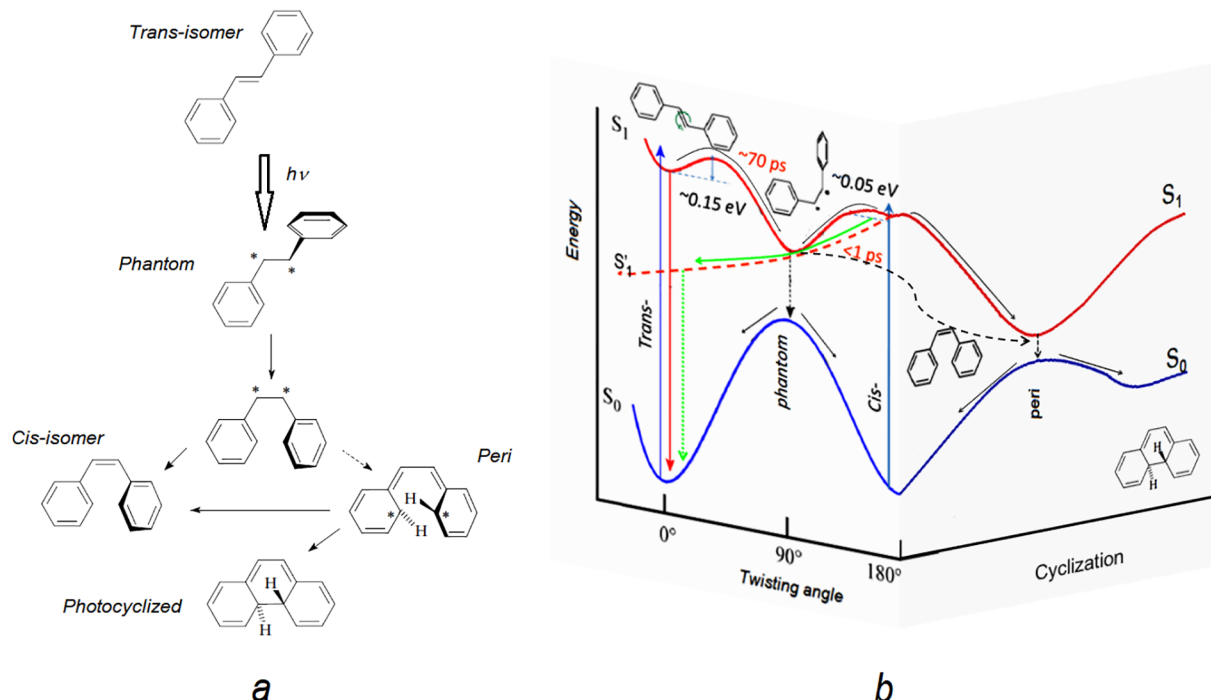


**Figure 26.** (a) Reaction scheme<sup>205</sup> and (b) energy scheme of diabatic photoisomerization and photocyclization of stilbene via intermediate phantom and peri states, respectively. Green arrows show an alternative, adiabatic route of photoisomerization.

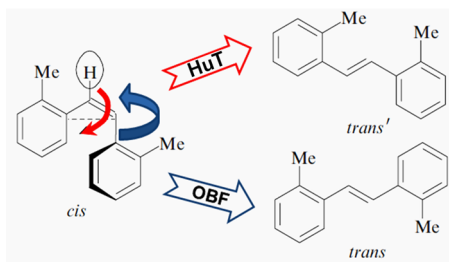


**Figure 27.** Scheme of OBF and HuT mechanisms of photoisomerization of stilbenes.<sup>207</sup>

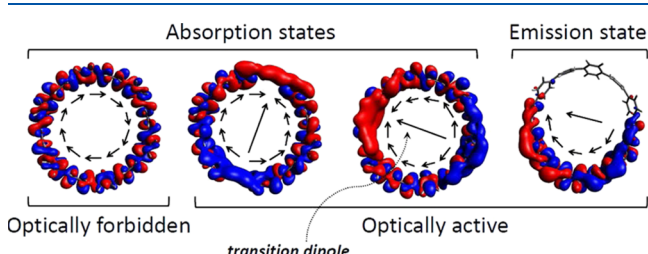


**Figure 28.** Orbital distribution of transition density and schematic of transition dipole shown (from the left to the right) for  $S_1$ ,  $S_2$ ,  $S_3$  (absorption), and relaxed  $S_1$  (emission) transitions in cycloparaphenylenes molecule with  $n = 12$ . Red and blue color corresponds to negative and positive values of the transition density, respectively. Reproduced from ref 209. Copyright 2014 American Chemical Society.

groups (PPGs), which are capable of releasing active groups to rearrange a supramolecular structure with light activation at a specific wavelength. Examples that demonstrate emerging fluorescence emission with high quantum yield of photolytic products through their release by change in supramolecular organization due to photolysis have been reported for

alkoxyanthracene-cucurbit[8]uril supramolecular polymer,<sup>224</sup> carboxylic acids conjugated with 4,5-dimethoxy-2-nitrobenzyl PPGs,<sup>225</sup> and coumarin photocages<sup>226</sup> (Figure 29a).

The reverse effect to the photolysis is a photoinduced fusion, which is widely known from the example of photopolymerization of some polymers like polyacrylates. Photopolymerization usually occurs as fusion of highly reactive radical monomer units, which are produced by UV light irradiation,<sup>227</sup> although new methods of photopolymerization are also rapidly being developed.<sup>228</sup> The examples of photoinduced fusion include photoconjugation reactions between two molecules, such as cyclic  $\alpha$ -diketones, benzobicyclo[2.2.2]octanes, polymers, etc., on one hand, and different C=C containing compounds, on the other hand, which occur via [2 + 2], [4 + 2], or [4 + 4] photocycloaddition pathways.<sup>229–231</sup> The mechanism of [2 + 2] photocycloaddition between enones and alkenes begins with photoexcitation of the enone to a singlet excited state. The singlet state is typically very short-lived due to intersystem crossing to the triplet state. This stage can be considered as an exciplex formation between the excited enone and the ground-state alkene, eventually forming a triplet diradical intermediate, followed by spin inversion to the singlet diradical before closure to the cyclobutane product occurs (Figure 29b).

Photoinduced fusion is also related to the great number of photoclick reactions, such as copper(I)-catalyzed alkyne–azide cycloaddition (CuAAC), thiol–ene or thiol–yne reaction, Diels–Alder reaction, Paternò–Büchi reactions, and photodimerization, which can proceed smoothly even when initiated by sunlight.<sup>232–234</sup>

Effects of exciton-induced molecular self-assembly of some conjugated chains, which are addressed to specific guest–host interactions, can also be considered as a kind of fusion reactions leading to a tight molecular association. Here, specific interactions can be classified as those that involve photoexcited charge transfer and those associated with the changing lability of

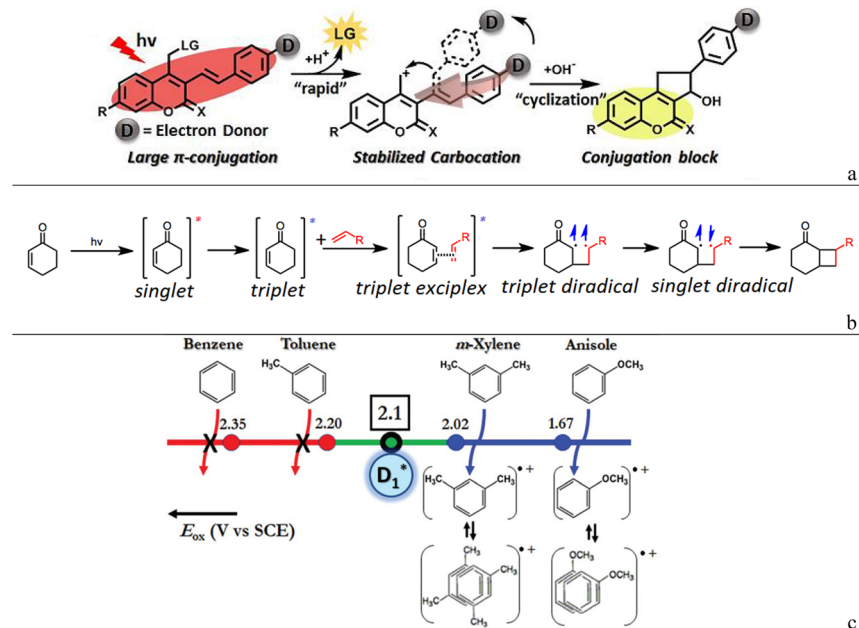


**Figure 29.** Examples of (a) photolysis of coumarin photocages, (b) photoinduced fusion in the form of [2 + 2] photocyclization between enone and alkene,<sup>237,238</sup> and (c) photoinduced assembly of *m*-xylene and anisole. In part a, the exciton formation is accompanied by photocleavage of the leaving group (LG) and molecular isomerization, followed by cyclization (Adapted with permission from ref 226. Copyright 2018 Wiley). In part c, a sacrificial agent provides bimolecular electron transfer oxidation reactivity with respect to molecules followed by their dimerization (Reproduced from ref 239. Copyright 2018 American Chemical Society).

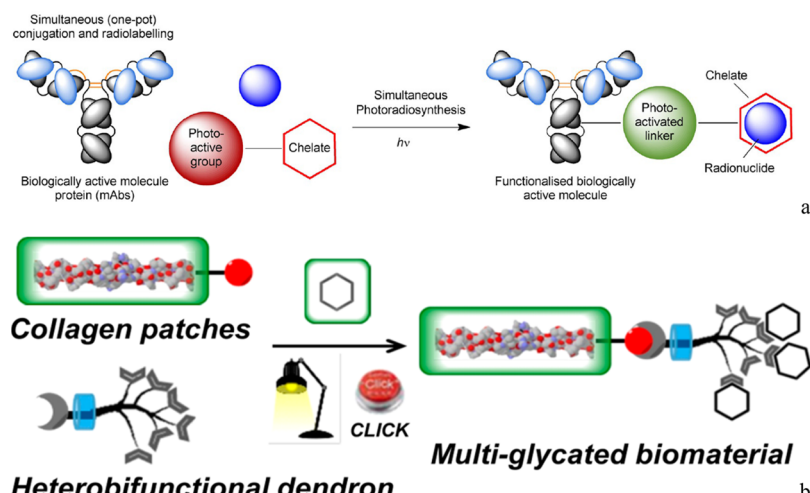


**Figure 30.** Examples of photoinduced guest–host supramolecular assembly. (a) Radionuclide labeling of protein. Reproduced with permission from ref 247. Copyright 2020 Wiley. (b) Scheme of collagen neoglycosylation mediated by photoclick thiol–ene reaction, where red ball corresponds to the thiol group and the crescent corresponds to the O–NH<sub>2</sub> group. Reproduced from ref 250. Copyright 2014 American Chemical Society.

a photoexcited molecule. Charge-transfer excitons can serve as a driving force for assembly of homo- or heteromolecules. Balzani and co-workers proposed that the photoexcited state of a certain molecular fragment can possess a pronounced electron donor or acceptor character,<sup>235</sup> which can facilitate an electron transfer from or to the excited state in the presence of a “sacrificial” agent, thus affording the oxidation or reduction of the compound while the sacrificial agent is consumed. High-valent earth abundant metal-oxo species were shown to be effective sacrificial agents, the excited D<sub>1</sub>\* states of which provide remarkable bimolecular electron transfer oxidation reactivity with respect to molecules with relatively low oxidation potentials, such as *m*-xylene and anisole, leading to formation of their corresponding π-dimer radical cations.<sup>236</sup> In contrast, no reactivity was observed with

respect to benzene and toluene possessing higher oxidation potentials (Figure 29c).

The ability of the tricarbocyanine near-infrared (NIR) dye to noncovalently self-assemble onto the surface of single-walled carbon nanotubes driven by light-induced charge-transfer interactions was demonstrated by Menon et al.<sup>240</sup> The ultrafast electronic process in the NIR dye, once immobilized onto SWCNTs, was shown to start with the formation of excited states, which decay to the ground state via the intermediate population of a fully charge-separated state, with characteristic time constants for the charge separation of 1.5 ps and charge recombination of 25 ps. Although the dye–SWCNT complex was stable in the dark as well, the role of the hot exciton generated in the dye molecule to provide the CT interactions

was shown to be of great importance for the complex formation. Thus, the exciton dynamics in this system provides a chemical strategy to assist in chemical functionalization of SWCNTs.

Photocontrolled molecular lability was demonstrated with respect to the ability of some artificial receptor systems to release metal ions,<sup>241</sup> anion ligands,<sup>242</sup> and neutral coordinated molecular species<sup>243</sup> after the photoexcitation. The general principle of photoinduced movements is generation of a new thermodynamically unstable configuration that spontaneously evolves to the thermodynamic well of the system, accompanied by geometric changes in the system.<sup>244</sup> The photorepulsion of metal ions from a crown-ether-linked merocyanine was reported to occur very rapidly, on a picosecond time scale, because the stability constant of the complex in the excited state is about 2 orders of magnitude lower compared to that in the ground state,<sup>245</sup> however, after deactivation of the excited state, the metal ion can reversibly be coordinated back. Photolytic release of bioactive carboxylic acids from fused pyran conjugates was demonstrated by Conceição et al., who showed that a correlation exists between the photolysis efficiency and the increasing extent of conjugation for both glycine and  $\beta$ -alanine.<sup>246</sup>

One of the interesting applications of photoinduced control of specific guest–host interactions is photochemical methods for labeling proteins. Recently, a concept of simultaneous photo-radiosynthesis of radio-labeled antibodies for the use in molecular imaging has been introduced.<sup>247</sup> This method involves a bifunctional photoactive substrate that, on one hand, reacts *in situ* with nucleophilic amino acid residues on a protein upon photoexcitation and, on the other hand, bears a specific chelate group that is able to take up a radionuclide (Figure 30a). A wide range of photoaffinity probes have been shown that react through the formation of intermediate carbenes, electrophiles, dienes, or radicals.<sup>247</sup>

Another application is photoinduced control of protein activity through photofusion, which was demonstrated through light-induced recruitment of different proteins to individual centromeres, kinetochores, mitochondria, and centrosomes in human cells.<sup>248</sup> Ballister et al. used a molecular linker that bears sequentially three functional groups, including a photocage, a photocaged ligand, and a Halo-ligand.<sup>249</sup> The photoinduced cleavage by UV light of the photocage allowed the ligand of the linker to bind to *Escherichia coli* dihydrofolate reductase (eDHFR), while the Halo-ligand covalently labeled a Halo-tag protein (Halo-enzyme), which thus resulted in linkage between eDHFR and Halo-enzyme. In a similar way, Bini et al. demonstrated immobilization of dendrons on collagen patches via thiol–ene photoclick reaction, on one hand, and chemoselective alkoxyamino–carbonyl conjugation to carbohydrates, on the other hand (Figure 30b).

### 3.3. Exciton-Induced Structural Reorganization

**3.3.1. Exciton-Induced Conformational Changes of Polymer Chains.** There is a mutual effect between torsion conformation of a polymer chain and electronic excitation of the chain. As was discussed in section 3.1.1, torsion fluctuations can strongly influence the exciton delocalization along the conjugated chain. On the other hand, electronic excitation of the molecule is a powerful tool that influences torsion conformation of the molecular structure in the excited state. In conjugated polymers that contain ring moieties, such as phenyls, fluctuations of ring orientation may originate from two factors, namely, intermolecular or intramolecular interactions. The intermolecular forces play a dominant role in dense films,

where molecules are closely packed. Due to the short distance between molecules, small fluctuations of the adjacent molecular orientations may produce a large steric energy. By contrast, the intramolecular forces are weak and the characteristic energy leading to the static torsional distortion of an isolated molecule in the ground state is quite small.

Exciton-induced conformational change of a molecule is related to symmetry-breaking effect of the molecular structure upon excitation. Here, a particular feature of such breaking is spatial distortion of the molecule with respect to its configuration in the ground state. Based on the observation of C–H bending and C–C and C–H stretching vibrational levels through high-resolution photoabsorption spectroscopy, Ma et al. concluded that simple molecules such as ethylene and benzene become nonplanar upon excitation, thus breaking their ground-state symmetry.<sup>192</sup>

Rather different behavior was predicted for long-chain conjugated molecules, where a strong coupling between the local electronic excitation and the mutual ring orientation is observed. First, the total energy of the excited state of a polymer chain that represents the alteration of benzene rings such as poly(*p*-phenylene) (PPP), strongly depends on the torsion angle unlike its ground state, which demonstrates only insignificant  $\pi$ -character in the bond connecting the neighboring benzene rings and which therefore provides nearly free rotation of the rings about this single bond.<sup>251</sup> Moreover, steric constraints between neighboring units tend to force these molecules to adopt a twisted structure in the ground state with nonzero torsional angles between the ring components. But for the excited state, the charge delocalization over the neighboring rings correlates with increased  $\pi$ -overlap between the rings, which facilitates their coplanar orientation.

Second, there is a subtle interplay between the length and the character of conjugation in polymer chains with ring units, such as PPP, polythiophenes, and related systems. Steric repulsion between atoms on the adjacent rings may strongly favor nonplanar geometries with torsional disorder in the ground state, especially for oligomer or short polymer chains, while electronic effects associated with increased conjugation length along the backbone are also very significant and in some cases may be sufficient to force an aromatic polymer structure with torsional disorder to adopt the planar quinoid structure (Figure 18). In the quinoid structure, the adjacent monomer units are connected through the double bonds, which, due to additional sideway overlap of  $\pi$ – $\pi$  electrons, hamper torsional motion of these units with respect to each other, whereas in the aromatic structure the ring units can freely rotate around the connecting single bond. Thus, excitation leads to a strengthening of the inter-ring bonds and causes a subsequent planarization of the molecular backbone.

By using a Hückel–Hamiltonian approach, Kurti and Surjan showed that the optimum geometry for short chains of polyisothianaphthene with monomer units  $n < 8$  should be aromatic. For long oligomers ( $n > 9$ ), the aromatic units become localized to the chain ends, whereas in the middle there is a quinoidal geometry.<sup>252</sup> Partial retention of diatomic differential overlap (PRDDO) and ab initio molecular orbital calculations for polythiophenes and related systems showed that polyisothianaphthene and polyisonaphthothiophene are nonplanar polymers in their aromatic forms, due to steric interactions between the sulfur and hydrogen atoms from adjacent monomeric units, even though the planar quinoid form of

polyisothianaphthene was calculated to be  $\sim 2$  kcal/mol more stable than the aromatic nonplanar form.<sup>253</sup>

The transformation of the conjugated structure from the aromatic to quinoid one is also related to the Peierls transition of a long conjugated chain, which, being a 1D structure, is spatially unstable due to the absence of stabilized forces from the environment.<sup>254</sup> Peierls transition leads to dimerization of the adjacent bonds, so that the single and double bonds that are available for free exchange in the aromatic ring are now faced with an energy barrier preventing such an exchange in the quinoid structure.

The analogous changes in chemical structure from aromatic to quinoid can be induced owing to electronic excitation of a long conjugated chain.<sup>255</sup> As discussed above, conjugated polymers undergo conformational changes after photoexcitation from aromatic toward quinoidal geometries. These changes modify torsion constants between conjugated repeat units, leading generally to their increase. Thus, the excited state structure shows reduced torsional disorder (more planar geometry) and reduced BLA in the middle of the molecule, as compared to the ground-state geometry<sup>70</sup> (Figure 31a,b). The dynamics of these changes is very fast and proceeds with a time constant less than a picosecond<sup>256</sup> (Figure 31c).

The excited state reorganization of the P3HT chain, which is driven by rearrangement of the conjugation character toward quinoidal structure, was demonstrated by Barford et al.<sup>257</sup>

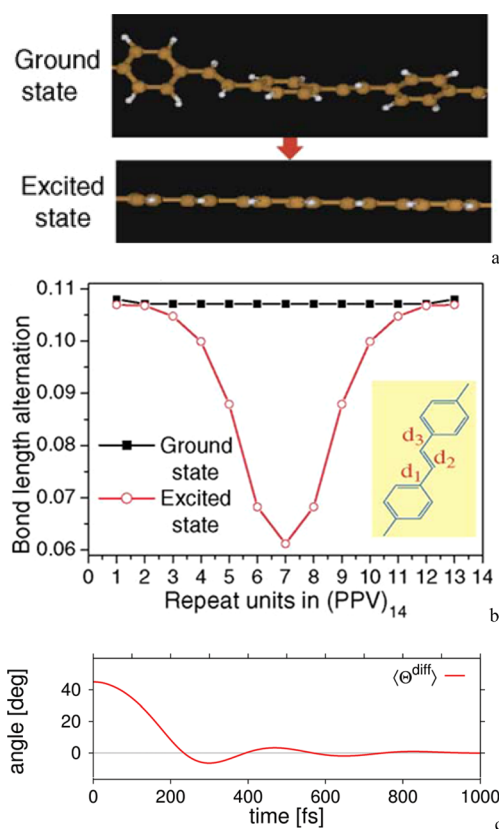


**Figure 31.** (a) Exciton-induced reduced torsional disorder (more planar geometry), (b) reduced BLA in the middle of the PPV molecule in the excited state as compared to the ground-state geometry, and (c) time evolution of the relative torsional angle of a PPV hexamer after photoexcitation. Parts a and b reprinted with permission from ref 70. Copyright 2002 American Physical Society. Part c reproduced with permission from ref 256. Copyright 2013 Royal Society of Chemistry.

Barford and coauthors showed that for well-solvated P3HT chains in solution, the ground-state inter-ring torsional angle represents a bimodal distribution centered at approximately  $60^\circ$  and  $110^\circ$  (where  $0^\circ$  corresponds to planar conformation) and that such torsional disorder provides less than 5% of conditions necessary for extended electronic conjugation. That means that the extent of ring-to-ring conjugation in the equilibrium ground state is minimal in well-solvated chains, unlike P3HT aggregates in the solid state, and it may extend only over single monomers or dimers.

Rather different behavior was found in polymers whose ring moieties in the backbone are separated by some linkages. In this case, the  $\pi$ -electron delocalization normally increases and produces a stabilization of single chains. In PPV polymers, whose benzenoid units are connected via a vinylene bridge, the rings of the polymer chain are more separated than, for example, in PPP or P3HT, which reduces their repulsive interactions and renders the PPV backbone more planar in the ground state. Milad et al. reported that essentially planar MEH-PPV in the ground state with effective conjugation length of 9 repeat units becomes strongly twisted when vinylene units are fluorinated to F-MEH-PPV structure, leading to strong localization of the effective conjugation length to just one repeat unit. The strong twist persists in F-MEH-PPV in the excited state as well, resulting in the reduced radiative and enhanced nonradiative rates and thus broadening the emission spectrum and quenching the fluorescence quantum yield.<sup>258</sup> In contrast, when an amine group is used as a linkage (i.e., polyaniline), a nonplanar polymer geometry is obtained again because NH groups have a tetragonal symmetry forcing the chain to go out of planarity, which results in a larger band gap and a smaller ionization potential as well.<sup>259</sup>

It should be noted that for conjugated polymers in the crystalline state their ground-state structure can be influenced by intermolecular interactions, so that the structure of PPV chains in the condensed state, for example, is not planar because the energy profile here is very shallow with respect to the librational motion,<sup>70</sup> so that the weak interactions can result in significant torsional disorder, with the neighboring phenyl-vinyl moieties twisted by  $15^\circ$ . Again, excitation leads to the changed torsional geometry, since the energy profile here is no longer shallow with respect to the torsional motion and leads to a planar structure with its global energy minimum.

**3.3.2. Exciton-Induced Structural Reorganization of Molecular Assemblies.** Energy of photoexcitation of conjugated molecules (1–3 eV) is well above the energy of intermolecular van der Waals interactions in molecular assemblies ( $\sim 4$  to 40 kJ/mol or 0.04–0.4 eV<sup>260</sup>); therefore, it is clear that under certain conditions the photoexcitation can cause dissociation or affect assembly of molecular aggregates. However, such influence is not displayed easily and was observed in rare cases and in few systems.

Coleman et al. reported self-assembled, vesicle-capped nanotubes that can be selectively disassembled by irradiation. The walls of the nanotubes were prepared as bilayers from amphiphilic molecules with two hydrophobic legs that interdigitate when the molecules self-assemble into bilayers. The amphiphilic molecules contained a photoswitchable and fluorescent core that allowed for a fast and highly controlled disassembly of the nanotubes upon photoexcitation, which was clearly observed in real time using fluorescence microscopy.<sup>261</sup> Goodwin et al. showed that a micellar assembly of molecules constituted from poly(ethylene glycol) as the hydrophilic component and 2-diazo-1,2-naphthoquinone as the hydro-

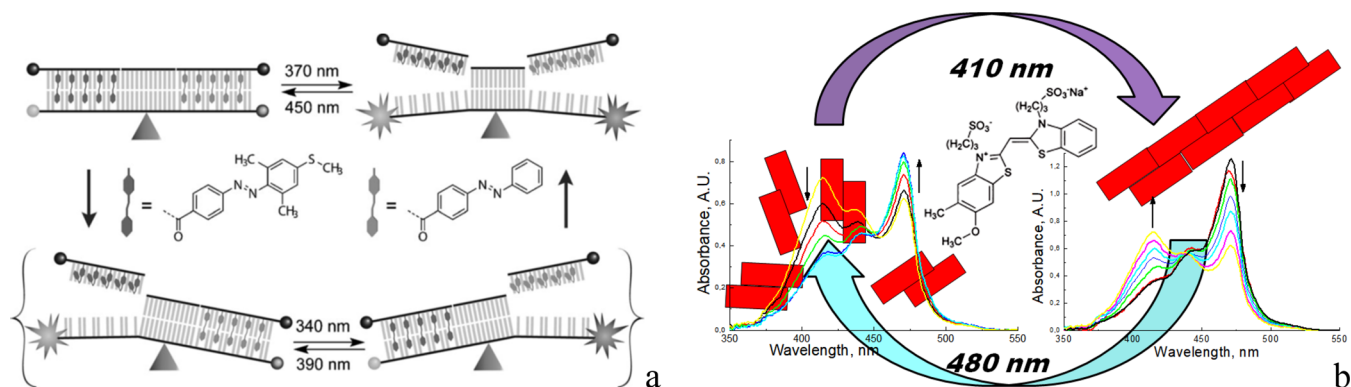


**Figure 32.** Reversible processes of photodissociation of (a) DNA and (b) J-aggregates of thiamonomethinecyanine dye. In part a, photodissociation is induced by incorporating two different azobenzene moieties into the DNA arms, that is, *trans*-2,6-dimethyl-4-(methylthio)azobenzene-4'-carboxylic acid and unsubstituted *trans*-azobenzene-4'-carboxylic acid, which undergo photoisomerization under visible and UV light, respectively, with complete dissociation and rehybridization realized with light of 370 and 450 nm, which leads to the seesaw-like motion. Reproduced with permission from ref 269. Copyright 2012 Wiley. In part b, the processes of dissociation of J-aggregate into dimers and reverse assembly of dimers into J-aggregate are controlled by specific wavelengths of light illumination; red bricks denote the specified molecule. Adapted with permission from ref 271. Copyright 2014 Wiley.

phobic component can be destroyed by a two-photon photoreaction triggered by infrared light with release of an encapsulated fluorescent probe molecule<sup>262</sup>

Azobenzenes are known as photoswitchable materials able to induce reorganization of molecular assemblies, owing to their intramolecular isomerization under light illumination. For example, domain structure rearrangement of azobenzene-containing samples during irradiation with polarized light was observed due to the process of photo-orientation consisting of growth of perpendicularly oriented domains and reduction of parallel domains via the movement of domain boundaries.<sup>263</sup> Light modulation of the aggregation behavior of ionic liquids composed of azobenzene compounds was observed in water, where due to the photoinduced transitions between *trans* and *cis* isomers it was found that small-sized aggregates of 63 nm formed from the *trans* isomer grew into large-sized aggregates of 125 nm formed mainly from the *cis* isomer after UV irradiation; the process was reversible after further irradiation with visible light.<sup>264</sup> Some of the azobenzene compounds demonstrated also changes in the aggregate structure upon photoexcitation from micelles into vesicles in aqueous solutions.<sup>265,266</sup> Reversible light-induced solubility of Disperse Red 1 (an azobenzene dye) in a hydroxypropyl cellulose matrix has been reported.<sup>267</sup> The dye solubilization was observed under illumination with visible light and was explained by the repeated *trans*–*cis* isomerization of the dye molecules, which promoted a photofluidity inside the cellulose matrix, breaking the cages in which aggregated molecules were trapped. Incorporation of azobenzene compounds into biological molecules allowed manipulation of organization of molecular assemblies such as DNA dissociation and rehybridization.<sup>268,269</sup> Nishioka et al. demonstrated a photoswitchable nanodevice by combination of two differently substituted azobenzene residues in DNA molecules that were able to produce repetitive seesaw-like motions upon wavelength-selective activation of different azobenzene switches in the DNA-based nanomachine<sup>270</sup> (Figure 32a).

It was shown that J-aggregates of thiamonomethinecyanine dyes in electrolyte KCl solution can be assembled from dye dimers by simple light illumination of the solution with light of wavelengths that correspond to excitation of the dye dimers.<sup>271</sup> A reverse process was also demonstrated by application of light wavelengths that induce excitation of J-aggregates (Figure 32b).

The feasibility of this effect is related to the fact that an electrolyte KCl solution of thiamonomethinecyanine dyes represents a dynamic equilibrium between dye dimers, which absorb at around 410 nm, and J-aggregates, which have an absorption maximum at  $\sim$ 480 nm, so the illumination of the solution by wavelengths in the range of either dimer absorption or J-aggregate absorption can change such an equilibrium relatively easily. Therefore, illumination of the dimers at 410 nm results in the decreasing absorption band of the dimers and increasing absorption band of J-aggregates, while illumination of J-aggregates at 480 nm results in decrease of their absorption band and increase of the dimer band with a corresponding isosbestic point present in the spectra (Figure 32b). Typical time constants of the kinetics of formation of J-aggregates in the dark upon addition of dimers to the solution, which is a non-equilibrium process, were several minutes, while kinetics of assembling dimers into J-aggregates in the solution at equilibrium under specific light illumination were about 1 order of magnitude longer, that is, several tens of minutes. The results indicated that the ground-state J-aggregation in the dark and formation of J-aggregates by light illumination has different mechanisms. In the dark, the increase in J-aggregation is due to predominant increase in the concentration of rather small J-aggregates. Under illumination, an increase in the aggregate size takes place according to autocatalysis growth, which occurs as a process of a subsequent attachment of dimers to available J-aggregates, rather than dimer–dimer fusion.<sup>271</sup>

The analogous effects of interconversion of aggregates under light illumination have been observed not only for other thiamonomethinecyanine dyes (which are small dipolar dyes), but for large dipolar D- $\pi$ -A merocyanines, whose  $\pi$ -bridge causes intermolecular binding beyond dipole-dipole interactions.<sup>272</sup> Herrmann-Westendorf et al. reported a contrast difference between the ground-state aggregation of dipolar D- $\pi$ -A merocyanines and aggregation of the photoexcited molecules. In the dark, dye aggregation is determined by cooperative binding that involves both dispersion binding between  $\pi$ -bridges and distinct interactions between the polar heads of the molecules. Irradiation with visible light causes formation of prototype H-aggregates, where aggregation is driven by the energetically favorable compensation of dipole moments, which are photoenhanced by a factor of ~2 for this

type of merocyanine.<sup>272</sup> Kinetics of assembly rearrangement for dipolar D–π–A merocyanines were similar to that reported for thiamonomethinecyanine dyes, that is, with time constants on the order of 10–20 min. However, the mechanism of photoinduced rearrangement was somewhat different. For large D–π–A merocyanines with relatively high dipole, the driving force for dimerization is compensation of the dipole moments of the neighboring molecules, which are significantly enhanced upon photoexcitation. Interestingly, the enhanced electric field due to photoexcitation was found to be a driving force for rearrangement in other systems. Photoalignment of gold nanoparticles in aqueous silver nitrate medium under irradiation with UV light due to strong plasmon resonance coupling has been reported.<sup>273</sup> Also, photoenhancement of molecular dipoles can apparently cause dissociation of large aggregates due to molecular reorientation.<sup>272</sup> For small dipole molecules, the situation is somewhat different. Whereas their photoexcitation can facilitate dissociation of large J-aggregates, whose structure is sensitive to local temperature, which can rise as a result of photoexcitation,<sup>274</sup> association of dimers into J-aggregates cannot be explained by that factor. Instead, this phenomenon was explained by a general thermodynamic principle stating that the system should minimize a free energy function of its internal states.<sup>275</sup> According to this principle, photoexcitation at a specific wavelength of a mixture of different species that are in a dynamic equilibrium, that is, the dimers and J-aggregates in the solution, should lead to accumulation of those species whose absorption is minimal. The system arrives to this result through many acts of photoexcitation and relaxation of the species, which facilitate their random-walk motion and rearrangement. When the arrangement with a minimum absorption and therefore a minimum free energy is casually achieved, the system becomes stable and reduces its random-walk activity. The J-aggregate formation in this case is driven thermodynamically rather than by the enhanced dipole–dipole interactions.

### 3.4. Effect of Specific Static Conformations on Exciton Formation in Conjugated Molecules

**3.4.1. Exciton Localization.** In addition to dynamic conformational changes discussed in section 3.1.1, the specific steady-state molecular conformation exerts significant influence on exciton behavior and optical properties of the molecule as well. One of the bright examples is the conformation of polyacetylene, which can exist in two different forms, *trans* and *cis* conformation (Figure 33). The energy of excitations of these

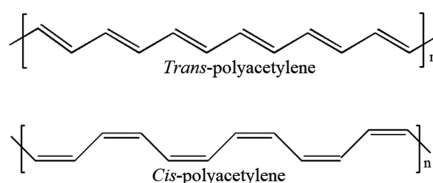


Figure 33. Conformational states of PA.

forms is different because the *trans* conformation gives rise to a highly delocalized exciton, whereas the *cis* conformation provides a localized one, leading to poor and good radiative recombination of excitons in such chains, respectively.

A similar situation takes place when a conjugated chain experiences torsional conformations. The planar molecular conformation facilitates exciton delocalization with relatively narrow bandwidth. If the torsion angle  $\varphi$  is sufficiently large, the

motion of excited electrons between adjacent rings is hindered and the exciton radius of photoexcited states becomes reduced too. Thus, the torsional disorder leads to a broader and blue-shifted band in the absorption spectrum. Torsional disorder also results in decreasing oscillator strength of the  $\pi-\pi^*$  transition according to the theoretical calculations and experiments reported by Harigaya.<sup>276</sup> Harigaya has found that ring torsions affect the long-range excitons in PANI more easily than in PPP, due to the larger torsion angle of PANI (about  $\varphi = 56^\circ$ ) and also due to the larger number of bonds between neighboring phenyl rings (i.e., two vs one in PANI and PPP, respectively), whose hopping integrals are modulated by torsions. Particularly, Harigaya showed that the long-range component of the oscillator strengths at  $\varphi = 56^\circ$  is about half of the magnitude of the system without ring torsions.<sup>276</sup>

Breaks in the  $\pi$ -conjugation due to torsional disorder along the chain, which separate corresponding conformational subunits, control exciton behavior in conjugated polymers as well. Scholes et al. reported that for conjugated polymers from the PPV family, the conformational subunits electronically couple to neighboring subunits, forming subtly delocalized collective states of nanoscale excitons that determine the polymer optical properties.<sup>277</sup> On the other hand, Barford et al. showed that for P3HT polymers with weak torsional potentials and consequently strong conformational static disorder, low-lying singlet excitons may be localized between such breaks depending on the distances between the breaks and the relative values of the disorder-induced localization length.<sup>278,279</sup> These excitons were assessed as virtually nodeless and classified as local exciton ground states (LEGSSs). Such an exciton confinement also causes specific changes in the optical properties due to the local spectrum of low-lying exciton states associated with the segments of the exciton localization. Dynamics of exciton localization driven by conformational disorder occurs on the time scale of about 200 fs. First, the Frenkel exciton tunnels between potential minima determined by the conformational disorder, which makes it highly delocalized. Then, within a time period of a single C–C bond oscillation, the exciton vibrationally relaxes and localizes through self-trapping into one of the potential minima within a chromophore (Figure 34). Thus, the localization length of the exciton decreases from 12 to 2.5 monomers in less than 100 fs.<sup>280</sup>

**3.4.2. Shift of Exciton Energy.** The effect of molecular conformation due to variation in regioregularity of polythiophenes on their photophysical properties is well-known. Xu and Holdcroft showed that regiorandom P3HT chains that possess increasing head-to-head (HH) content (Figure 35) due to steric repulsive forces between adjacent thiens have such features as blue-shifted wavelengths of maximum absorption and emission, pronounced Stokes shift due to the partial relaxation of the above repulsive forces, and greater relief from conformational strain in the excited state compared with the corresponding flat head-to-tail (HT) conformer. Particularly, P3HT solutions with HT content of 80, 60 and 50% demonstrate excitation energy of 2.82, 2.95, and 3.00 eV, and Stokes shift of 0.69, 0.78, and 0.81 eV, respectively.<sup>281</sup>

The reason for the blue shift of the exciton energy can be attributed to the reduced exciton delocalization due to torsional conformational disorder of the molecule. A similar phenomenon was found in PANI chains, which demonstrated a blue shift of the CT exciton energy, which was explained by specific compact-coil chain conformations.<sup>282,283</sup> Specifically, two

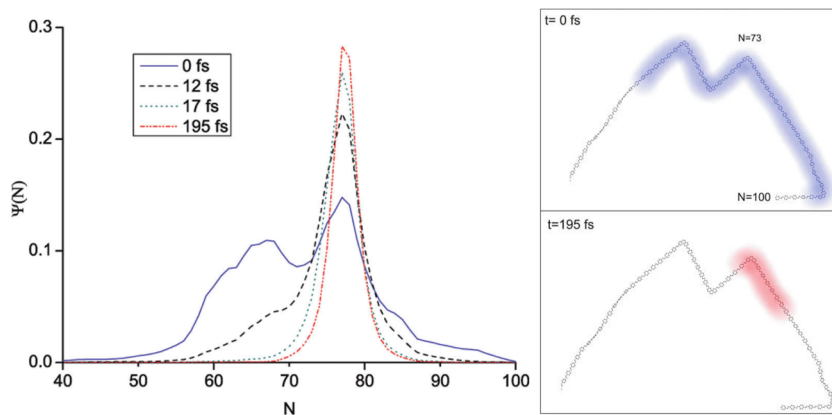


**Figure 34.** Exciton center-of-mass wave function,  $\Psi(N)$ , where  $N$  is the monomer label and the standard deviation of the torsional angle is  $5^\circ$ , as a function of time in PPV chain. The LEGS corresponds to the wave function at  $t = 0$ , which is spatially delocalized as shown at the upper-right scheme. Regions of negative curvature for the LEGS indicate that the Frenkel exciton is tunneling between potential minima determined by the conformational disorder. Vibrational relaxation through a single C–C bond oscillation leads to exciton localization into one of the potential minima within a chromophore as shown at the lower right scheme. Reproduced from ref 280. Copyright 2011 American Chemical Society.

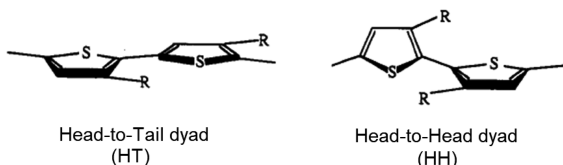


**Figure 35.** Coplanar and twisted conformers of P3HT dyad. Adapted from ref 281. Copyright 1993 American Chemical Society.

different mechanisms of formation of PANI films have been shown.<sup>284</sup> The first one is observed in relatively thick films due to entanglement of different polymer chains with plenty of entrapped solvent molecules when the film is formed, which results in relatively loose film morphology with fractal dimensionality of 1.68 and blue color of the film (Figure 36), where the CT exciton behavior is the same as in free polymer chains dissolved in the solution. The second mechanism is normally observed for thin films cast from solutions of low concentration and is due to a prevailing tendency toward intramolecular compact-coil conformation, which results in formation of films of the grained morphology with fractal dimensionality of 1.56 and violet color, where the CT exciton can be blue-shifted from 638 nm (observed in thick films and

solutions) to as far as 553 nm. It was discussed that the blue shift of the CT exciton is driven by two major factors, the loss of the entrapped solvent molecules from the film and the polymer–substrate interactions. Although the CT exciton is sensitive to changes in dielectric constant of the environment, which can be induced by the first factor, both factors result in local deformation of the polymer 3D coil to a more planar 2D structure to which the CT exciton is also sensitive. Particularly, such a deformation may result in increased interchromophore interactions, that is, the formation of the interchain CT exciton.

## 4. TRANSPORT OF EXCITONS

### 4.1. Energy Funneling through the Manifold of Hot States

In molecular photophysics, energy transfer can be considered as a process of changing energy level for the excited electron–hole pair either horizontally (i.e., from the excited level of donor to the excited level of acceptor, which are separated by some distance by intermediate species or blank space) or vertically (i.e., via downhill transfer of an excited electron from higher excited molecular orbital to lower excited molecular orbital within the same species). The latter takes place already in the first hundreds of femtoseconds after the excitation, where a hot

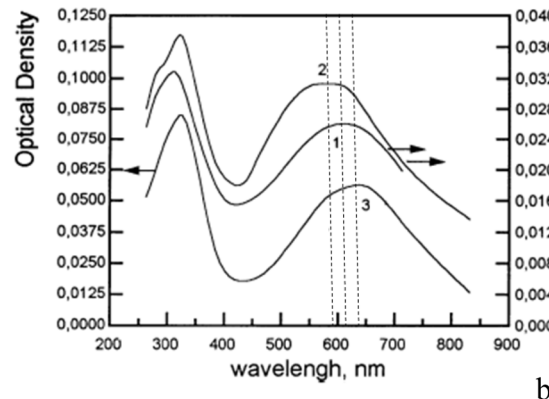
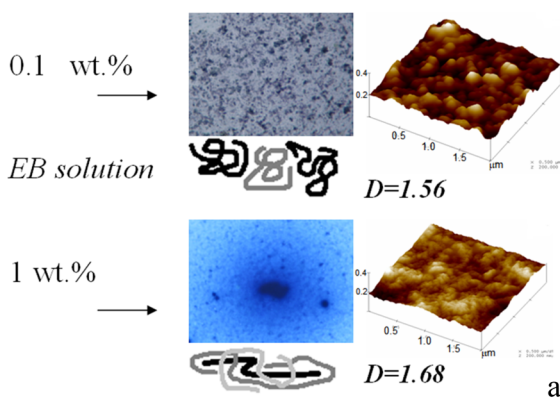


**Figure 36.** (a) Sample color, surface morphology, fractal dimension ( $D$ ), and typical solution concentrations from which PANI films were cast. (b) Electronic absorption spectra of PANI films with different energy of the CT exciton formed: thin film on (1) hydrophobic and (2) hydrophilic quartz surface and (3) thick film on quartz substrate. Part a reprinted with permission from ref 284. Copyright 2015 Elsevier. Part b reprinted from ref 283 with permission from Elsevier. Copyright 2001 Elsevier.

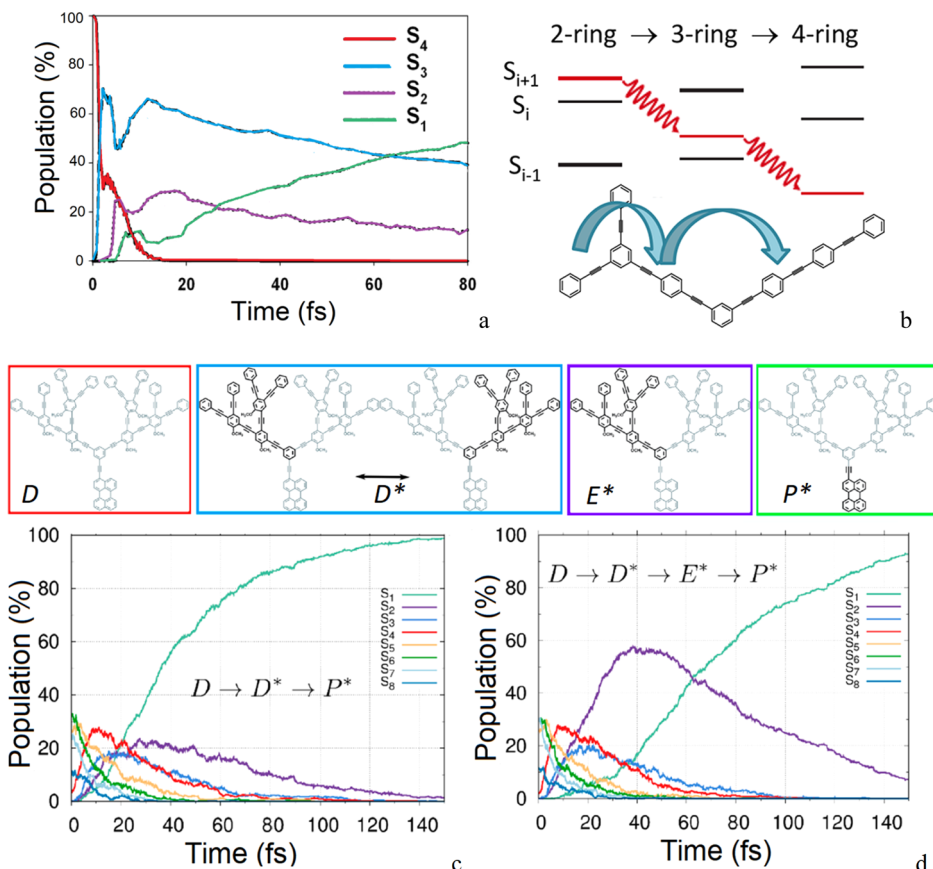


**Figure 37.** (a) Calculated populations of the lowest and hot excited states of light-harvesting dendrimers with directional energy transfer between PE units. (b) Jablonski diagram depicting the unidirectional energy transfer mechanism. (c) Direct and (d) indirect energy transfer between PPE and EPer units at a given time after the excitation. Dendrimer structures are shown on the top with bold lines that indicate equal probability of excitation of dendrimer arms ( $D^*$ ), exciton localization on one arm ( $E^*$ ), and excitation of EPer unit ( $P^*$ ). Part a reproduced from ref 285. Copyright 2010 American Chemical Society. Part b reproduced from ref 288. Copyright 2017 American Chemical Society. Parts c and d reproduced from ref 287. Copyright 2020 American Chemical Society.

exciton is formed first. The process of the vertical energy transfer is also known as a nonadiabatic interconversion (IC).

An ultrafast intramolecular vertical energy transfer was demonstrated by Fernandez-Alberti et al. for light-harvesting dendrimers composed of two-, three-, and four-ring linear phenylene ethynylene (PE) units linked through meta-substitutions.<sup>285</sup> In PE units, an ultrafast directional  $S_4 \rightarrow S_3 \rightarrow S_2 \rightarrow S_1$  electronic energy transfer was observed, corresponding to sequential two-ring  $\rightarrow$  three-ring  $\rightarrow$  four-ring transfer, which was accompanied by vibrational energy transfer through a dominant C≡C stretching motion. A rapid increase in the  $S_{n+1} \rightarrow S_n$  energy gaps and a decrease in the corresponding values for  $S_n \rightarrow S_{n-1}$  gaps upon  $S_{n+1} \rightarrow S_n$  population transfer were shown, which resulted, on one hand, in the  $S_{n+1}$  and  $S_n$  states becoming less coupled and, on the other hand, in the  $S_n$  and  $S_{n-1}$  states becoming more coupled, which yielded efficient  $S_{n+1} \rightarrow S_n \rightarrow S_{n-1}$  unidirectional energy funneling in light-harvesting dendrimers (Figure 37a,b).

In a dendrimer with donor poly(phenylene ethynylene) (PPE) units connected via ortho, meta, and para links to the energy sink of ethynylene perylene (EPer), the calculated time evolution of the populations of  $S_1$  and hot  $S_n$  states revealed efficient ultrafast electronic energy transfer from the initially excited high energy states ( $S_n, n \geq 3$ ) to the lowest  $S_1$  excited state in less than 500 fs, involving a transient population trap at the  $S_2$  state.<sup>286</sup> These processes were shown to result in the

populations of  $S_3$  and higher states decreasing rapidly, the population of  $S_2$  increasing and decaying, and the  $S_1$  state population increasing to a final value of  $\sim 100\%$  after 500 fs. Moreover, two regimes of energy funneling have been distinguished.<sup>287</sup> In the direct mechanism, the exciton experiences an ultrafast exchange between hot exciton states involving different degrees of delocalization between two donor dendrimer arms in the first 40 fs, followed by energy transfer to the EPer trap (denoted as the  $P^*$  state, Figure 37c) without being self-trapped in either of the two arms. In the indirect mechanism, the exciton is transiently self-trapped in the  $S_2$  state, represented as  $E^*$ , and localized on one donor arm for times longer than 10 fs, which slows down the intramolecular donor  $\rightarrow$  acceptor energy funneling (Figure 37d).

Energy funneling in the form of a nonadiabatic IC from higher energy quasi-extended exciton states to lower energy more localized local exciton ground states (LEGS) followed by vibrational relaxation of the LEGS to self-trapped polarons is also available in single polymer molecules within the period of the first C–C bond oscillation following photoexcitation.<sup>288</sup> This energy funneling causes fluorescence depolarization due to rotation of the exciton transition dipole moment as it relaxes. The higher the exciting energy the larger fluorescence depolarization is, because the higher excited states have a larger initial delocalization. Thus, fluorescence depolarization in general is a function of the excitation energy.

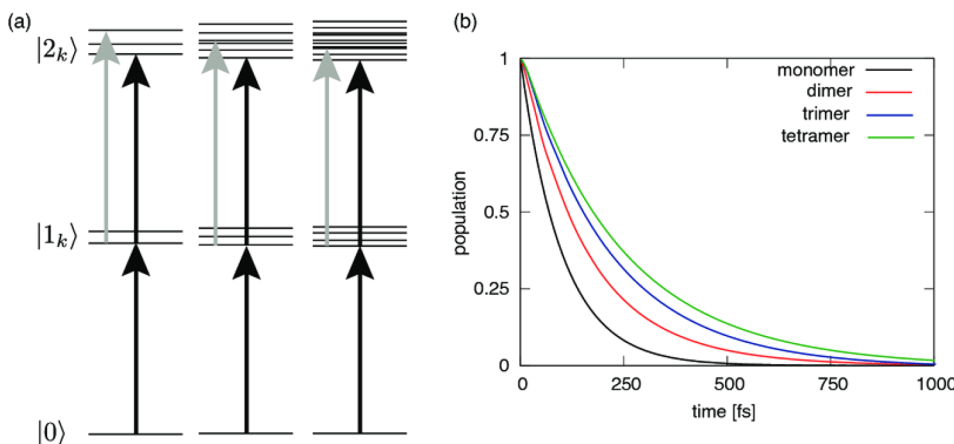


**Figure 38.** (a) Energy level scheme for exciton eigenstates of the dimer, trimer, and tetramer. Black arrows mark formation of the exciton (transition to the exciton band), and gray arrows mark formation of the hot exciton. (b) Size dependence of the interband decay from the hot to the lowest exciton manifold. Reprinted from ref 291, Copyright 2015, with permission from Elsevier.

The angle at which the transition dipole moment rotates between absorption and emission determines the fluorescence anisotropy,  $r_p$ , of an individual molecule, which for an ensemble of isotropically oriented molecules is defined as

$$\langle r \rangle = 0.4 \frac{\sum_i f_i r_i}{\sum_i f_i} \quad (9)$$

where  $f_i$  is the oscillator strength of the  $i$ th molecule and the factor of 0.4 originates from the assumption that the initial transition dipole moments have an isotropic distribution.<sup>289</sup> For fluorescence anisotropy, a value of  $\langle r \rangle = 0.4$  implies that the emitted light is parallel to the initial transition dipole moment, whereas a value of  $\langle r \rangle = 0$  implies that the emitted light is isotropically depolarized.

The rate of the vertical energy transfer is dependent on the amount of interacting chromophores. This rate becomes slower as size of the system increases (Figure 38). Specifically, as was shown by Kühn et al., the interband energy transfer rate between the second and first exciton manifold slows down as one goes from the monomer to the tetramer.<sup>290,291</sup>

#### 4.2. Factors Controlling Different Regimes of Exciton Energy Transfer in Multichromophoric Systems

**4.2.1. Exciton–Phonon Coupling.** Exciton–phonon coupling is a powerful tool that controls energy transfer and can either facilitate or suppress it. First, the effect of the exciton–phonon coupling on exciton transport is similar to the effect of vibrational excitations on charge carrier transport. The coupling of vibrational excitations and a free charge carrier converts the latter to a polaron, that is, to the charged particle clothed by a phonon cloud whose effective mass increases due to the accompanying phonon cloud that moves along with the charge and leads to its reduced mobility. In a similar way, the exciton–phonon coupling provides formation of a phonon cloud around the electron–hole pair, which lowers the system free energy due to distortion of the local environment around an electronically excited chromophore.

Weak exciton–phonon coupling is associated with the free and coherent exciton, where the exciton has a certain coherence length that well exceeds the interatomic distance in a molecular crystal or ordered polymer chain and dynamics of the exciton carrier density and polarization are identical. Delocalization of the coherent exciton implies formation of the exciton band, so

that the transport of free excitons occurs essentially within the exciton band.

Scattering by optical and acoustical phonons as well as by structural defects such as intermolecular dipole reorientations leads to temperature dependence of the exciton transport. The coherent character of the exciton persists if its energy level width  $\Gamma$  caused by scattering is small enough compared to the exciton bandwidth  $\Delta E_e$ ; then, its transport can be considered as a diffusion of delocalized excitation. In case of scattering of coherent excitons by optical phonons, the diffusion coefficient  $D$  is described as<sup>292</sup>

$$D \approx e^{\theta/T} \quad (10)$$

where  $\theta = \hbar\omega_0/k$  is the characteristic temperature of the optical phonon oscillating with frequency  $\omega_0$ . In case of scattering of coherent excitons due to acoustic phonons, the diffusion coefficient is described as

$$D \approx \frac{1}{\sqrt{T}} \quad (11)$$

but for low temperatures, it becomes temperature independent, that is,  $D = \text{const.}$ <sup>292</sup>

In the case of a strong exciton–phonon coupling, where at least one exciton counterpart (electron or hole) experiences strong coupling to the crystal lattice or molecular vibrations and acquires polaronic features, the exciton transfer rate ( $k_e \approx \Delta E_e/\hbar$ , where  $\Delta E_e$  is the exciton bandwidth) becomes small compared to the rate of the lattice deformation ( $k_d \approx E_d/\hbar$ , where  $E_d$  is the energy of local deformation), where the latter arises as a result of excitation. Under such a condition, that is,  $E_d > \Delta E_e$ , the local deformation accompanies the exciton transport, thus increasing the effective mass of the exciton and decreasing its mobility. If the exciton bandwidth decreases as a result of increasing exciton–phonon coupling below the value of  $\hbar/\tau_e$ , where  $\tau_e$  is the exciton free-path time, the band description of the exciton becomes invalid.<sup>292</sup> In this case, the exciton is considered to be localized or self-trapped where one or both of its carriers are small polarons in its own lattice distortion field, and the exciton transport acquires essentially noncoherent character, being a random walk. The diffusion of the localized exciton is predominantly thermally activated and its diffusion coefficient is described as<sup>292</sup>

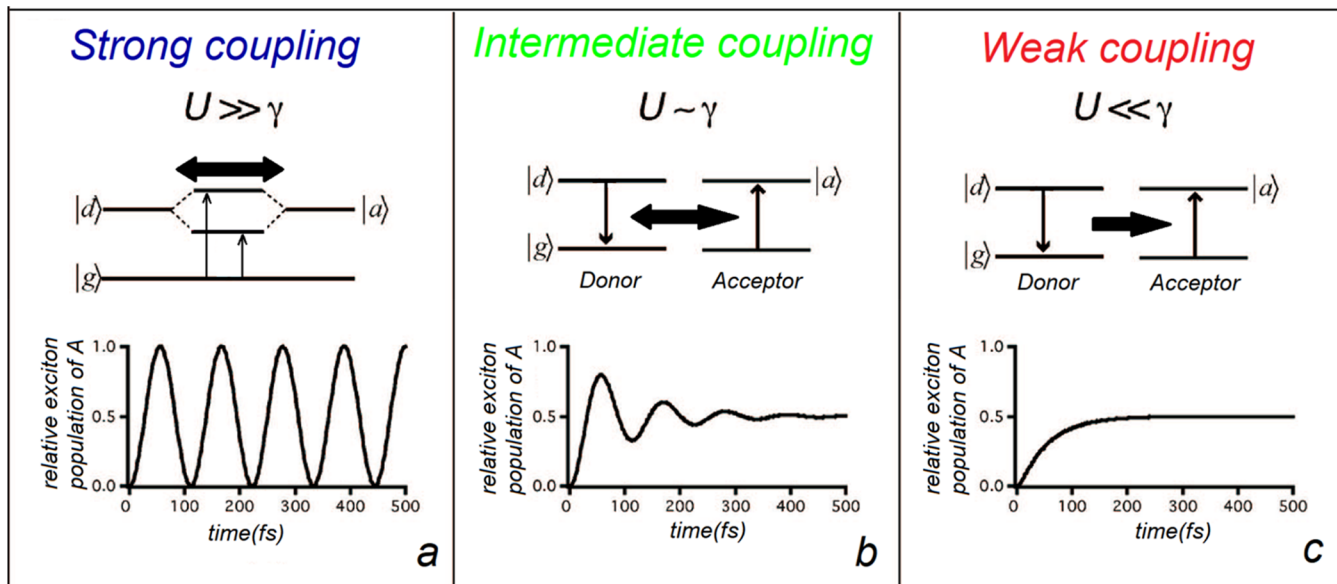


**Figure 39.** Different regimes of EET according to relationship between the electronic coupling  $U$  and the dephasing constant  $\gamma$ , shown as evolution of the exciton population of the acceptor: (a) the strong coupling limit; (b) the intermediate coupling limit; (c) the weak coupling limit. Adapted from ref 304. Copyright 2009 American Chemical Society.

$$D \approx e^{-E_a/(kT)} \quad (12)$$

where  $E_a$  is the activation energy.

On the other hand, coherent electron-vibrational dynamics initiated by nonadiabatic transitions between excited states can contribute to coherent resonance energy transfer (CRET). Here, the excited state dynamics is accompanied by a specific asymmetric vibrational excitation that can modulate subsequent spatial evolution of the electronic wave function, which behaves as wave-like motion.<sup>293,294</sup> The coherent electron-vibrational dynamics initiated by nonadiabatic transitions between excited states can promote a dynamic regime in which vibrations may coherently transfer the electronic excitation across molecular constituents.<sup>295</sup> The modulation of energy transfer by the vibrational excitations can also lead to the phenomenon of quantum oscillations or quantum beating of the excitonic population of the acceptor. However, dynamic disorder due to incoherent exciton–phonon coupling as a result of random nuclear motions results in time-dependent exciton decoherence and exciton self-trapping on the femtosecond time scale,<sup>296</sup> this leads to switching of the coherent regime of energy transfer to the incoherent hopping of energy described by the Förster resonance energy transfer (FRET) mechanism.<sup>95</sup>

**4.2.2. Donor–Acceptor Coupling.** The strength with which the donor and acceptor chromophores communicate with each other via the long-range dipole–dipole interaction, along with the role of perturbations imposed on these communications both from the bath of fluctuating nuclear motions in the molecule and from the surrounding external medium, is another important factor that determines the regime of energy transfer. In a model established by Kimura et al.<sup>297–299</sup> and intensively developed by Ishizaki and Fleming and Scholes,<sup>300–303</sup> it is proposed that the mechanism of excitation energy transfer (EET) is dependent on the ratio between the intermolecular electronic coupling  $U$ , responsible for exciton formation and excitonic coherence, and the dephasing constant  $\gamma$ , which is the inverse of decoherence time,  $\tau_c^{-1}$ , of the molecule's reorganization describing how the system interacts with the environment.

Thus, the coupling regimes can be distinguished through the relation between terms  $U$  and  $\gamma$ .

The weak coupling limit of EET is determined when  $U$  is much smaller than  $\gamma$ ; then the rate of nuclear motions of the system is faster than the rate of the donor–acceptor exciton transfer, and therefore, EET follows complete vibrational equilibration at the photoexcited state of the donor. In this way, the decoherence factor due to interaction with the vibrational degrees of freedom completely destroys the excitonic coherence between the donor and acceptor excited states, which leads to localization of the exciton on either the donor or acceptor, but not on both simultaneously. In this case, the EET dynamics follows the classical Förster mechanism, that is, its rate constant is given by the Fermi Golden rule,

$$k_{DA} = \frac{2\pi}{\hbar} |V_{DA}|^2 J_{DA} \quad (13)$$

and it is proportional to the overlap integral  $J_{DA}$  between the emission spectrum of the donor and the absorption spectrum of the acceptor and their electronic coupling  $V_{DA}$ , which depends on the D–A distance. Here, the excitation probability of the acceptor increases exponentially with time (Figure 39), and the excitation energy is transferred incoherently and irreversibly between different sites as described by an incoherent (Markovian) and irreversible hopping motion between the molecules.<sup>304</sup> In this way, the Förster theory is just formulated for the weak coupling limit.<sup>305</sup>

The opposite case corresponds to the strong coupling limit: when the electronic coupling  $U$  is sufficiently large compared to  $\gamma$ , then the donor and acceptor electronic states mix strongly and produce new delocalized states, where the energy is shared quantum mechanically among several chromophores. The probability to find the excitation on the acceptor site is an oscillating function with period depending on the electronic coupling  $U$  (Figure 39a). The excited-state wave function of such a system can be constructed by taking appropriate linear combinations of the wave functions of each chromophore, so that the excited states of each chromophore are then spread out

in bands throughout the entire system. Such an excitonic coherence between the donor and acceptor excited states is usually little perturbed by the interaction with vibrations.

In the intermediate case,  $U$  is comparable to  $\gamma$ , which determines a competition between formation of a delocalized exciton state and its localization due to relatively high perturbation from the vibration bath. Relatively strong electronic coupling between the donor and acceptor thus provides retention of quantum information (exciton wave function phase) during EET, whereas relatively high perturbation due to vibrations leads to nonequilibrium (non-Markovian) effects on ultrafast time scales that originate from lattice distortion dynamics, so that the vibrational coherence transfer persists for less than 1 ps. In this way, the intermediate regime provides a coherent exciton transfer. This mechanism contrasts with the classical hopping mechanism in which the excitation moves randomly, dissipating quantum information at each step and localizing just at each site sequentially. In the intermediate regime, the excitation can be simultaneously on the donor and the acceptor at any time, sharing the amplitude and phase of the wave function at each site, but the dynamical evolution of the system results in displacement of the excitation from the donor to the acceptor in a deterministic, classical way (Figure 39b), with a preferred path chosen due to partial delocalization of the wave function. For CRET, where EET is modulated by vibrational excitations, a nontrivial dependence of energy transfer rate on the donor–acceptor distance was theoretically predicted. It was shown that the rate in general deviates from the inverse sixth power distance dependence as it should be for the original FRET. On one hand, the donor–acceptor quantum coherence makes the distance dependence steeper than the sixth power; on the other hand, the non-Markovian bath perturbation makes the distance dependence more moderate than the sixth power.<sup>306</sup> Such nontrivial behavior may be due to the presence of strong electron–phonon coupling, which creates specific vibrational excitations that spatially modulate the excited electronic state before localizing it into a self-trapped exciton.<sup>307</sup> It should be noted that excitons with longer coherence lengths have a higher probability to diffuse coherently in an extended system.<sup>308,309</sup>

#### 4.3. Coherent Exciton Delocalization

Coherent exciton delocalization takes place in the case of strong coupling between the donor (D) and acceptor (A) when both molecules equally share their excitations, resulting in a common exciton that is largely delocalized over the DA pair. The description of coherent exciton delocalization remains correct as long as the fluctuations between the two sites introduce only small perturbations; in this case, an exciton oscillates coherently between sites D and A before the fluctuations eventually lead to the decay of the coherence.<sup>310</sup>

Depending on the mutual orientation of the dipole moments of molecules in the DA pair, coherent exciton delocalization may correspond to the well-known cases of red or blue shift or Davydov splitting of the energy levels in spectra of J-, H-, or J–H aggregates, respectively (Figures 12 and 39a). Systems that possess coherent exciton delocalization are perspective materials for tuning and extension of spectral features to be used in light-harvesting devices, optical sensors, quantum computers, etc. For example, Cannon et al. reported tuning the optical properties of Cy5 dye aggregates controlled by a DNA template and salt concentration.<sup>311</sup> Specifically, this system exhibited switching between J-aggregate and H-aggregate behavior, with H-tetramer

aggregate showing a surprisingly large Davydov splitting that produced a visible color change of the solution from cyan to violet due to the coherent exciton delocalization.

It was found that coherent exciton delocalization is strongly dependent on temperature. For example, in the photosynthetic complex of purple bacteria B850 at  $T = 1.2$  K, the exciton delocalizes over the entire ring of 18 strongly interacting bacteriochlorophyll chromophores due to the strong electronic coupling ( $\sim 300\text{ cm}^{-1}$ ) and weak disorder ( $\sim 125\text{ cm}^{-1}$ ), whereas at room temperature, the exciton is initially delocalized over 5–13 molecules, but then it rapidly decoheres into the exciton size of 4 molecular units within 100 fs.<sup>312</sup>

Dubin et al. described extended spatial coherence of the radiating states over a space region comparable to the total chain length ( $10\text{ }\mu\text{m}$ ) of polydiacetylene (PDA) at low temperature (10 K), which could be observed as an interference pattern obtained from two  $1\text{ }\mu\text{m}$  wide emitting regions of the chain.<sup>313</sup> Specifically, this effect was explained by interaction of a quantum “wavepacket” composed of a coherent superposition of the different  $k$ -states of the chain, being in phase at  $x = 0$  and extending over the area of the exciting incident light ( $\sim 1\text{ }\mu\text{m}$ ), with acoustical phonons in a picosecond time range that dephase the different  $k$ -modes over the entire PDA chain. The estimated exciton diffusion coefficient ( $D \approx 10^4\text{ cm}^2\text{ s}^{-1}$ ) was 7–8 orders of magnitude higher compared to the diffusion coefficient for incoherent hopping of singlet excitons, and the exciton speed from the above data can be estimated to be only 1 order of magnitude lower than the speed of light. Therefore, this case can be related to the coherent exciton delocalization, an ultrafast process approaching the speed of light.

Although normally there is no long-range energy transfer in case of the coherent exciton delocalization, it does influence the long-range exciton transport nevertheless. This influence can be separated into two cases. First, exciton energy transfer can serve as the origin of the coherent exciton delocalization at specific sites. Second, the preliminary coherent exciton delocalization can impact a subsequent transport of the exciton.

In the first case, the coherent exciton delocalization is the result of exciton energy transfer. This case often corresponds to formation of an excimer or exciplex in multichromophoric systems, where an exciton must migrate before it meets a ground-state molecule, to which it shares its excitation and forms an excited homo- or heterodimer or more extended excited species. Shepherd et al. reported on exciplex formation in composites containing two functionalized anthradithiophene (ADT) derivatives, ADT-TES-F (donor, D) and ADT-TIPS-CN (acceptor, A) as a result of FRET from D to A depending on the D–A distance.<sup>314</sup> The result of such an exciton transport was a delayed charge carrier photogeneration, which occurred on nanosecond time scales in composites, in contrast to sub-500 ps carrier photogeneration observed in ADT-TES-F pristine films. The authors emphasized that such an effect could be beneficial for applications requiring effective storage of photogenerated charge carriers such as bistable optical switches, photodetectors, and image storage devices.

Specific excimer formation with larger exciton delocalization can be found in J-aggregates, where delocalization extends over the coherence length of the J-aggregate plus a dimer with which an exciton interacts. Delayed photoluminescence was found in homogeneous<sup>148</sup> and heterogeneous<sup>315</sup> J-aggregate systems of thiamonomethinecyanine dyes, which was explained by formation of excimers and exciplexes, respectively, with preliminary migration of a free exciton along the J-aggregate

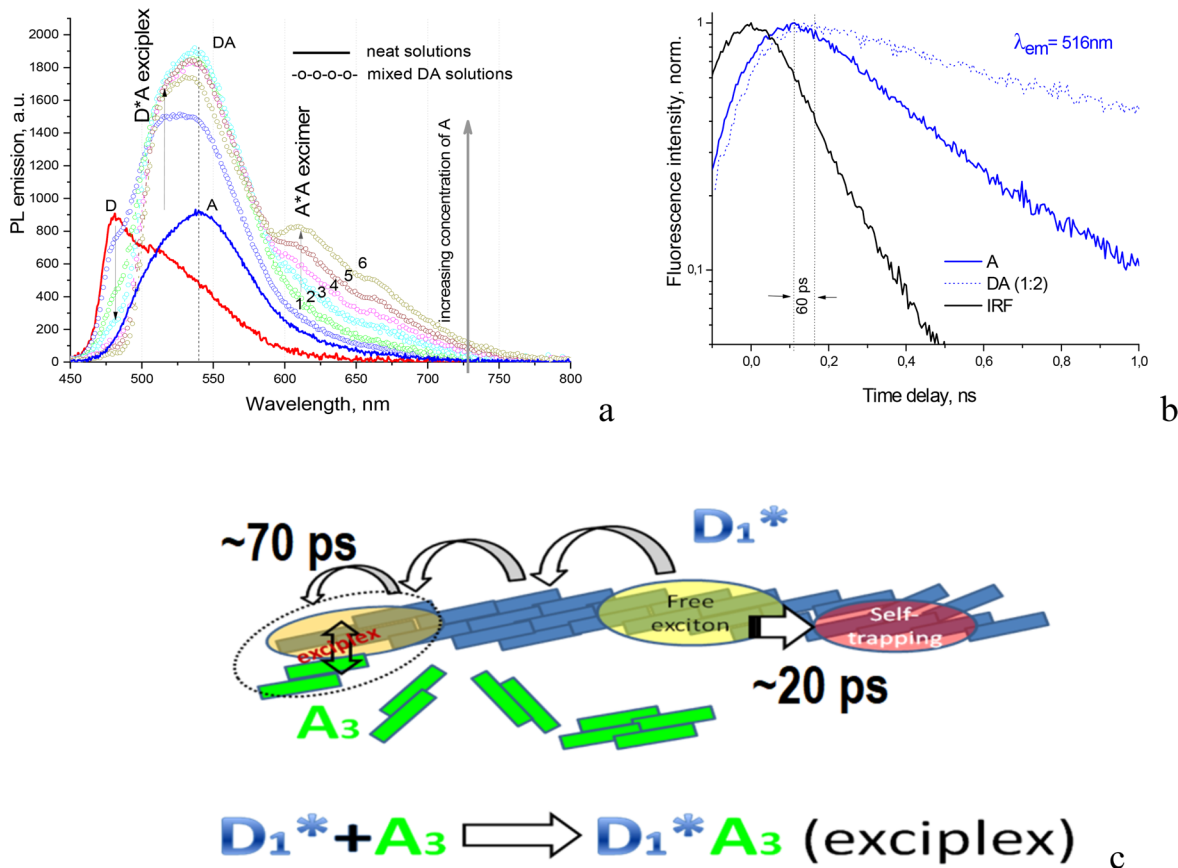


**Figure 40.** (a) PL emission ( $\lambda_{\text{exc}} = 405 \text{ nm}$ ) of solutions of the neat A and D (solid curves) and DA mixtures (symbols) of aggregates of thiamonomethinecyanine dyes upon increasing concentration of A in the DA mixture at D/A molar ratios of 1:1 (blue), 1:2 (green), 1:3 (cyan), 1:4 (magenta), 1:5 (brown), and 1:6 (dark-yellow) and unchanged concentration of D ( $1 \times 10^{-5} \text{ M}$ ) in both individual (red curve) and mixed solutions. (b) Emission time profiles at 516 nm of D, A (solid curves), and DA (dotted curves) solutions after excitation at 405 nm with concentrations of  $C_D = 1 \times 10^{-5} \text{ M}$  and  $C_A = 2 \times 10^{-5} \text{ M}$ . (c) Scheme of exciplex formation in the heterogeneous J-aggregate systems of thiamonomethinecyanine dyes with preliminary migration of an exciton to specific sites. Reproduced from ref 315. Copyright 2019 American Chemical Society.

to specific sites where it can interact with the ground-state dimers being the building blocks of the J-aggregates in the solution. In aggregates of homomolecules, the exciton migration took  $\sim 200 \text{ ps}$  before the excimer was formed, whereas in the heterogeneous system of two different thiamonomethinecyanine dyes, the exciton migration was shorter and took about 70 ps (Figure 40). The other interesting phenomenon due to coherent exciton delocalization in the heterogeneous system was enhanced emission of the exciplex, which even surpassed the sum of emissions of the neat donor and acceptor J-aggregate solutions, and also an extended excitation lifetime that exceeded the lifetime of the free exciton in the neat J-aggregate solution.

The case where the coherent exciton delocalization influences EET can be considered in view of the relationship between the exciton size and exciton vibrational coupling (Figure 5). The larger is the exciton delocalization, the smaller is the exciton vibrational coupling, which affects the exciton coherence and the exciton diffusion length consequently. This was demonstrated with the example of the antenna size effect of a J-aggregate of pseudoisocyanine (PIC) dye coupled to a CdTe nanocrystal. Specifically, a 30-fold increase in the quantum yield of fluorescence of PIC J-aggregates in the vicinity of CdTe nanocrystals was observed as a result of the resonant energy transfer from the nanocrystals to PIC J-aggregates in aqueous solutions. However, this enormous effect was observed only when the exciton coherence length in the J-aggregate was  $N_{\text{coh}} \geq$

6, whereas no energy transfer was observed when the coherence length was as small as 3–4 monomers.<sup>316</sup>

Singh et al. reported on the relation between the exciton size and dynamics in stacks of graphene quantum dots of different planar size, that is, hexabenzocoronene (HBC) consisting of an aromatic core of 42 carbon atoms and a carbon quantum dot (CQD) with 78 carbon atoms.<sup>317</sup> Although the exciton was delocalized over  $\sim 1\text{--}2$  molecular units in both assemblies, the exciton diffusion length along the stacks was essentially different, being 16 and 3 nm for HBC and CQD, respectively. The obtained results suggested that delocalization of exciton in the plane may affect its migration in the perpendicular direction.

On the other hand, it was found that in coupled polymer chains the interchain singlet exciton transfer is significantly easier than that for triplet excitons under the same interchain coupling conditions.<sup>318</sup> This result was explained by the fact that the singlet exciton is more delocalized than the triplet exciton and that the interchain hopping is facilitated for electrons with opposite spins. It should be noted, however, that singlet and triplet excitons can be transferred by different mechanisms (i.e., Förster and Dexter).

#### 4.4. Exciton Diffusion

**4.4.1. General Characteristics of the Exciton Diffusion Process.** Whereas the coherent, ballistic processes of excitonic energy transfer take place on the ultrafast ( $<100 \text{ fs}$ ) time scale, the incoherent or diffusive process of exciton migration spans

longer time scales on the order of 0.1–1 ns.<sup>319</sup> The incoherence arises because of a faster dissipation rate owing to nuclear motion or phonons, which have typical relaxation times of  $10^{-13}$  to  $10^{-12}$  s compared to the exciton lifetimes of  $\sim 10^{-10}$  to  $10^{-8}$  s.

Excitons are neutral boson quasi-particles; therefore, excitons with the same energy are able to arise together at high concentration. An inhomogeneous concentration of particles in homogeneous medium causes their diffusion to space regions where their concentration is low, which can be described by the diffusion equation as applied to excitons:

$$\frac{\partial n}{\partial t} = D \nabla^2 n - n/\tau_0 \quad (14)$$

where  $n$  is the exciton concentration,  $D$  the diffusion coefficient,  $\nabla^2$  the Laplace operator, and  $\tau_0$  the exciton lifetime. The diffusion process is characterized by the diffusion length, which is the root-mean-square displacement of a particle from its initial position, given by

$$L_D = \sqrt{\frac{\sum dL_i^2}{N}} = \sqrt{2ZD\tau_0} \quad (15)$$

where  $dL_i$  is the displacement of an  $i$ th exciton from its original position,  $N$  is the total number of excitons, and  $Z$  is the dimensionality of the diffusion process (along the line or surface or in bulk, equal to 1, 2, or 3, respectively).<sup>320</sup>

However, the presentation of the exciton diffusion should not be confused with the mass diffusion of neutral particles driven by thermodynamic laws such as entropy increase, because individual Frenkel excitons are usually confined to their host molecules and therefore their “diffusion” is different in details and is largely dependent on the distribution of the acceptors of energy around the donor. Instead, the elementary steps of exciton diffusion between the donor and the acceptor should be considered as a radiationless transfer of a virtual photon driven by dipole–dipole interaction, where an excited donor is quenched and an acceptor acquires an excited state, which is described by a FRET mechanism that imposes three main conditions on this process, namely, energetic proximity (i.e., the overlap of the acceptor absorption and the donor emission spectra), distance proximity, which usually should be less than 10 nm, and dipole orientation proximity, because mutually orthogonal dipoles are not able to transfer the energy. In general, Förster type excitation energy transfer between donor and acceptor may occur not only through dipole–dipole resonance when both molecules have an allowed dipole transition but through dipole–quadrupole resonance as well, when one of the molecules has a forbidden dipole transition. Then, the transfer rate is proportional to  $R^{-6}$  for dipole–dipole resonance and  $R^{-8}$  for dipole–quadrupole resonance ( $R$  is the distance between the molecules).<sup>321</sup> In the case of dipole–dipole FRET, if the molecular motion is frozen, the exciton population in the donor molecules,  $n_D$ , decreases depending on the acceptor concentration, according to the expression that was first obtained by Förster:<sup>292,305</sup>

$$n_D(t) = n_0 \exp\left(-\frac{t}{\tau_0} - 2q_1 \sqrt{\frac{t}{\tau_0}}\right) \quad (16)$$

where  $q_1 \approx 3.71 R_0^3 c_A$ ,  $c_A$  is the acceptor concentration, and  $\tau_0$  is the donor lifetime.

The diffusion equation for excitons (eq 14) is different from the diffusion equation for mass by the last term, which describes

a limited lifetime of excitons that contribute to the diffusion process. A further difference of the Frenkel exciton diffusion compared to mass diffusion is the large difference of the exciton diffusion coefficient, being on the order of  $10^{-4}$  to  $10^{-3}$  cm $^2$ /s,<sup>322</sup> compared to that found for the solute–solvent diffusion of mass in liquids ( $\sim 10^{-5}$  cm $^2$ /s). However, the diffusion length of Frenkel excitons is limited by their lifetimes (approximately nanoseconds) and constitutes usually values on the order of  $\sim 10$  nm.

Energy transfer can occur not only via the Förster mechanism, the efficiency of which decreases with the distance  $R$  between donor and acceptor as  $R^{-6}$  and which is effective at distances up to  $\sim 10$  nm, but also via the Dexter mechanism through electron exchange as a result of physical contact of the molecules with intermolecular distance less than 1 nm when there is a significant overlap of molecular orbitals<sup>323,324</sup> (Figure 41). Dexter energy

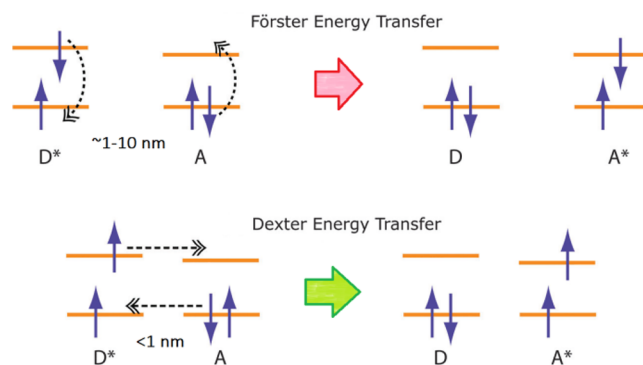


**Figure 41.** Schemes for Förster energy transfer of a singlet exciton via long-range dipole–dipole interaction and Dexter energy transfer, which enables diffusion of a triplet exciton via direct electron exchange. Adapted with permission from ref 322. Copyright 2015 Royal Society of Chemistry.

transfer enables diffusion of triplet excitons, because their transfer by Förster mechanism requires spin flip upon excitation of the acceptor for every transfer step, which has low probability. Since triplet excitons undergo diffusion via short-range Dexter energy transfer, they have lower values of diffusion coefficient, being on the order of  $10^{-7}$  to  $10^{-4}$  cm $^2$ /s, but they have longer diffusion length than singlets, up to micrometers, due to their much longer lifetime (approximately microseconds).<sup>322</sup>

**4.4.2. Driving Forces for Exciton Diffusion.** **4.4.2.1. Energy Gradient.** As noted previously, exciton diffusion cannot be considered the same as mass diffusion, because Frenkel excitons are bound to their host sites and the exciton diffusion process is associated with a succession of quenching and excitation acts at different sites in the organic material, where long-range energy transfer in the form of FRET is realized by dipole–dipole interactions between these sites. Nevertheless, although no charge transfer takes place in the above process, the understanding of the excitonic energy transfer can be borrowed from the model of hopping charge transport in disordered organic material via localized states,<sup>325</sup> where the charged localized states are described by the wave function  $\Psi_a(\vec{r}) \approx \exp(-r/a)$ ,  $a$  being the characteristic Bohr radius of the localized state. In this model, charge hopping between different sites occurs, which is driven by two factors: first, the overlap of wave functions between sites  $i$  and  $j$  (the overlap integral) due to the extended Bohr radius of the states,

$$\int \Psi_a^*(\vec{r} - \vec{R}_i) \Psi_a(\vec{r} - \vec{R}_j) dV \approx \exp\left(-\frac{|\vec{R}_i - \vec{R}_j|}{a}\right) \quad (17)$$

which assists the charge carrier to make a distant hop and to occupy the site with more profitable energy; second, the thermal activation factor, which allows the charge carrier to overcome the energy barrier between sites  $i$  and  $j$ ,

$$\Delta_{ij} = \epsilon_i - \epsilon_j \quad (18)$$

Thus, the probability of charge hop between the sites  $R_i$  and  $R_j$  is a result of contribution of both the square of the overlap integral

$$\alpha_{ij} = \exp\left(-\frac{2|\vec{R}_i - \vec{R}_j|}{a}\right) \quad (19)$$

and activation factor

$$f_{ij} = \exp\left(-\frac{|\Delta_{ij}|}{kT}\right) \quad (20)$$

which after averaging and optimization yield the conductivity in a 3D continuum as follows:

$$\langle \sigma \rangle_{3D} \approx \exp\left\{-\frac{4}{3}\left(\frac{4\pi r_s}{a}\right)^{3/4}\left(\frac{W}{kT}\right)^{1/4}\right\} \quad (21)$$

where  $W$  is the energy corridor determined by the minimal and maximal energy of sites in which the charge can move (Figure 42).

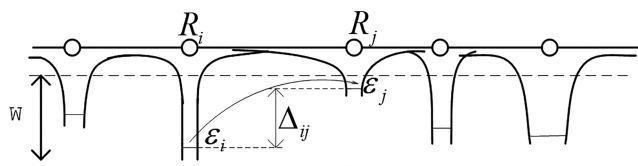


**Figure 42.** Linear chain of sites with energetic disorder in the form of a varied depth of the energy wells,  $\epsilon_i$ , between which the charge transport occurs.

The energy gradient that drives a charge toward lower accepting energy levels in the hopping model of charge transport due to the overlap of wave functions of respective sites (eq 19) can be also considered as a driving force for the downhill migration or cascaded energy transfer of a singlet exciton, which attains energy gain due to the long-range overlap of wave functions of the sites  $i$  and  $j$  spatially separated by distance  $R_{ij}$ , which provides certain tunneling transition probability of the exciton from a localized state  $i$  to a localized state  $j$  that is lower in energy.

As both thermal activation and downhill migration mechanisms can be competitive, the latter is predominant at low temperatures (Figure 43). At low temperatures, the exciton–phonon coupling is weak and the excitons retain coherent character, which implies transport within the exciton band. In conjugated polymers, the downhill migration can be considered as exciton transport between spectroscopic units, that is, the different spatial segments of the chain, which are responsible for the spectroscopic properties of the polymer and possess exciton states with shorter and longer effective conjugation length, respectively.<sup>326</sup> The downhill migration can be presented here as a unidirectional communication between spectroscopic units,

which can be as long as a few monomers on a polymer chain and where the coherent exciton is freely delocalized over the spectroscopic unit, while a distribution of spectroscopic unit sizes gives a distribution of exciton energies, with the lowest energy excitons being on the longest spectroscopic unit.<sup>327–329</sup> In poly- and oligothiophenes, an intramolecular downhill migration due to an energy gradient can exist in molecules as small as 16-mer ( $16 \times 4$  thiophene units).<sup>330</sup>

A striking feature of the downhill migration of singlet excitons is that the hop distance between the sites or spectroscopic units in this process is strongly dependent on approaching the exciton energy to the energy of site with the lowest band gap or the bottom of the exciton band. The closer is the exciton energy to the bottom of the exciton band, the larger is its each subsequent hop, and the longer is the hop time compared to previous hops,<sup>331,332</sup> which results in the diffusion coefficient varying in time from larger to smaller values.<sup>333</sup> The reason for this phenomenon can be understood from the fact that although there are plenty of neighboring sites with lower energy compared to the just generated exciton, this amount of sites rapidly decreases as the exciton loses its energy, so that the exciton needs to look for more remote sites that possess acceptable energy that it can occupy (Figure 43). It should be noted that the spatial energetic disorder here is related to the different conjugation length associated with the different sites, rather than to the Gaussian disorder. The above energetic disorder is influenced by such factors as variation in intermolecular packing, conformational changes, and defects in conjugated polymer chains.

The diffusion coefficient for the downhill migration of singlet excitons is temperature-independent for both conjugated polymers<sup>333</sup> and small molecular systems.<sup>334</sup> The processes of downhill migration were observed for triplet excitons too; however, an elementary step in migration of triplet excitons is a short-range Dexter energy transfer, which limits the number of available hopping sites and therefore may prevent triplet excitons from diffusing over long distances making their diffusion length often comparable to that for singlet excitons ( $\sim 10$  nm) despite much longer lifetimes of the triplet excitons.<sup>335–337</sup> Tamura et al. showed that although the triplet exciton hardly diffuses in a rubrene crystal, it may serve for regeneration of the singlet exciton via the triplet–triplet annihilation mechanism, which thus revives the long-range exciton diffusion.<sup>338</sup> Yeboah and Singh found that the singlet exciton diffusion length increases with spectral overlap integral and photoluminescence quantum yield but decreases with refractive index of the photoactive material, whereas diffusion length of triplet excitons increases with photoluminescence quantum yield and decreases with dipole moment.<sup>339</sup>

**4.4.2.2. Thermal Activation.** An activation factor (see eq 20) that contributes to the charge transport also plays a role in exciton transport through the thermally activated hopping mechanism. Temperature activated hopping has a dominant contribution at relatively high temperatures (above 150 K), and in contrast to the downhill migration such a transport occurs among sites of similar energy (isoenergetically) at nearly constant site-to-site distances. At high temperatures, the frequency of scattering events of an exciton increases and the condition for its free traveling time,  $\tau > \hbar/kT$ , weakens, which makes the exciton transport essentially incoherent and the exciton band representation invalid as the exciton bandwidth decreases exponentially with increasing temperature.<sup>292</sup> In this

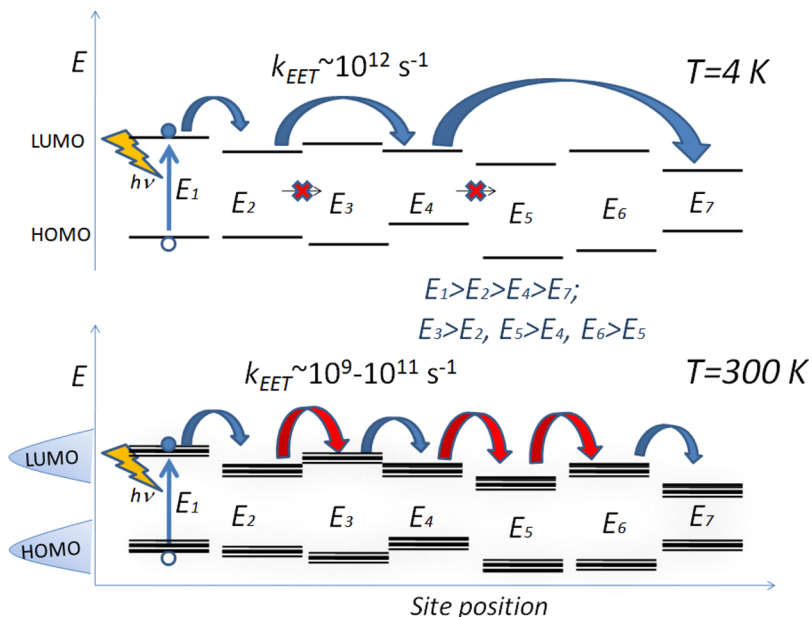


**Figure 43.** Illustration of the exciton diffusion process via downhill migration (shown by blue arrows) and thermally activated hopping (red arrows). HOMO and LUMO energies are represented as delta-function for the downhill migration and as Gaussian density of states for thermally activated hopping. The characteristic difference of the downhill migration and thermally activation hopping is the exciton transfer rate (indicated values are typical for polythiophenes) and the length of hopping.

case, the exciton hops are thermally activated in accordance with eq 21.

It should be noted that energy transfer via thermal activation can occur from the donor with a smaller band gap than that of the acceptor. The energy difference required to overcome the barrier comes with simultaneous excitation of a phonon, which makes the exciton hot and thus able to hop to the acceptor. The phonons that accompany exciton formation thus lead to inhomogeneous broadening of energy levels on the order of  $kT$ , the distribution of which is described by Gaussian disorder. That is why thermal activation hopping is considered between Gaussian density of states (DOS) rather than between narrow levels; the latter is valid for the downhill migration only (Figure 43). DOS broadening can also be induced due to diagonal and off-diagonal disorder originating from static energy fluctuations of the sites and torsional fluctuations, respectively, which make the exciton strongly localized at a certain energy level within the DOS.<sup>331</sup>

Variation of the DOS width due to energetic disorder among different sites, however, leads to only marginal changes in exciton diffusion length, as was shown for NRS- (poly[2-(4-(3',7'-dimethyloctyloxyphenyl))-co-2-methoxy-5-(3',7'-dimethyloctyloxy)-1,4-phenylene vinylene]), BEH- (poly[2,5-bis(20-ethyl-hexyl)-1,4-phenylenevinylene]), and MEH-PPV copolymers.<sup>340</sup> On one hand, the DOS width in disordered medium is determined by Gaussian distribution of energy levels, which for reduced disorder results in a smaller DOS width, which correlates well with larger exciton diffusivities. On the other hand, decreasing energetic disorder causes a reduced exciton lifetime due to an increase in access to quenching sites within the polymer film.<sup>341</sup>

Inhomogeneous broadening of energy levels into DOS leads also to the phenomenon of random walk of an exciton within the DOS or so-called spectral diffusion. This spectral diffusion usually results in exciton relaxation to the demarcation level or thermal equilibrium energy from which it recombines. The

primary excitation executes a random walk within the DOS only when the excitation energy is higher than the demarcation energy.<sup>137</sup> This demarcation energy is at  $\Delta\varepsilon = -\sigma^2/(kT)$  below the center of DOS and causes the commonly observed bathochromic shift of the PL emission of singlet excitons at reduced temperatures due to reduction of this thermal equilibrium energy.<sup>342</sup> However, spectral diffusion of triplet excitons within the DOS is suppressed, since the triplets jump over the shortest distance and experience a shortage of target sites to which they can transfer the energy. If these sites have higher energy that cannot be overcome by the available thermal energy, the exciton diffusion stops. This phenomenon was called a frustration, which leads to hypsochromic shift observed at low temperatures for triplets in disordered compounds.<sup>342</sup>

In an ensemble of chromophores whose electronic transitions are inhomogeneously broadened due to disorder, the incoherent exciton spectral migration results in an energy transfer where the exciton energies will be dispersed as a result of hopping.<sup>343</sup> Being far from the demarcation energy level within inhomogeneously broadened DOS, the exciton has more time for hopping; therefore, the mean hopping time of the excitation strongly depends on its energy. For example, exciton hop along the chain of spectroscopic units of poly(3-(2,5-diethylphenyl)thiophene) (PDOT) with inhomogeneous broadening on the order of  $kT$  corresponds to a transfer time of  $\sim 10\text{ ps}$ .<sup>344</sup>

Although both downhill migration and thermally activated diffusion are random-walk processes due to the disordered nature of organic solids, a clear difference between these transport mechanisms consists in that the latter involves essentially incoherent excitons that undergo true diffusion with time-independent average hopping length, which results in slower rates of the exciton transport. For polythiophenes, it was reported that the downhill migration occurs very rapidly, on time scale of  $\sim 1\text{ ps}$ , while the time scale for the intrachain thermally activated diffusion, which is comparable to that for interchain diffusion, is on the order of  $10\text{--}100\text{ ps}$ .<sup>255,330,345</sup> A

similar time scale for exciton diffusion was found in J-aggregates of cyanine dyes,<sup>148,346</sup> which is naturally limited by the exciton lifetime in J-aggregates. Interestingly, the time for an elementary hop of the exciton was calculated for porphyrin J-aggregates to be 1.2 ps,<sup>347</sup> from which the quantity of ~100 hops can be evaluated in the exciton diffusion process. The time scale in the range of 10–1000 ps depending on the guest concentration was reported for incoherent exciton diffusion in the conjugated polyindenofluorene host–perylene guest system.<sup>319</sup> The diffusion coefficient for the downhill migration in polythiophenes was reported to be 2 times lower than that of thermally activated diffusion ( $1.4 \times 10^{-4}$  vs  $3.2 \times 10^{-4}$  cm<sup>2</sup>/s), although the downhill migration cannot be considered as a normal diffusion since its average hopping length is changing as it moves downward in the DOS.<sup>333</sup>

**4.4.2.3. Nonuniform Internal Electric Field.** Although an exciton is an electrically neutral particle, it consists of coupled positive and negative charges, each of which can be influenced by external or internal electric fields. If the electric field is uniform, its action on both charges has no result. However, if the electric field is nonuniform, its local magnitudes on positive and negative charges of the exciton can be different, so that the Coulomb forces acting on the different counterparts of the exciton are not compensated and a net driving force arises, which results in exciton transport that is headed by that exciton charge that experiences the stronger force.

Organic semiconducting systems often contain trapping charges and heterogeneous organic systems also have a mismatch of energy levels at the donor–acceptor heterointerfaces, all of which produce nonuniform internal electric fields, which thus influence the migration of excitons in such systems. Yang et al. theoretically simulated the exciton migration dynamics in a polymer-based D/A photovoltaic system and found that the exciton becomes polarized under the nonuniform electric field, which is distributed as a linear gradient.<sup>348</sup> The authors concluded that this additional exciton migration mechanism might provide a new strategy to optimize the photovoltaic efficiency of the devices. However, it should be noted that in real organic semiconducting systems nonuniform internal electric fields are spatially localized and randomly oriented due to nonuniform distribution of various factors, such as the complex morphology of polymer-based structures, stochastic distribution of traps, and charge screening.<sup>349</sup> Considering that these space regions where the nonuniform field is produced are space limited and comparable to the Frenkel exciton radius, the role of the nonuniform internal fields in unidirectional exciton transport may be reduced. Instead, the role of defects which possess local electric fields, such as weakening or strengthening of conjugation, can play the role of energy wells or energy barriers, which induce delay, blocking, trapping, or interchain hopping of excitons.<sup>350</sup>

The exciton dynamics in a nonuniform electric field is different from that in a uniform one. Meng et al. theoretically simulated exciton behavior along a polymer chain consisting of 120 sites when a positive trapped charge is located at one end of the chain, which creates a linear field gradient along the chain, under the assumption that the exciton can produce fractional free charge, that is, it can dissociate partially.<sup>349</sup> The authors showed that when an exciton is photogenerated in the middle of the chain, where the field inhomogeneity is strong enough to drive the exciton, the exciton begins to migrate to the region of increasing electric field or to the positive trap, because the attraction of a negative charge to this trap is stronger than the

repulsion for the positive charge of the exciton from this trap, according to the exciton driving force

$$F = -Q_p [E(n_c^-) - E(n_c^+)] \quad (22)$$

where  $n_c^-$  and  $n_c^+$  are the central coordinates of the polarized negative charges,  $-Q_p$ , and positive charges,  $Q_p$ , respectively, and  $E$  is the electric field at the indicated sites. Thus, it enters a region of strong enough electric field (at about  $t = 400$  fs, Figure 44), where the condition of its dissociation is available.

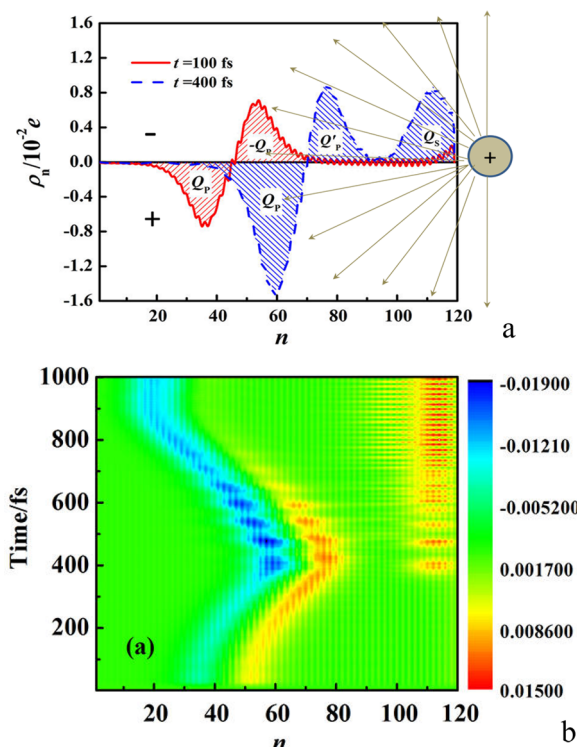


**Figure 44.** (a) Instantaneous net charge distribution,  $\rho_n$ , of an exciton on a polymer chain consisting of 120 sites at time  $t = 100$  fs (red regions show symmetric negative and positive charge distribution relative to the exciton center) and  $t = 400$  fs (blue regions show partial exciton dissociation as it migrates to the positively charged trap). (b) Dynamics of the net charge distribution of an exciton during 1 ps. The exciton is initially generated at chain site  $n = 40$ . Adapted from ref 349. Copyright 2017 American Chemical Society.

However, the exciton splits fractionally, indicating three parts of the charge distribution, which includes the polarized positive charge,  $Q_p$ , polarized negative charge,  $Q_p'$ , and the negative separated charge,  $Q_s$  (Figure 44a); these parts meet the charge conservation condition, that is,  $Q_p = -(Q_p' + Q_s)$ .

At this stage, as the net negative charge of the exciton decreases, the exciton is no longer a neutral particle but bears an excess of positive charge, and the driving force for that exciton toward the positive trap,  $F = [-Q_p'E(n_c^-) + Q_p'E(n_c^+)] - Q_sE(n_c^-)$ , becomes weaker, and it even can change sign if the separated negative charge,  $Q_s$ , is large enough. In this case, the exciton migration will be reversed back in the opposite direction of the polymer chain after  $t = 400$  fs (Figure 44b). This reversed migration pushes the exciton to the region of the weak electric field where it stays in the partially dissociated state. Meng et al. evaluated a fractional charge of 0.16e, which is separated from the exciton in a nonuniform electric field.<sup>349</sup>

**4.4.3. The Role of Dynamic Disorder.** The dynamics of the donor–acceptor configuration in the form of diffusional motion of the molecules, which proceeds on a time scale faster than the lifetime of the donor itself, plays an essential role in efficiency of the energy transfer to the acceptor, as was shown already in early works on FRET. In the case when molecules have a rotational degree of freedom of their dipole moments, the parameter  $q_1$  in eq 16 should be replaced by  $q_2 \approx 3.71R_0^3c_A$ <sup>292</sup> which yields faster quenching of the donors and a higher rate of energy transfer. In the case of diffusional motion of molecules, for example, for dye solutions, eq 16 should be further modified as<sup>292,351</sup>

$$n_D(t) = n_0 \exp\left(-\frac{t}{\tau_0} - 2q_2\sqrt{\frac{t}{\tau_0}} - 2.72\pi R_0^{3/2}(D\tau_0)^{3/4}c_A\frac{t}{\tau_0}\right) \quad (23)$$

where  $D$  is the diffusion coefficient. Comparing eq 16 and eq 23, one can see that translational diffusion of molecules stimulates faster quenching of the donors and a higher rate of energy transfer as well. Saini et al. found that the rate of EET can be underestimated by ~20% compared to the actual rate in case of orientational dynamics of the D–A pair.<sup>352</sup>

Recently, Di Maiolo and Painelli compared theoretically the rate of exciton populations during the first 4.5 ps after the excitation in the organic dye donor (D) and acceptor (A) in liquid and glassy chloroform.<sup>353</sup> It was shown that the FRET rate is similar in the above two systems in the early time up to 0.5 ps, when the exciton in D is formed, but as soon as the liquid solvent diffusion enters into play, FRET becomes much favored in the liquid solvent, so that after 4.5 ps only a residual exciton population in  $D^*$  is observed, because the excitation energy almost completely transferred to the acceptor, whereas in glassy chloroform at the same delay time, the exciton population in  $D^*$  is only depleted due to distribution of dye dipoles, which allow effective energy transfer along special directions, and the overall FRET process dramatically slows down. The authors explained that in either liquid or glassy matrices, energy transfer occurs first along the fastest channels where good alignment of the involved energy levels is achieved, while in the frozen matrix, once the population of these fastest channels is depleted, FRET can only proceed along slower channels. However, in the liquid solvent the fastest channels are retained due to continuous solvent rearrangement, leading to an overall faster population of DA\* (Figure 45).

On the basis of a combined experimental–theoretical investigation, Beljonne et al. predicted that off-diagonal dynamic disorder is beneficial to exciton transport in the incoherent regime, where the hopping rates scale with the thermal average of the squared couplings in regioregular P3HT fibers prepared by living crystallization self-assembly.<sup>354</sup> The calculated singlet exciton diffusion coefficient was shown to be highly sensitive to dynamic disorder and with larger dynamic fluctuations of the excitonic couplings (the nonlocal exciton–phonon interactions) can approach values of ~1 cm<sup>2</sup>/s, whereas it is extremely resilient to static disorder, such as the degree of film paracrystallinity. Sneyd and coauthors proposed that the enhanced diffusivity along P3HT one-dimensional stacks is due to a transient delocalization mechanism, where the excitonic density of states comprises states that spatially extend over a few polymer chains and can be thermally accessible at room temperature from the localized states being at the bottom of the above density of states, so that these extended states can be

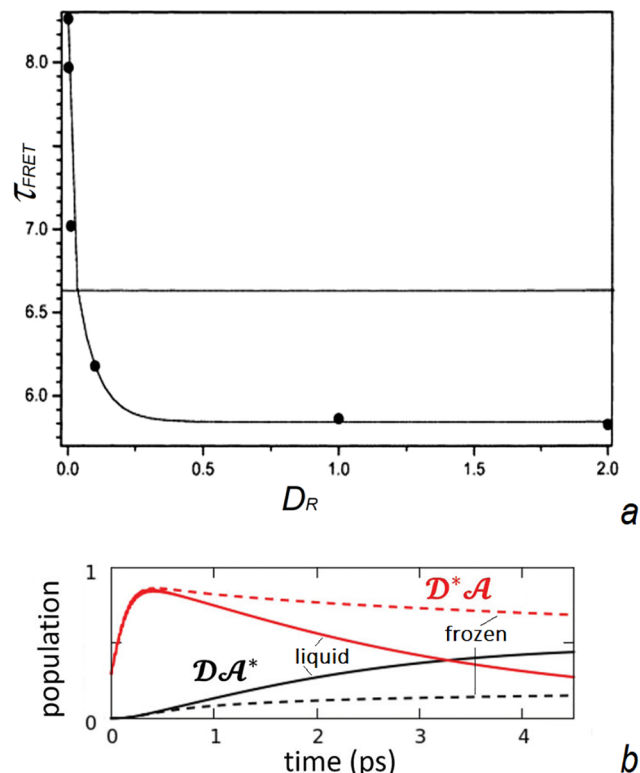


**Figure 45.** (a) Brownian dynamics simulations (filled circles) of the FRET time as a function of rotational diffusion coefficient  $D_R$  for a pair of mobile donor and mobile acceptor molecules. The horizontal line corresponds to  $\tau_{\text{FRET}}$  in the dynamically averaged limit. Reproduced from ref 352. Copyright 2009 American Chemical Society. (b) Time-dependence of population of  $D^*A$  (black) and  $DA^*$  (red) states for liquid (continuous curves) and glassy (dashed curves) chloroform matrix. Reproduced with permission from ref 353. Copyright 2020 Royal Society of Chemistry.

transiently populated during the exciton lifespan, promoting energy transport along the stacking direction.<sup>355</sup> A similar mechanism was proposed by Wittmann et al. for H-type supramolecular aggregates based on a carbonyl-bridged triarylamine trisamide, where increasing the degree of coherence, that is, exciton delocalization, via supramolecular architectures enhances exciton diffusivities up to 1 order of magnitude at room temperature.<sup>356</sup>

Dynamic disorder, which originates from thermal energy and creates a fluctuating landscape for excitons via energy exchange with vibrational modes, was shown to promote the EET process through oscillatory behavior of the exciton population in the site basis for the different types of chromophore systems, such as chlorosomes, bioinspired tubular aggregates, or other light-harvesting complexes.<sup>357</sup>

#### 4.5. Coherent Energy Transfer

**4.5.1. Exciton Transport Driven by Torsional Dynamics in a Polymer Chain.** The coherent excitation energy transfer was observed experimentally in conjugated polymers in the intermediate coupling regime where the delocalization is perturbed by nuclear vibrational modes. In this case, a partially delocalized exciton undergoes quantum-assisted transport within long polymer chains on the ~100 fs time scale before the exciton evolves to a more localized state. Fleming and co-workers reported that a coherence energy transfer can take place at 77 K between closely spaced chromophores in protein light-

harvesting complexes during 440 fs, which was considerably longer than the exciton transfer time of ~250 fs and explained this phenomenon by correlated fluctuations in the protein that surrounds the chromophores.<sup>358</sup> Collini and Scholes revealed coherent intrachain (but not interchain) electronic energy transfer at room temperature in conjugated polymer samples with different chain conformations examined as a model multichromophoric system.<sup>304</sup> The energy fluctuation during exciton propagation causes a reduction in the size of the interchain excited-state wave function, which results in an ultrafast decay of  $N_{coh}$  to smaller values while persisting the coherence along the polymer chain. These results suggested that room temperature quantum transport occurs when chemical donor–acceptor bonds help to correlate dephasing perturbations.<sup>359</sup>

Brédas and Silbey explained the preservation of coherence in the energy transfer process along the polymer chain due to correlations in fluctuations of energies  $E_1$  and  $E_2$  between sites 1 and 2 (Figure 46), which share a common structural framework



**Figure 46.** Schematic presentation of exciton transfer between sites along a poly(*p*-phenylene vinylene) conjugated polymer chain. Coherence upon exciton transfer is preserved here due to the coupling of the excitation to a vibrational rotational mode (shown by the arrows) with a correlation length longer than the spacing between sites 1 and 2. Reprinted from ref 310 with permission from AAAS. Copyright 2009 American Association for the Advancement of Science.

and where the correlations may arise due to a vibrational mode strongly coupled to the excitation, which has a correlation length longer than the donor–acceptor spacing along the conjugated chain.<sup>310</sup> This vibrational mode was referred to as the phenylene ring rotations along the chains, because the  $E_1$  and  $E_2$  energy levels strongly depend on the extent of chain planarity.

Dynamics of exciton delocalization in a polymer chain across its different spectroscopic segments, being in a close spatial proximity, proceeds via Coulomb-induced resonant exciton transfer, which leads to phase coherent transition dipole moments. Exciton transfer along a conjugated chain with torsional disorder that locally breaks the  $\pi$ -conjugation in a PPV oligomer was studied using quantum dynamical methods by Binder et al.<sup>256</sup> The observed Frenkel exciton dynamics revealed two characteristic time scales. The first is a very rapid and coherent transient on a 10–100 fs scale, which influences both BLA determined by Rabi type oscillations and population of each site of the polymer lattice. If the initial excited state is centered to the left of the conjugation break, then it immediately evolves toward a symmetric distribution spanning the complete lattice (Figure 47). Subsequently, the exciton contracts to yield the stationary state that is mirrored by the BLA lattice displacements. Thus, the full electron–hole dynamics showed evolution of the exciton coherence size, which was found to involve a rapid expansion and subsequent contraction during this time scale (Figure 47). The second is a slower time scale within ~500 fs that leads to planarization of the torsional disorder, that is, a “healing” of the torsional defect, and determines the onset of a trapped quasi-stationary exciton– polaron state.

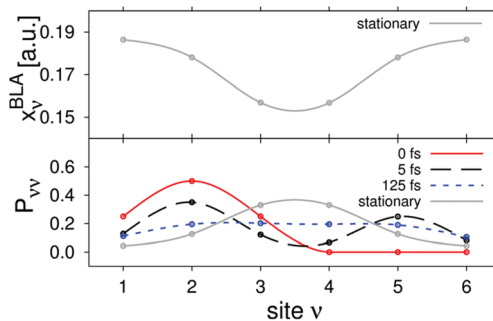


**Figure 47.** BLA displacements (upper panel) characteristic of the trapped stationary exciton state, juxtaposed with site populations  $P_{vv}$  of PPV hexamer at selected times from excitation (lower panel). Reproduced with permission from ref 256. Copyright 2013 Royal Society of Chemistry.

A similar mechanism of coherent exciton transfer dynamics was shown for P3HT at low temperature, assisted by torsional relaxation, which occurs on an ~400 fs time scale and is the driving force for exciton migration, as initial conjugation breaks are removed by dynamical planarization.<sup>94</sup>

In another study, Wells and Blank observed that initial exciton relaxation in P3HT is not primarily a stochastic self-trapping process and that a strong exciton–phonon coupling with torsional motions provides large, coherent spectral migration and subsequent dissipation in the initial 200 fs.<sup>96</sup> The coherent spectral migration or correlation was referred to as retaining of exciton energy during spectral migration. The authors explained the retention of correlation by a model of a dynamically broadened spectroscopic ensemble of chromophoric subunits that experience a strong, selective exciton–phonon coupling and a lack of reasonably well-defined boundaries between them, instead of the coupling between thiophene monomers as a function of the dihedral angle. This is rather different from exciton creation in other conjugated polymers such as MEH-PPV, where the initial excitation into an exciton band created by coupling between multiple chromophoric units follows by a stochastic self-trapping and localization of the exciton, which thus destroys spectral correlation in MEH-PPV in less than 30 fs.<sup>360</sup>

**4.5.2. Quantum Coherent Transport of Excitons in Natural Photosynthetic Systems.** Coherent transfer effects that are expected for intermediate coupling regimes between the donor and the acceptor occur on very short (~100 fs) time scales; therefore, the experimental observation of these effects in real systems is challenging, as the very fast dephasing time destroys coherent superposition states and precludes observation of them, particularly at room temperature. Nevertheless, the search for a quantum mechanism of energy transfer in photosynthetic systems has been progressing well.<sup>358,361,362</sup> Such work was preceded by development of a quantum model proposed by Fleming et al. and Scholes to explain the unusually high efficiency of photosynthetic energy transfer, particularly, in some marine algae, by involvement of quantum oscillations in this process.<sup>363,364</sup> According to the proposed model, the remarkably long-lived wavelike electronic quantum coherence plays an important part in energy transfer processes during photosynthesis, which can explain the extreme efficiency of this process because the system in this way is able to probe all the potential energy pathways and choose the most efficient one with low losses. Although this claim has been argued in several publications later,<sup>365–367</sup> nevertheless, recent efforts were quite

successful to get evidence of quantum character of EET in photosynthetic systems and that this mechanism of EET can surpass the classical trajectories of EET even at physiological temperatures.<sup>368</sup> Most of the recent efforts are summarized in reviews by Fleming and Scholes et al.,<sup>308,369–371</sup> and some examples are given herein.

The numerical results of Ishizaki et al. revealed that quantum wave-like motion in the Fenna–Matthews–Olson photosynthetic pigment–protein complex persists for several hundreds of femtoseconds even at physiological temperature, which makes this complex potentially feasible to work as a rectifier for unidirectional energy flow from the peripheral light-harvesting antenna to the reaction center by taking advantage of quantum coherence in the energy landscape of pigments tuned by the protein scaffold.<sup>372,373</sup> A special role of the surrounding protein in protecting the long-lived quantum coherence mechanism of EET and its non-Markovian interplay with the protein environment has been suggested, which was explained by strong correlation between the protein-induced fluctuations in the transition energy of neighboring chromophores.<sup>318,374</sup>

Ghosh et al. found that in the photosynthetic system of peridinin–chlorophyll (*Chl*) *a* protein (PCP), the S<sub>2</sub> (1<sup>1</sup>B<sub>u</sub><sup>+</sup>) state of peridinin plays the role of the donor for two channels of energy transfer; one channel transfers energy while retaining of quantum coherence during 30 fs and yields delocalized peridinin–Chl states, and the other provides an incoherent 2.5 ps process initiated by dynamic exciton localization, which accompanies the formation of a conformationally distorted intermediate in 45 fs.<sup>375</sup> Interestingly, the coherence is provided by lengthening the lifetime of the S<sub>2</sub> state in PCP due to its intramolecular charge-transfer character, which increases the system–bath coupling and slows the torsional motions that otherwise promote nonradiative decay to the S<sub>1</sub> (2<sup>1</sup>A<sub>g</sub><sup>-</sup>) state.

Hu et al. emphasized the role of dark states in the coherent energy transfer.<sup>376</sup> The dark states prevent exciton recombination and therefore enhance energy conversion efficiency. The dark states are available in multichromophoric systems and in photosynthetic antenna particularly; therefore, increasing the number of chromophores increases the number of dark states and the associated enhanced energy conversion efficiency. However, the negative side of this effect is that excitations also delocalize away from the trapping center and reduce the energy conversion rate. Hu and coauthors considered a competition between the dark state protection and delocalization effects and showed that dark state protection is the dominant mechanism and is dependent on the parity of the number of chromophores in a chain-structured antenna.<sup>376</sup>

The role of vibronic states becomes an important issue in understanding the amazing EET efficiency in photosynthetic complexes, where coupling between electronic excitations and nuclear movements can essentially modulate the EET. On one hand, vibrations in the form of random thermal fluctuations affect energy transferring characteristics through adding incoherence. On the other hand, vibrations intertwined with electronic excitations through coherent superposition can create specific vibronically hot excitonic energy transfer pathways where the superposition energy matches the donor–acceptor energy gap. In this case, a resonant condition for energy transfer takes place and EET occurs by the coherent mechanism, which can significantly speed up the EET rate, for example, by a 4-fold enhancement in the PC645 complex.<sup>377</sup> However, if energetic disorder exceeds the coupling between the donor and

vibrationally excited acceptor states then the incoherent vibronic transport is more efficient than a coherent mechanism.<sup>378</sup>

Direct evidence of the coherent energy transfer is quantum oscillations or quantum beats in the excitonic population of an acceptor (Figure 39b). The long-lived electronic quantum beating was theoretically predicted and observed recently by two-dimensional electronic spectroscopy experiments in different photosynthetic light-harvesting systems.<sup>379–384</sup> Coherent EET in the Fenna–Matthews–Olson complex was shown to be driven via the redox state of its internal cysteine residues, which tune the resonance between its excitons and a pigment vibration to steer excess excitation toward a quenching site.<sup>385</sup>

**4.5.3. Quantum Coherent Transport of Excitons in the Network of Protein Structures (Microtubules).** The search for quantum coherent transport of energy in biological tissues, particularly in neurons and brain, was fueled by the idea that consciousness is an emergent property grounded on a quantum level. Such an idea was developed by Penrose,<sup>386</sup> Beck and Eccles,<sup>387</sup> Reimers et al.,<sup>388</sup> Vaziri and Plenio,<sup>389</sup> Mensky,<sup>390</sup> Lowenstein,<sup>391</sup> Fisher,<sup>392</sup> Jedlicka,<sup>393</sup> and other scientists who speculated that quantum processes can control in some way the operation of our mind. It was established that quantum coherent oscillations play a role in neuronal signaling triggering a cascading pattern of processes required for neuronal activity, such as consciousness and perceptual binding, working memory, and anticipatory attention, as well as perceptual stabilization.<sup>394,395</sup>

Microtubules play an important role in the functioning of the brain.<sup>396</sup> Microtubules contain protein tubulins, which constitute a hollow cylindrical polymer structure. On one hand, these structures are important building blocks in the cytoskeleton of the cell and are essential to maintain the complex architecture and inner network of brain cells. The protein tubulins are responsible not only for maintaining cell morphology but also for trafficking cell cargo and for cell motility and can play a role in signal transduction. Microtubules are also to be more favorable for quantum energy transfer than other parts of the cytoskeleton because they contain 3 times more tryptophan molecules than other parts of the cytoskeleton, and the tryptophan network within an individual tubulin dimer possesses significant dipolar couplings, which are potentially capable of quantum coherent energy transfer similar to those observed in photosynthetic complexes. On the other hand, the microtubules are closely connected to the mitochondria, which are evolutionarily close to bacteria and plant chloroplasts, where the quantum coherence for efficient energy transfer is feasible.<sup>394</sup> Tubulin aggregated into microtubule geometric lattices may thus support such quantum coherent beating effects, which could be important for biological signaling and communication accompanying living processes.

Craddock et al. performed a computational investigation of energy transfer between chromophoric amino acids (tryptophan) in tubulin subunit proteins<sup>397,398</sup> and provided plausible arguments in favor of the quantum mechanism of signal propagation along a microtubule by establishing that coherent energy transfer in tubulin and microtubules is biologically feasible. Particularly, it was determined that coherent beatings last from ~300 to 600 fs depending on the excitation start in the tryptophan cluster and it has a pure dephasing rate of 50 cm<sup>-1</sup>.<sup>394</sup> Craddock and coauthors also predicted that the energy transfer between clusters of tryptophans in tubulin and microtubule structures are possible at physiological temperatures.

#### 4.6. The Preferred Pathways and Control of Exciton Energy Transfer

**4.6.1. Intrachain versus Interchain Energy Transfer in Conjugated Polymers.** Interchain and intrachain exciton transport mechanisms have important influence on the optical properties of conjugated polymers. For example, the photoexcitation of short conjugation segments in polymer chains usually results in radiative recombination of excitons in competition with exciton migration to longer conjugation segments, resulting in fast decay of short-wavelength PL and red shift of time-resolved PL spectra with time, respectively. The red shift of PL spectra with time was observed in different polymers, such as PDPA,<sup>399</sup> PPV and its derivatives,<sup>400</sup> and LPPP.<sup>401</sup>

In the case of PPV and its derivatives, the red shift was explained by the exciton diffusion from the short to long conjugation segments, which yields a fast multiexponential PL decay at short wavelengths and a slow single-exponential decay at longer wavelengths because long conjugation segments are the final destination and are not affected by loss of excitons due to further diffusion.<sup>400</sup> On the other hand, in LPPP, the red shift was explained by the presence of two different emitting species, i.e., singlet exciton states and aggregate states, between which the exciton transfer occurs.<sup>401</sup> An ultrafast red shift of exciton transient absorption in P3HT films during the first 300 fs after the laser excitation was explained by energy transfer from the disordered amorphous to more ordered crystalline regions in the P3HT film.<sup>402</sup> In PDPA, the red shift was interpreted according to the one-dimensional model of exciton diffusion among randomly distributed recombination centers along the chain, where the portion of the spectrum at short wavelengths decays faster than that at longer wavelengths because the excitons in the short segments do not diffuse as far as those in the longer conjugation segments.<sup>399</sup> On the other hand, a blue shift of PL emission in PDPA, which originates from the exciton confinement in intramolecular stack structure and *trans*–*cis* chain isomerization through thermal annealing, was also observed.<sup>403</sup>

Nguyen et al. studied the energy transfer in MEH-PPV chains, which are aligned in silica pores but are randomly coiled outside of the pores.<sup>404</sup> Polarized femtosecond spectroscopy revealed that excitons migrate from aggregated, randomly oriented conjugated polymer segments outside of the pores to isolated and straight segments that are held rigidly in the pores. Energy migration was observed as a red-shift of the emission polarized parallel to the pores relative to the emission polarized along the excitation direction and as initial loss of anisotropy in the first few picoseconds following excitation. The initial loss of anisotropy was assigned to interchain energy transfer between the conjugated polymer segments that are in contact on the outside of the pores. It was found that energy migration along the polymer backbone proceeds more slowly than Förster energy transfer across the polymer chains in the aggregate.<sup>405</sup>

Beljonne et al. reported on the balance between intra- and interchain hopping in a polyindenofluorene polymer with a perylene derivative grafted to its ends.<sup>406</sup> Based on transient absorption experiments in both solution and films and also confirmed by calculations, the authors found that interchain energy transfer is faster than intrachain energy transfer and that the interchain interactions are significant even in unfavorable conformations.

Unfavorable EET along the polymer chain can be understood in view of the fact that EET in conjugated polymers proceeds as hopping of Frenkel excitons localized on extended segments of

the conjugated backbone; however, these conjugated segments can be broken by conformational defects, so that disorder in the chain conformation disrupts the energy transfer. In contrast, the closer proximity of the dipoles on the adjacent packed chains makes the interchain Förster transfer mechanism more favorable compared to the intrachain transfer, where larger average hopping distances in the chains with large conjugation lengths have to be overcome.<sup>407</sup>

In the later works, it was confirmed that exciton transport is significantly enhanced in regioregular phases of H-type aggregates with a break in long-range intramolecular chain order but stacking of oligomers in a face-to-face fashion<sup>133,408–410</sup> and that this process occurs mainly through interchain hops from chromophores on the aggregate surface toward the aggregate core,<sup>411,412</sup> making the core largely responsible for the major emission of the polymer aggregate. Very long diffusion lengths over 200 nm and a large diffusion coefficient,  $D = 5 \times 10^{-1} \text{ cm}^2/\text{s}$ , were reported for organic semiconducting nanofibers comprising a crystalline poly(*di-n*-hexylfluorene) core with  $\pi$ -stacked polymer chains and a solvated segmented corona consisting of poly(ethylene glycol) in the center and polythiophene at the fiber ends.<sup>413</sup> The effective exciton transport was explained by the fact that the exciton generated in the polyfluorene core could not migrate toward the poly(ethylene glycol) layer and therefore the exciton transfer occurred along the core to the lower-energy polythiophene coronas in the end blocks, in the direction of the interchain  $\pi$ – $\pi$  stacking. Barford and Duffy theoretically confirmed that a high degree of interchain coherence in a polyfluorene film can yield an increased mean exciton hopping range and therefore a larger diffusion length.<sup>414</sup>

A similar trend was observed for the energy transfer between donor and acceptor moieties in a donor polyindenofluorene end-capped with an acceptor perylene derivative.<sup>406</sup> Time-resolved experiments have shown different rates of exciton motion through intrachain and interchain channels. Intrachain processes dominated in solution where photoexcitation of the polyindenofluorene units induced relatively slow energy transfer to the perylene end moieties. In films, where close contact between chains is available, the favored mechanism was the interchain transport of the excited singlet species from the conjugated bridge of one chain to the perylene unit of a neighboring one. The Monte Carlo simulations indicated a two-step mechanism for intrachain energy transfer with hopping along the conjugated chains as the rate limiting step being on the order of  $10^{-9} \text{ s}^{-1}$  in long chains essentially due to modest electronic couplings; therefore, the limiting step for the intrachain mechanism is the incoherent transport of the electronic excitations among localized segments along the polyindenofluorene chains. In contrast, direct contact between a conjugated segment of one macromolecule and the perylene moiety attached to a neighbor chain or between two conjugated polymer chains resulted in both large electronic matrix elements and good spectral overlap for intermolecular energy transfer, which was characterized by increase in the transfer rate by 1 order of magnitude with respect to solution.<sup>406</sup> Surprisingly, the interchain electronic coupling showed rather weak dependence on the relative geometric arrangement of the donor–acceptor pair and remained significant even in *a priori* unfavorable situations such as orthogonal orientations.

It is interesting that the higher driving force for the interchain EET compared to intrachain EET stimulates in turn the intrachain exciton transport itself, but it depends on specific

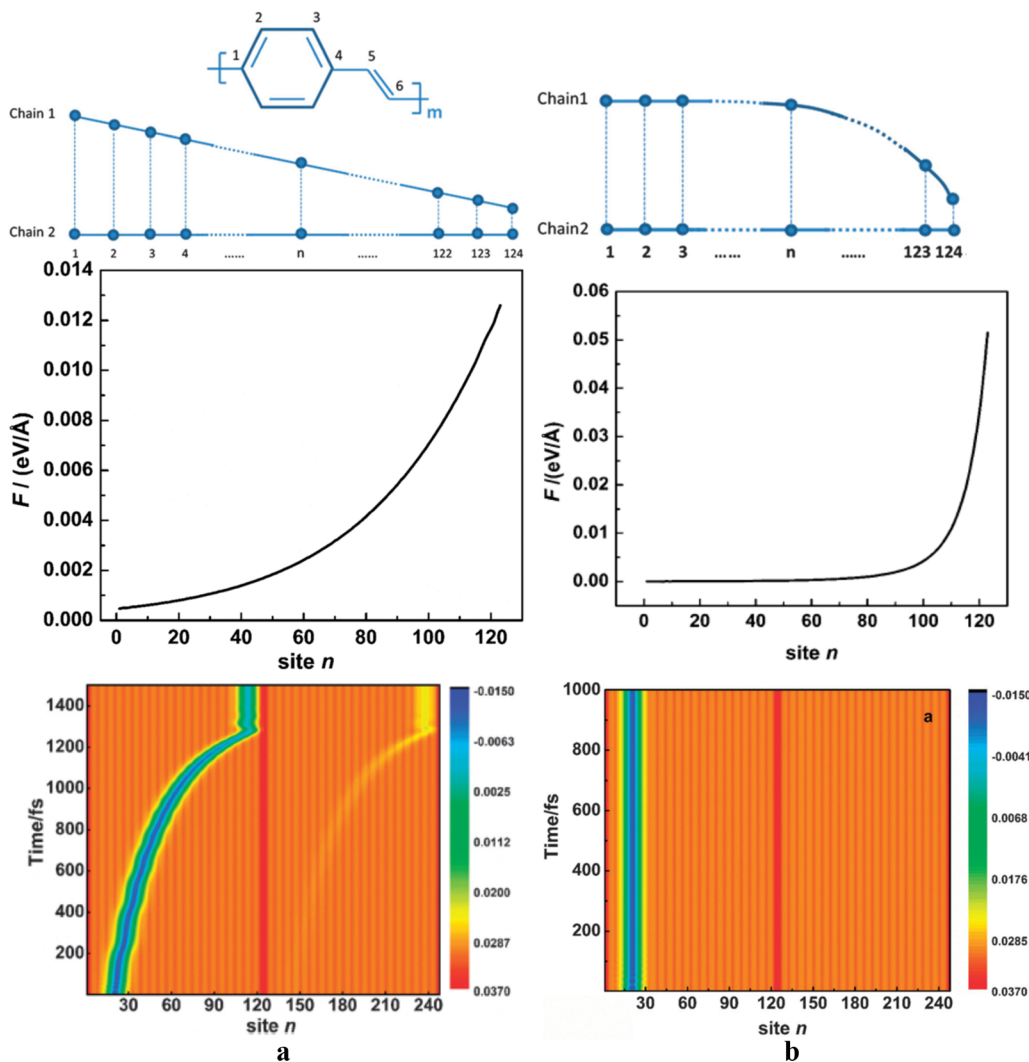


**Figure 48.** (a) Linear and (b) exponential interchain packing configurations of two coupled PPV chains (top), the associated induced driving forces  $F$  along the chain (middle), and exciton intrachain transport dynamics in the coupled polymer chains, which is initially photogenerated near the 20th site (bottom). Reproduced with permission from ref 415. Copyright 2015 Royal Society of Chemistry.

chain packing. Brédas and Silbey explained that exciton intrachain transport can only take place when its creation energy varies along the chain backbone, which may result from ring rotations or variation in the surroundings of the chain segments.<sup>310</sup> Meng et al. considered two different forms of interchain packing configurations, namely, linear and exponential interchain packing configurations (Figure 48), for which the dynamical processes for the exciton intrachain transport were theoretically simulated. Meng and coauthors found that the driving force for intrachain exciton transport is smoother for linear than for exponential interchain packing so the exciton cannot move in the latter case when it is photogenerated far away from the neighboring chain.<sup>415</sup>

**4.6.2. Control of the Exciton Energy Transfer by Conformational Changes.** Conformational changes of the conjugated polymer chain not only influence exciton formation and delocalization effects considered in section 3, but also influence long-range exciton energy transfer, which is well documented.<sup>416–420</sup> First, torsional conformations of a polymer chain lead to torsional defects arising from rotation around the single bonds on the backbone of a conjugated molecule and thus decrease the effective conjugation length of the molecule and

limit its ability to shuttle the charge and electronic energy. Second, polymer intrachain disorder and intermolecular packing results in varying concentration of chain–chain contacts through which the exciton can migrate. As the rates for intra- and interchain energy transfer are different, the overall rate of energy transfer will be controlled by the ratio of intra- and intermolecular EET channels resulting from a certain conformation of the chain.

Vanden Bout et al. revealed fast and slow energy transfer dynamics in single regioregular (*rr*) and regiorandom (*rra*) P3HT chains, respectively, embedded into a PMMA matrix.<sup>421,422</sup> Absorption and emission spectra evidenced that *rr*-P3HT chains were tightly packed in the matrix with ordered conformation, while *rra*-P3HT chains were not due to the high intramolecular conformational disorder. The unfavorable slow EET along the *rra*-P3HT chain can be understood in view of the incoherent exciton hopping in the disordered system, where conjugated segments are broken by conformational defects, whereas EET in the ordered *rr*-P3HT chains can proceed as a fast downhill migration both along the ordered chain and between tightly packed chains. The latter EET resulted in a red shift of the emission maximum and reduced final number of

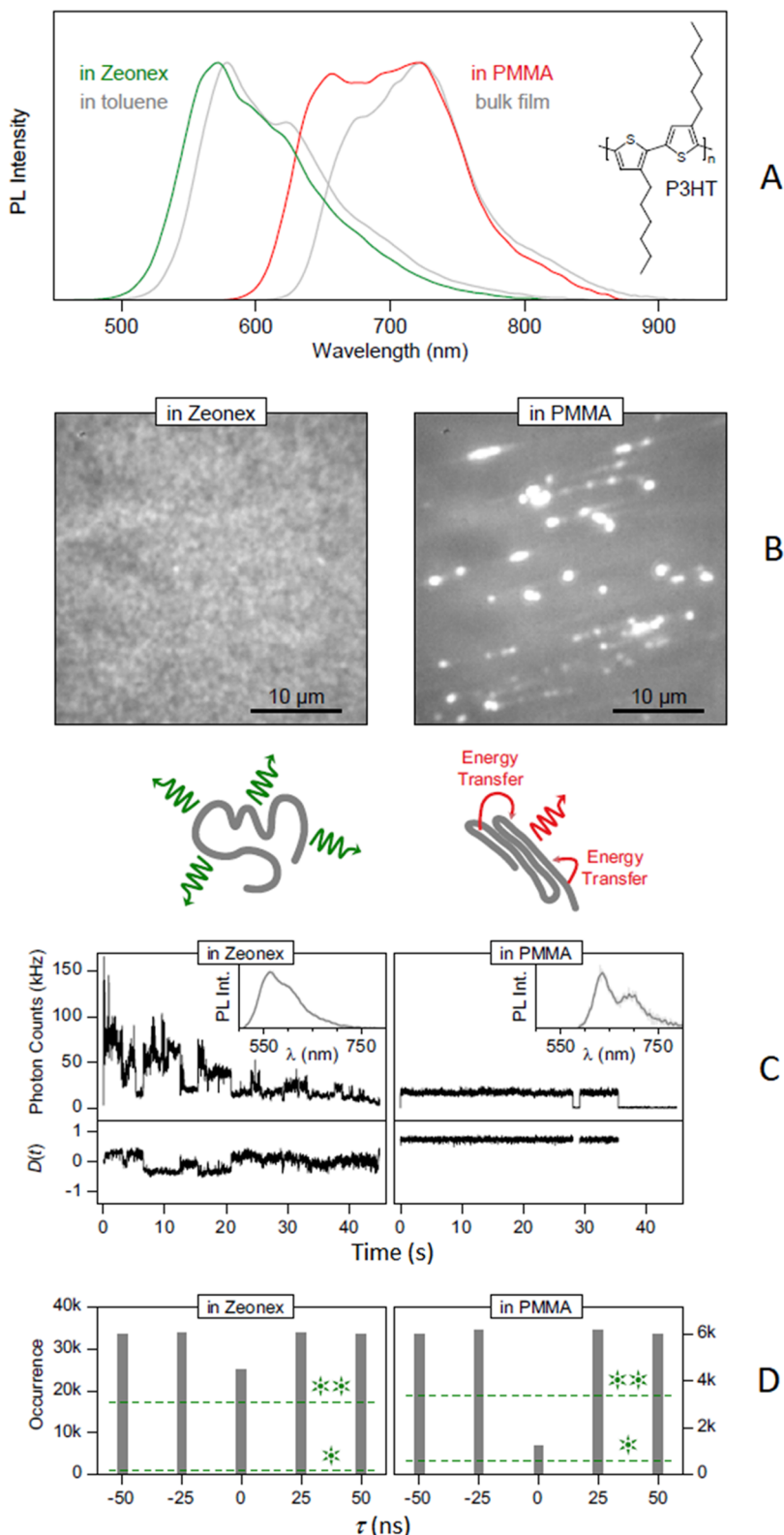


**Figure 49.** (a) PL spectra of P3HT chains dispersed in the inert Zeonex matrix (green) compared to the spectrum of isolated chains in toluene (gray) and those of P3HT chains dispersed in PMMA matrix (red) compared to the spectrum of bulk film emission (gray). In both matrixes, the concentration of P3HT is the same. (b) Fluorescence micrographs of the spin-coated films prepared in the Zeonex and PMMA matrixes. (c) Cartoon of the chromophores emitting independently of each other in isolated chains and emitting from the lowest-energy chromophore in collapsed chains and fluorescence intensity and linear dichroism  $D$ , determined by splitting the emission into two orthogonal polarization components,  $I_x$  and  $I_y$ , and recorded with two separate photodiodes,  $D = \frac{I_x - I_y}{I_x + I_y}$ . (d) Photon statistics in emission, given by the cross-correlation of two photodetectors in the two emission pathways divided with a (nonpolarizing) beam splitter and excited by a pulsed laser with a period of 25 ns, while the photon arrival times  $\tau$  are controlled. In this technique, a single photon emitted by the molecule per laser pulse cannot be simultaneously picked up by both detectors, which

Figure 49. continued

results in the cross-correlation dropping to zero at delay time  $\tau = 0$  between detector signals (photon antibunching effect). Since in Zeonex the cross-correlation signal at  $\tau = 0$  is nearly identical to that at other delays, multiple chromophores on the polymer emit at once and do not couple efficiently. In PMMA, the coincident photon counts at  $\tau = 0$  drop to 20% compared with  $\tau \neq 0$ , which demonstrates predominant single-chromophore emission. Reproduced with permission from ref 423. Copyright 2013 National Academy of Sciences, U.S.A.

emitting sites with a more uniform spectrum. For example, it was found that ~5% of emitting sites for the ordered conformation and ~10% for the disordered conformation can be reached.<sup>421</sup> As a result, the larger number of emitting sites in the *rra*-P3HT yielded a broader distribution of emission energies that have not been transferred to the lowest energy sites. In this way, better energy transfer efficiency can be concluded from the reduced amount of sites that the exciton can reach and from which it ultimately emits.

Similar results were obtained by Thiessen et al.<sup>423</sup> by comparing exciton dynamics of P3HT chains incorporated into Zeonex and PMMA matrixes, where the polymer adopts conformations of single isolated chains and collapsed aggregated chains in the ordered structure, respectively (Figure 49a). Several facts provided evidence in favor of the aggregated chains in PMMA possessing fewer emission centers compared to the isolated chains in Zeonex. First, fluorescence micrographs revealed that the P3HT/Zeonex film has a uniform emission, whereas the P3HT/PMMA film showed discrete bright spots when both images were displayed on the same intensity scale (Figure 49b). Second, the isolated chains in Zeonex emitted independently of each other, showing a multistep blinking and weak polarization of the emission (the linear dichroism was  $D \approx 0$ ), which had slight fluctuations as different chromophores switched on and off, whereas the fluorescence intensity in the collapsed-chain configuration in PMMA was constant, showed almost no blinking, and was strongly polarized ( $D \neq 0$ ) with no fluctuations (Figure 49c). Poor linear dichroism indicates the involvement of multiple independent chromophores in the emission, whereas high static  $D$  can be due to either cooperative dipole orientation along the same axis or only a single chromophore in the polymer being active at once. Third, photon statistics using cross-correlation between two photodiodes detecting the fluorescence divided into two pathways and different delay times showed that photodetector coincidence rates for the Zeonex sample at  $\tau = 0$  were nearly identical with only 20% dip compared to that at other delays, whereas for PMMA a dip in coincidence rate by 80% at  $\tau = 0$  was observed (Figure 49d). Poor cross-correlation indicates that multiple chromophores on the polymer emit at once and do not interact efficiently, whereas a significant drop in the cross-correlation at  $\tau = 0$  implies predominant single-chromophore emission.<sup>423</sup>

From the microscopic point of view, the energy migration along the polymer backbone requires not only unbroken conjugation between adjacent polymer segments but also a favorable orientation of the polymer segments, which can provide a lower degree of inhomogeneity and larger average hopping distances as a result of improved intramolecular electronic coupling. Torsion conformation plays a major role in facilitating or suppressing the energy transfer along the chain. Förster dipole–dipole energy transfer is favorable when the donor and acceptor transition dipoles are collinear. In the case that chain twisting results in orthogonal orientation of the donor and acceptor dipoles, Förster energy transfer ceases. In this way, the torsional conformational changes can play the role of a valve that controls the exciton energy transfer along the chain.

The effect of torsion angle on the rate of intramolecular triplet energy transfer was simulated for the ruthenium(II)/osmium(II) donor/acceptor binuclear complex linked by a biphenyl bridge (Figure 50). Benniston and coauthors showed that the

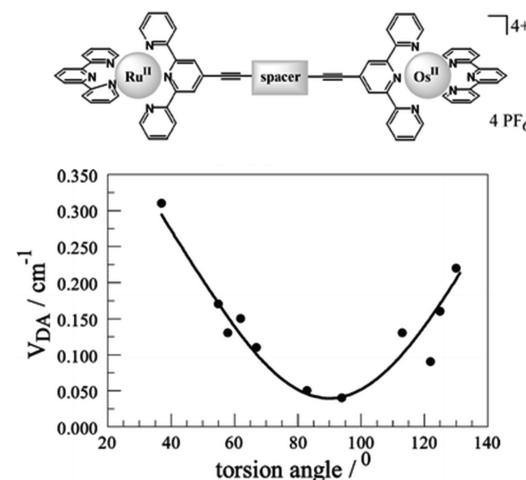


Figure 50. Structural formulas for the binuclear complexes and electronic coupling between the terminal chromophores as a function of the dihedral angle around a bridging biphenyl group. Reproduced with permission from ref 424. Copyright 2005 Royal Society of Chemistry.

magnitude of the donor–acceptor electronic coupling,  $V_{DA}$ , between the terminal chromophores depends on the dihedral angle around the bridging biphenyl group; that is, small torsion angles provide higher coupling, whereas orthogonal orientation of phenylene rings yields a clear minimum in  $V_{DA}$  with 80-fold variation in the rate as the torsion angle between phenylene rings changes from 0° to 90°.<sup>424</sup>

Specifically, this triplet energy transfer occurs by the Dexter mechanism, yielding here nonzero coupling even in orthogonal geometry (Figure 50) by way of nuclear tunneling through the connecting  $\sigma$  bond of the bridge. However, it was shown that energy transfer of the singlet exciton depends on the torsion angle on a polymer chain in a similar way. Particularly, it was shown that electronic coupling in the rigid rod conjugated oligomers and poly(*p*-phenylenebutadiyne) becomes maximal when the torsion angle  $\varphi$  between two subsequent phenylenebutadiyne units is zero and it reaches a minimum for  $\varphi = 90^\circ$ .<sup>425</sup> Although the electronic couplings are reduced with increasing size of the conjugated oligomers as a result of wave function dilution effects and the increased donor-to-acceptor distance within the conjugation chain,<sup>426</sup> there was a 2-fold variation in the coupling as the torsion angle changed from 0° to 90°.<sup>425</sup> However, because longer average conjugation lengths provide better spectral overlap as well as smaller conformational energetic disorder and narrower inhomogeneous energetic distribution, it was predicted that the diffusion of the electronic excitations along the polymer chains becomes more efficient in

polymer chains with longer conjugation lengths, despite, on average, each hopping step taking longer.<sup>425</sup>

These theoretical predictions have been consistent with experimental observation of the conformational dependence of energy migration in a conjugated polymer end-capped with low-energy anthracene trapping sites.<sup>427,428</sup> These studies revealed that the planar order of the polymer backbone imposed by the nematic liquid crystal solvent increased the energy transfer efficiency to the low-energy anthracene termini, which was observed as a significant increase in the fluorescence quantum yield of anthracene emission.

**4.6.3. Energy Transfer via the Dark States in Large Multichromophoric Assemblies.** The discovery of an anomalously high rate of energy transfer from the B800 to the B850 ring in the light-harvesting antenna complex LH2 of photosynthetic purple bacteria<sup>429,430</sup> stimulated interest in EET in large molecular systems consisting of aggregates of tens to hundreds of molecules. It was revealed that the description of EET in large multichromophoric systems of nanoscale size is often inconsistent with the classical Förster model. The EET rate in the above case of photosynthetic purple bacteria is underestimated within the Förster model, and the observed rate is amazingly fast despite of poor overlap of the luminescence spectrum of B800 and the absorption spectrum of B850. The inconsistency between the experimental data and the theoretical description encouraged researchers to reconsider the classical Förster model. Sumi<sup>431</sup> first noted that the point-dipole approximation for transition dipoles of molecules participating in EET is not valid in large aggregates. The dipole–dipole approximation works well when calculating separate pairwise donor–acceptor couplings; however, Förster theory does not work when donor or acceptor molecules act collectively in large molecular aggregates.<sup>324</sup>

In the excited states in large systems of strongly interacting chromophores, excitons are delocalized over many molecules in the form of a coherent superposition of the excited states in an aggregate, which results in collective behavior of all individual transition dipole moments. Due to such spatial delocalization of excitons, whose length may be comparable to or even exceed the separation distance between the donor and acceptor systems, the effective interaction between the extended donor system and the extended acceptor system cannot be equivalent to the interaction between the two point transition dipoles, each of which represents a sum of the dipoles in the donor and acceptor system. Instead, if there are  $m$  molecules that comprise a donor and  $n$  molecules that represent an acceptor, then the EET dynamics must be considered as EET between each pair of the exciton states resulting from interaction of individual transition dipoles in the donor and acceptor aggregates determined by  $(m \times n)$  electronic couplings. Owing to the specific orientation of the dipoles and intermolecular distances within each pair, these  $(m \times n)$  couplings will produce a manifold of ways for energy transfer. Thus, EET in multichromophoric systems can result in some unusual phenomena, such as excitation transfer from or toward dipole forbidden (optically dark) exciton states,<sup>432,433</sup> anomalously high<sup>434</sup> or anomalously low<sup>435</sup> transfer rates, enhancement of the exciton diffusion length by a factor of  $n$  or exciton supertransfer, where  $n$  is a quantity of chromophores in cylindrically symmetric structures or spiral arrays,<sup>436</sup> and non-Förster distance dependence of the EET rate.<sup>437–439</sup>

Specific dependence of EET on the system dimensionality can be traced using the example of interactions of a semiconductor quantum dot (QD) with another QD, a 2D layer, or the 3D bulk,

where the energy transfer rate is proportional to the 6th, 4th, or 3rd power of the inverse donor–acceptor distance, respectively,<sup>440</sup> whereas the EET rate between two layers is distance-independent (Figure 51). A more complex distance dependence

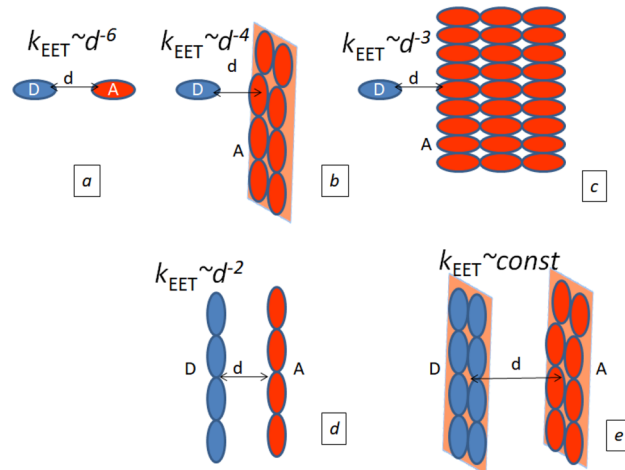


**Figure 51.** Distance dependence of the EET rate in the near-zone in case of interactions of (a) the donor and acceptor point dipoles, (b) the donor point dipole and the acceptor layer, (c) the donor point dipole and the acceptor bulk, (d) the donor and acceptor nanowires (according to ref 439), and (e) the donor and acceptor layers.

exists for two linear nanowires (NWs) of length  $L$  separated by a distance  $d$ . For  $L \gg d$ , Weeraddana et al. calculated that NW–NW interaction is proportional to  $J_0^2(kd) + Y_0^2(kd)$ , where  $J_0$  and  $Y_0$  are Bessel functions of the first and second kind, respectively, and  $k$  is the wavenumber.<sup>441</sup> Chuang et al. found that the electronic coupling scales as  $d^{-1}$  in the near-field limit,<sup>437</sup> while Barford predicted by the line dipole approximation that the EET rate should be proportional<sup>439</sup> to  $(Ld)^{-2}$  (Figure 51d).

Thus, more accurate approaches have been developed in order to properly describe EET in multichromophoric systems. These approaches include the transition density cube method,<sup>442</sup> line dipole approximation,<sup>443</sup> nonperturbative approach,<sup>435</sup> multicentric transition density approach,<sup>444</sup> and generalized Förster theory.<sup>445</sup>

The difference in electronic coupling,  $V$ , of a donor molecule and an acceptor aggregate based on the approach of distributed dipoles and point-dipole approximation is shown in Figure 52. The total dipole moment of the aggregate can be zero if equal amounts of dipoles within the aggregate have antiparallel orientations. In this case, the aggregate possesses a dark optical state. Therefore, coupling of the donor dipole with this dark state of the acceptor does not result in any energy transfer within the point-dipole approximation. However, within the approach of distributed dipoles, the coupling of the donor dipole with each dipole on the acceptor will result in total nonzero coupling, which provides the energy transfer.

The restricted validity of the point-dipole approximation can lead to either overestimated or underestimated rates of energy transfer. For example, in the case of interaction of SWCNTs, the point-dipole approximation strongly overestimates their coupling even at separations of several times of the tube diameter (e.g., at  $R \approx 10$  nm) for the SWCNT–SWCNT pair<sup>445</sup> (Figure 53a). In contrast, in the case of interaction of a single donor molecule and an acceptor H-aggregate, the point-dipole

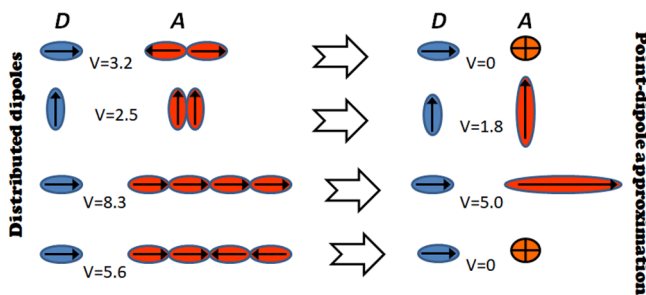


**Figure 52.** Electronic couplings,  $V$ , of a donor molecule and an acceptor aggregate based on the approach of distributed dipoles and point-dipole approximation.<sup>324</sup> The latter approximation considers interaction of the donor dipole and the resulting dipole of the acceptor system, whereas the former takes into account the interaction with each individual acceptor.

approximation usually underestimates the coupling (Figure 53b). Scholes showed that a donor–acceptor separation of more than 100 Å is needed for acceptable point-dipole approximation, when the spectral dependence of the donor–acceptor coupling follows the absorption spectrum of the acceptor, whereas at smaller donor–acceptor separations new spectral features appear in the region of the dark states of the acceptor.<sup>324</sup> Bondarenko et al. compared different methods for calculation of EET between a single donor and a multichromophoric acceptor system and found good match between the methods only for a small amount of acceptor dipoles in the system,  $N_A \leq 3$ , but a great discrepancy in description of the energy transfer rates as the system size increases (Figure 53b).

The role of the dark states in EET was shown in the light-harvesting complex (LH I), where a centralized acceptor is surrounded by a one-dimensional circular array of coupled donors.<sup>446</sup> It was shown that the energy transfer occurs just through the dark states as the EET efficiency is insensitive to the decay of the donors, which proceeds via the optically bright levels.

Communication between H- and J-aggregates through dark states in the same sample is another example demonstrating the unusual properties of condensed films of cyanine dyes. Kobayashi et al. showed that if H-aggregates locate close to J-

aggregates with a mutual distance not larger than their physical size and if the density of states of the H-aggregates at the low energy side overlaps with the DOS of the J-aggregates at the high energy side, then the excited H-band can assist J-aggregates to emit fluorescence at the J-band through exciton energy transfer to their optically forbidden high energy state.<sup>448</sup> The opposite case of energy transfer from the bright level of the J-aggregate to the dark energy level of the H-aggregate was proposed by Dimitriev et al. and provides a certain perspective for energy upconversion mediated by a transient absorption of the dark exciton to a higher bright level of the H-aggregate.<sup>449</sup>

In a similar way, communication between the polar and the multipolar (quadrupolar, octupolar, etc.) chromophores can occur through the dark states of the latter. In this case, the total dipole moment of the multipolar chromophore is zero, and dipole–dipole interaction between the polar and multipolar molecules is not available when the intermolecular distance well exceeds the molecular size. However, at small distances, the interactions of the dipole molecule both with the local dipole of one arm of the multipolar chromophore and with its multipole moment become possible (Figure 54). The relationship between these interactions is dependent on the mutual orientation of the chromophores. Sissa et al. showed that in the case of coplanar orientation of the polar and quadrupolar or octupolar molecules the interaction of the dipole transition of the former and the transition from the ground to the one-photon allowed state of the latter is possible, whereas there is no interaction of the former dipole with quadrupolar or octupolar moment of the latter. In the case of orthogonal orientation of the polar molecule with respect to the plane of the multipolar molecule, the interaction of the dipole transition of the former is only possible with the transition from the ground to the dark (two-photon allowed) state of the latter.<sup>450</sup> Thus, depending on mutual orientation of the chromophores, the exciton energy transfer rate through the dark states can be even larger than that relevant to the allowed states. When the distance between the molecules increases, both channels for EET do not work (Figure 54).

#### 4.6.4. Enhancement of Exciton Energy Transfer by Using Floquet Engineering.

Floquet engineering represents an emerging technique that allows one to greatly enhance the

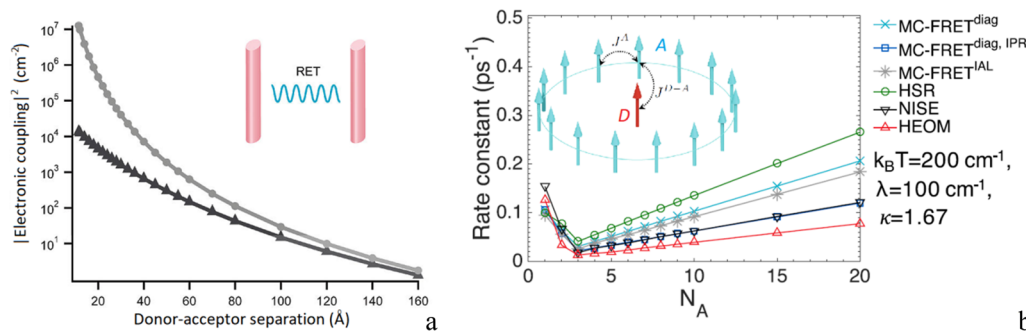


**Figure 53.** (a) Squared electronic couplings predicted by the point-dipole model (circles) and by a multicentric transition density approach (triangles) as a function of the donor–acceptor center-to-center separation for two parallel (7,5) semiconducting single wall carbon nanotubes. Reproduced from ref 445. Copyright 2009 American Chemical Society. (b) Donor–acceptor EET rate constant behavior in the symmetric system indicated in the inset of a monomeric donor (red) and  $N_A$  acceptors constituting the ring (light blue or blue) with transition dipoles oriented perpendicularly to the plane of the ring, calculated for the different indicated models at intermediate regime and room temperature: Multichromophoric Förster resonance energy transfer (MC-FRET) with diagonal approximation (MC-FRET<sup>diag</sup>), inverse participation ratio approximation (MC-FRET<sup>diag, IPR</sup>), ideal absorption line shape approximation (MC-FRET<sup>IAL</sup>), Haken–Strobl–Reineker (HSR) model, numerical integration of the Schrödinger equation (NISE) method, and hierarchy of equations of motion (HEOM) method. Adapted with permission from ref 447. Copyright 2020 Elsevier under the CC BY license (<https://creativecommons.org/licenses/by/4.0/>).

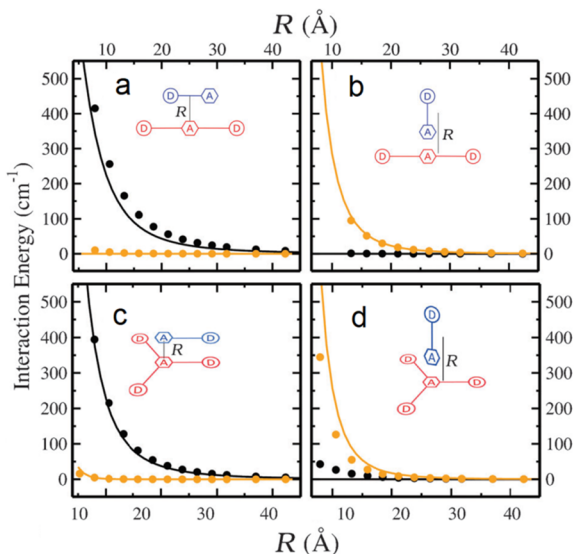


**Figure 54.** Coupling (a, b) between the polar molecule (energy donor, shown in blue) and the quadrupolar molecule (energy acceptor, shown in red) and (c, d) between the polar molecule (energy donor) and the octupolar molecule (energy acceptor) as a function of intermolecular distance for different geometries. Lines and dots represent two different calculated models.  $R$  is the interplanar distance between the two chromophores in panels a and c, and it is the distance between the centers of mass of the two dyes in panels b and d. Black lines and dots refer to the transition from the ground to the one-photon allowed state. Orange lines and dots refer to the transition from the ground to the dark (two-photon allowed) state. Reproduced with permission from ref 450. Copyright 2011 Royal Society of Chemistry.

EET rate between donor and acceptor molecules.<sup>451–453</sup> According to the Förster theory, the EET rate is strongly suppressed when the excitation energy difference between the donor and acceptor molecules is large and the spectral overlap between absorption of the acceptor and emission of the donor is low. Floquet engineering allows one to assist EET in this case. Here, the difference in the excitation energy between the donor and acceptor is periodically modulated by application of an external electromagnetic field with a frequency  $\omega$ .

Specifically, the origin of Floquet modes can be understood from solution of the Schrödinger equation for a one-dimensional quantum system,<sup>454</sup> which is written as

$$\left( H(x, t) - i\hbar \frac{\partial}{\partial t} \right) \psi(x, t) = 0 \quad (24)$$

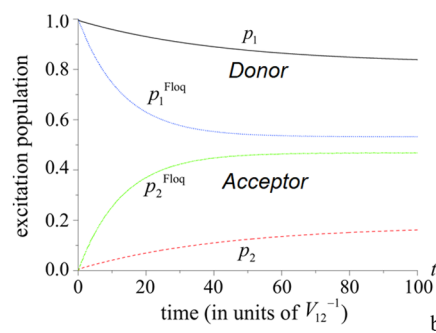
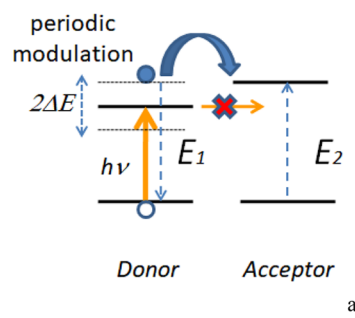


**Figure 55.** (a) Scheme of Floquet engineering through periodic modulation of energy of the donor–acceptor system and (b) comparison of the exciton population of the donor (1) and acceptor (2) as a function of time with periodic modulation ( $p_1^{\text{Floq}}$  and  $p_2^{\text{Floq}}$ ) and without it ( $p_1$  and  $p_2$ ). Panel b is reproduced from ref 455. Copyright 2018 American Chemical Society.

with

$$H(x; t) = H_0(x) + V(x; t); \quad V(x; t) = V(x; t + T) \quad (25)$$

where  $H_0(x)$  is the unperturbed Hamiltonian and  $V(x; t)$  is the perturbation energy, which yields the Floquet modes as follows:

$$\psi_{\alpha'}(x, t) = \psi_{\alpha}(x, t) \exp(i n \omega t) \equiv \psi_{\alpha n}(x, t) \quad (26)$$

with  $n$  being an integer number,  $n = 0, \pm 1, \pm 2, \dots$ , and a quasi-energy,

$$\epsilon_{\alpha'} = \epsilon_{\alpha} + n \hbar \omega \equiv \epsilon_{\alpha n} \quad (27)$$

that is shifted with respect to the energy of an unperturbed system by  $\Delta E = n \hbar \omega$ . Since the energy is transferred to the acceptor resonantly, that is, isoenergetically, the periodically driven system can be tuned to this condition and therefore facilitates enhanced EET via absorption (emission) of  $n$  energy quanta from the driving source for negative (positive) energy difference  $\Delta E$  between the donor and the acceptor (Figure 55).

The rate of EET is dependent on the modulating frequency. The frequency of an applied electromagnetic field can modulate the excitation energy of a permanent dipole moment of a molecule either through the field–dipole interaction or, if the molecule does not possess a dipole moment, through the *ac* Stark effect. Thanh Phuc and Ishizaki demonstrated analytically and numerically that Floquet engineering greatly enhances the EET rate even in the presence of strong dissipations and fluctuations induced by coupling of the donor molecule with the surrounding environment.<sup>455</sup> The driving frequency should be close to an integer multiple of the static excitation energy difference between the two molecules,  $\Omega_2 - \Omega_{10} \approx n \omega$ . Particularly,  $\omega = 18$  THz ( $\sim 600$  cm<sup>-1</sup>) has been found as the resonant frequency, which was shown to depend on the relative magnitudes of the characteristic time scales of the system and the environment, whether the motion induces homogeneous broadening (fast environmental fluctuations) or inhomogeneous broadening (slow environmental fluctuations).<sup>455</sup>

Specific polarization of the modulating electromagnetic field also plays a role. Particularly, it was shown that if a system is modulated with elliptically polarized laser light, a coherent interchromophoric exciton hopping is accompanied by formation of an excitonic Aharonov–Bohm phase due to time-reversal symmetry breaking.<sup>456</sup>

**4.6.5. Mediation of the Exciton Energy Transfer by a Third Particle.** The effects of a third particle, M, which can be an atom, a molecule, a cluster, or a QD crystal, on EET between donor D and acceptor A molecules can be considered in

different configurations, that is, the DMA configuration, where M plays the role of a bridge, or DAM and MDA configurations, where M plays the role of an external perturbing agent.<sup>457,458</sup>

A macroscopic approach to the problem represents the influence of a uniform polarizable environmental medium in the form of its dielectric constant, which influences the rate of resonant transfer of excitation energy between donor and acceptor species. Andrews and Ford showed that the effect of the dielectric constant of the surrounding medium on EET between donor and acceptor molecules embedded into this medium is not trivial. Particularly, a detailed picture of individual photon interaction with vicinal, nonabsorbing chromophores in the neighborhood of other chromophores that have a slightly shorter wavelength of absorption leads to a passive effect exerted on the energy transfer at wavelengths where the photons display no significant absorption.<sup>459</sup>

Salam studied the influence of a third molecule on the rate of EET using diagrammatic perturbation theory within the framework of molecular quantum electrodynamics and particularly considered the distance dependence of the EET rate.<sup>460</sup> It was shown that in the near-zone the indirect rate contribution exhibits inverse sixth power dependence on relative distances of the donor and the acceptor relative to the third body, whereas in the far-zone it exhibits inverse square behavior. The interference term between direct and indirect exchange demonstrated an inverse cubic dependence on all three distance vectors at short-range and inverse behavior in the far-zone. Salam also found that for a collinear arrangement of the three molecules in the near-zone, the interference term is negative and leads to decreasing overall rate of energy transfer.<sup>460</sup>

The most interesting case of stimulating the EET between D and A molecules is the configuration where the transition dipole moments of A and B are orthogonal and at least one is also perpendicular to their mutual displacement vector. In this case, FRET between D and A is forbidden and therefore orientation of the bridge molecule leading to an indirect form of EET is of great importance, as it can be used as a precise switch for controlling energy transfer between nearby chromophores in nanostructures.

Ford and Andrews theoretically studied the effect of a bridge molecule M, which either is located on the line connecting D and A or forms a triangle with these molecules, depending on the polar  $\beta$  and azimuth  $\alpha$  angles of its transition dipole moment with respect to the DA frame.<sup>461</sup> It was found that when all molecules lie on the same line, EET is better facilitated in the case when the polar angle  $\beta = \pi/2$  and the azimuth angle  $\alpha = n\pi/2$ , where  $n = 1, 3, 5$ , or 7 (Figure 56).

Salam theoretically considered mediation of EET between D and A molecules by two proximal particles.<sup>462</sup> In this case, the total transfer probability contained contributions arising from two-body–four-body and three-body–four-body interference terms, which resulted in complicated dependences on the relative orientations of the interacting particles. Particularly, an inverse cube dependence on each of the relative particle separation distances was found.

There are only few experimental works demonstrating the effect of a third particle on EET between donor and acceptor species. Dimitriev et al. investigated the triggering of intramolecular energy transfer in aniline-3-methylthiophene copolymer (PANIMT) by inorganic QDs.<sup>161</sup> It was found that in the system of PANIMT–CdSe QDs, in addition to the energy transfer between the copolymer and the QDs, the CdSe nanoparticles were able to initiate an intramolecular energy

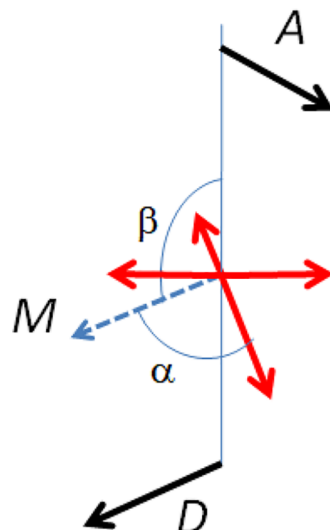


**Figure 56.** Collinear DMA configuration with mutually orthogonal D and A transition dipole moments. The orientation of M is favorable for EET when  $\beta = \pi/2$  and  $\alpha = n\pi/2$  ( $n = 1, 3, 5, 7$ ), shown by red arrows.

transfer in the copolymer itself as an intermediate step. The PL emission of the composite PANIMT–CdSe taken within the time interval of 0–0.7 ns from the laser impulse showed a red shift of the PANIMT emission upon increasing the concentration of CdSe indicating the downhill migration of the exciton to longer conjugated regions of the copolymer, while no notable energy transfer to CdSe nanoparticles was seen within this period of time (Figure 57). The mechanism by which the exterior nanoparticles trigger the intramolecular energy transfer can be due to the local field enhancement near the nanoparticle being in the dielectric medium with a lower refractive index.<sup>463</sup>

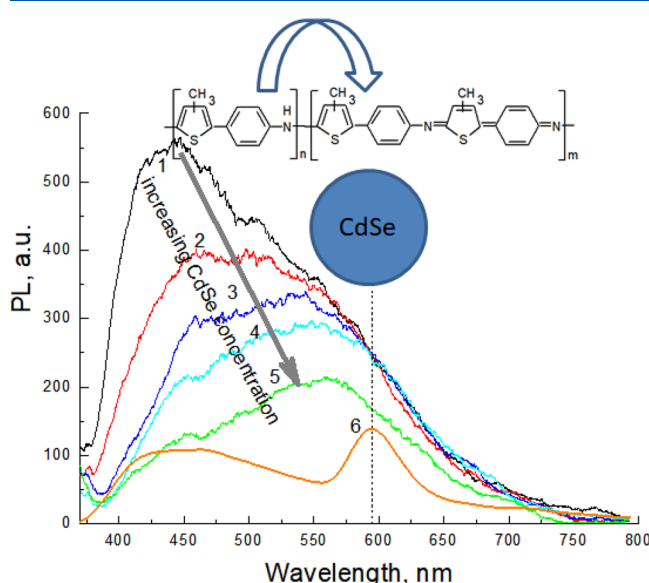


**Figure 57.** Time-resolved PL emission taken at  $t = 700$  ps from the laser impulse of PANIMT–CdSe mixture in acetonitrile solution upon increasing concentration of CdSe nanoparticles (1–5) and steady-state PL emission (6) of mixture 5. The emission band near 600 nm belongs to CdSe QDs. The structure of PANIMT and suggested intramolecular EET are indicated. Adapted from ref 161. Copyright 2008 American Chemical Society.

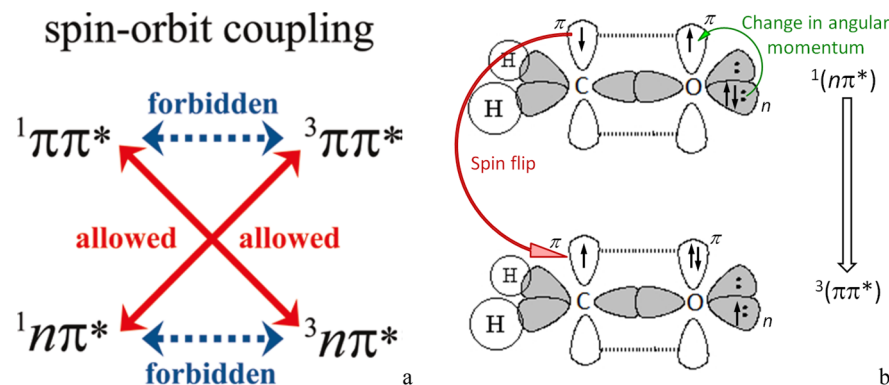


**Figure 58.** (a) Schematic of the El-Sayed rules and (b) presentation of the ISC process in a carbonyl compound. In part b, an excited electron is transferred from the lone pair of the oxygen atom to the  $\pi^*$  orbital leading to the  ${}^1(n\pi^*)$  singlet excited state, which is accompanied by ISC and formation of the  ${}^3(\pi\pi^*)$  triplet excited state (bottom). The changes in angular momentum due to the spin flip and due to transition from the orthogonal doubly occupied n orbital compensate each other. Part a is reproduced from ref 490. Copyright 2011 American Chemical Society.

Recent attempts were directed toward mediating EET with a surface plasmon, which can provide energy transfer between D and A separated by much longer distance than the range allowed by FRET.<sup>464</sup> An et al. reported mediation of EET across the metallic cathode by a strong electrically pumped surface plasmon polariton, with donor and acceptor molecules located at opposite surfaces of the metal film.<sup>465</sup> An and coauthors explained that the donor molecular layer resonantly excites surface plasmon modes on both sides of the optically thick metal film, where the plasmon field evanescently couples to the acceptor molecules near the electrode's exterior surface. The EET was proven via a 6.5-fold increase in intensity of the dye fluorescence in the capping layer on the exterior of the device.

Yang et al. demonstrated a surface plasmon-enhanced energy transfer in an organic light-emitting device structure.<sup>466</sup> In order to localize surface plasmons, Yang and coauthors deposited silver nanoclusters close to the cathode separated by a 1 nm thick LiF spacer and showed that the surface plasmon formed on the silver nanocluster provides a strong donor decay channel and increases the donor–acceptor dipolar interaction resulting in a 3.5-fold enhanced acceptor emission intensity, compared with the emission of the sample that has no Ag nanocluster.

## 5. CONVERSION AND DECAY OF EXCITONS

### 5.1. Conversion Dynamics via Intersystem Crossing

**5.1.1. Rates of Intersystem Crossing.** Intersystem crossing (ISC) is a nonradiative transition between states of different electron spin multiplicity, that is, the singlet and triplet ones, which plays an important role in the excited state decay dynamics of many molecular systems. Since electron transition between states of different spin multiplicity is forbidden, occurrence of such a transition requires certain conditions to compensate the changes in the spin magnetic moment and to sustain the complete angular momentum of the system, which can occur, for example, due to collisions with paramagnetic particles, the influence of heavy atoms, the change of molecular orbital type according to the El-Sayed rules,<sup>467</sup> and the energy gap law.<sup>468</sup> The latter normally requires relatively small energy gap between singlet and triplet energy levels filled with the dense manifold of vibrational levels of a corresponding lower-lying state (i.e., the triplet for a singlet exciton or the singlet ground state for a triplet exciton), which assists in this transition through vibronic coupling.<sup>469</sup> However, ISC is different from internal conversion (IC), which is also governed by a manifold of

vibrational levels but does not change the spin of the relaxed electron. As a consequence, whereas IC proceeds very rapidly at rates on the order of  $10^{11}$ – $10^{14}$  s<sup>-1</sup>, ISC is a slow process and a  $S_1(\pi, \pi^*) \rightarrow T_1(\pi, \pi^*)$  transition in  $\pi$ -conjugated organic molecules typically occurs at rates of  $10^3$ – $10^6$  s<sup>-1</sup>.<sup>470</sup> In addition, the spin-forbidden radiationless process requires much higher density of vibrational states compared to IC, on the order of  $\sim 10^4$  states per cm<sup>-1</sup>, that is, the vibronic energy separation should be  $\ll 0.0001$  cm<sup>-1</sup>. As the density of vibrational states increases with molecular size, therefore, for an energy gap of 10<sup>4</sup> cm<sup>-1</sup> a medium-size molecule with 5 atoms will show IC, while ISC will be observed only in a 10-atom molecule.<sup>471</sup>

The ISC rate can increase significantly to  $k_{\text{ISC}} \approx 10^8$ – $10^{10}$  s<sup>-1</sup> if the transition involves a change of molecular orbital type, for example, transition from a  ${}^1(n\pi^*)$  to a  ${}^3(n\pi^*)$  state or from a  ${}^1(n\pi^*)$  to a  ${}^3(\pi\pi^*)$  state in some heterocycles or carbonyl compounds, such as aromatic ketones, acetone, or benzophenone.<sup>472</sup> These transitions are dictated by the El-Sayed rules, which state that the rate of ISC is relatively large if the radiationless transition involves a change of orbital type and the transitions are forbidden between orbitals of the same type (Figure 58a). A physical meaning of these rules can be given with the example of a carbonyl group (Figure 58b), where the n– $\pi^*$  transition can be considered as a transfer of charge from the lone pair of the orthogonal doubly occupied n orbital of the oxygen atom to the  $\pi^*$  orbital. This  $S_1$  state is the  ${}^1(n\pi^*)$  state, which cannot couple with the  ${}^3(n\pi^*)$ . However, the spin–orbit coupling between the  ${}^1(n\pi^*)$  and  ${}^3\pi\pi^*$  is allowed and driven by the compensation mechanism of the spin flip against the change in angular momentum due to the n– $\pi^*$  transition from the orthogonal orbital as a result of 90° rotation around the O nucleus.<sup>473</sup> Here, the change in spin is accompanied by a corresponding change in angular momentum of the electron arriving from the orthogonal orbital, so that the total angular momentum is conserved.

The rates of triplet formation further increase to  $10^9$ – $10^{11}$  s<sup>-1</sup> when ISC is mediated by charge recombination from an intermediate low-lying charge transfer state,<sup>474,475</sup> facilitated by orthogonal conformation of the donor and acceptor parts of the molecule (see section 5.1.2). In this process, the angular momentum conservation in the aforementioned spin–orbit charge transfer is achieved due to compensation of the large orbital angular momentum change induced by charge recombination by a spin flip.<sup>476</sup> The ISC rate can also be

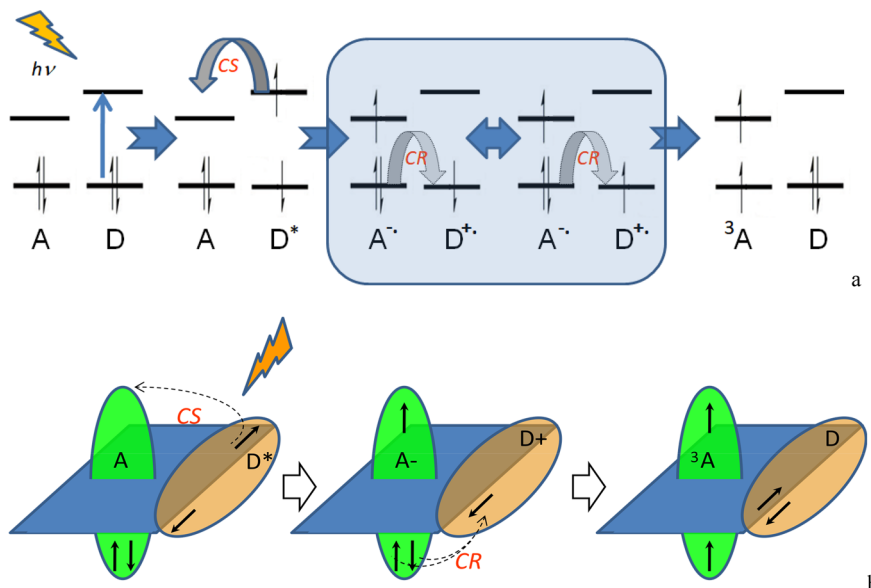


**Figure 59.** (a) Energy scheme and (b) pictorial presentation of ISC by charge recombination in a D–A system with orthogonal conformation. In part a, only HOMO and LUMO levels of A and D moieties are shown. Upon excitation of the D–A pair, charge separation gives rise to the radical anion ( $A^{-\bullet}$ ) and the radical cation ( $D^{+\bullet}$ ). As there is no a second spin in  $D^{+\bullet}$  with which to correlate, the up and down orientations of the only spin in  $D^{+\bullet}$  have equal probabilities (outlined in the box). Charge recombination from  $A^{-\bullet}$  to  $D^{+\bullet}$  can involve either of spins of the ground state of  $A^{-\bullet}$  depending on what the spin orientation in  $D^{+\bullet}$  is; one of these options leads to formation of an acceptor triplet. In part b, spins of D and A are shown in different projections to show that both CS and CR occur with the change in the angular orbital momentum of the transferred electron. Again, CR can involve either of electrons as long as their spins do not correlate with the spin of D. Note that all indicated processes are spin-allowed.

accelerated if assisted by a dark state. Wang et al. showed that ISC in an epigenetic DNA nucleoside proceeds via a dark  ${}^1n\pi^*$  state in acetonitrile solution with time constant of  $\sim 3$  ps.<sup>477</sup>

Finally, ISC can be accelerated in the presence of heavy atoms, such as Ir, Pt, Br, I, or S, to values as high as  $k_{ISC} \approx 3 \times 10^{10} \text{ s}^{-1}$  for poly(3-hexylselenophene),  $k_{ISC} \approx 5 \times 10^{11} \text{ s}^{-1}$  for poly(3-hexyltellurophene),<sup>478</sup> and  $k_{ISC} > 10^{13} \text{ s}^{-1}$  for platinum(II)<sup>479</sup> and transition metal<sup>480</sup> complexes. Here, the ISC rate constant is proportional to the eighth power of the atomic number ( $k_{ISC} \approx Z^8$ ).<sup>481</sup> The variation of the rate and efficiency of ISC in organometallic  $\pi$ -conjugated donor–acceptor systems is dependent on the acceptor strength and the extent of the charge transfer interaction, as was deduced by Cekli et al.<sup>482</sup> Cekli and coauthors discussed that the ISC efficiency is controlled by the energetic separation between the heavy metal (platinum) center and the LUMO of the acceptor unit, with an inverse relationship between excited state energy (acceptor strength) and ISC efficiency. This argument was also extended to unmetalated donor–acceptor–donor chromophores, particularly, to the thiophene-containing  $\pi$ -conjugated D-A-D-type molecules, where S atoms are located on the donor units spatially distant from the acceptor moiety.<sup>482</sup> However, Ang et al. showed an important role for the halogen bond (XB) length in complexes of benzaldehyde···XF (X = Br and I), rather than the atom mass, where the ISC between singlet and triplet excited states becomes increasing rapidly to values of  $k_{ISC} > 10^{10} \text{ s}^{-1}$  with increasing but not with decreasing XB length, with minimal enhancement beginning from XB bond length beyond 3.0 Å.<sup>483</sup>

A rapid ISC dynamics, which competes with IC rates was found in more simple compounds, such as toluene, *p*-xylene,<sup>484,485</sup> and 6-thioguanine, which is a cytotoxic analogue of the canonical DNA/RNA base guanine.<sup>486</sup> Toluene and *p*-xylene showed evidence for ultrafast triplet formation competing with internal conversion ( $k_{isc} \approx 10^{13} \text{ s}^{-1}$ ). A similar ultrafast ISC

rate with time constants of  $\leq 100$  fs to  $< 10$  ps was revealed in nitroarenes.<sup>487,488</sup> These rates are driven by a strong coupling between nuclear motion, electronic structure, and the electron spin magnetic moment. In this way, the ultrafast spin-vibronic mechanism is important for spin–orbit couplings and induction of rapid ISC.<sup>489</sup>

**5.1.2. Intersystem Crossing Facilitated by Nonplanar Conformation.** Production of triplet states in organic molecules free of heavy atoms remains a challenging process. However, recent studies revealed novel options that lead to ISC even in the absence of heavy atoms or paramagnetic species. These options are due to specific molecular conformations, which can be conventionally separated here into ISC mediated by charge recombination in the case of a steady-state orthogonal conformation of the donor and acceptor parts of a molecule and ISC due to dynamic conformation of a molecule, which facilitates mixing of the singlet and triplet states.

ISC in the case of steady-state orthogonal conformation of the donor and acceptor moieties of a molecule has been observed in a series of donor–bridge–acceptor molecules.<sup>476,491–493</sup> Here, the ISC can proceed much faster than the direct  $S_1 \rightarrow T_1$  intersystem crossing between  $(\pi, \pi^*)$  states under favorable conditions, and it is largely controlled by spin-allowed transitions, which include successive charge separation (CS) and charge recombination (CR) allowed processes. The solid explanation of this phenomenon was found relatively recently and assigned either to proton hyperfine interactions (electron–nuclei spin–spin coupling that facilitates spin-flip) or to strong spin–orbit coupling, or both.<sup>473</sup> It should be noted that specific mutually orthogonal orientation of aromatic units in D and A moieties in  $\pi$ -systems is of great importance for fast triplet formation by charge recombination and is mostly provided due to the  $\pi-\sigma$  orbital mixing, which increases spin–orbit interaction leading to spin flipping. Apart from the proton hyperfine interactions, which lead to relatively slow rates ( $\sim 10^8$

$s^{-1}$  or slower) and can alone be responsible for ISC in some coplanar D–A systems,<sup>494</sup> substantially faster rates (up to  $\sim 10^{10} s^{-1}$ ) are attributed to strong spin–orbit coupling effects, which are observed in orthogonal systems.<sup>476</sup> For example, in BODIPY-based D–A dyads, the strength of the spin–orbit coupling of  $^1\text{CS}/\text{T}_1(\pi, \pi^*)$  is 2–3 orders of magnitude greater than that of ordinary  $S_1(\pi, \pi^*)/\text{T}_1(\pi, \pi^*)$ , which makes the spin–orbit, charge-transfer ISC process proceed faster than the ordinary ISC under favorable conditions.<sup>495</sup> Thus, the orthogonal orientation of the neighbor D–A chromophores is essential to induce efficient ISC.

The mechanism of efficient ISC in orthogonally distorted systems can be explained from the general point of view that the momentum of a system must be conserved, that is, a change in electron spin momentum has to be compensated by a change in electron orbital angular momentum.<sup>467</sup> When the molecular orbitals of D–A pairs are perpendicular to each other, their orbital angular momenta have a large enough difference to assist in compensating a spin flip through spin–orbit interaction.<sup>495</sup> Thus, the change in orbital magnetic momentum of the orthogonal orbitals due to charge transfer compensates the change in electron spin magnetic momentum.

However, this phenomenon can be explained also from a viewpoint of quantum mechanics, which states, according to the Pauli principle, that two electrons on the same energy level must have antiparallel spins. According to this principle, the CR process should pick up the electron that has an antiparallel spin with respect to the target spin of the lone electron. Excitation of the D–A system leads to intramolecular CS and formation of the radical pair  $\text{D}^{+\bullet}-\text{A}^{-\bullet}$  (Figure 59). If suitable donor and acceptor orbitals are nearly perpendicular, then the spin–spin correlation is strong between electrons that are both on the donor or between electrons that are both on the acceptor, but it becomes weak between an electron on the donor and an electron on the acceptor. When the back CR takes place, the electron does not “remember” its former spin orientation assigned to the ground state of D, and therefore it jumps to the donor with an accidental spin orientation (depending on the current lone spin on  $\text{D}^{+\bullet}$ ), which can leave behind the triplet state of the acceptor ( ${}^3\text{A}$ ). This scheme is shown pictorially in Figure 59b.

Recently, many D–A dyads that experience the ISC phenomenon have been synthesized.<sup>474,496–499</sup> The majority of such D–A complexes have specific conformation in the form of orthogonal orientation of donor and acceptor groups. The ISC in these complexes is preceded by a CT process with the CS kinetics on the picosecond time scale, followed by CR to the triplet state, which proceeds with time on the order of nanoseconds.<sup>495</sup> The efficiency of ISC can be very high, with quantum yield of up to 65%,<sup>500</sup> and the lifetime of the triplet states can be amazingly long, on the order of several hundreds of microseconds, which can even exceed that accessed with heavy-atom effects.<sup>501</sup>

Liu et al. revealed the effects of conformation and solvent polarity on ISC quantum yield in BODIPY dimers.<sup>502</sup> Whereas a symmetry-breaking charge transfer (SBCT) took place for both orthogonal and nonorthogonal conformations, charge recombination led to triplet states only in the orthogonally linked symmetric BODIPY moieties. In addition, the triplet-state quantum yield was highly dependent on the solvent polarity, with the CR-induced ISC being the primary driving force for solvents with moderate polarity.

It should be noted that in addition to static nonplanar conformational states, ISC can be driven also by dynamic

conformational changes induced by photoexcitation leading to nonplanar distortion of the molecule. Here, spin-vibrational coupling becomes involved, which has a linear dependence of the electronic spin–orbit matrix elements on the nuclear coordinates.<sup>503</sup> Ohmori et al. noted that the low-frequency torsional modes of benzaldehyde and the internal rotation of the methyl group in acetophenone play a dominant role in the intersystem-crossing processes in these isolated molecules.<sup>504</sup> In benzaldehyde, the fast  $S_1 \rightarrow T_2$  intersystem crossing ( $k_{\text{ISC}} \approx 8 \times 10^{10} s^{-1}$ ) is facilitated not only because of a large spin–orbit matrix element (i.e., El-Sayed’s rule) but also because of a casually small energy barrier between energy levels of different multiplicity.<sup>505</sup>

Datko et al. reported that vibrational displacements contribute to ISC events in an alkyl substituted thienylene–vinylene dimer, where efficient triplet formation was initiated by vibrational relaxation dynamics of the dominant out-of-plane torsional mode that induced *trans* to *cis* conformational change of the molecule.<sup>506</sup> ISC was found to occur from the excited state of the dimer in both *trans* and *cis* conformation; however, the ISC rate in the latter case is higher by a factor of 7 and occurs with a time constant of 200 ps versus 1.4 ns for the *trans* conformation, followed by triplet dynamics on time scales of  $\sim 7 \mu\text{s}$  (Figure 60). ISC was facilitated by the torsional rotation of the photoexcited molecular fragments leading to the principal relaxation channel via the  $S_1-T_2$  intersection.

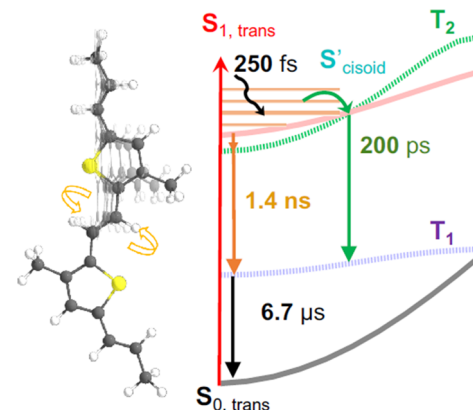


**Figure 60.** Scheme of ISC in the thienylene–vinylene dimer upon molecular torsional rotation. Reproduced from ref 506. Copyright 2019 American Chemical Society.

Nagarajan et al. studied aromatic compounds with different degrees of twisting, where the different moieties of the molecule are not strictly orthogonal, but can twist out of the molecular plane with either single or double twisted conformations (Figure 61). In this case, enhanced out-of-plane C=C and C–H vibrations facilitated efficient ISC from a  $\pi\pi^*$  type singlet to a  $\pi\pi^*$  type triplet with triplet quantum yield values of 10% and 30% in the aromatic derivatives that possess single and double twisted conformations, respectively.<sup>507</sup> In contrast, the flat aromatic analog did not demonstrate ISC. Thus, a clear role of nonplanarity driven by Herzberg–Teller vibronic coupling in facilitating ISC has been established.

The other examples concern molecules that have no torsional degree of freedom and possess flat ground-state geometry, such as benzene and metal-free porphyrins, but that nevertheless demonstrate significant ISC rates. In benzene, the ISC rate takes place on the same time scale as IC.<sup>508</sup> The ultrafast ISC in

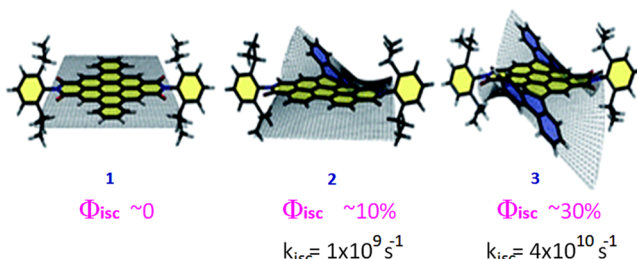


**Figure 61.** Aromatic compounds with (1) planar, (2) single twisted, and (3) double twisted conformations. Reproduced from ref 507. Copyright 2017 Royal Society of Chemistry under a Creative Commons Attribution 3.0 Unported License.

benzene was explained by Minns et al. by the near degeneracy of the  $S_1$  and  $T_2$  states over a wide range of geometries traversed by the wave packet as it moves away from the Franck–Condon region.<sup>484</sup> On the other hand, Penfold and Worth explained this phenomenon by the effect of exciton-induced molecular distortions on spin–orbit coupling where the terms arising from molecular distortions play a significant role in any fast ISC.<sup>509</sup> Upon photoexcitation, the out-of-plane C–H bends, which lead to the hybridization of  $\sigma$  and  $\pi$  orbitals, are responsible for the significant ISC, whereas at equilibrium the spin–orbit coupling is negligible. In a similar way, Stephansen et al. explained this phenomenon by out-of-plane symmetry breaking in benzene as a result of excitation to  $S_2$ , where distortions activated at early times make spin-forbidden ISC become partly allowed.<sup>485</sup> By using natural bond orbital analysis, Stephansen and coauthors showed that the distortion of the aromatic plane in benzene and related molecules upon exciting to  $S_2$  changes the hybridization of the pinnacle carbon atoms between the planar Franck–Condon geometry and the deformed (boat-shaped)  $S_2$  equilibrium geometry (Figure 62).

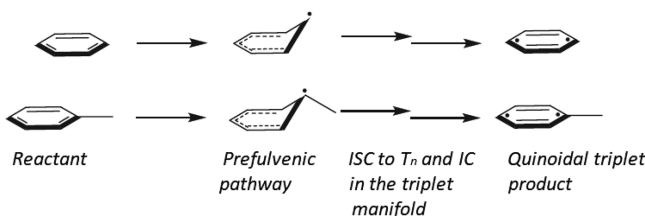


**Figure 62.** Scheme of a partly allowed intersystem crossing process in benzene (top row) and toluene (bottom row) via out-of-plane distortions of the molecular ring upon photoexcitation. Reproduced with permission from ref 485. Copyright 2017 Authors under a Creative Commons Attribution (CC BY) license (<http://creativecommons.org/licenses/by/4.0/>).

This distorted prefulvenic pathway facilitates formation of the quinoidal triplet product. This effect increases in the presence of methyl groups on the pinnacle carbon atoms, where the largest extent of  $\sigma$  and  $\pi$  orbital mixing is observed.<sup>485</sup>

A fine example of how spin-vibrational coupling influences ISC can be found in metal-free porphyrins. Metal-free porphyrin presents planar equilibrium geometry in both the ground and  $S_1$  excited states. Moreover, all low-lying electronic states of the molecule are  $\pi\pi^*$  states, and therefore ISC does not obey El-Sayed's rule. At the planar  $S_1$  equilibrium geometry, the  $S_1$ – $T_1$  energy separation is relatively large ( $\sim 2400 \text{ cm}^{-1}$ ) while their direct spin–orbit coupling is small ( $< 0.05 \text{ cm}^{-1}$ ). Porphyrin derivatives have nevertheless an ISC rate constant as high as  $k_{\text{isc}}$

$\approx 10^7 \text{ s}^{-1}$  making ISC competitive with fluorescence rate in this molecule. The enhancement in ISC was shown to be due to out-of-plane vibrations that leave the energy gap between the  $S_1$  and  $T_1$  states nearly unchanged but increase their spin–orbit coupling substantially by mixing some  $\sigma\pi^*$  character into the electronic wave functions.<sup>510</sup>

**5.1.3. Reverse Intersystem Crossing via Thermal Activation Leading to Delayed Fluorescence.** Proximity of the singlet and triplet energy levels can facilitate not only the transition of a singlet exciton to a triplet one but also a reverse transition due to the thermally activated process, although reverse intersystem crossing (RISC) occurs at rates normally 1–2 orders of magnitude slower than the rates of direct ISC at room temperature.<sup>511,512</sup> This can then result in a subsequent radiative recombination of the singlet exciton, whereas the fluorescence itself is delayed with lifetimes being on the microsecond time scale due to usually long lifetimes of the initial triplet states and slow rates of RISC. Such a phenomenon is known as thermally activated delayed fluorescence (TADF). The experimental rates,  $k_{\text{RISC}}$ , vary substantially by several orders of magnitude, from  $10^2$  to  $10^9 \text{ s}^{-1}$ ,<sup>513,514</sup> whereas the lifetime of TADF has roughly a reverse dependence on the rates of RISC; that is, the slower the RISC rate, the longer the TADF lifetime.<sup>515</sup> For example, for benzil-9,10-dihydroacridine (DC-ACR) and dicyano-pyrazine-3,6-di-*tert*-butylcarbazole (PyCN-TC) compounds  $k_{\text{RISC}}$  of  $1.1 \times 10^6$  and  $1.1 \times 10^3 \text{ s}^{-1}$  have been reported, whereas their  $\tau_{\text{TADF}}$  are 3 and  $210 \mu\text{s}$ , respectively.<sup>515</sup>

The concept of TADF was first proposed by Delorme and Perrin in 1929,<sup>516</sup> but it has become a hot topic since the discovery in 2012 by Adachi et al.<sup>517</sup> that the TADF mechanism can be applicable for creation of efficient organic light-emitting diodes (OLEDs) by escaping phosphorescence, which usually occurs at very low temperatures in conventional organic aromatic compounds.<sup>518</sup> In an OLED, an exciton is formed via injection of electrons and holes into the material by the applied electric field. Due to the uncorrelated spin statistics, 75% of injected charge carriers form triplet excitons and 25% form singlet excitons.<sup>519</sup> Depending on whether ISC and RISC are available, three options for the emission can be realized, fluorescence, phosphorescence, and TADF, leading to the different generations of OLEDs (Figure 63).

In order to realize RISC for efficient TADF, the energy splitting between the  $S_1$  and  $T_1$ , that is,  $\Delta E_{\text{ST}}$ , should be much smaller than 100 meV.<sup>517</sup> The relative population of the above two states that leads to TADF can be estimated from the Boltzmann distribution,

$$K = \frac{[S_1]}{[T_1]} = \frac{k_{\text{RISC}}}{k_{\text{ISC}}} = \frac{1}{3} \exp\left(-\frac{\Delta E_{\text{ST}}}{k_B T}\right) \quad (28)$$

where  $k_B T \approx 26 \text{ meV}$  for room temperature. For  $\Delta E_{\text{ST}} = 100 \text{ meV}$ , eq 28 yields the relative population ratio of about 0.7%; however, the population of  $S_1$  increases exponentially as the energy gap  $\Delta E_{\text{ST}}$  decreases. A small singlet–triplet energy splitting is relatively easy to achieve in molecules with orthogonally linked electron donor (D) and acceptor (A) moieties; therefore, most TADF systems are broadly based upon orthogonally coupled D–A and D–A–D units.<sup>520</sup> In such donor–acceptor systems, both ISC and RISC have a charge-transfer character; therefore,  $S_1$  and  $T_1$  are associated with  ${}^1\text{CT}$  and local excitonic triplet  ${}^3\text{LE}$  states.<sup>521</sup>

The second parameter influencing the TADF efficiency is the temperature (see eq 28). At room temperature, the RISC rate is

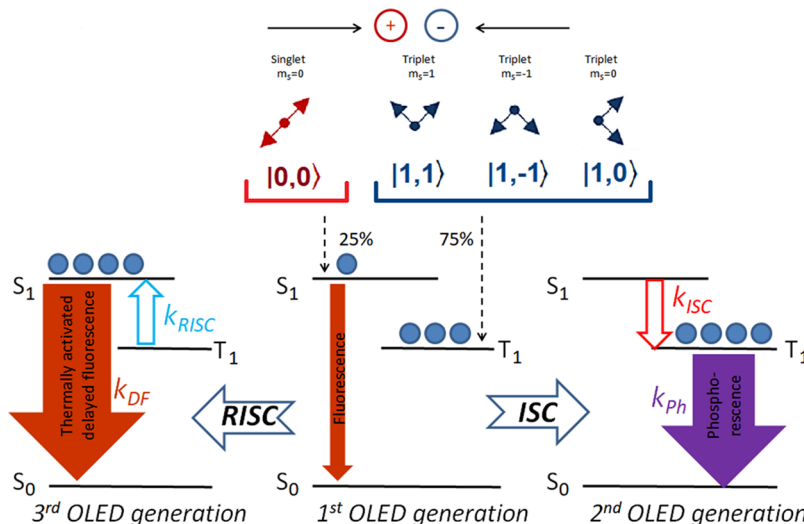


**Figure 63.** Scheme of the singlet and triplet exciton yield due to electron and hole injection into organic material and their conversion leading to TADF. Singlet and triplet excitons are generated in a 1:3 ratio depending on the spin degeneracy. DF, Ph, ISC, and RISC are abbreviations for delayed fluorescence, phosphorescence, intersystem crossing, and reverse intersystem crossing, respectively. Spin states are labeled by  $|s, m_s\rangle$ , which represents the total spin angular momentum ( $s$ ) and projection along the  $z$  axis ( $m_s$ ).

about 1 order of magnitude lower than the ISC rate, being in the range of  $k_{\text{RISC}} \approx 10^2\text{--}10^7 \text{ s}^{-1}$ .<sup>515,522</sup> However, with decreasing temperature, the RISC rate drops significantly. For example, at 30 K,  $k_{\text{RISC}}$  can decrease with respect to  $k_{\text{ISC}}$  by 8 orders of magnitude.<sup>523</sup>

Still, however, efficient TADF was observed in materials with singlet–triplet energy splitting well above 100 meV, that is, with  $\Delta E_{\text{ST}}$  up to 530 meV.<sup>524,525</sup> This implies that RISC in TADF can be facilitated by other mechanisms than the energy gap law. Moreover, when RISC takes place between electronic states with the same orbital type, that is, between those for which the transition is forbidden according to the El-Sayed rule, it is necessary to go beyond the Condon approximation.<sup>503</sup>

The additional factors that contribute to enhancement of RISC rates are related to the substantial CT contribution to T<sub>1</sub>, the different natures of the S<sub>1</sub> and T<sub>1</sub> states (which is consistent with the El-Sayed rule for ISC rates), and spin-vibronic coupling. Penfold and coauthors<sup>526</sup> demonstrated that spin–vibronic coupling, operative for efficient TADF, can overcome the limitation caused by undesirably large singlet–triplet energy splitting. Spin-vibronic coupling is a second-order mechanism that is analogous to the superexchange mechanism identified in a wide variety of artificial light harvesting systems,<sup>527</sup> which besides the initial local excitonic triplet <sup>3</sup>LE (T<sub>1</sub>) and final charge-transfer singlet <sup>1</sup>CT (S<sub>1</sub>) involves also an intermediate <sup>3</sup>CT (T<sub>2</sub>) state (Figure 64), which is crucial for providing an enhanced rate of RISC. Nonadiabatic coupling between the lowest two triplet states gives rise to a strong enhancement of the RISC rate via a second order mechanism and promotes population transfer between the T<sub>1</sub> and T<sub>2</sub> states. For example, spin–orbit coupling in Spiro-CN compound increases by a factor of 60, and the RISC rate increases by 3 orders of magnitude if mediated by the T<sub>2</sub> state compared to the direct transition from T<sub>1</sub> to S<sub>1</sub>.<sup>522</sup> Consequently, the RISC mechanism here is actually operative through the energy gap, which is smaller than that between the T<sub>1</sub> and S<sub>1</sub> states.<sup>464</sup> In addition, in accordance with El-Sayed's rule,<sup>467</sup> a large change in the orbital angular momentum between S<sub>1</sub> and T<sub>2</sub> consisting of different

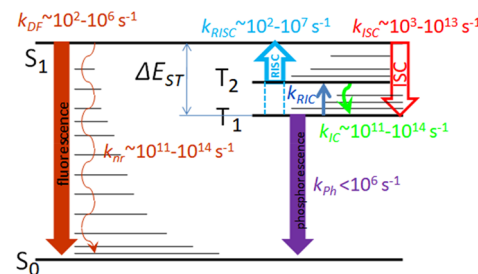


**Figure 64.** Exciton dynamic processes for a typical TADF emitter. Abbreviations DF, Ph, ISC, IC, RISC, and nr are for delayed fluorescence, phosphorescence, intersystem crossing, internal conversion, reverse internal conversion, reverse intersystem crossing, and nonradiative decay, respectively. Typical rates of the processes are indicated. RISC rate can depend on whether it proceeds immediately from T<sub>1</sub> or is mediated by T<sub>2</sub>.

electronic configurations induces an effective spin–orbit coupling and thus enables spin flipping.<sup>513</sup>

Isomerization can be another unusual factor that assists TADF. Huang et al. reported on delayed fluorescence generated from the S<sub>1</sub> state of *trans*-Cy5 through a reverse intersystem crossing from the *cis*-triplet state T<sub>1</sub> to the *trans*-singlet state S<sub>1</sub> via thermal activation.<sup>528</sup> In this process, the back-isomerization from *cis*-triplet state to *trans*-singlet state facilitated reduction in the singlet–triplet energy splitting, thus leading to the RISC.

## 5.2. Upconversion Dynamics of Excitons

Upconversion and the related anti-Stokes photoluminescence (ASPL) phenomenon are the processes of conversion of low-energy photons to photons of higher energy. These processes require additional energy input coming from either additional photon(s) or thermal (phonon) energy absorption. Usually these processes include a sequential absorption of two or more photons or accompanying absorption of phonons, which results in an exciton of a higher energy whose radiative recombination yields a shorter emission wavelength than the excitation wavelength. Very often, the processes of simultaneous absorption of two or more photons in nonlinear media, which results in lifting an electron to higher energy levels, are also

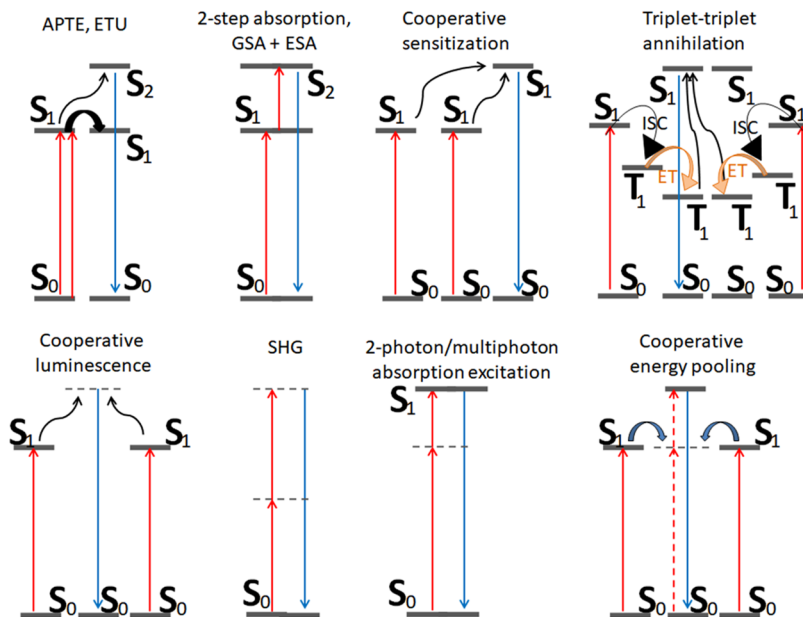


**Figure 65.** Schematic of two-photon upconversion processes.<sup>534,535</sup> Real electronic levels are shown by solid bars, while virtual levels are indicated by the dashed lines. Abbreviations: ISC, intersystem crossing; ET, energy transfer.

considered as photon upconversion. Below we consider both multiphoton and single photon processes leading to conversion of the absorbed light to photons of higher energy.

Photon upconversion can be applied as an additional tool for improving photovoltaic (PV) conversion efficiencies in solar cells. The use of energy upconversion in nonconcentrated single-junction PV cells brings additional gain in the detailed balance limit and results in an increase of the theoretical power conversion limit from 31% to 49%, albeit the maximal realistic efficiencies should be expected <40%, that is, ~1.25 times the theoretical efficiency of conventional single-band gap PV cells.<sup>529,530</sup>

**5.2.1. Multiphoton Upconversion.** Multiphoton upconversion processes are based on either sequential or simultaneous absorption of two or more photons; it should be noted, however, that the probability of a multiphoton absorption decreases with increasing photon quantity involved in the process. Multiphoton absorption can be conventionally separated into the two groups: in the first group, the excitation to the higher energy level proceeds sequentially through temporally separated absorption acts with the electron climbing up via real electronic levels. In the second group, multiphoton absorption proceeds practically simultaneously, it involves virtual electronic levels, and its rate is much faster than in the first group. Therefore, the first group normally requires long-lived intermediate electronic states where an electron is able to await a subsequent photon that promotes electron transfer to the neighboring donor (sensitizer) level of energy instead of relaxing back to the ground state. In general, upconversion due to sequential absorption of photons includes a variety of processes such as APTE (addition de photon par transfert d'énergie) or ETU (energy transfer upconversion), ground state absorption (GSA) followed by excited state absorption (ESA), and cooperative sensitization that can be provided either due to singlet–singlet or triplet–triplet annihilation (TTA) (Figure 65, top row). Usually, these processes (except for ESA) involve at least two players, one of which serves as a donor (sensitizer) of energy and the other as an emitter (annihilator), as well as a relatively long lifetime of the

electron at the intermediate level being necessary. In well-known rare-earth ion systems, characteristic lifetimes of excited electrons in the 4f inner shell are micro- to milliseconds.<sup>531,532</sup> In the TTA process, triplet excitons, which have lifetimes in the range of microseconds, are involved; therefore, TTA is a very efficient process compared to another cooperative sensitization process which proceeds via singlet–singlet annihilation (Figure 65).

The second group of multiphoton processes includes second-harmonic generation (SHG), two-photon absorption (2PA), cooperative energy pooling (CEP), and cooperative luminescence; these processes use intermediate or upper virtual levels (Figure 65, bottom row). As the lifetime of the electron on the virtual level is too small (within a femtosecond time scale), high light intensity or photon concentration is needed to facilitate absorption of an additional photon by the excited electron–hole pair to move the excitation to the higher energy level. For example, SHG takes place when excitation intensities reach up to  $10^{13}$  W/m<sup>2</sup>, which corresponds to about  $10^{10}$  times the integrated intensity of solar radiation at the earth's surface.<sup>533</sup>

In organic materials, few options for the multiphoton upconversion can be realized that have been documented experimentally; these are due to 2PA,<sup>536,537</sup> SHG,<sup>538</sup> CEP,<sup>539,540</sup> or TTA<sup>541–543</sup> mechanisms. As these multiphoton processes often need unique conditions, particularly, high pump intensity in the case of SHG and 2PA<sup>544</sup> or matching of energies of sensitizer and annihilator in the case of TTA,<sup>545</sup> these have restrictions for certain applications. For example, SHG and 2PA can be ruled out as viable mechanisms for application in solar cells as they require extremely high light intensities, on the order of  $10^{10}$  times the usual solar intensity on a sunny day. The TTA mechanism is based on energy transfer and requires two players in the system, a donor (sensitizer) and an acceptor (emitter), as has been mentioned previously. On one hand, TTA does not require high excitation power density (solar light is sufficient), possesses relatively high upconversion quantum yield, and allows one to readily tune excitation/emission wavelengths and strong absorption of the excitation light. On the other hand, the

TTA mechanism normally requires the presence of heavy atoms in organic chromophores, such as rare-earth metals, in order to provide a strong spin-orbit coupling and ISC from excited singlet to triplet states. Efficient ISC in heavy-metal-free organic chromophores was also observed but in only a few compounds.<sup>546</sup> The other drawback of the TTA mechanism of upconversion is its sensitivity with respect to molecular oxygen, which easily quenches the photon upconversion process and therefore necessitates development of protective coatings with high barrier properties.<sup>547</sup> Most TTA processes also have restricted spectral range with visible to visible upconversion. A decade ago, it was reported that the longest excitation wavelength for the TTA system based on the pair of PdTAP-rubrene is close to 780 nm;<sup>548</sup> this means that application of such systems are limited to solar cell materials with relatively wide band gaps only. However, recent years yielded significant progress and dozens of developed organic TTA systems now demonstrate upconversion from the NIR to the visible region.<sup>541</sup> For example, the system based on Yb-L/rubrene (Figure 66) can

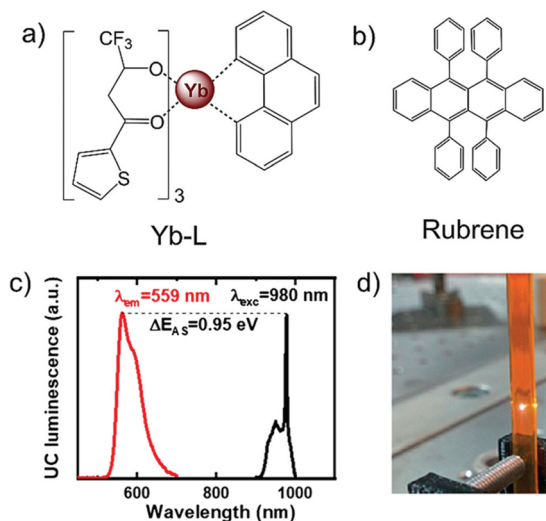


**Figure 66.** Molecular structures of (a) Yb-L (sensitizer) and (b) rubrene (annihilator), (c) upconversion emission spectrum of rubrene (red curve) excited with a 980 nm laser and excitation spectrum of TTA-upconversion with laser intensity maintained at 100 W/cm<sup>2</sup> (black curve), and (d) unfiltered photograph of upconversion emission ( $\lambda_{\text{exc}} = 980$  nm, 300 W/cm<sup>2</sup>). Reproduced from ref 549. Copyright 2020 American Chemical Society.

harvest NIR energy as low as 1.265 eV (980 nm) through TTA photon upconversion.<sup>549</sup> The system based on the combination of Pt(II) meso-tetraphenyltetrazenoporphine (PtTPBP) heavy atom triplet sensitizer and 9,10-bis[((triisopropyl)silyl)-ethynyl]anthracene (TIPS-Ac) annihilator can directly generate triplets upon NIR photon excitation at 785 nm and yield an anti-Stokes shift of 1.03 eV.<sup>550</sup>

Still, upconversion emission quantum yield,  $\Phi_{\text{UC}}$ , in most such systems is low, that is, several percent at best, and depends on the excitation intensity as well. Whereas the best inorganic solid system of  $\beta\text{-NaYF}_4\text{:Er}^{3+}$  demonstrates ETU multiphoton upconversion with quantum yield of 16.2% at excitation densities of  $\sim 10^2$  W/cm<sup>2</sup>,<sup>551</sup> the organic system based on the PdPc/rubrene pair demonstrates TTA upconversion from 730 to 560 nm with  $\Phi_{\text{UC}} = 5.6\%$  at similar excitation densities.<sup>552</sup> However, progress in this direction for some systems was achieved also. Huang et al. reported red-to-green light

upconversion in the PdTNP/PyS pair with  $\Phi_{\text{UC}} = 16.7\%$  (when excited at 653 nm) and  $\Phi_{\text{UC}} = 14.1\%$  (when excited at 720 nm) with a low-power density of excitation of 0.1 W/cm<sup>2</sup>.<sup>553</sup> Fan et al. observed red-to-blue (635 to 409 nm) TTA upconversion in Pt(II)-Schiff base complex/diphenylanthracene pair with  $\Phi_{\text{UC}}$  as high as 21% (assuming the theoretical maximum efficiency of 50%).<sup>554</sup> Recently, the highest recorded red-to-blue (635 to 446 nm) TTA upconversion quantum yield,  $\Phi_{\text{UC}} = 27\%$ , was demonstrated for the organic PtTPBP/TIPS-Ac pair, with a low-power excitation density of 6 mW/cm<sup>2</sup> and TTA efficiency of 77%, with a relatively small driving energy for the TTA of less than 0.32 eV.<sup>550</sup>

Dynamics of TTA is governed by intersystem crossing of the singlet exciton into the triplet one in the sensitizer followed by triplet-triplet energy transfer and triplet exciton fusion into the singlet one in the emitter. The time profiles of phosphorescence of the sensitizer,  $I_{\text{ph}}(t)$ , and upconversion emission,  $I_{\text{UC}}(t)$ , can be described by the following equations:

$$I_{\text{ph}}(t) \approx [{}^3\text{S}^*] \approx \exp(-t/\tau_{3\text{S}}) \quad (29\text{a})$$

$$I_{\text{UC}}(t) \approx [{}^1\text{E}^*] \approx [{}^3\text{E}^*]^2 \approx (1 - \exp(-t/\tau_{3\text{S}}))^2 \exp(-2t/\tau_{3\text{E}}) \quad (29\text{b})$$

where  $[{}^3\text{S}^*]$  denotes the molar concentration of triplet sensitizer,  $[{}^1\text{E}^*]$  and  $[{}^3\text{E}^*]$  denote the concentrations of the singlet and triplet emitters, respectively, and  $\tau_{3\text{S}}$  and  $\tau_{3\text{E}}$  are the time constants of the triplet sensitizer and triplet emitter, respectively.<sup>555</sup> According to eqs 29, the upconversion emission is characterized by bimolecular dynamics and the rise of emission intensity with a characteristic time constant in the microsecond range, which is mostly determined by the diffusion of triplet excitons before their fusion (Figure 67).

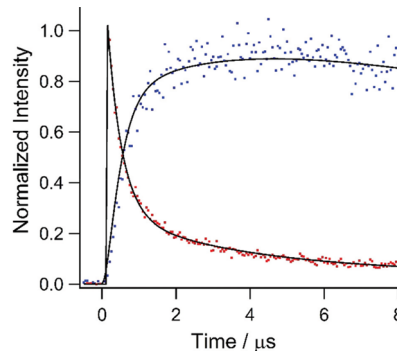


**Figure 67.** Time profiles of upconversion emission of 9,10-diphenylanthracene (DPA) emitter in toluene solution (blue dots) and phosphorescence of Pt(II) coproporphyrin I (PtCP) sensitizer fixed to glass that was immersed in DPA/toluene solution (red dots) with the corresponding fitting curves (black line). The sample was deaerated by Ar bubbling. Reproduced with permission from ref 555. Copyright 2020 Royal Society of Chemistry.

Much faster rate of TTA annihilation can be obtained by using semiconductor quantum dots as a sensitizer. For example, effective extraction of triplet excitons from PbS QDs by 5,11-bis(triethylsilylethynyl)anthradithiophene (TES-ADT) annihilator with a rate constant of  $k \approx 2 \times 10^8$  s<sup>-1</sup> was assigned to the association of the thiophene group of TES-ADT with PbS QDs, which assisted in avoiding transmitter losses.<sup>556</sup> Other examples demonstrate triplet energy transfer from PbS QDs to 5-carboxylic acid tetracene with  $k = 5.91 \times 10^9$  s<sup>-1</sup>, CdSe

QDs to bis(pyridine) anthracenes with  $k = (0.96–1.28) \times 10^9 \text{ s}^{-1}$ <sup>558</sup> and CdS QDs to 2,5-diphenyloxazole with  $k = 1.5 \times 10^{10} \text{ s}^{-1}$ <sup>559</sup>.

CEP is another energy transfer mechanism that provides an alternative route toward efficient and applicable photon upconversion.<sup>539,540</sup> CEP is the process where two photoexcited sensitizing chromophores nonradiatively transfer their energy to a single higher-energy state in an acceptor chromophore (Figure 65). CEP is different from the Förster resonance energy transfer process, because it employs coupling of the emissive states of both sensitizers with the 2PA tensor of the acceptor; thus, CEP occurs through the virtual state of the acceptor.<sup>560</sup> In this way, both sensitizers act as photon storage centers that facilitate 2PA in the acceptor and thus enable upconversion with greater efficiency and at reduced excitation intensities.

**5.2.2. Single-Photon Upconversion.** The single-photon upconversion phenomenon employs only one photon for excitation; however, additional energy is still needed to add to the excited system so that it can emit afterward a photon of higher energy than the exciting one. Such additional energy is normally taken from the thermal bath in which the system is located, that is, due to excitation of phonons or vibrational modes at environmental temperature.<sup>561</sup> In one case, excitation of phonons is followed by absorption of a photon from the hot ground state (Figure 68a); this leads to hot-band absorption

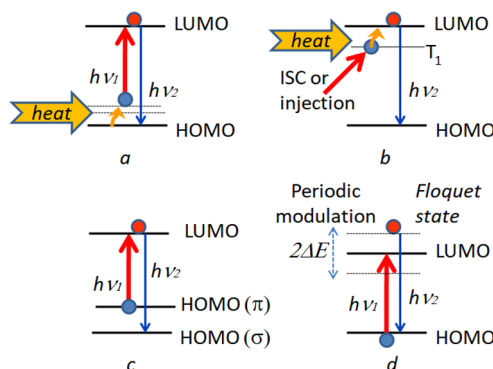


Figure 68. Schematic of one-photon upconversion processes: (a, b) thermal-induced;<sup>578</sup> (c) due to splitting in HOMO;<sup>562</sup> (d) via the Floquet state.

(HBA)-assisted anti-Stokes photoluminescence (ASPL). HBA-assisted ASPL does not require sensitizer or intensive excitation conditions, but it employs additional energy of vibrational modes at environmental temperatures.<sup>562</sup> HBA-assisted ASPL has attracted growing interest in recent years due to potential application in various fields, such as optical refrigeration,<sup>563–566</sup> sensitizing of photovoltaic cells,<sup>567</sup> photoluminescence bio-imaging,<sup>568</sup> and thermal probes.<sup>569</sup> However, there are only few classes of organic materials that are able to demonstrate single-photon upconversion; these include xanthene-based chromophores such as luciferin and rhodamine derivatives,<sup>570,571</sup> Alexa Fluor,<sup>572</sup> porphyrin,<sup>573</sup> spirolactam moieties under acidic conditions,<sup>574</sup> polymethines,<sup>575,576</sup> oxazine,<sup>562</sup> diarylethenes,<sup>577</sup> and carbon nanodots<sup>578,579</sup> as well.

In the other specific case, delivery of an excited electron to the triplet state by ISC or by injection with an electric field is followed by absorption of phonons (Figure 68b), resulting in the TADF phenomenon that has been considered previously. Emission intensities for both HBA-assisted ASPL and TADF mechanisms are dependent on activation energy, that is, the

major vibrational mode of the molecule and thermal population  $P_i$  of the vibrational levels of the ground state or triplet state of the molecule, respectively, according to Boltzmann distribution (eq 28 for TADF) or eqs 30 for HBA-assisted ASPL,

$$I(\lambda) = \exp\left(-\frac{E_a}{kT}\right) \quad (30a)$$

$$P_i \approx \exp\left(-\frac{\epsilon_i}{kT}\right) \quad (30b)$$

where  $I(\lambda)$  is the intensity of the ASPL process,  $E_a$  is the activation energy,  $k$  is the Boltzmann constant,  $\epsilon_i$  is the energy of the vibronic level, and  $kT \approx 26 \text{ meV}$  for room temperature. The activation energy due to vibrational excitation can be smaller than the  $S_1-T_1$  bandgap in the case of TADF or  $E_g-E_{\text{exc}}$  ( $E_g$  is the LUMO–HOMO gap and  $E_{\text{exc}}$  is the excitation photon energy) in case of HBA-assisted ASPL. For example, it was shown that activation energy in tricarbocyanine dyes is relatively low (~55 meV), which corresponds to the low-energy skeletal CNC in-plane bending deformation of the chromophore chain, whereas HBA can proceed from a relatively high vibrational level corresponding to the CN stretch as well.<sup>580</sup> According to eq 30b, the relative population ratio for the CNC bending level (670 cm<sup>-1</sup>) is about 4%, that for the CH bending (910 cm<sup>-1</sup>) is 1.2%, and that for the CN stretch (1360 cm<sup>-1</sup>) is only 0.14%. This leads to the fact that HBA-assisted ASPL should be more effective by 1 order of magnitude when it is assisted by low-energy bending than when it is assisted by high-energy stretching vibrations (Figure 69). That means that the quantum yield of ASPL is largely dependent on the excitation energy. As higher excitation energy captures electrons from the deeper vibronic levels, which are better populated according to the Boltzmann distribution, this yields brighter anti-Stokes emission but lower anti-Stokes shift. On the other hand, the decrease in

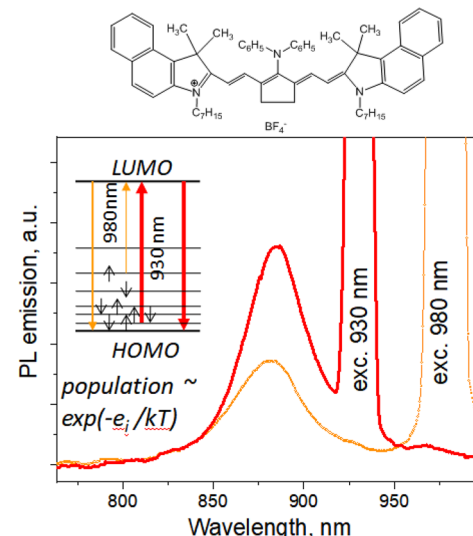


Figure 69. Illustration of ASPL assisted by high-energy stretching and low-energy bending vibrational levels in tricarbocyanine dye with the indicated structure. Photons of low energy (980 nm) pick up electrons from the shallow vibrational levels, which are poorly populated, whereas photons of high energy (930 nm) pick up electrons from the deep vibrational levels, which are highly populated. Note that excitation power at 980 nm (390 mW) is 4 times excitation power at 930 nm (97 mW). Reprinted from ref 580, Copyright 2021, with permission from Elsevier.

the excitation energy leads to higher anti-Stokes shift but low intensity of ASPL emission, as high-energy vibrational levels with lower population are involved in the HBA process in this case (Figure 69).

Recently, other specific mechanisms for single-photon upconversion have been proposed. Ma et al. observed efficient single-photon upconversion photoluminescence in lead halide perovskite semiconductors.<sup>581</sup> Ma and coauthors assigned it to coexistence of a free exciton (FE) and a STE, where an electron photoexcited to the STE well then is capable of thermal activation and overcoming of an energy barrier between STE and FE of 103.7 meV for  $\text{CsPbBr}_3$  and 45.2 meV for  $\text{CsPb}(\text{Br}/\text{I})_3$ . The authors, however, did not consider that the STE is usually a relaxed form of a FE;<sup>130,131</sup> therefore, direct excitation of the STE is hardly possible.

Shen et al. reported upconversion fluorescence in graphene QDs, which was assigned to the splitting of the HOMO into  $\pi$  and  $\sigma$  orbitals separated by about 1.1 eV.<sup>582</sup> The exciton is formed due to the electron transition from the higher  $\pi$  orbital of the HOMO but relaxes to the lower  $\sigma$  orbital (Figure 68c). Although the electrons of the  $\sigma$  orbital can also be excited to the LUMO, they can only result in down-conversion emission.

Another specific one-photon upconversion process can proceed via a Floquet state. In this process, a photoexcited system is simultaneously modulated by a periodic field, which moves the electron to a higher excited level from which it emits a photon of higher energy than the absorbed one (Figure 68d). Nagai et al. reported the observation of high-order sideband generation at photon energies of  $\hbar(\omega_{\text{NIR}} + m\omega_{\text{MIR}})$  with integer  $m$  from an inorganic 2D system (a monolayer of  $\text{MoS}_2$ ) by simultaneously applying near-infrared (NIR) and mid-infrared (MIR) pulses.<sup>583</sup> However, no similar effect was reported for conjugated molecules so far.

### 5.3. Down-Conversion Dynamics of Excitons

Down-conversion is a process by which one high energy photon splits into two or more lower energy photons. In organic materials, one can distinguish two qualitatively different down-conversion processes, exciton singlet fission and multiple exciton generation. Whereas both processes start with absorption of a single photon leading to excitation of a singlet exciton, the intermediate products and their yields are different. First, the exciton fission quantum yield is limited by generation of two excitons only, while for multiple exciton generation, there is no formal limitation in the number of the produced excitons. Second, the exciton fission process requires the presence of two or more molecules together to generate the two excitons, whereas multiple exciton generation occurs via a single particle. Third, exciton fission converts singlet excitons to triplet ones, whereas multiple exciton generation does not change the multiplicity of the excitons. In addition to these multiphoton processes, there is also a one-photon process where one-photon absorption is followed by one-photon emission at lower energy, which is an exciton down-shifting conversion.

**5.3.1. Exciton Down-Shifting.** Down-shifting conversion is a single-photon process that results in decreased energy of the emitted photon compared to the absorbed one. There are different mechanisms of exciton down-shifting in conjugated molecules after photoexcitation, which include vibronic non-radiative relaxation of the excited molecule, energy migration in the system of chromophores, charge redistribution, symmetry breaking, molecular isomerization, and conformational changes (Figure 70).

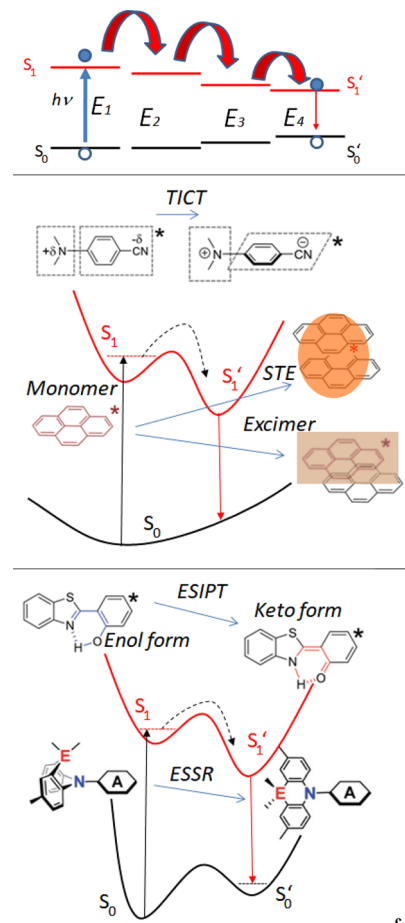


**Figure 70.** Main mechanisms of down-shifting conversion processes: (a) Energy funneling to sites with smaller band gap; (b, c) photoinduced structural changes followed by relaxation to unstable and stable ground states, respectively: twisted intramolecular charge transfer (TICT), self-trapped exciton (STE), excimer formation, excited-state intramolecular proton transfer (ESIPT), or excited-state structural relaxation (ESSR).

Down-shifting due to energy migration in conjugated polymers to regions of longer conjugation length and a smaller band gap (Figure 70a) was considered in the previous sections; this process is time-dependent and results in temporal shift of the emission maximum to longer wavelengths on picosecond time scales. For example, in MEH-PPV average pairwise hopping time between adjacent spectroscopic units, that is, the spatial segments of the chain, which are responsible for the spectroscopic properties of the polymer (see section 4.4.2.1), was found to be 0.3 ps, while the exciton travels over a distance of about 7 spectroscopic units.<sup>584</sup>

Down-shifting due to photoinduced structural relaxations can be divided into two major groups. The first one describes photoinduced structural changes that possess lower band gap but unstable ground state, which leads to reversible structural relaxation to the initial state. The second group provides photoinduced structural changes that possess a stable ground state, and therefore these are irreversible (Figure 70b,c). For example, excited states of conformers can be separated by a small energy barrier, which can be overcome by photoexcitation via a hot exciton, but the barrier between their ground states can be higher than the thermal energy at ambient temperature.<sup>585</sup> On the other hand, down-shifting due to a twisted intramolecular

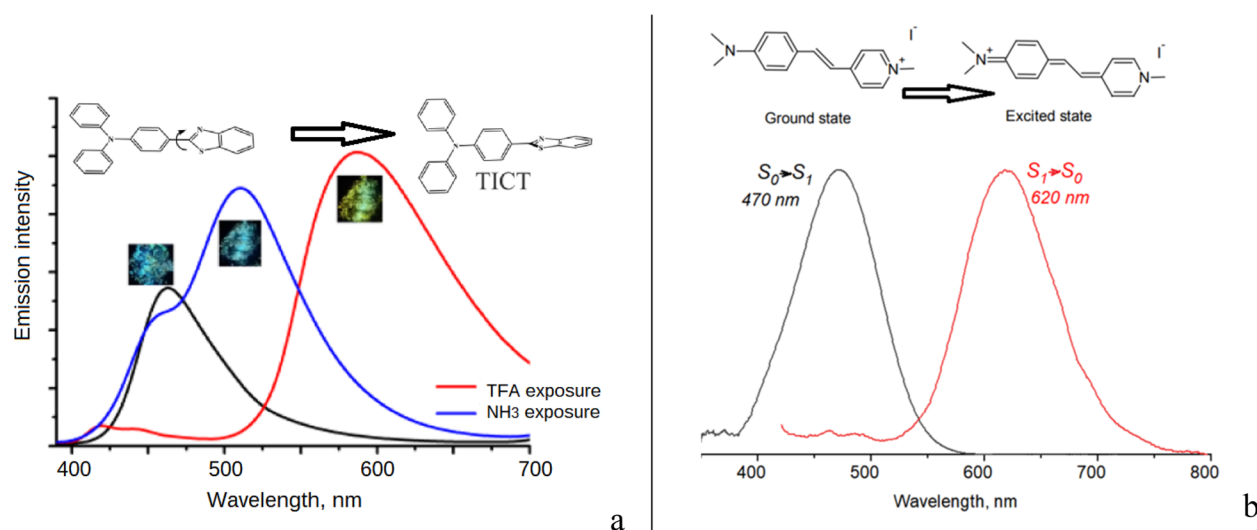


**Figure 71.** (a) Solid-state PL emission spectra of triphenylamine–benzothiazole derivative (black) upon exposure to trifluoroacetic acid (TFA, red) and NH<sub>3</sub> (blue). Adapted from ref 588. Copyright 2019 American Chemical Society. (b) Ground state ionic and excited quinoid forms of stilbazolium dye according to Todorova et al.<sup>587</sup> and corresponding ground-state absorption (black) and excited-state emission (red,  $\lambda_{\text{exc}} = 405 \text{ nm}$ ) spectra.

**Table 1. Chemical Structure and Selected Characteristics of IR-780 and HCy2 in the Ground and Excited States in DMSO Solution<sup>589</sup>**

Stokes shift (eV)					
0.04			0.35		
BLA in the ground state (left and right part of polymethine chain, respectively, Å)					
0.015	-	0.015	0.113	-	0.089
BLA in the first excited state (left and right part of polymethine chain, respectively, Å)					
0.011	-	0.011	0.023	-	0.022
Ground-state charge distributions (left subunit - central ring - right subunit of polymethine chain, respectively)					
0.464	-	0.072	-	0.464	0.322
First excited state (vertical) charge distributions (left subunit - central ring - right subunit of polymethine chain, respectively)					
0.439	-	0.122	-	0.439	0.372

charge-transfer (TICT) state yields a decreased band gap of the excited molecule as a result of intramolecular charge-transfer accompanied by molecular rearrangement into the twisted form. This mechanism can be assisted by a polar environment of the molecule (Figure 71a), but it is usually reversible as a relaxed molecule returns charge back, which leads to the recovery of the initial conformation after emission of a photon. The TICT state can be dark due to molecular vibrations that quench PL emission. Li et al. proposed a pressure-induced approach to light up the dark TICT state through the use of a pressure-related liquid–solid phase transition of the surrounding solvent.<sup>586</sup>

In stilbazolium dyes the positive charge of the chromophore is localized on the pyridinium moiety, but it shifts upon photoexcitation toward the amino moiety, giving rise to the different forms of the chromophore, that is, ionic in the ground state and quinoid in the excited state, from which photoluminescence occurs (Figure 71b). This results in one of the

largest Stokes shifts, up to  $\sim 7000 \text{ cm}^{-1}$  ( $\sim 0.87 \text{ eV}$ ), reported by Todorova et al.<sup>587</sup> In addition, solvents of different polarity interact differently with the two forms, making it possible that either ionic or quinoid forms are present in various solvents. Todorova and coauthors showed that Stokes shift increases from stilbazolium dyes with pyridinium and benzene nuclei (mononuclear) to quinolinium and benzene nuclei (one and half nuclear), and finally to those possessing quinolinium and naphthalene nuclei (binuclear) in almost all solvents compared.

Another example demonstrates tuning of the band gap of the excited state due to the changes in BLA and charge distribution in the polymethine chain of substituted heptamethine cyanine dyes (HCy2). Specifically, different substituents at the meso-position in the chromophore of these dyes lead to different BLA and charge distribution from the left and right sides of the polymethine chain. Sissa et al. showed that the change of the Cl substituent in a typical cyanine dye, IR-780, for a specific octyl

chain linked to the cyclohexenyl ring via a nitrogen atom strongly affects the conjugation of its polymethine chain, leading to a broken-symmetry ground state of the resulting HCy2.<sup>589</sup> However, the symmetry is partially restored in the first excited state (upon relaxation), leading to a large structural rearrangement of the molecule that results in increasing Stokes shift in HCy2 by almost 1 order of magnitude compared with IR-780 (Table 1).

Even larger Stokes shift,  $11760\text{ cm}^{-1}$  (1.458 eV), observed in *N*-(2-(6-chloro-*s*-tetrazin-3-yloxy)ethyl)-naphthalimide (NITZ) down-shifting molecule absorbing at 334 nm and emitting at 550 nm has been reported.<sup>590</sup> However, this large Stokes shift is due to a different mechanism. In NITZ, different parts of the molecule are responsible for the absorption and the emission. The NITZ molecule (Figure 72) absorbs UV light

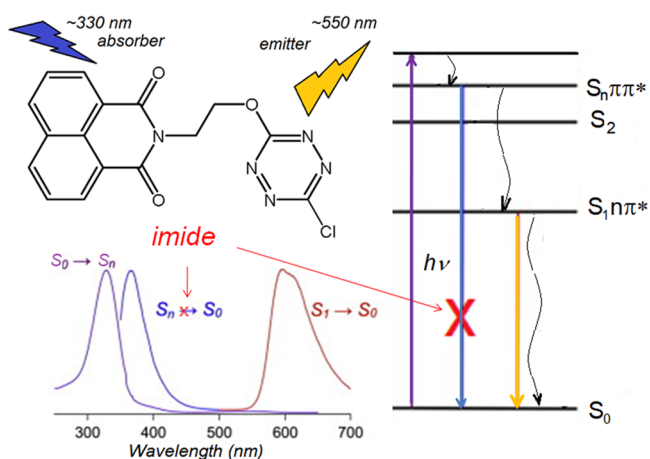


**Figure 72.** Structure of the NITZ molecule, energy scheme, and excitation/emission spectra of the tetrazine core without the imide part and the forbidden transition (blue) in the presence of the imide indicated by the red cross. The spectra and energy scheme of tetrazine are reprinted from ref 593, Copyright 2012, with permission from Elsevier.

mainly due to the imide part, but it transfers the exciton to the tetrazine core, which emits a yellow-orange light with relatively high QY of 30%.<sup>591</sup> A very low absorption coefficient of the tetrazine core in the visible range is because the first excited state  $S_1$  involves  $n-\pi^*$  transition, which is forbidden and possesses a very long decay time in the range of 10–160 ns.<sup>592</sup> Therefore, the oscillator strength of the  $S_0-S_n$  ( $n > 1$ ) transition is 2 orders of magnitude larger than that of  $S_0-S_1$ , and the excitation of tetrazine occurs mostly through the higher-energy levels  $S_n$ , from which it can emit also as its rate of internal conversion  $S_n \rightarrow S_1$  is surprisingly slow ( $\sim 20$ –30 ps);<sup>593</sup> however, the emission from the  $S_n$  levels is suppressed by the imide part in the NITZ molecule (Figure 72).

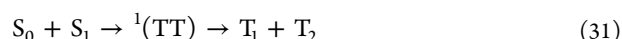
A large Stokes shift can be induced by the vibration-induced emission (VIE) mechanism, which produces dynamical conformation changes of the photoexcited molecule to the planar configuration responsible for the low-energy emission (Figure 73a). In general, VIE is widely applied to V-shaped polycyclic conjugated molecules such as *N,N'*-disubstituted dihydrobenzo[*a,c*]phenazines (DHPs) with flexible units rotating around an N–N axis, which can undergo a bent-to-planar geometrical change in the excited state that is not accompanied by nonradiative energy dissipations caused by rotational motion mechanisms.<sup>594</sup> As a result, a Stokes shift up

to  $12000\text{ cm}^{-1}$  (1.488 eV) was observed in DHPs with absorption at 351 nm and emission at 613 nm.<sup>595</sup> In the solid state, where rotation of molecular fragments toward optimal conformation is suppressed, no large Stokes shift can be achieved (Figure 73b). In order to tune different degrees of molecular planarization through the VIE mechanism, Chen et al. applied a strategy of molecular cyclization by introduction of alkyl chains of different lengths at the flexible groups of 9,14-diphenyl-9,14-dihydrodibenzo[*a,c*]phenazine (DPAC).<sup>596</sup> This imposed various degrees of constraint to impede the structural deformation of DPAC and resulted in different degrees of molecular planarization (Figure 73c), which, in turn, modulated emission covering the entire visible spectrum (Figure 73d).

A specific down-shifting mechanism has been found in carbon dots whose multiple emission surface centers can be tuned dependent on polarity of the solvent used. Ren et al. observed luminescent down-shifting in a wide spectral range, from  $\sim 525$  to  $625\text{ nm}$ , when exciting the carbon dots at  $460\text{ nm}$  wavelength.<sup>597</sup> In particular, it was shown that the fluorescence of the carbon dots can be linearly modulated by adjusting the polarity of the employed solvent, which was explained by the dominant role of surface states of the carbon dots in controlling the emission.<sup>598</sup> The surface states in carbon dots are due to abundant nitrogen- and oxygen-containing groups and substructures like hydroxyl, carbonyl, and amino, which provide stabilization of the excited state due to a strong solvent polarity.<sup>599</sup> The increased solvent polarity causes the increase of electron density through the addition of lone pair electrons in a nitrogen of the amine groups, which reduces the energy gap and results in bathochromic shift of fluorescent emission.<sup>600</sup>

The exciton down-shifting phenomenon has been applied for collection of high-energy photons in photovoltaics, because direct absorption of such photons by materials with lower band gap leads to waste dissipation of the energy excess. A design of molecular luminescent down-shifting sensitizers has been reported based on the C54ST fluorescent doped tris(8-quinolinolato) aluminum (C54ST:Alq<sub>3</sub>) molecule (excitation in the range of 400–500 nm, emission between 500 and 650 nm),<sup>601</sup> NITZ,<sup>602</sup> *N,N'*-di-(1-naphthalenyl)-*N,N'*-diphenyl-[1,1':4',1":4",1'''-quaterphenyl]-4,4"-diamine (4P-NPB),<sup>603</sup> and *trans*-5-(*p*(*N,N*-diphenylamino)styryl)-1,3-di(2-pyridyl)-benzene<sup>604</sup> (excitation at  $\sim 350\text{ nm}$ , emission at  $\sim 450\text{ nm}$ ), and anthracene derivatives (excitation at 300–400 nm, emission at 500–700 nm),<sup>605</sup> which were successfully applied in solar cells.

**5.3.2. Exciton Fission.** Singlet fission (SF) is a photochemical process in which a singlet exciton decays into two triplet states. The process is distinct from intersystem crossing, because SF does not involve a spin flip but is mediated by two triplets coupled into an overall singlet.<sup>606</sup> Therefore, SF is a spin-allowed process. In order to provide such a spin balance, two chromophores are needed that are appropriately electronically coupled in either dimer, oligomer, or molecular crystal configuration, thus providing two pairs of spins, whose combination can just result in two triplet states without breaking of the zero magnetic moment of the system overall (eq 31 and Figure 74).



Because the SF process is spin allowed, it usually occurs at ultrafast rates, on time scales from  $\sim 80$  fs to 25 ps in single-crystal, polycrystalline, and amorphous solids and dimers with orthogonal arrangement, where a systematic alteration of the

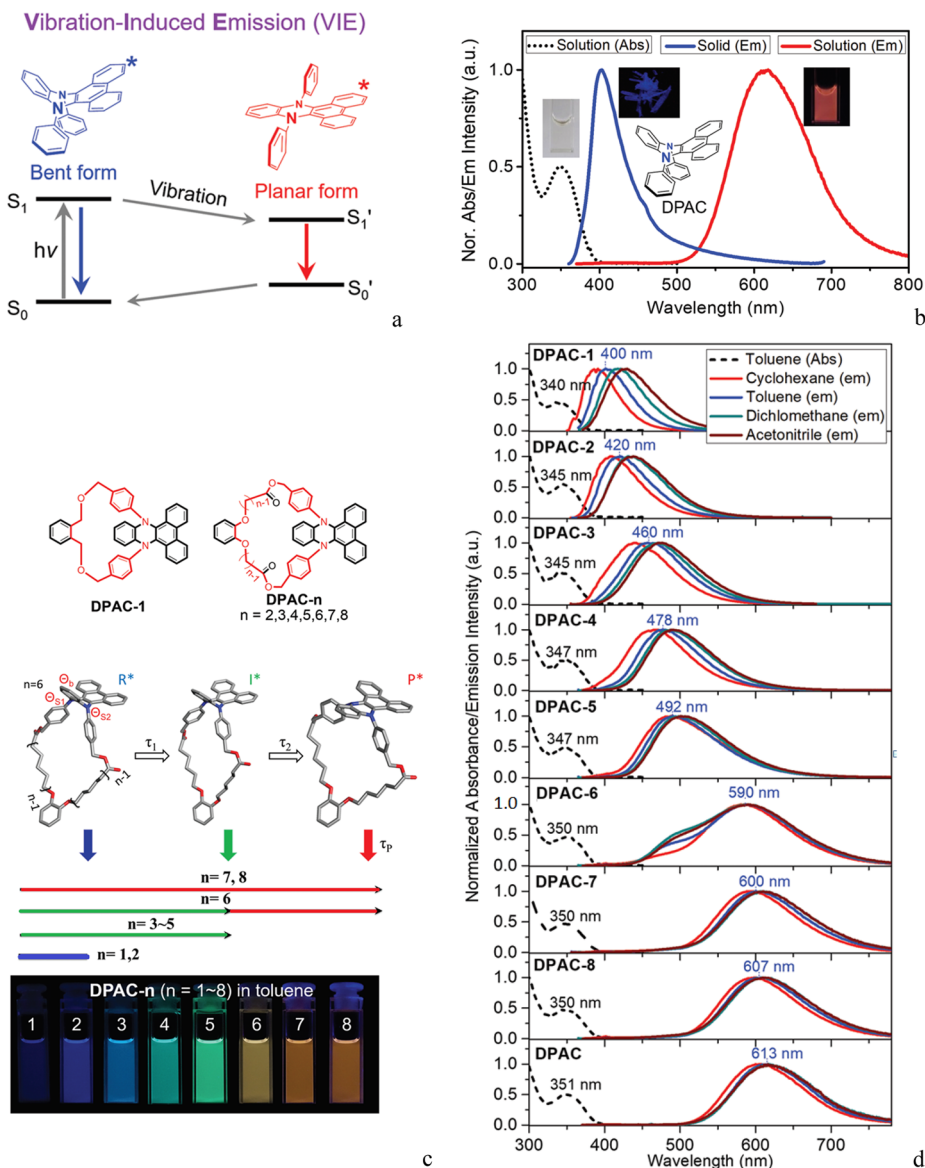


**Figure 73.** (a) Illustrative scheme for VIE involving excited-state configuration transformation from bent (blue emissive state) to planar (red emissive state) via the vibration of two aryl rings along the flexible unit (i.e., N–N axis). (b) Typical absorption and emission spectra of DHPs (using DPAC (*N,N'*-diphenyl) as a prototype), indicating a remarkable Stokes shift due to VIE in the dispersed solution. (c) Molecular structures of DPAC-*n* (*n* = 1–8) with schematic illustrations of their bent to planar process in the excited state and their fluorescence images in toluene under UV light irradiation (365 nm). (d) Steady-state absorption and emission spectra of DPAC-*n* (*n* = 1–8) at room temperature in various solvents. Parts a and b reproduced with permission from ref 594. Copyright 2020 Wiley. Parts c and d reproduced with permission from ref 596. Copyright 2017 American Chemical Society.

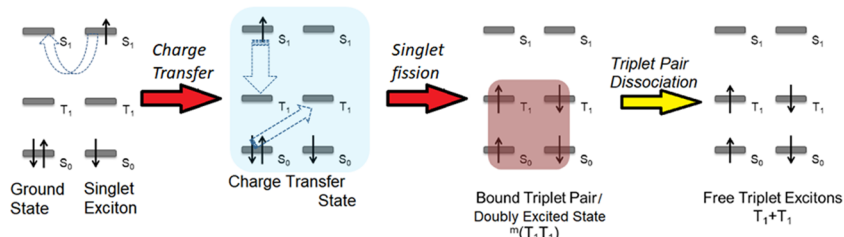


**Figure 74.** Scheme of the singlet exciton fission. The charge-transfer mediated step is indicated by the light-blue box. Note that the total spin of the system is zero at all stages.

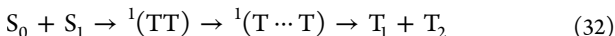
relative distance, solvent polarity, or effective  $\pi$ -conjugation between two molecules enables fine-tuning of the electronic coupling,<sup>607,608</sup> to nanoseconds in pentacene dimers where one

of the molecules is placed in a bent geometry.<sup>609</sup> Therefore, the radiative decay that generally occurs on a nanosecond time scale does not usually affect the SF process. However, Bardeen

reported that correlations between pairs of triplets can persist in crystalline tetracene up to  $\sim 10$  ns after the fission.<sup>610</sup>

The SF phenomenon is unique to molecular photophysics and has been mostly observed in organic crystals, aggregates, disordered thin films, donor–acceptor polymers, and covalently linked dimers of acenes, pentacenes or tetracenes, where the chromophores are oriented such that the electronic coupling between the singlet and the double triplet states is large.<sup>611,612</sup> Singlet fission is considered to be useful for organic photovoltaics, since it could provide higher yield of charge carriers due to involvement of high-energy photons with energy twice the band gap of the PV device and thus can improve the photoconversion efficiencies. An external quantum efficiency (EQE, charge carrier pairs generated per incident photon) of up to 126% and internal quantum efficiency (IQE, charge carrier pairs generated per absorbed photon) reaching 200% have been achieved using SF and harvesting triplet excitons in solar cells based on layered donor–acceptor heterojunctions.<sup>613,614</sup>

The detailed mechanism of the SF process has long been a subject of debate. Both direct and mediated mechanisms have been proposed in theoretical studies, which are highly system-specific. In the direct mechanism, the lowest-lying absorbing state ( $S_1$ ) transforms into a correlated triplet pair  ${}^1(TT)$ , also referred to as a multiexciton (ME) state, a doubly excited state (DE), or a dark state (D).<sup>562</sup> The  ${}^1(TT)$  pair then dissociates into two noninteracting ( $T_1$ ) states, called ( $T_1 + T_1$ ). The bound triplet pair, that is,  ${}^1(TT)$ , is an important state that mediates SF. Many studies indicated that there is an energetic stabilization of triplet-pair states relative to free triplets. This stabilization enables endothermic SF processes and often results in long lifetimes of the bound triplet-pair state. However, triplets in close proximity demonstrate enhanced recombination and reduced excited-state lifetimes.<sup>615</sup> Therefore, the necessity of a spatially separated triplet pair state  ${}^1(T\cdots T)$  has been introduced recently implying its origin from  ${}^1(TT)$  separation by triplet energy transfer,<sup>616,617</sup> which gives rise to a modified version of eq 31 as follows:



However, the dissociation step is dependent on the optimal range of strength of interaction between the bound triplet pair. On one hand, if coupling is too weak, it will be insufficient to permit the formation of a correlated triplet-pair state rapidly enough to compete with other events such as fluorescence. A consequence of the weak interaction of the two triplets can be also relaxation of  ${}^1(T_1T_1)$  into the triplet  ${}^3(T_1T_1)$  and quintet  ${}^5(T_1T_1)$  states on a time scale of nanoseconds,<sup>618</sup> which represents the intersystem crossing aspects of SF.<sup>611</sup> On the other hand, if coupling is substantially stronger than  $kT_B$  then the  ${}^1(TT)$  state is tightly bound so that it cannot dissociate into a pair of triplet excitons on the feasible time scales. Pensack et al. showed by transient absorption spectroscopy that three intermediate steps should be considered before the final formation of two independent triplet excitons occurs, where the first step represents the initially photogenerated singlet exciton, whereas the second and third steps represent bound  ${}^1(TT)$  and spatially separated  ${}^1(T\cdots T)$  but distinctly correlated triplet-pair intermediates, respectively. For the statistical mixture of 2,9- and 2,10-dichloro-6,13-bis(triisopropylsilylithynyl)-pentacene (Cl<sub>2</sub>-TIPS-Pn) aggregates, the time constants of these steps are 0.2, 2, and  $\gg 200$  ps, respectively.<sup>619</sup> Wang et al. suggested the possible existence of a direct channel of  $S_1 \rightarrow$

${}^1(T\cdots T)$  for singlet fission in addition to the singlet fission that proceeds via an exchange-coupled state, that is,  $S_1 \rightarrow {}^1(TT) \rightarrow {}^1(T\cdots T)$  for tetracene crystals.<sup>620</sup> On the other hand, the two triplet pairs give rise to the reverse process via triplet fusion (Figure 75). The spin-entangled correlated triplet pair is mobile

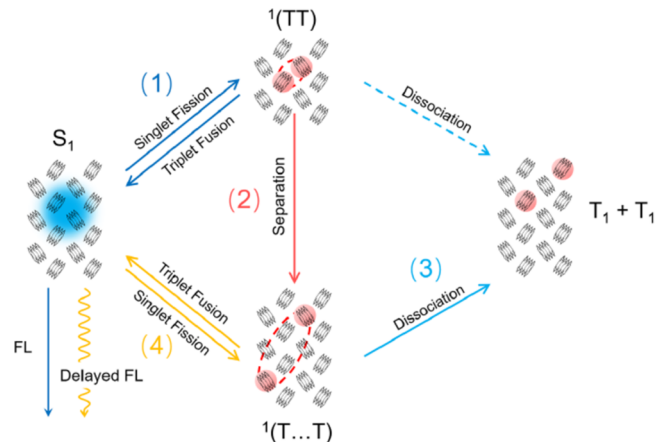


**Figure 75.** Schematic diagram of the singlet fission process in tetracene crystals. Reprinted from ref 620 with the permission of AIP Publishing. Copyright 2019 AIP Publishing.

and in tetracene crystals was shown to possess a similar mechanism and rate of diffusion as for the bright singlet excitons.<sup>621</sup>

The mediated mechanism occurs via concerted or stepwise electron transfer events that involve virtual or real intermediates, and it is facilitated by coupling to higher-lying CT states.<sup>622</sup> Detailed calculations of this mechanism showed that SF is mediated by a two-electron process, where only three classes of states are close to the energy of the singlet monomer with the total zero spin angular momentum projection, namely, the singly excited singlet,  $|S\rangle$ , the charge transfer state,  $|CT\rangle$ , with three electrons on one chromophore, and the doubly excited states,  $|TT\rangle$ <sup>623</sup> (Figure 74). In the high-temperature limit, the transfer rates between  $|S\rangle$  and  $|CT\rangle$  and from  $|CT\rangle$  to  $|TT\rangle$  can be described in the form of a Marcus rate:<sup>624</sup>

$$k_{S \rightarrow CT} = J^2 \sqrt{\frac{\pi\beta}{\Lambda}} e^{-(\beta/4\Lambda)(E_{CT} - E_S + \Lambda)^2} \quad (33a)$$

$$k_{CT \rightarrow TT} = J^2 \sqrt{\frac{\pi\beta}{\lambda + \Lambda}} e^{-(\beta/[4(\lambda + \Lambda)])(E_{TT} - E_{CT} + \lambda + \Lambda)^2} \quad (33b)$$

In eqs 33,  $\Lambda$  is the reorganization energy associated with interchromophoric electron transfer,  $\lambda$  is the reorganization energy for intramolecular charge redistribution in the excited state,  $J$  is the coupling constant, and  $\beta = 1/(k_B T)$ .

A substantial role of the exciton coupling with inter- and intramolecular vibrational modes in SF processes was shown both experimentally and theoretically.<sup>625</sup> Electron–vibrational coupling can provide energy to bring the singlet and triplet states into resonance or cause fluctuations in the electronic coupling matrix elements,<sup>622</sup> so the definition of exciton coupling with intramolecular and intermolecular vibrational modes can be referred to as local (Holstein) and nonlocal (Peierls) coupling, respectively.<sup>626</sup> It was shown that Peierls vibrational coupling in the Redfield density matrix study of perylenediimide (PDI) molecules shifts the rate of triplet pair state formation from a picosecond to a sub-picosecond time scale.<sup>627</sup> A thermally

activated mechanism of SF in rubrene crystals (which is formally symmetry forbidden) via symmetry breaking by nuclear vibration has been shown by Xie et al.,<sup>628</sup> who also emphasized that these vibrations are relatively slow compared to the rates of SF itself in rubrene and can be considered as static disorder.

As a rule, most SF events have been observed as an intermolecular process (xSF) in solid state materials containing an ensemble of molecules or as a result of intermolecular collisions.<sup>629–631</sup> However, it has been shown recently that it is possible to observe intramolecular singlet fission (iSF) in single chromophores,<sup>632,633</sup> covalently linked dimers,<sup>634,635</sup> or tetramers.<sup>636</sup> The advantages of application of iSF materials in photovoltaics is that the rate of SF and the lifetime of generated triplets is not affected by solid state packing of the molecules. Furthermore, the iSF materials are processable through solution casting methods instead of having to use expensive crystal deposition techniques.

There are some peculiarities of the iSF process compared to xSF. First, xSF is normally mediated by CT states and depends sensitively on crystal packing or molecular collisions. In contrast, the iSF occurs mostly via a direct coupling mechanism that is independent of CT states,<sup>637</sup> although a CT-mediated mechanism was reported also.<sup>638</sup> Second, there is somewhat different dynamics of iSF and xSF. The xSF rate is about 1–2 orders of magnitude faster in solid-state pentacene samples ( $k_{\text{SF}} \approx 10^{12}$  to  $10^{13} \text{ s}^{-1}$ ) compared to iSF in pentacene dimers.<sup>638</sup> At the same time, the two triplets that are generated due to iSF are tightly bound because the two chromophores participating in iSF are linked. This leads normally to shorter lifetimes of the correlated triplets generated in closely linked chromophores due to triplet–triplet annihilation, which shows time constants of ~450 ps in bipentacenes,<sup>639</sup> tens of picoseconds to several hundreds of nanoseconds in pentacene dimers of different geometry,<sup>634</sup> and tens to hundreds of nanoseconds in terphenyl-bridged TIPS–pentacene tetramers.<sup>636</sup> iSF in a series of pentacene–tetracene heterodimers demonstrated biexponential decay, assigned to the fast triplet–triplet annihilation of correlated triplets (~10 ps to ~9 ns) and slow recombination dynamics of uncorrelated triplet pairs (~2 to 45 ns), with different yields of uncorrelated triplets after the photo-excitation.<sup>640</sup> On the other hand, because the xSF systems possess favorable transport properties, which provide diffusion of triplet excitons, this process allows one to extend the triplet exciton lifetimes to the microsecond time scale<sup>641,642</sup> until they either recombine or dissociate into the free charge carriers (Figure 75).

**5.3.3. Multiple Exciton Generation.** The exciton multiplication process or multiple exciton generation (MEG) occurs when the energy of the absorbed photons exceeds at least twice the band gap ( $E_g$ ) of the absorber.<sup>643,644</sup> The MEG phenomenon is ideal for application in solar cells, because  $N$  excitons can be generated when an absorbed photon has energy that is  $N$  times  $E_g$ , which yields an increasing conversion efficiency of the solar cell due to a staircase function of exciton quantum yield versus photon energy<sup>645</sup> (Figure 76). MEG was first discovered in inorganic QD nanocrystals, such as colloidal PbSe, PbS, PbTe, CdS, CdSe, InAs, Si, or InP.<sup>646–648</sup> In carbon materials with conjugated bonds, this phenomenon was first demonstrated in SWCNTs.<sup>649,650</sup> Wang and coauthors showed that the absorption of single photons with energy that exceeds the energy gap of (6,5)-SWCNTs by three times leads to exciton generation efficiency of 130% per photon,<sup>649</sup> which suggested that the multiple exciton generation threshold in SWCNTs can

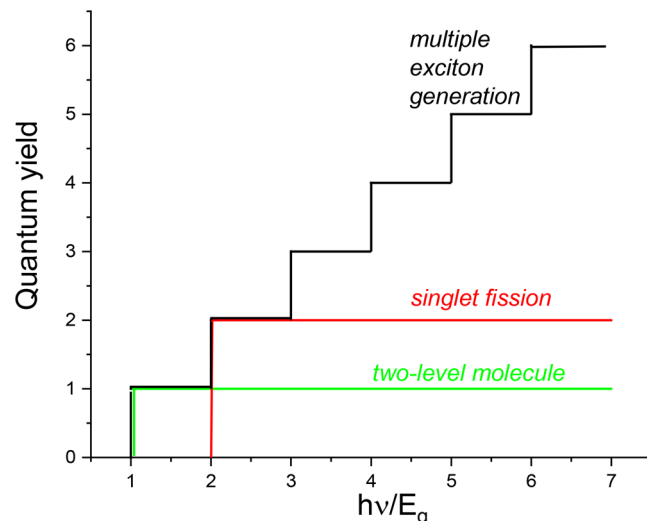


**Figure 76.** Comparison of the maximum QY of photogenerated excitons in a single molecule, in MEG and in SF processes as a function of the absorbed photon energy normalized to the absorber band gap.<sup>645</sup>

be close to the limit defined by energy conservation. Kryjevski et al. predicted efficient MEG in (6,2)- and (6,5)-SWCNTs within the solar spectrum range starting at the  $2E_g$  energy threshold with quantum efficiency reaching ~160% at about  $3E_g$ .<sup>651,652</sup> On the other hand, Kanemitsu argued that although SWCNTs give rise to the MEG phonomenon, the strong exciton–exciton interactions and complicated exciton structures in SWCNTs affect the quantized Auger rate and the MEG efficiency, leading to estimated MEG efficiency of only 130% at  $3.8E_g$  energy.<sup>653</sup> The reason for the reduced MEG efficiency in SWCNTs is the presence of the underlying dark excitons and trions, which strongly affect the observation of Auger recombination and MEG processes of the bright excitons, that is, the excitons with the odd-parity, spin singlet, and zero angular momentum.<sup>654</sup>

Graphene is another carbon material that demonstrated the MEG phenomenon.<sup>655</sup> McClain and Schrier estimated that absorbed photons in optimal graphene structures can generate between 1.3 and 1.8 biexcitons per absorbed photon.<sup>656</sup> Graphene QDs were applied in dye-sensitized solar cells (DSSCs), where they converted UV light to the blue and green region, leading to enhancement of  $J_{\text{SC}}$  by 21% compared to the reference cell.<sup>657</sup>

#### 5.4. Dynamics of Direct Decay of Singlet Excitons

**5.4.1. Decay via Radiative Recombination.** **5.4.1.1. Factors Influencing Recombination Rate.** Quantum mechanics dictates that the radiative decay rate,  $k_{\text{rad}}$ , of exciton should be proportional to the spectral bandwidth  $\Delta E$  of the radiative transition,<sup>61</sup>

$$k_{\text{rad}} = \frac{1}{\tau} = 2\Delta E/\hbar \quad (34)$$

However, this relation works in a limited number of cases for simple emitters only. Overall, the radiative recombination rates are controlled by various factors such as the spatial dimensionality  $D$  of the system, rigidity and conformational change of the conjugated molecule, its band gap, the exciton–phonon coupling, the oscillator strength of the first excited singlet state, the extent of exciton delocalization over emitting chromophores coupled in a multichromophoric system, and the energetic disorder of the system as well. Most of these factors

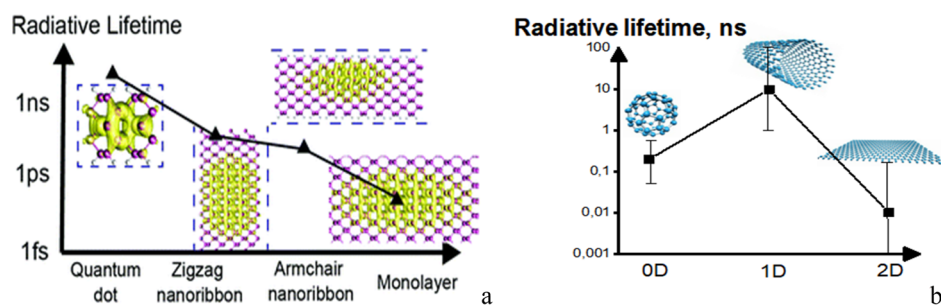


**Figure 77.** Dependence of the exciton lifetime on dimensionality of the system in (a) phosphorene and (b) carbon nanostructures. Part a reproduced with permission from ref 658. Copyright 2019 Royal Society of Chemistry. Part b was plotted based on literature data reported (see text).

influence a quantum mechanical reorganization of the wave function of the excited state ( $\Psi(S_1)$ ) compared to the ground state ( $\Psi(S_0)$ ), which can be due to the change in electronic structure, nuclear geometry and spin configuration of the excited molecule and which can lead to the poor mixing of  $\Psi(S_1)$  and  $\Psi(S_0)$ ; therefore, poor coupling of the excited state and the ground state wave functions results in slowing of the radiative excited state decay,  $k_{\text{rad}}$ , compared with the resonance (zero-point motion) excitation rate,  $k_{\text{max}}^0$  ( $\sim 10^{15} \text{ s}^{-1}$ ):

$$k_{\text{rad}} = k_{\text{max}}^0 f_e f_v f_s \quad (35)$$

where  $f_e$ ,  $f_v$ , and  $f_s$ , are prohibition factors due to changes in electronic, nuclear, and spin configuration, respectively.<sup>472</sup>

The effect of dimensionality D on the radiative recombination rate in organic conjugated systems can be nontrivial and differs from that known for inorganic low-dimensional systems, such as 0D, 1D, and 2D phosphorene nanostructures, where each dimensionality reduction yields the increase of the exciton radiative lifetime by 3 orders of magnitude, that is, from  $\sim 100 \text{ fs}$  for 2D to  $\sim 10\text{--}100 \text{ ps}$  for 1D, then to  $\sim 10\text{--}100 \text{ ns}$  for 0D,<sup>658</sup> which is consistent with the general experimental observations that the exciton radiative lifetime is much longer in inorganic low-dimensional systems (Figure 77a).

For conjugated molecules, however, the situation is different. Upon reduction of dimensionality, the Frenkel exciton attains increasing binding energy,<sup>74</sup> leading to the increasing probability and rate of exciton recombination. The change in radiative lifetimes as a function of dimensionality, however, is not straightforward. A relevant example can be considered for the carbon cluster family. The exciton lifetime in the quasi-0D cluster C<sub>60</sub> was reported to be 40 ps in the solid film<sup>659</sup> and 650 ps in solution<sup>660</sup> with the exciton binding energy estimated as 1.1 eV for PC<sub>61</sub>CM.<sup>661</sup> For the 1D system, such as an isolated SWCNT, the fluorescence emission was found to decay on a time scale of 10 ps. However, this fast relaxation originates mostly from nonradiative processes and the existence of dark excitons whose energy is close to that of each bright exciton, while the presence of dark states is known to have a strong impact on the coherence lifetime of optically accessible states, which represents a possible scattering channel that can be accessed via emission or absorption of phonons.<sup>662</sup> Therefore, a neat radiative lifetime on the order of 1–10 ns<sup>663,664</sup> to as much as 110 ns<sup>665</sup> at room temperature has been estimated for SWCNTs. The exciton binding energy for nanotubes with diameters between 6.8 and 9.0 Å was found to be 0.3–0.4 eV.<sup>666</sup> For the 2D system of graphene nanoribbons, exciton lifetimes from sub-picosecond<sup>667</sup> to over 100 ps<sup>668</sup> were reported, which is due to the strong electron–hole binding energy up to  $\sim 0.7 \text{ eV}$ . As can be seen from the above data, the exciton decay rate in

carbon clusters better correlates with the exciton binding energy than with their dimensionality (Figure 77b).

System dimensionality nevertheless influences temperature dependence of the radiative recombination. The temperature dependence of the recombination lifetime is calculated as

$$\tau(T) = \frac{\tau_0}{f(T)} \quad (36)$$

where  $\tau_0$  is constant and  $f(T)$  is the oscillation strength. The latter is dependent on temperature as  $kT^{-D/2}$ . Therefore, for excitons of D-dimensionality, the radiative recombination lifetime is dependent on temperature as  $kT^{D/2}$ .<sup>669</sup> Using Fermi's golden rule within the Bethe–Salpeter equation approach, a similar temperature dependence of the exciton radiative lifetime at low temperatures, proportional to  $T^{3/2}$  in 3D, to  $T$  in 2D, and to  $T^{1/2}$  in 1D materials was predicted by Chen et al.<sup>670</sup>

System rigidity obtained by corresponding molecular design or by embedding the molecule into a highly viscous medium or solid matrix leads to suppression of its rotational degrees of freedom and corresponding suppression of nonradiative transitions that occur via emission of vibronic quanta (see below), and thus it promotes increasing exciton lifetimes and quantum yield of the emission. A particular way to suppress intramolecular vibrations is molecular aggregation, which leads to the phenomenon of aggregation-induced emission (AIE), where aggregate formation enhances light emission<sup>671,672</sup>

Rigidity or flexibility of a molecule is related to its static and dynamic conformations, which influence exciton recombination rates differently. Dynamic conformations are related to those attained by a conjugated molecule as a result of photoexcitation, which can either block or facilitate a subsequent emission; in some cases, such conformational changes can enhance emission rates dramatically. Ghosh et al. studied ultrafast dynamics of a bichromophore compound, AnBT, consisting of anthracene (An) and benzothiazole (BT) units connected by a single bond, which exists in the out-of-plane ground state conformation with a dihedral angle of about 65°.<sup>673</sup> The authors found that, depending on the protonation state, AnBT can undergo either an ultrafast planarized motion with time constant of 1.5 ps, which leads to a delocalized emissive excited state with lifetime of 5.4 ns, or a perpendicular torsion during  $\sim 5$  ps resulting in a practically nonemissive twisted intramolecular charge transfer state (Figure 78a).

Static conformational disorder influences the exciton emission rates via control of exciton delocalization length more smoothly. Hollingsworth et al. compared radiative emission dynamics of a rigid conjugated ladder polymer (LP1) prepared with a low backbone defect density and a nonrigid analogue (CP1), with a similar carbazole backbone

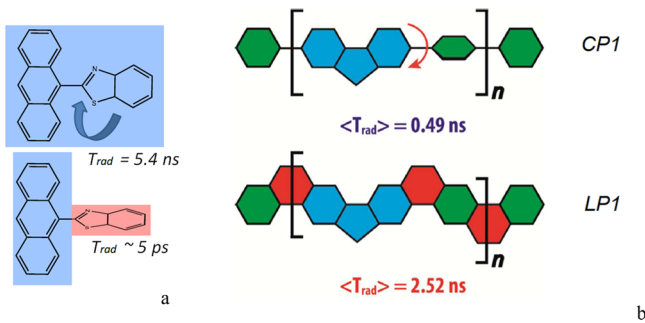


**Figure 78.** (a) Molecular structure of AnBT with a twisting degree of freedom. Adapted from ref 673. Copyright 2019 American Chemical Society. (b) Influence of the chain rigidity on the lifetime of the excited state. Reproduced from ref 674. Copyright 2017 American Chemical Society.

moiety (Figure 78b). The singlet exciton lifetime of LP1 contained a large-amplitude component with a lifetime of 5 ns, which was longer than that for any previously reported ladder conjugated polymer and was attributed to the low defect density of the polymer backbone. The average exciton lifetime in LP1 was also longer by a factor of  $\sim 5$  compared to its flexible CP1 analogue.<sup>674</sup>

Suppression of the torsional vibration amplitude can be fulfilled in the same polymer chain by specific chain–chain rearrangement, which creates a flatter ground-state conformation with smaller torsional disorder. It was reported that for P3HT embedded into PMMA matrix, the torsional relaxation leading to planarization of P3HT chains upon photoexcitation occurs faster than that of the aggregates in the neat P3HT film, implying that the torsional angle is smaller, which results in an increasing QY of PL of the P3HT particles embedded in the PMMA matrix and is accompanied by increasing ratio of 0–0 to 0–1 components in the PL spectrum, narrowing exciton band, and reduced recovery time of the ground state bleaching

associated with radiative recombination from  $\sim 425$  to  $\sim 300$  ps, respectively.<sup>675</sup>

However, the information on influence of the conformational change of an isolated long molecule on its emission quantum yield and radiative rate is controversial. On one hand, it is known that localization of an exciton in *cis* conformation PA leads to its bright luminescence compared to that in the *trans* conformation, which is essentially nonemissive due to the fast relaxation of the photoexcited state into soliton pairs.<sup>103</sup> On the other hand, it was reported that a flat HT conformation of single-molecule P3HT is accompanied by higher quantum yields of fluorescence from polymer solutions, which was explained due to a larger conjugation length, higher rigidity, and reduced nonradiative recombination owing to torsional quenching processes compared to the twisted HH conformer (see Figure 35).<sup>281</sup> In contrast, QY of fluorescence in P3HT aggregates is higher for the disordered, less planar configurations with significant fractions of dyads, since the low quantum yield in the planar ordered configuration is associated with classical concentration quenching effects.<sup>676</sup>

This controversy with QY of emission in polymer chains can be resolved upon identifying whether the conformational twisting or bending is located within the chromophore unit (the region of exciton delocalization) or outside of it. In the former case, a defect in the chromophore is merely created, which quenches the emission, while in the latter case the chromophore unit is not affected, and therefore this case promotes the emission. However, misalignment of transition dipole moments of chromophoric units on the chain with the bending direction selectively influences emission intensity of the bands originating from the different vibronic sublevels.

Hestand and Spano theoretically showed that the absorption and PL spectral shapes behave very differently depending on the chain bending of a linear J-aggregate (Figure 79a). While the absorption spectrum is less sensitive to morphological changes and shows no change in vibronic progression even at low

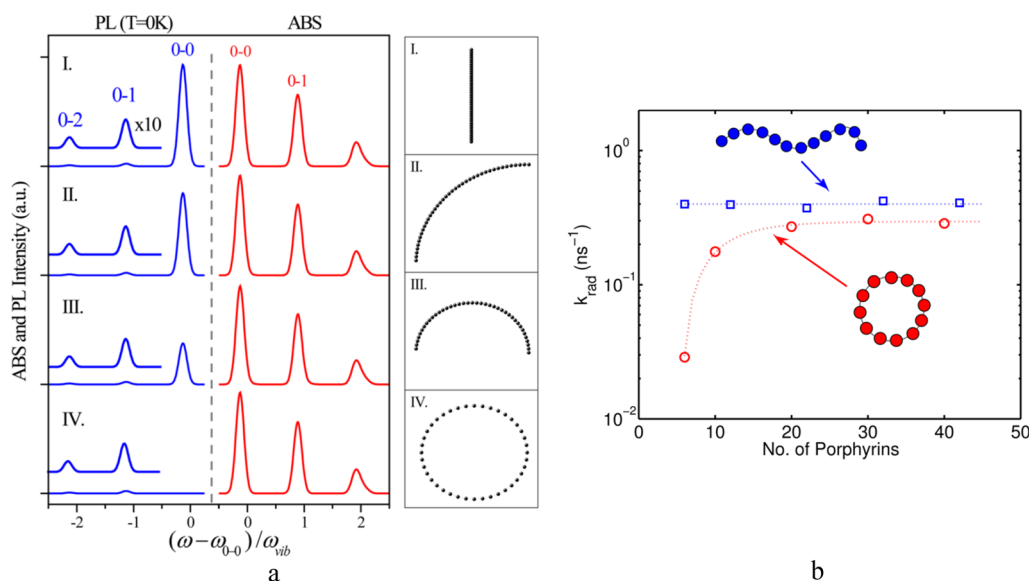


**Figure 79.** (a) Calculated absorption (red) and PL spectra (blue) of bent J-chains with the chain morphologies defined by the bend angle, which is  $\theta = 0$  (I),  $2\pi/160$  (II),  $2\pi/80$  (III), and  $2\pi/40$  (IV). The PL spectra are calculated at  $T = 0$  K. The 0–1 and 0–2 peaks in the PL spectrum are shown at 10× magnification in the insets. Here, the bending mostly affects the intensity of the 0–0 peak in the PL spectrum. Reproduced from ref 677. Copyright 2014 American Chemical Society. (b) Rate of radiative decay calculated for the linear molecules (blue squares) and the cyclic nanorings (red circles). Dotted lines are a guide to the eye. Reproduced from ref 679. Copyright 2014 American Chemical Society.

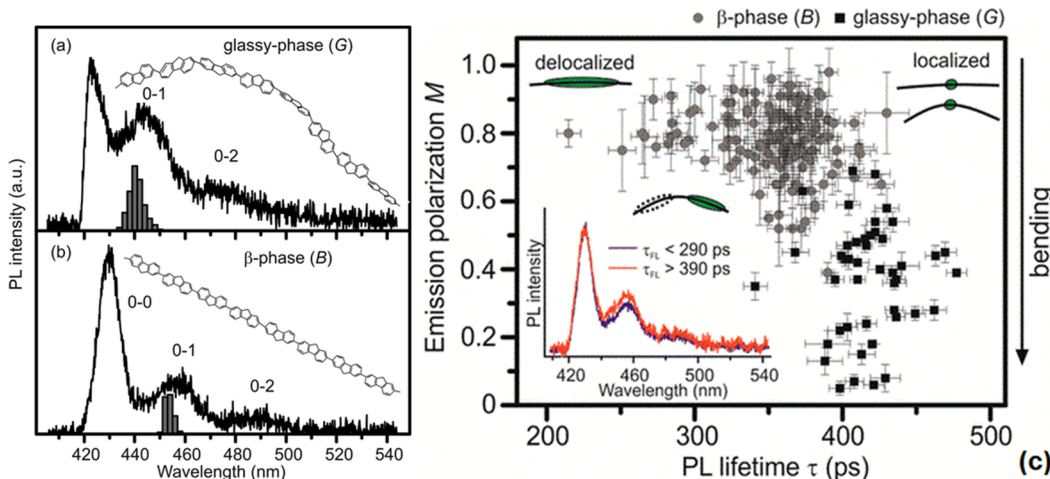


**Figure 80.** Room-temperature single molecule PL spectra showing differentiation between (a) twisted glassy-phase (G) and (b) planarized  $\beta$ -phase (B) polyfluorene. Histograms of the 0–1 peak positions were constructed from 147 molecules of each species. (c) Correlation between PL lifetime and PL emission anisotropy (which reflects the extent of chain ordering) of single PF chains. For each data point, a PL spectrum was obtained, allowing the differentiation between B and G conformations. On average, emission from G (black squares) is less polarized than that from B (gray circles) because multiple chromophores are involved in luminescence and the chain is disordered, and the lifetime of B is reduced with respect to G due to greater delocalization of the excited state. However, although B is more ordered than G, B shows a greater relative scatter of  $\tau$ , whereas there is only a small scatter in lifetime for G. In addition, B also displays a large scatter in the emission polarization values, even though there is only one active chromophore on the chain that is responsible for both absorption and emission. The inset shows average PL spectra of B selected by the lifetime. Reproduced from ref 682. Copyright 2014 American Chemical Society.

temperatures, both the 0–0/0–1 ratio in the PL spectrum and the radiative decay rate decrease with chain bending. The latter changes become more pronounced at lower temperatures where exciton coherence extends over a larger portion of the chain, while reducing exciton coherence length with increasing temperature or static disorder suppresses the sensitivity to bending. This effect was explained by misalignment of monomeric transition dipole moments with bending direction, which selectively attenuates the 0–0 PL peak intensity while leaving the 0–1 intensity practically unchanged, because the 0–0 line strength originates from the square of sum over monomeric transition dipole moments, which lie within the exciton coherence length and hence are sensitive to bending angle between the dipoles.<sup>677</sup> Therefore, in a linear J-aggregate with no bending this sum is maximal at low temperature and in the absence of defects. Conversely, the sideband line strengths are due to the sum of the squares of the transition dipole moments, which are incoherent constructs that are independent of chain bending and coherence length.<sup>678</sup>

Parkinson et al. compared the effect of chain topology on radiative decay rate of the exciton in linear and cyclic conjugated molecules containing different amounts of butadiyne-linked porphyrin units.<sup>679</sup> It was demonstrated that the rate of radiative decay of the nanoring approaches that of a similarly sized linear molecule when the diameter of the nanoring increases beyond  $\sim 10$  nm ( $> 20$  porphyrin units), as a result of exciton localization on a subsegment of the ring (Figure 79b).

The exciton–phonon coupling is another important factor that determines both rates and Stokes shift magnitude of the emission maximum. The exciton–phonon interaction depends on the length of the spectroscopic unit and increases as the latter decreases (Figure 5a). Increasing exciton–phonon coupling leads to increased Stokes shift and normally changes the shape of the emission spectrum with redistribution of the emission intensity in favor of vibronic sidebands (see eq 6), but it also results in shortening of the exciton coherent length or its reduced delocalization in long chains, particularly leading to the

phenomenon of exciton self-trapping. This is normally accompanied by decreasing emission rate and increasing exciton lifetime. On the other hand, radiative decay to vibrationally excited sublevels of the electronic ground state is strongly suppressed for delocalized excitons.<sup>680</sup>

There is a straightforward relation between exciton delocalization and its radiative decay rate. The fluorescence decay rate of an exciton that is delocalized over  $N$  monomers in a one-dimensional molecular ensemble is  $N$  times faster than the monomer decay rate; however, there is some limiting factor,  $N_{coh}$ , independent of further increase of the ensemble size, where  $N_{coh}$  represents the maximum coherence size attainable by an aggregate at a temperature  $T$ , which eventually leads to a convergent, size independent decay rate, which is faster than the monomer decay rate by the above factor  $N_{coh}$ .<sup>681</sup> Specifically, delocalization length of exciton in polyfluorene (PF) chains was shown to be changed owing to different extent of disorder between the twisted glassy-phase (G), where the polymer is essentially disordered, and the planarized  $\beta$ -phase (B), where the polymer exhibits a high degree of structural order, which arises from the monomer units adopting a planar configuration with respect to each other.<sup>682</sup> Shorter delocalization length of exciton in G is accompanied by stronger exciton–phonon coupling, which is displayed as enhanced emission of sidebands (Figure 80a,b). As a result of greater exciton delocalization, the lifetime of B is reduced with respect to G (Figure 80c).

A similar trend exists in linear J-aggregates with no disorder and periodic boundary conditions, where exciton delocalization over  $N$  monomers leads to the low-temperature photoluminescence 0–0 to 0–1 line strength ratio being rigorously equal to  $N/S$ , where  $S$  is the Huang–Rhys factor of the coupled vibrational mode. The result is independent of exciton bandwidth and therefore remains exact from the weak to strong exciton–phonon coupling regimes.<sup>135</sup> In the presence of disorder and for  $T > 0$  K,  $N$  represents the exciton coherence number,  $N_{coh}$ , thus giving a clue for extracting  $N_{coh}$  from the photoluminescence spectrum.<sup>135</sup>

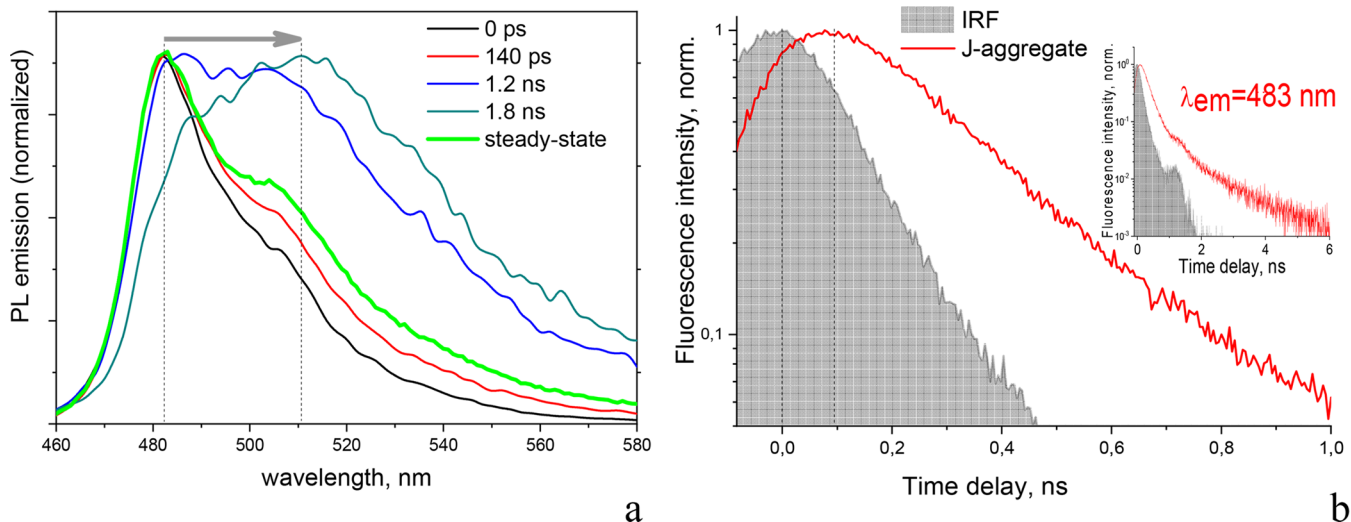


**Figure 81.** (a) Dynamics of the PL emission at indicated time intervals from the laser excitation and (b) kinetics of the emission at 483 nm of J-aggregate of thiamonomethinecyanine dye in solution (gray curve is the instrument response function). Note that emission spectra in part a are normalized to the same maximum, but the components taken at longer delay times have smaller contribution to the steady-state spectrum. Adapted from ref 315. Copyright 2019 American Chemical Society.

Structural disorder in organic films influencing exciton delocalization is related to energetic disorder as well, which is associated with the different diffusion lengths of excitons that encounter different numbers of nonradiative recombination centers and experience a different degree of quenching. As a result, the exciton lifetime is correlated with energetic disorder. Rörich et al. showed that better ordered polymer chains exhibit a single exponential photoluminescence decay with exciton lifetimes of a few hundred picoseconds, whereas polymers with larger disorder show multiexponential PL decays with exciton lifetimes in the nanosecond regime, which are also accompanied by a higher PL quantum yield due to the slower diffusion of exciton toward nonradiative quenching sites, thus resulting in longer lifetime.<sup>683</sup>

Finally, the increase in oscillator strength of the first excited singlet state normally leads to increase in the radiative rate. In turn, the oscillator strength of the emitter is dependent on the solvent polarity and the length of the emitter. Wagner et al. showed that variation of solvent can result in change of the fluorescence lifetime of peridinin by an order of magnitude.<sup>684</sup> The trend was that increasing solvent polarity enhanced the formation of the intramolecular charge transfer state in peridinin, which evolved via excited-state bond-order reversal and solvent reorganization in polar media and exhibited not only large oscillator strength but also enhanced coupling to the ground state via internal conversion. An increase in the oscillator strength (and thus in the radiative rate) occurs for relatively short oligomers, where the oscillator strength scales linearly with the number of repetition units  $n$ , as long as  $n$  is relatively small.<sup>685</sup> In the polymer limit, however, the oscillator strength and  $k_{\text{rad}}$  tend to saturate due to nonradiative decay facilitated by excited-state torsions in long chains.<sup>686</sup>

**5.4.1.2. Dynamics of Radiative Recombination.** It is normally assumed that dynamics of spontaneous radiative recombination of a single emitter is driven by exponential decay of the excited state population,  $n(t)$ , according to eq 37:

$$\frac{dn(t)}{dt} = -n(t)/\tau_1 \quad (37)$$

Integration of eq 37 yields  $n(t) = A e^{-t/\tau_1}$ , where  $\tau_1$  is the intrinsic lifetime of the exciton.

However, this simple decay kinetics becomes infringed if the excited state is accompanied by some additional processes like energy transfer to or from this state or interaction with a quencher. EET results in the dynamic Stokes shift of fluorescence together with the initial fast rise of the emission and longer lifetimes of fluorescence.<sup>687</sup> It has been reported that the 0–0 emission maximum experiences red shift by  $\sim 350 \text{ cm}^{-1}$  during  $\sim 3 \text{ ns}$  for samples of MEH-PPV and  $180 \text{ cm}^{-1}$  for PPV.<sup>688</sup> For J-aggregates of thiamonomethinecyanine dye, the emission maximum can be red-shifted by as far as  $\sim 1370 \text{ cm}^{-1}$  (32 nm) during the first 2 ns after the laser excitation<sup>315</sup> (Figure 81a); however, the delayed components have a reduced contribution to the steady-state spectrum, as the most intensive contribution to the PL emission is formed during first 100–150 ps, which is also accompanied by the corresponding rise of the fluorescence kinetics (Figure 81b). Also, a simple exponential decay of the emission maximum of J-aggregate does not work, because the decay rate gradually decreases with time (inset in Figure 81).

Dynamics of the energy shift of the emission can be influenced by ultrafast torsional relaxation of the polymer chain after the photoexcitation. For example, H-aggregates have a symmetry-forbidden 0–0 emission, which however can be observed in torsionally disordered aggregates of conjugated polymers at early (approximately picosecond) times after the photoexcitation that drives the torsional disorder to ordered flat conformation and therefore to the cofacial H-aggregate symmetric chain–chain arrangement as the exciton is cooled down. This results in a non-monoexponential picosecond dynamics of the emission decay observed in P3HT aggregates embedded into an ultrahigh-molecular-weight polyethylene matrix.<sup>689</sup>

Dynamics of the spectral distribution of the PL emission is largely dependent on the DOS of the exciton band. The spectrum observed from the very beginning (in the first picoseconds) can be different from the steady-state spectrum even if the exciton–phonon coupling is small and EET is absent. Dykstra et al. found that the crucial role in the recombination

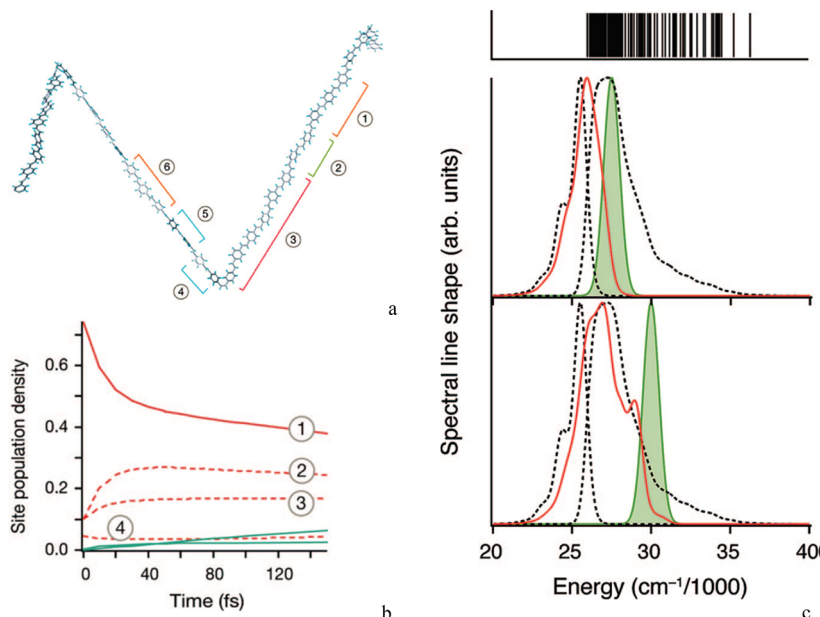


**Figure 82.** (a) Scheme of a conjugated polymer chain, indicating the effect of torsional disorder on break of the conjugation into a series of chromophore units, labeled 1–6. (b) Redistribution of exciton density (between the chromophore units) for the initially delocalized exciton. Each trace corresponds to a different site/conformational subunit,  $n$ , on the polymer chain. (c) Effect of the excitation energy on the early time fluorescence. Shown are calculated absorption and steady-state fluorescence spectra by the dotted black lines, the excitation pulse as a green Gaussian, and the emission at 100 fs by red. The density of states is shown at the top of the figure for reference. In the lower plot the abnormal shape of the early time fluorescence is because even though the states nearest in energy to the excitation each contribute significantly to the early time fluorescence, the higher density of states further to the red sums to give a greater overall contribution, even though the contribution from each state is small. This accounts for the appearance of the peak at lower energies. Reproduced from ref 277. Copyright 2009 American Chemical Society.

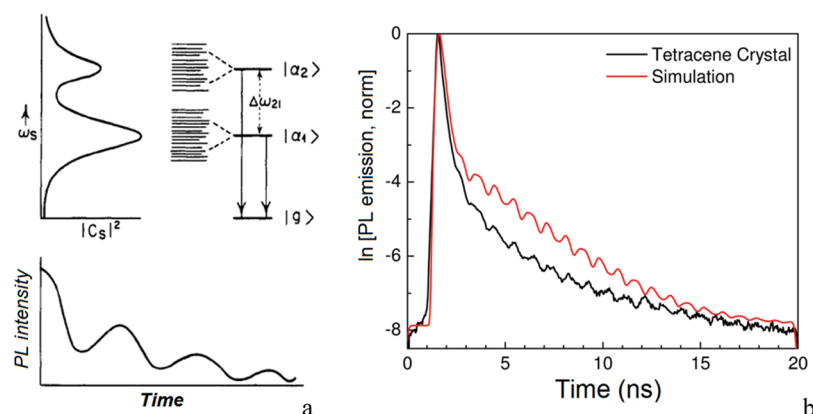


**Figure 83.** (a) Scheme of arising quantum beats in a system containing two molecular resonances and (b) experimental observation of the quantum beats in time-resolved fluorescence of a solution-grown single crystal of tetracene (black) along with simulated data convolved with an instrument response (red). In part a, an absorption spectrum containing two molecular resonances, each composed of many (unresolved) molecular eigenstates (upper left), a coupling scheme for the associated molecular resonance states, which are coupled radiatively to ground state  $|g\rangle$  (upper right), and the time-dependent fluorescence intensity resulting from coherent pulse excitation of the two resonances (lower) are shown. Part a reproduced from ref 690. Copyright 1983 American Chemical Society. Part b reproduced from ref 698. Copyright 2012 American Chemical Society.

dynamics belongs to the changes in exciton size or location, which have a significant effect on the exciton relaxation pathway, and that the various types of effective chromophores in the polymer chain that may be excited by the same laser pulse can lead to very different relaxation decays.<sup>277</sup> Dykstra and coauthors calculated that in the first  $\sim 100$  fs after the photoexcitation the exciton in a single MEH-PPV chain is quickly redistributed among the chromophores that comprise the collective electronic state of several contributing chromophores with overlapping wave function coefficients, where the redistributed exciton density, that is, the probability distribution of finding a portion of the exciton on a site  $n$  at a given time, is

dependent on the conformation and conjugation length of the chromophore unit (Figure 82a,b). This has a direct impact on the evolution of the early time (first 100 fs) emission spectra as a function of excitation wavelength. Since the exciton population is shifted very rapidly (over  $\sim 100$  fs) to a low energy distribution, the DOS increases toward the low-energy edge of the exciton band accordingly. The higher density of states at the low-energy edge, even though the contribution from each state is small in the case of high excitation energy, has totally a greater overall contribution compared to the low density of states in the high-energy part of the spectrum, thus creating the abnormal shape of the early time fluorescence (Figure 82c).

When emitted radiation intensity is in a superposition from the different excited states of a molecular system, then the emission dynamics can occur as oscillatory behavior via so-called quantum beats. The quantum beats were discussed in the context of coherent energy transfer between resonant energy levels of donor and acceptor (see sections 4.2.2 and 4.5.2), but these can be displayed also when an exciton recombines radiatively. Here, quantum beats arise in molecules containing multilevel excited states or resonances. Rhodes, who elegantly explained the quantum beat phenomenon in polyatomic molecules,<sup>690</sup> proposed that each excited state or resonance contains a manifold of eigenstates  $|s\rangle$  rather than an individual eigenstate, which form a Lorentzian profile of width  $\Delta\omega_n$ . If a molecule is excited at  $t = 0$  by a coherent pulse of width  $\Delta\omega_p$ , which is much higher than the separation between two distinct molecular resonances,  $\Delta\omega_{21}$  (see Figure 83a), then the resulting wave function of the excited state is a coherent superposition of these two resonance states, that is,  $|\Psi(0)\rangle = a_1|\alpha_1\rangle + a_2|\alpha_2\rangle$ . At the same time, each molecular resonance state is a nonstationary superposition of eigenstates  $|\alpha_n\rangle = \sum_s^{\Delta\omega_n} C_s|s\rangle$ , which decays radiatively to  $|g\rangle$  or nonradiatively through vibronic relaxation within its manifold of molecular states of width  $\Delta\omega_n$ . The superposition of the two radiative transitions associated with these resonances represents a time-dependent pattern of constructive and destructive interference, which oscillates with frequency  $\Delta\omega_{21}$ . Thus, the resulting decay kinetics of the emission is modulated by a quantum beat oscillatory pattern. In the case when the molecule possesses more than two resonances that are excited coherently, the beat pattern becomes more complicated.

Quantum beats of the exciton states have been observed experimentally and theoretically as periodic oscillations of the intensity in time-resolved luminescence of molecules due to their structural photoisomerization,<sup>691</sup> photoisomerization with an intramolecular proton transfer (the keto and enol forms),<sup>692</sup> in short-lived radicals with spin-correlated pairs,<sup>693</sup> in acetaldehyde due to the coherent excitation of  $S_1-T_1$  eigenstates,<sup>694</sup> in *trans*-polyacetylene oligomers due to dynamic interaction of two resonant states of the molecule with their decay to a common third state of the molecule,<sup>695</sup> in crystalline tetracene due to spin coherence of the correlated triplet pairs, which is sensitive to the magnitude and direction of the applied magnetic field,<sup>696</sup> or in rubrene single crystal under magnetic field due to singlet fission that can undergo geminate recombination back to the singlet state,<sup>697</sup> to mention just a few.

Burdett and Bardeen reported observation of quantum beats in delayed fluorescence of crystalline tetracene due to triplet pair superposition produced by direct singlet fission via a direct coupling of the initially excited singlet exciton to the triplet pair manifold (Figure 83b). Although no electronic coherence between the singlet and triplet pair states exists, a coherent superposition of three zero-field triplet pair states,  $|xx\rangle$ ,  $|yy\rangle$ , and  $|zz\rangle$ , with overall singlet character was achieved by the rapid singlet decay time of  $\sim 200$  ps in single crystals of tetracene, leading to the impulsive coherent-like population transfer. This superposition of the three states produced three quantum beat frequencies observed at 1.06, 1.82, and 2.92 GHz.<sup>698,699</sup>

#### 5.4.2. Decay via Nonradiative Recombination.

**5.4.2.1. Vibronic Assisted Relaxation.** When the exciton concentration is low, the major mechanism responsible for the nonradiative exciton decay is due to the exciton–vibration coupling along with the high density of energy levels in the vibrational ladder through which an electron can relax down

from the excited to the ground state (Figure 84). This process can be considered as a resonance energy transfer from the lowest

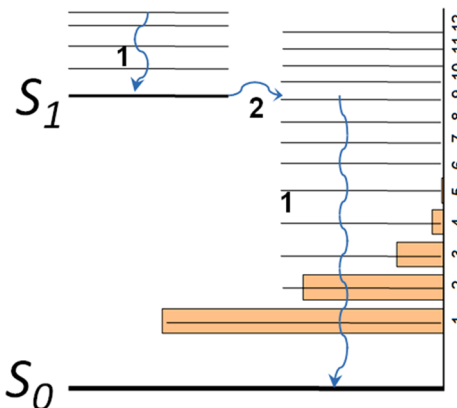


**Figure 84.** Mechanism of nonradiative decay of excited electron to the ground state in an isolated molecule: (1) vibrational relaxation of the hot exciton; (2) transition from lowest vibrational level of the excited state to a high vibrational level of the ground state via overlap of the wave functions of the levels. Poisson probability of the vibronic excitations with Huang–Rhys factor  $S = 1$  in eq 37 is shown by horizontal yellow bars. Although the spacing between adjacent vibronic levels decreases with increasing quantum number because of anharmonicity in the vibration and the density of the vibronic levels increases accordingly, the probability of the vibronic excitations at high quantum numbers decreases dramatically.

vibrational level of the excited state to a high vibrational level of the ground state.<sup>700</sup> Such a nonradiative exciton decay, which in fact corresponds to internal conversion, is accompanied by emission of phonons, which dissipate the excitation energy into heat.

The probability of such a relaxation, however, is largely dependent on the process order, that is, how many phonons can be emitted simultaneously, and therefore it decreases with increasing HOMO–LUMO gap, because it requires increased amount of emitted phonons, whereas the transition probability decreases dramatically as a function of the number of phonons simultaneously emitted in the optical transition.<sup>701</sup> The expression for such a transition probability, which is generally referred to as the zero temperature Franck–Condon factor, is proportional to the integral square that describes the overlap of wave functions of vibrational ground state  $m = 0$  and different vibrational final states  $N$ , which is described by Poisson distribution for emission of  $N$  phonons around an average of  $S$ , where  $S$  is the parameter characterizing the strength of lattice relaxation (Huang–Rhys factor or the average number of emitted phonons), as follows:<sup>702,703</sup>

$$F_N^0 = \left| \int \Psi_0^* \Psi_N \, dQ \right|^2 = \frac{e^{-S} S^N}{N!} \quad (38)$$

It was a discussion in the literature which vibrations are responsible for the nonradiative relaxation of the exciton if the band gap is well above the energy of phonons, while multiphonon processes have a decreasing probability. It is accepted that high-frequency vibrations with participation of light atoms like hydrogen are predominant in the nonradiative transitions in contrast to the radiative transitions where low-frequency vibrations prevail.<sup>702</sup> It is clear that a lower amount of high-frequency phonons in a multiphonon process releasing certain energy can be taken compared to the low-frequency

phonons. At the same time, the upper rates for nonradiative decay for conjugated molecules such as chrysene, 1,2-benzanthracene, perylene, coronene, naphthalene, anthracene, phenanthrene, pyrene, and triphenylene were estimated to be in the range of  $10^{10}$  to  $10^{13} \text{ s}^{-1}$ , that is, comparable to the frequencies of low-energy vibrations ( $\leq 300 \text{ cm}^{-1}$ ).<sup>704</sup>

This trend of decreasing nonradiative probability with increasing band gap is translated to the energy gap law,<sup>704</sup> which describes the rate of intramolecular nonradiative transition,  $k_{\text{NR}}$ , between two weakly coupled electronic states, that is, LUMO and HOMO:

$$k_{\text{NR}} \approx \frac{\sqrt{2\pi} C^2}{\hbar \sqrt{\hbar \omega_M \Delta E}} \exp\left(-\frac{\Delta E}{\hbar \omega_M} \left(\ln\left(\frac{\Delta E}{l \lambda_M}\right) - 1\right)\right) \quad (39)$$

where  $C$  is an effective electronic coupling constant,  $\omega_M$  is the highest energy vibrational mode involved in the nonradiative transition,  $\Delta E$  is the HOMO–LUMO energy band,  $\lambda_M$  is the reorganization energy of the promoting modes, and  $l$  is the number of vibrational modes that induce the nonradiative transition. For an intermolecular CT exciton, there is an analogue of the energy gap law that states that the nonradiative recombination rate of the CT exciton at an organic heterojunction increases exponentially with decreasing energy difference between the LUMO of the acceptor and the HOMO of the donor.<sup>705</sup>

In addition to the energy gap law, for effective nonradiative decay, the density of the intramolecular vibrational states around the HOMO should be large enough. Translating this to the energetic criterion means that the interaction energy has to be much larger than the energy difference between consecutive states.<sup>471</sup> The estimates give a critical number of intramolecular vibrations to be  $\sim 100$  states per  $\text{cm}^{-1}$ , that is, the vibronic energy separation  $\ll 0.1 \text{ cm}^{-1}$ , which is realized in polyatomic molecules with a minimum critical size of five atoms characterized by equal vibrational frequencies of  $1000 \text{ cm}^{-1}$ .<sup>471</sup> From this estimate, it follows that in large conjugated molecules nonradiative transitions become dominant. This is related to the exciton lifetime and the fluorescence QY as well, as both the measured averaged lifetime of singlet excitons,  $\tau_{\text{AVE}}$ , and emission QY are determined by both radiative and nonradiative photophysical processes, according to the following equations:<sup>706</sup>

$$\tau_{\text{AVE}} = 1/(k_R + k_{\text{NR}}) \quad (40a)$$

$$\text{QY} = k_R/(k_R + k_{\text{NR}}) \quad (40b)$$

where  $k_R$  is the rate of radiative decay and  $k_{\text{NR}}$  is the rate of nonradiative recombination decay. Then, the dominant nonradiative processes lead to shorter lifetime of excitons and poor QY of luminescence in longer molecular complexes. It is well-known that NIR dyes, having both increasing molecular size and decreasing band gap compared to the other organic dyes, suffer from low quantum yield of PL, being several percent at best.<sup>707</sup> The only exclusion is known for tricarbocyanine dyes, which demonstrate QY up to 15% with emission wavelength above 830 nm.<sup>580</sup> Combination of eqs 39 and 40a leads to the conclusion that the measured lifetime of the exciton should increase with increasing band gap of the molecule. This was particularly demonstrated experimentally by Dimitrov et al. by comparing 16 conjugated polymers with different band gaps<sup>708</sup> (Figure 85).

Internal reorganization energy is also a key factor that facilitates nonradiative recombination decay and affects photo-

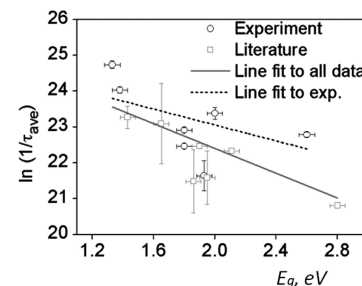


**Figure 85.** Natural logarithm of the rate of singlet exciton decay plotted as a function of optical bandgap for 16 conjugated polymer films. The broken line is the best fit straight line to experimentally determined rates of exciton decay for seven polymer films obtained by ultrafast transient absorption spectroscopy; the solid line is the best fit straight line to all data points (experimental and literature). Reproduced from ref 708 with permission. Copyright 2016 the Authors (licensee MDPI, Basel, Switzerland) under the Creative Commons Attribution License.

luminescence quantum yield (Figure 86a). However, the magnitude of reorganization energy can be suppressed in large aggregates. This is because the same reorganization energy is partitioned among  $N$  molecules in an aggregate; therefore, the reorganization energy per each molecule decreases by a factor of

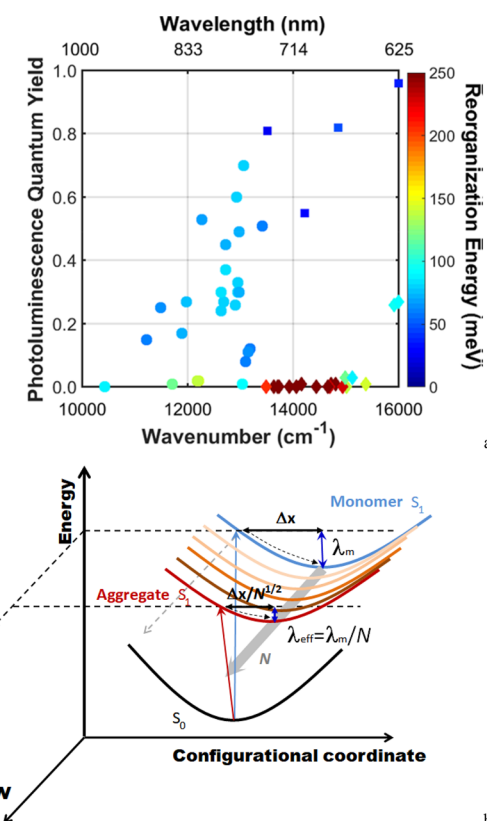


**Figure 86.** (a) Experimental emission wavelength, photoluminescence quantum yield, and calculated internal reorganization energy of a collection of 45 Pt(II) complexes. Reproduced from ref 710. Copyright 2019 American Chemical Society. (b) Illustration of the mechanism of the partitioning of reorganization energy by exciton delocalization, where the reorganization energy of monomer  $\lambda_M$  is partitioned into multiple  $N$  excitation modes of the aggregate state. Several excitation curves with increasing  $N$  are shown, whereas excitation into an aggregate state does not change the configurational coordinate. Redrawn from ref 709.

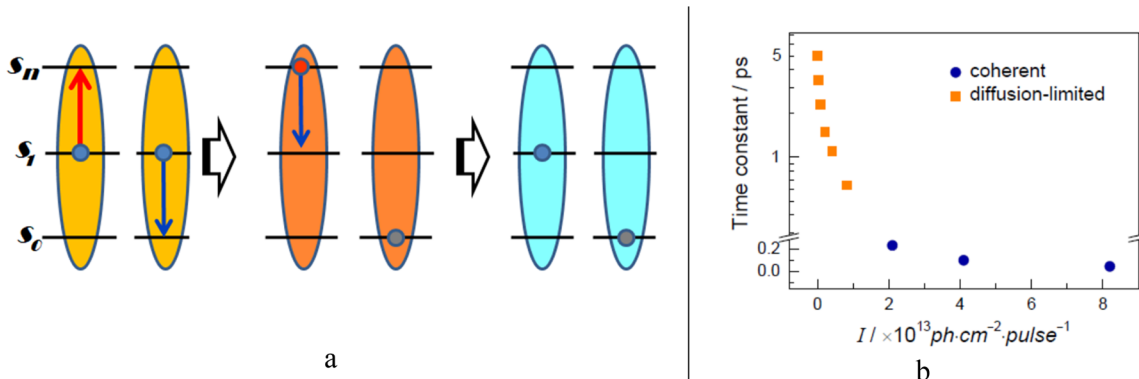


**Figure 87.** (a) Energy level scheme demonstrating exciton–exciton (singlet–singlet) annihilation. Shown are the ground state ( $S_0$ ), the first excited state ( $S_1$ ), and a higher excited state ( $S_n$ ) of a pair of molecules (the blue, red, and gray spheres indicate the degree of excitation): (left) both molecules are in their first excited state; (center) de-excitation of the right molecule and hot exciton formation on the left molecule due to exciton fusion; (right) internal conversion process moves the left molecule into its first excited state (exciton annihilation). Exciton–exciton fission is highlighted if one moves from the central part to the left part. (b) Dependence of the time constants of the coherent (blue circle) and diffusion-limited (orange square) EEA on the excitation fluence  $I$ . Reproduced from ref 716. Copyright 2018 American Chemical Society.

$N$  (Figure 86b). The related analogue for better understanding is the displacement of a bundle of  $N$  parallel coupled springs, which is less by a factor  $N$  compared to an isolated spring under the same applied force. Thus, the suppressed probability of the excited states at low vibrational levels in an aggregate can improve QY of radiative emission. Recently, an exciton–vibration decoupling strategy has been demonstrated in order to overcome the energy gap law and suppress nonradiative losses in OLEDs. This strategy employs exciton delocalization in aggregates of Pt(II) molecular complexes to decouple the exciton band from highly vibrational ladders in the  $S_0$  ground state, which leads to substantial enhancements in the photoluminescence quantum yield of the emitters.<sup>709</sup> This strategy allowed Wei et al. to achieve emission in the NIR region at  $\sim 930$  nm with a quantum yield of 5–12% and high external quantum efficiency up to 2.14% in an NIR OLED.

**5.4.2.2. Exciton–Exciton Annihilation.** Exciton–exciton annihilation (EEA) is a bimolecular process that depends on concentration of excitons in the medium and requires high excitation intensities. EEA usually represents a two-step process (Figure 87a). First, two spatially close excitons in the  $S_1$ -state give rise to the fusion process, which creates a higher excited  $S_n$ -state ( $n > 1$ ) at one molecule and leaves behind the other molecule in the  $S_0$  ground state. In a second step, an ultrafast internal conversion process brings the molecule that is in the higher excited  $S_n$ -state back to the  $S_1$ -state followed by its relaxation to the ground state or by production of polaron pairs.<sup>711</sup>

Two regimes of EEA can be distinguished, the diffusion-limited and coherent types. The first one occurs when the excitons are generated at spatially separated chromophores or domains and need a diffusion to meet each other. Therefore, relatively high exciton concentration is needed to provide the average interexciton distance comparable to or less than the diffusion length of the exciton. Decay dynamics of exciton density  $n(t)$  due to the diffusion-limited EEA is described by eq 41:

$$\frac{dn(t)}{dt} = -\frac{n(t)}{\tau_1} - (1/2)\gamma(t)n^2(t) \quad (41)$$

where the annihilation rate  $\gamma(t)$  is dependent on dimensionality of the system and in case of 1D migration of excitons is a

function of the diffusion constant  $D$ , the lattice constant  $a$ , and the molecule density  $N_0$ :<sup>712</sup>

$$\gamma(t) = \frac{1}{aN_0} \sqrt{8D/\pi t} \quad (42)$$

In the case of 3D migration of excitons, the annihilation rate should be written as follows:<sup>713</sup>

$$\gamma(t) = 8\pi DR \left( 1 + \frac{R}{\sqrt{2\pi Dt}} \right) \quad (43)$$

where  $R$  is the effective interaction radius of singlet excitons.

The coherent regime of EEA occurs when excitons are generated in the same coherent domain (for example, in J-aggregates) or within a cluster like carbon nanotube<sup>714</sup> or graphene nanoribbon.<sup>715</sup> The time scales of the coherent and incoherent regimes are different. Whereas diffusion-limited EEA has typical time constants on the order of picoseconds, coherent EEA proceeds on a sub-picosecond time scale (Figure 87b). Due to the ultrafast dynamics, determination of the coherent EEA regime experimentally is difficult and may experience artifacts;<sup>716</sup> however, it cannot be attributed to the first-order dynamics, as it depends on the simultaneous absorption of two photons; thus, it is a nonlinear optical process and the probability of coherent EEA should be proportional to the square of the light intensity. For example, the coherent EEA regime in J-aggregates of organic dyes starts with pump intensities above  $10^{13}$  photons/ $\text{cm}^2$  per pulse, which is notably higher than the pump fluence of  $10^{11}$  photons/ $\text{cm}^2$  per pulse necessary for diffusion-limited EEA.<sup>716</sup>

Both coherent and diffusion-limited EEA can coexist in the same system. With increasing excitation intensity, coherent EEA becomes more prominent as a consequence of the increased probability to excite coherent excitons belonging to the same domain. However, due to interactions with phonons, exciton coherence length rapidly decreases; as a result, the diffusion-limited annihilation process starts to dominate.<sup>714</sup> It was reported that exciton–phonon interaction in the coherent EEA regime facilitates formation of self-trapped excitons in J-aggregates as coherent EEA produces many more phonons in a short time, which induces a trapped potential well on the excited-state potential energy surface.<sup>716</sup> On the other hand, formation of hot excitons in MEH-PPV films promotes

diffusion-limited EEA as hot excitons have a higher mobility than thermalized (i.e., relaxed to the lowest excited state) excitons.<sup>717</sup>

Coherent EEA strongly depends on the phase relation of the excitons, which originates from the dipole relation of interacting molecules in an aggregate. Tempelaar et al. demonstrated that the sign of dipole–dipole couplings between molecules performs a crucial role in the annihilation rate between singlet excitons through interference of the phase relations of the two-exciton wave functions.<sup>718</sup> In H-aggregates with positive couplings, this interference was shown to be destructive and results in a significantly suppressed annihilation rate. For J-aggregates, where couplings are negative, no such coherent suppression occurs. Overall, the annihilation rates for typical J- and H-aggregates at room temperature were found to differ by a factor of ~3 (Figure 88), while at low temperatures, this difference reaches 1 order of magnitude due to improved ordering in aggregates.<sup>718</sup>

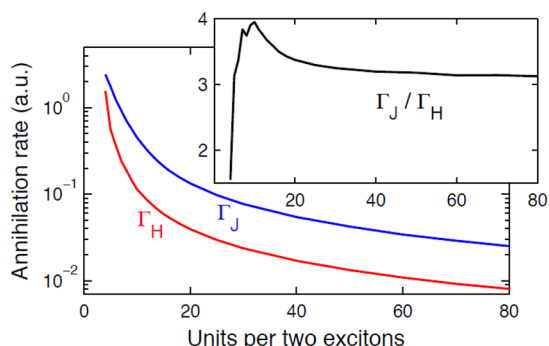


**Figure 88.** Annihilation rates  $\Gamma_J$  and  $\Gamma_H$  calculated for linear J- and H-aggregates, respectively, as a function of the number of molecular units per two excitons. Inset shows the ratio between the rates. Reproduced from ref 718. Copyright 2017 American Chemical Society.

**5.4.3. Decay via Exciton Dissociation.** Exciton dissociation in low-dimensional organic materials is normally hindered due to the relatively small exciton size, which saturates at around 0.7 nm for one-dimensional molecules with a size longer than ~4 nm, and also due to relatively high Coulomb barrier ( $E_b$ ) for charge separation with a lower limit of the exciton binding energy,  $E_b = 0.3$  eV.<sup>74</sup> Benatto et al. theoretically determined that the Coulomb barrier after photoexcitation somewhat decreases for non-fullerene but increases for fullerene acceptors (Figure 89); this helps to explain the delayed charge generation measured in some acceptor systems.<sup>719</sup> The Coulomb barrier for charge separation substantially decreases in systems of higher

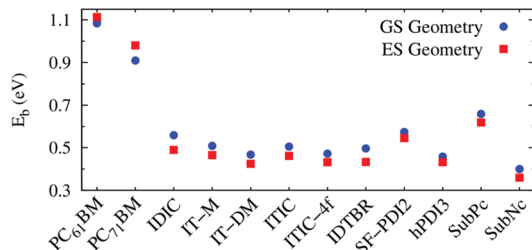


**Figure 89.** Exciton binding energy for fullerene and non-fullerene acceptors in the ground state (GS) and excited state (ES) geometry obtained by first-principle calculations. Reproduced with permission from ref 719. Copyright 2019 Royal Society of Chemistry.

dimensions<sup>720</sup> or in an assembly of coupled molecules;<sup>719</sup> therefore, higher-dimensional organic semiconductors have inherent advantages for charge separation, which can be already seen for 3D organic semiconductors like C<sub>60</sub>, which plays an important role in OPV cells.

CS leads to formation of free carriers (FCs); however, this process normally proceeds in two stages. In the first stage, the electron and hole are separated at the D–A interface, but they still are bound by weak electrostatic interaction and represent a geminate pair. The binding energy of this pair is lower compared to the exciton in the homogeneous medium by the difference in electron affinities of the contacting materials, that is, D and A. At this stage, the geminate pair is still capable of reverse charge recombination. Below I will refer to time constant of the CS process just at this stage. At the second stage, the electron and hole become completely unbound and diffuse independently of each other. Of particular importance is the relation between time constants that characterize the charge transfer or charge separation and the reverse charge recombination processes. When the latter is much longer than the former one, then application of such materials in solar cells is feasible. CS time constants vary from sub-picosecond to hundreds of picoseconds and even nanosecond time scales, whereas CR varies from picoseconds to milliseconds (Table 2). The CS rate strongly depends on the electronic coupling between donor and acceptor moieties, which is responsible for electronic communication between them, is often controlled by the D–A distance, and proceeds by orders of magnitude faster between donor and acceptor moieties if they are on the same molecule than on different molecules. An elegant way of switching of an intramolecular charge transfer to the intermolecular one was shown to occur through excimer formation in self-assembled donor–acceptor dyads of a triphenylamine–oligothiophene conjugated unit (TPA) as donor and a perylenemonoimide unit (PMI) as acceptor.<sup>721</sup> In this case, the difference between intra- and intermolecular CS rates constitutes 2 orders of magnitude (Table 2).

Other factors that facilitate CS rate include conformational change of the donor polymer chain and exciton delocalization. Similar to the above example, exciton delocalization over many polymer units in ordered packed chains impedes exciton dissociation at the interface with an acceptor, whereas exciton localized near the interface in the disordered polymer chain facilitates it.<sup>734–740</sup> For example, much faster decay of excitons due to CS was found in disordered as-prepared P3HT/PCBM films cast from chloroform as compared to the annealed film or films prepared from solvents with high boiling temperatures, resulting in about 74% and 50% of excitons dissociated at the interfaces of P3HT/PCBM bulk heterojunction blends with disordered and ordered arrangement of the polymer chains, respectively.<sup>402</sup> Nonuniform packing of polymers at donor/acceptor interfaces facilitates exciton dissociation even in the “cold” charge-transfer state, that is, after vibronic relaxation on a time scale of 200 fs,<sup>741</sup> contrary to a few tens of femtoseconds typical for dissociation from the hot CT state (see below).

At the same time, symmetry breaking or disorder leads to delayed charge transfer between the same molecules. For example, in dimers of 1,7-bis(pyrrolidin-1'-yl)-perylene-3,4:9,10-bis(dicarboximide) (SPDI) with cofacial ordering, an intradimer electron transfer occurs with  $\tau = 0.17$  ps in toluene, whereas for linear dimers where the chromophores are on the same line but their molecular planes are perpendicular to each

**Table 2. Dynamics of Exciton Dissociation in Different Donor–Acceptor Pairs<sup>a</sup>**

donor/acceptor pair	lifetime of donor fluorescence	time constant of CS	time constant of CR (lifetime of CT state)	character of CT	ref
MDMO-PPV/PCBM	0.36 ns	45 fs	~1 $\mu$ s	intermolecular	722
regioregular P3HT/PCBM (1:1) before/after annealing	0.3 ns	<100 fs* (50%); 6 ps/8 ps (50%)	500 ps/250 ps (33%/24%); ~1 ms (67%/76%)	intermolecular	723
regiorandom P3HT/PCBM (1:1)		<100 fs (65%); ~200 fs (35%)	~800 ps (70%); ~1 ms (30%)	intermolecular	723
regioregular P3HT film (spin-coated from chlorophorm): chain/chain		~500 fs* (57%); ~12 ps (43%)	~500 fs (45%); ~15 ps (40%); >100 ps (15%)	intermolecular	402
zinc- <i>meso</i> -tetrasulfonatophenyl-porphyrin ( $ZnTPPS^{4-}$ )/methyl viologen $MV^{2+}$	1.3 ps*	<200 fs*	0.8 ps	intermolecular	724
zinc porphyrin ( $ZnTTP$ )/ $ZnTTP$ -L-Ru(bpy) <sub>3</sub> complex	1.4 ps* (ethanol)	~1.6 ps*; ~100 ps	15 ps	intermolecular	725
tricarbocyanine NIR dye/SWCNT	0.5 ns	1.5 ps*	25 ps	intermolecular	240
1,7-bis(pyrrolidin-1'-yl)-perylene-3,4:9,10-bis(dicarbox imide) (SPDI): SPDI/SPDI cofacial SPDI <sub>2</sub> dimer; linear SPDI <sub>2</sub> dimer	3.3 ns	0.17 ps; 55 ps	222 ps; 99 ps	intermolecular	726
Tricarbocyanine dye: J-aggregate/H-aggregate	95 ps	~18 ps	2.8 ns	intermolecular	449
heptamethine dye covalently linked to fullerene $C_{60}$	1.9 ns	3 ps*; 12 ps	400 ps	intramolecular	727
Zn porphyrin ( $ZnTTP$ ) covalently linked to $C_{60}$ : $ZnTTP$ - $C_{60}$	1.8 ns (ethanol)	~100 ps	500 ps (up to ~400 ns with the longer linker)	intramolecular	728
hexadodecyl-substituted zinc phthalocyanine ( $ZnPc$ ) covalently linked through a flexible spacer (x) to fullerene: $ZnPc$ -x- $C_{60}$	3.2 ns	7.4 ps	2.2 ns	intramolecular	729
3,5-dimethyl-4-(9-anthracenyl)-julolidine (DMJ) covalently linked to naphthalene-1,8:4,5-bis(dicarboximide) (NI): DMJ-NI		6 ps	158 ps	intramolecular	476
DMJ linked to NI via a phenyl bridge (Ph): DMJ-Ph-NI		10 ps	10 ns	intramolecular	476
triphenylamine–oligothiophene (TPA) covalently linked to perylenemono-imide (PMI): TPA-PMI monomer		1 ps	30 ps	intramolecular	721
TPA-PMI···PMI-TPA dimer	3.1 ns	400 ps	4.3 $\mu$ s	intermolecular	721
phenothiazine (PT) covalently linked to 1,6-bis(methoxy phenylethynyl)pyrene (BPEP): BPEP-PT dyad	1.3 ns (emission of BPEP)	157 ps	30 $\mu$ s	intramolecular	730
$Rh^{III}(dcb)_2$ -(BL)- $Ru^{II}(dmp)_2$ dyad/TiO <sub>2</sub>	15 ns (68%) and 120 ns (32%)	~30 ns	1 $\mu$ s to 1 ms	intermolecular	731
diphenyldiaminopolyene (DPAP) covalently linked to $C_{60}$ : DPAP- $C_{60}$ dyad	1.8 ns	9 ps	~1 ms	intramolecular	732
triphenylamine donor–Ir(III) bis-terpyridine complex–naphthalene bisimide acceptor (D-Ir-A) triad	0.45 ns	two-step CT: $D^* \rightarrow Ir^- \rightarrow A$ (20 ps); $D^* \rightarrow Ir^- \rightarrow A^-$ (400 ps)	120 $\mu$ s	intramolecular	733

<sup>a</sup>Lifetimes with an asterisk (\*) correspond to PL and CS which occur from the hot excited states.

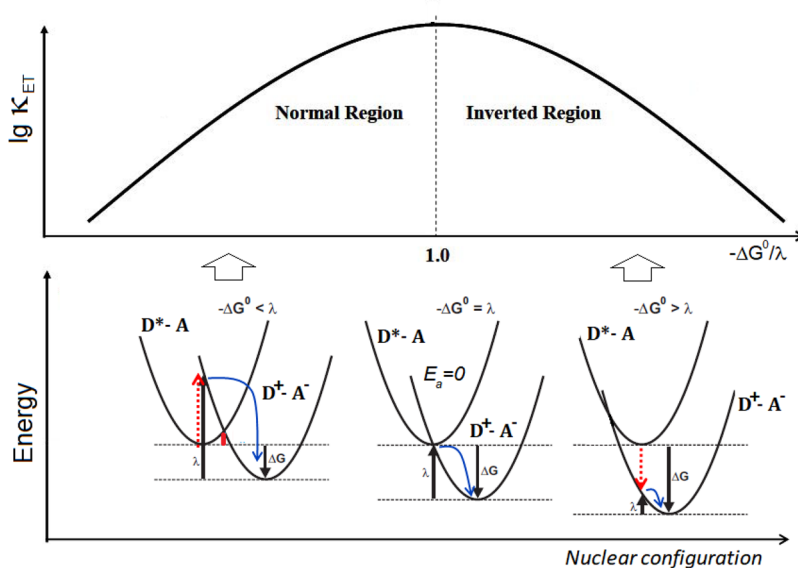


**Figure 90.** Marcus theory diagram. (top) Plot of  $lg(k_{ET})$  vs  $-\Delta G^\circ/\lambda$  as predicted by Marcus theory. (bottom) Potential energy surfaces for electron transfer from an excited donor ( $D^*$ ) to an acceptor (A) in the normal, activationless, and inverted regions. Red bar shows the barrier height in the normal region; red and blue arrows show the excitation and transfer of electron, respectively.

other, photoinduced electron transfer occurs only in more polar solvents with  $\tau = 55$  ps<sup>726</sup> (Table 2).

Understanding of factors that promote long-lived charge separation states is poor. In addition to the above-mentioned electronic coupling, the reorganization energy and the Marcus

inverted region have been identified recently as reasonable factors influencing the CR rates.<sup>742</sup> The effect of reorganization energy on the extension of lifetime of the intramolecular charge-transfer state of 9-mesityl-10-methylacridinium ion ( $\text{MesAcr}^+$ ) by its encapsulation in porous frameworks has been shown by Garcia and Kowalczyk.<sup>743</sup> Since reorganization energy includes both molecular structure reorganization upon electron transfer and solvent shell reorganization, the reduced reorganization energy of  $\text{MesAcr}^+$  in solvent-free mesoporous substrate leads to increasing activation barrier, which prevents excited-state charge recombination.

Exciton dissociation in the Marcus inverted region has been rarely achievable despite its theoretical prediction. According to the Marcus theory,<sup>744</sup> the rate of nonadiabatic electron transfer can be described by the following semiclassical equation:

$$k_{\text{ET}} = \sqrt{\frac{4\pi^3}{h^2\lambda k_B T}} H_{\text{AB}}^2 \exp\left(-\frac{(\lambda + \Delta G^\circ)^2}{4\lambda k_B T}\right) \quad (44)$$

where  $H_{\text{AB}}^2$  is the electronic coupling between donor and acceptor,  $\lambda$  is the reorganization energy, and  $\Delta G^\circ$  is the Gibbs free energy, which is also called a driving force for CT as it corresponds to the difference between ionization potential of the donor and electron affinity of the acceptor and therefore should be negative in order to drive an electron to lower energy level. According to eq 44, the exciton dissociation rate increases with the increasing driving force (which corresponds to the normal Marcus region) and achieves a maximum when it is equal to  $\lambda$  where the activation barrier for the charge transfer,  $E_a = \frac{(\lambda + \Delta G^\circ)^2}{4}$ , becomes zero. Further increase in the driving force leads to the anomalous inverted region, where the activation barrier for CT is still absent (Figure 90) but the CT rate decreases (eq 44). This anomaly just means that charge separation is extended in time, whereas the CR process is suppressed. Inverted-region electron transfer was reliably confirmed in organic radical anions,<sup>745</sup> ruthenium tris(bipyridyl)-viologen dyad,<sup>746</sup> porphyrin–fullerene dyad with parachute topology,<sup>747</sup> 1,6-bis(methoxyphenylethynyl)pyrene–phenothiazine dyad,<sup>730</sup> and recently  $\text{MesAcr}^+$  ions,<sup>743</sup> coumarin and *N,N*-dimethylaniline pair,<sup>748</sup> and a native photosynthetic protein complex under physiological conditions.<sup>749</sup>

Another strategy to prolong the lifetime of the charge separation and prevent CR is spin control of the photoexcited electron through triplet-sensitized generation of a long-lived intramolecular charge-separated excited state.<sup>750</sup> Hviid et al. showed that the lifetime of the triplet excited state at room temperature can be 5 orders of magnitude longer compared to that of the corresponding singlet CS state in an electron donor–acceptor molecule with a short distance between the donor and the acceptor.<sup>751</sup> Wilson et al. demonstrated delayed population of CT states mediated by singlet exciton fission in polycrystalline pentacene into triplet excitons, which then decay into CT states from nanosecond to microsecond time scale (Figure 91).

CT states are associated with formation of a CT exciton, which is thus an important intermediate through which a decay of photoexcitations at the donor–acceptor interface via electron–hole dissociation occurs.<sup>752</sup> Therefore, energetics and density of CT excitons are important issues in understanding geminate pair recombination and the formation of free carriers. In general, singlet CT energy levels are formed at the donor–acceptor (D–A) interface due to interaction of the D and A molecules at lower energies compared to the optical band

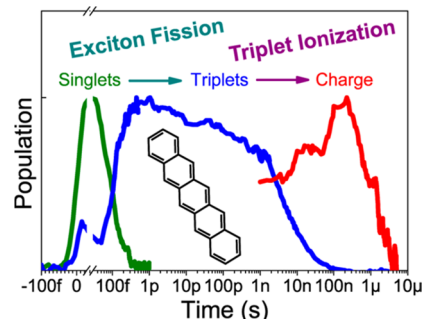


**Figure 91.** Population dynamics in a pentacene crystal after photoexcitation, leading to SF, triplet pair dissociation, and triplet exciton ionization, respectively. Reproduced from ref 629. Copyright 2013 American Chemical Society.

gaps of the individual D and A materials (Figure 92). For instance, Zheng et al. showed that there could be more than 20

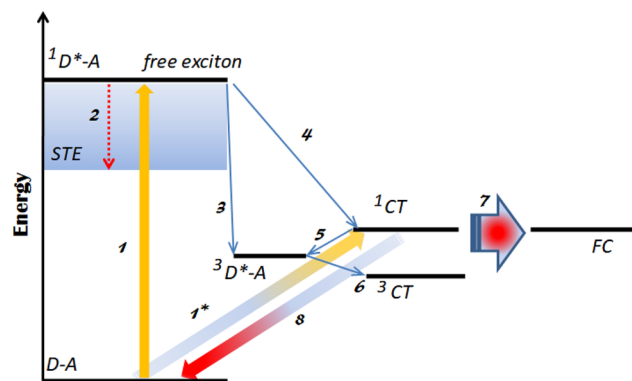


**Figure 92.** Energy diagram showing the quenching pathways involving CT states. Here, the electron donor is assumed to be the main absorber, with the excited donor states indicated by  $D^*$ . The major photophysical processes are indicated as (1) excitation of singlet exciton, which competes with (1\*) excitation of singlet charge-transfer exciton in the case when the CT state is not dark; (2) relaxation of the free singlet exciton to a self-trapped exciton (STE); (3) intersystem crossing; (4) photoinduced charge transfer with formation of a singlet geminate pair at the D–A interface; (5) population of triplet states of the donor; (6) charge transfer with formation of a triplet geminate pair at the D–A interface; (7) dissociation of the geminate pair into the free carriers (FC), that is, polarons.

intermolecular CT states in pentacene-to- $C_60$  or pentacene-to-pentacene complexes consisting of  $C_60$  and three pentacene molecules, which appear below the bright pentacene local state at 2.2 eV.<sup>753</sup> Close packing and efficient electron overlap allows formation of CT excitons in aggregates of molecules of the same type at the interface between ordered and disordered domains, driven by such factors as energetic and structural disorder<sup>754,755</sup> or the large exciton bandwidth.<sup>756</sup> CT states can be bright, resulting in red-shifted absorption and emission spectra.<sup>757</sup> But often CT exciton states are dark because the transition dipole moment from the ground state to the CT state is small in the case of relatively large separation between the donor and the acceptor,<sup>758</sup> which favors relatively long lifetimes of the CT state on the order of microseconds or more (Table 2). To attain long-lived CT states, the CT energy level should be even lower than the triplet excited state of a donor. In systems where CT exciton states are dark, relaxation of the singlet exciton through this nonradiative channel leads to decreasing QY of fluorescence. Hu

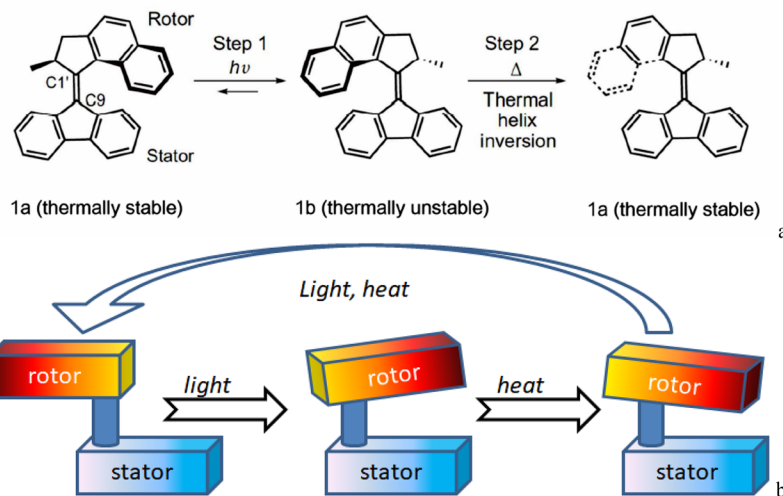


**Figure 93.** (a) Photomolecular rotor photocycle. Absorption of a photon reduces the olefinic bond order giving rise to isomerization of **1a** to yield the metastable ground state **1b**. A second thermally activated step completes the isomerization and reforms the initial ground state. The cycle is then repeated. (b) Pictorial scheme of the photoinduced motion of a molecular rotor with respect to the stator. Reproduced from ref 785. Copyright 2017 American Chemical Society.

et al. showed that through the influence on energetics of CT states by change in the dielectric constant of the environment from  $\sim 2$  to 4 the drop in QY of fluorescence of triblock P3HT-*b*-poly(*tert*-butyl acrylate)-*b*-P3HT copolymer aggregates reaches 1 order of magnitude, that is, it changes from  $\sim 30\%$  to 2–5%.<sup>759</sup> At high dielectric constant, poorly emissive CT states are energetically stabilized by lowering their energy levels, and thus they increase the driving force for quenching the excited electron, whereas at low dielectric constant, CT states have increased energy relative to the singlet exciton emissive level, thus leading to high QY of the emission. However, the decreasing fluorescence QY due to CT states was found to not be accompanied by noticeable changes in the emission decay dynamics,<sup>759</sup> which suggests that a direct formation of CT excitons competes with formation of singlet excitons and that CT states are attributed to static rather than dynamic centers of fluorescence quenching.<sup>676</sup> In this case, however, CT states cannot be considered as completely dark (Figure 92).

A specific mechanism of excitation quenching due to CT states is high delocalization of the CT exciton with a wide potential energy surface in the planarized structure of the conjugated molecule. For the planar geometry of a conjugated molecular chain, which undergoes rotation during the charge transfer, there can be a significant conical intersection of the CT state potential energy surface with the potential energy surface of the ground state. In such cases, the probability of a nonradiative pathway of the electronic transitions of the excited state to the ground state greatly increases.<sup>760</sup>

Hot (nonthermalized) excited states of the donor play an important role in exciton dissociation at the donor–acceptor heterojunction and were proposed to convert excitons directly into free charges without evolving through a bound CT state.<sup>761</sup> It has been shown that the rate of CS that proceeds from the hot excited states is about 1–2 orders of magnitude higher than the one that proceeds from the thermalized lowest excited state<sup>724,727,762</sup> (see also Table 2). The competition between charge transfer and internal conversion and vibrational relaxation, which occur on the same picosecond time scale, is remarkable. Guo et al. found that about half of polarons generated in P3HT are due to immediate dissociation of hot

excitons at the interface with an acceptor, which occurs with time constant of  $<100$  fs, while the other half is thermalized excitons owing to diffusion to the interface with a time delay of  $\sim 10$  ps.<sup>723</sup> Other than the hot excited states of a donor, Tamura and Burghardt introduced the concept of a vibronically hot CT state, which assists in overcoming the Coulomb barrier and thus promotes charge dissociation beyond this barrier.<sup>763</sup> Jalaubekov et al. showed that hot CT excitons at the phthalocyanine/fullerene interfaces are formed in  $10^{-13}$  s, followed by their relaxation to lower energies and shortening of electron–hole distances on a  $10^{-12}$  s time scale, so that this hot CT exciton cooling process and collapse of charge separation sets the fundamental time limit for competitive charge separation channels that lead to efficient photocurrent generation.<sup>764</sup>

## 6. CURRENT CHALLENGES AND FUTURE DIRECTIONS

Exciton dynamics issues not only represent academic interests but are important for the development of optoelectronic devices, where exciton generation, conversion, transport, and dissociation play key roles. These processes lead to applications in photovoltaic energy generation, controlled photochemical reactions, high-speed excitonic circuits, quantum computing, etc. In this section, we consider some examples and trends of exciton applications in various fields.

### 6.1. Light-Driven Molecular Machines

Excitons can induce mechanical motion of molecular fragments, which forms the basis of the concept of light-driven artificial molecular machines and actuators that have been actively developed during the last decades<sup>728,765,766</sup> and resulted in award of the Nobel prize in Chemistry in 2016 to Jean Pierre Sauvage, Sir James Fraser Stoddart, and Bernard (Ben) Feringa for their contributions to the design and synthesis of molecular machines.<sup>767</sup> These machines enable directional movements of molecular components upon photoexcitation.

The driving force for molecular rotary motors at nanoscale is a photochemical *cis/trans* isomerization in sterically crowded chiral alkenes. A typical molecular motor is shown in Figure 93, presenting stator and rotor parts. A photoisomerizable group in the molecular axle experiences an optically triggered clockwise rotation upon photoexcitation from the stable ground state of

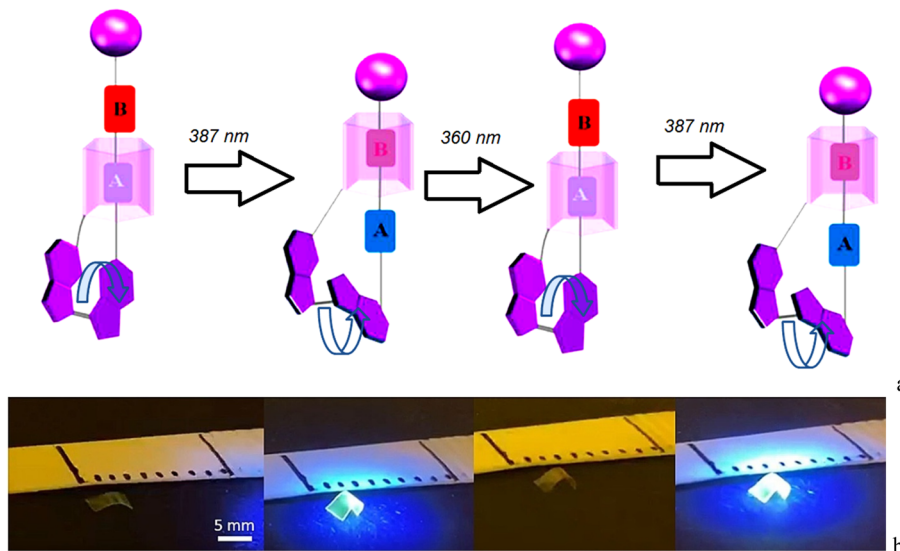


**Figure 94.** (a) Schematic presentation of the directional motion of the wheel triggered by photoisomerization of a stiff stilbene. The blue (A) and red (B) rectangles represent two localization sites of the “wheel”. Adapted with permission from ref 786. Copyright 2018 Royal Society of Chemistry. (b) Photoinduced walking of a liquid-crystal ribbon with embedded molecular rotary motors on a glass surface driven by UV light at 365 nm. Reproduced with permission from ref 779. Copyright 2021 The Authors. Published by Wiley-VCH GmbH under the terms of the Creative Commons CC BY license.

the *cis*-isomer toward an unstable excited state of the *trans*-isomer. The unstable isomer transforms to the stable form of the *trans*-isomer due to the thermal activation step, which induces a helical chirality inversion. On the other hand, photoexcitation of the stable *trans*-isomer at the other wavelength can reforms the initial ground state isomer (Figure 93).

It is noteworthy that this photoisomerization is accompanied by chirality transfer or transfer of stereoinformation, which can be used as a photocontrol of enantioselectivity in asymmetric catalysis using catalysts built with molecular motor scaffolds.<sup>768,769</sup> In this strategy, a small amount of responsive molecules is sufficient to induce changes in a larger system. Dynamic control of the helicity of polyisocyanate through terminal functionalization of the helical isocyanate polymer with a small molecular motor unit that allowed one to control the helicity of the entire polymer chain has been reported.<sup>770</sup>

Photoisomerization can be translated into both rotary and linear motions of a molecule. The rotary motion can be visualized by fluorescence microscopy through attachment of a fluorescent label to the motor arm, which was first demonstrated by Noji et al.<sup>771</sup> Direct visualization of a single molecular rotary motion allows one to determine both positional and orientational order of the motors and to separate the motion of a single molecular motor from the random Brownian motion.<sup>772</sup>

Recently developed light-driven molecular motors can undergo 360° unidirectional rotary motion due to the interplay between point and helical chirality.<sup>773</sup> A new family of light-driven molecular rotary motors that utilize the fulgide motif to perform pure unidirectional axial rotation of the rotor moiety with high quantum efficiency of  $\Phi \approx 0.55\text{--}0.68$  and ultrafast dynamics with time constant of 200–300 fs of its successive photoisomerization steps was reported.<sup>774</sup> On the other hand, a strategy was developed to decrease the rotation of light-driven molecular motors by attachment of a biphenol moiety to the rotor, which serves as a “handle” to alter the rotary behavior of the motor through noncovalent substrate binding.<sup>775</sup>

A linear motion of the molecular motor can be achieved by two subsequent photoisomerization steps that shift the molecule

over a certain distance (Figure 94). Even a more exciting perspective in this direction is opened owing to synthesis of molecular motors of the third generation, which represents a combination of two parallel motors with opposite helicity.<sup>776</sup> In these mesostructures with a pseudoasymmetry center, one rotor rotates clockwise and the other rotates anticlockwise with respect to the central aromatic core, resulting in the unidirectional rotary motion of the parallel rotors.<sup>777</sup> This particular feature was conceptually demonstrated with the nanocar where the unidirectional rotary motions of the two rotors resulted in unidirectional translation, which proved that this generation of motors can lead to particular application for locomotion and cargo transport.<sup>778</sup>

Rotary motors that allow the conversion of light energy into reversible helical motion have been designed by Hou et al.<sup>779</sup> This specific photochemically driven motion was achieved due to a dual function of the molecular motor, which acts as both chiral dopant and unidirectional rotor that amplifies molecular motion into a controlled and reversible left- or right-handed macroscopic twisting movement. Complex mechanical motions including bending, walking, and helical motion were demonstrated in a soft liquid-crystal network by combination of a set of the system properties, such as dynamic chirality, directionality of motion, and shape change of a single motor.<sup>779</sup>

A feasible strategy for the fabrication of a photodriven molecular machine operating as a “lock” was proposed by Yang et al.<sup>780</sup> Yang and coauthors used a complex of  $[\text{Ru}(\text{bpy})_2(\text{hpip})]^{2+}\text{--MV}^{2+}$  (**1**) and a host molecule of cucurbit[8]uril (CB[8]), which resembles a U-shaped conformation in aqueous solution. Upon light irradiation, two complexes **1** become reversibly locked through the formation of a  $\text{MV}^{\bullet+}$  radical dimer that is stabilized in the cavity of CB[8] with Ru complexes as blockers, while complex **1** is transformed from the U-shape to an interlocked complex conformation.

Light-driven autonomous supramolecular pumps were demonstrated by combination of specific macrocycles and nonsymmetric axles. Directional threading and dethreading of the macrocycle through the axle in these systems can be fulfilled

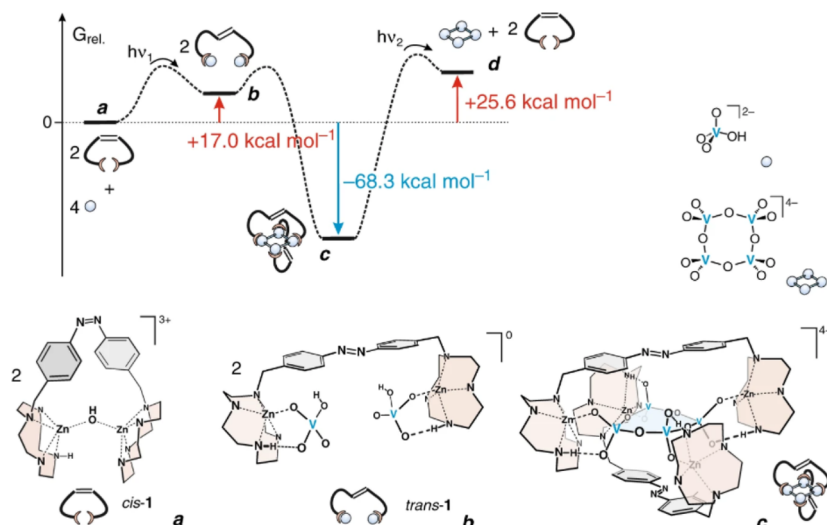


**Figure 95.** Scheme of a cyclic process of photoswitchable ligand **1** driving the condensation of monovanadate to cyclic tetravanadate. The change in the Gibbs free energy of the ligand-driven vanadate condensation is shown in the upper scheme. The different stages of the reaction path are labeled as follows: (a) initial *cis*-isomer of **1**; (b) photoinduced formation of *trans*-isomer, which capable of monovanadate capture; (c) dimerization reaction converting four monovanadates to cyclic tetravanadate; (d) photoinduced release of tetravanadate.  $h\nu_1$  and  $h\nu_2$  correspond to the excitation wavelengths of 430 nm and 365 nm, respectively. Reprinted with permission from ref 800. Copyright 2019 The Author(s) under the terms of the Creative Commons CC BY license.

either due to photoinduced oxidation/reduction processes of the macrocycle, which thus controls the electrostatic barrier when moving along the charged axle,<sup>781</sup> or due to photoisomerization of the functionalized end group of the axle, that is, azobenzene, possessing two isomer forms, one of which provides kinetic preference for threading while the other does not.<sup>782,783</sup>

An example of a spin-filtering device that can switch the spin polarization direction upon light irradiation or thermal treatment was demonstrated by Suda et al.<sup>784</sup> The rotation cycle of this device includes 4 times chirality inversion of molecular motors, induced by alternation of light illumination at 435 nm and thermal activation, resulting in 4 times switching of the spin-polarization direction of currents passing through the system. The results are beneficial to the development of a light-driven reconfigurable spin filter owing to the chiral-induced spin selectivity effect for spintronics applications.

These findings provide important steps in the development of multiresponsive light-driven molecular machinery in the near future.

## 6.2. Supramolecular Photochemistry

Light can be used as an elegant and versatile tool to control chemical reactions either through direct photoexcitation of the reagents or photoexcitation of their environment, giving rise to the concept of supramolecular photochemistry. Although this subject of research has been active during about the last three decades,<sup>785</sup> it still brings new insights into such fields as artificial photosynthesis, vision, photolithography, photodynamic therapy, etc.<sup>786</sup>

Recently, new concepts within the field of supramolecular photochemistry have been proposed. A concept of reversible covalent bond formation and scission mediated by light implies that products at thermodynamic equilibrium can be engaged in a reversible photochemical transformation of their isomers, wherein selective excitation of either product breaks the thermal equilibrium, can enhance or reduce the reactivity in a dynamic covalent reaction, and reversibly drives either bond formation or scission even under energetically and chemically disfavored

conditions.<sup>789</sup> This concept was demonstrated on the example of light-driven tautomerization cycles that reverse the reactivity of  $\text{C}=\text{O}/\text{C}=\text{N}$  electrophiles to activate substrates and remove products, respectively, induced by specific illumination wavelengths.<sup>790</sup> In this system, photoexcitation with red or blue light induced selective and nearly quantitative intermolecular bond formation or scission, respectively, even if the underlying condensation or hydrolysis equilibrium was thermodynamically disfavored. Regulation of the dynamics of the covalent system by actively and reversibly removing specific components through the light-driven  $\text{C}=\text{N}$  exchange was interpreted as a molecular and bidirectional version of a macroscopic Dean–Stark trap.<sup>790</sup>

Application of this concept allows one to realize light-driven chemical transport and mass delivery through subsequent switches of chemical bonds that bind a chemical “cargo”. A molecular walker was demonstrated, composed of two orthogonal dynamic covalent reactive functionalities, thiol and hydrazide, where the walker was capable of a directional transfer of the molecular macrocycle along a four-foothold molecular backbone due to UV-light induced photoisomerization switching.<sup>791</sup> By assembling photocontrolled DNA nanomachines embedded into artificial nanochannels, Li et al. performed selective transport of ATP biomolecules across a polymer membrane.<sup>792</sup> Under light irradiation with two different wavelengths, the Azo-DNA aptamers that decorated the nanochannels were able to capture and release the ATP molecules, thus regulating their flux through the pores. Other examples include proton transport due to photoisomerization reactions in the Janus graphene oxide membrane, which was fabricated by sequential deposition of graphene oxide (GO) nanosheets modified with photobase (BOH) and photoacid (HA) molecules.<sup>793</sup> Light induces opposite changes in local proton concentration and electric potential on the two parts of the membrane, which drives a net proton flux from the HA–GO to the BOH–GO side. These findings provide new opportunities for light-controlled manipulation of the mass transportation and separation of reagents for chemical reactions.

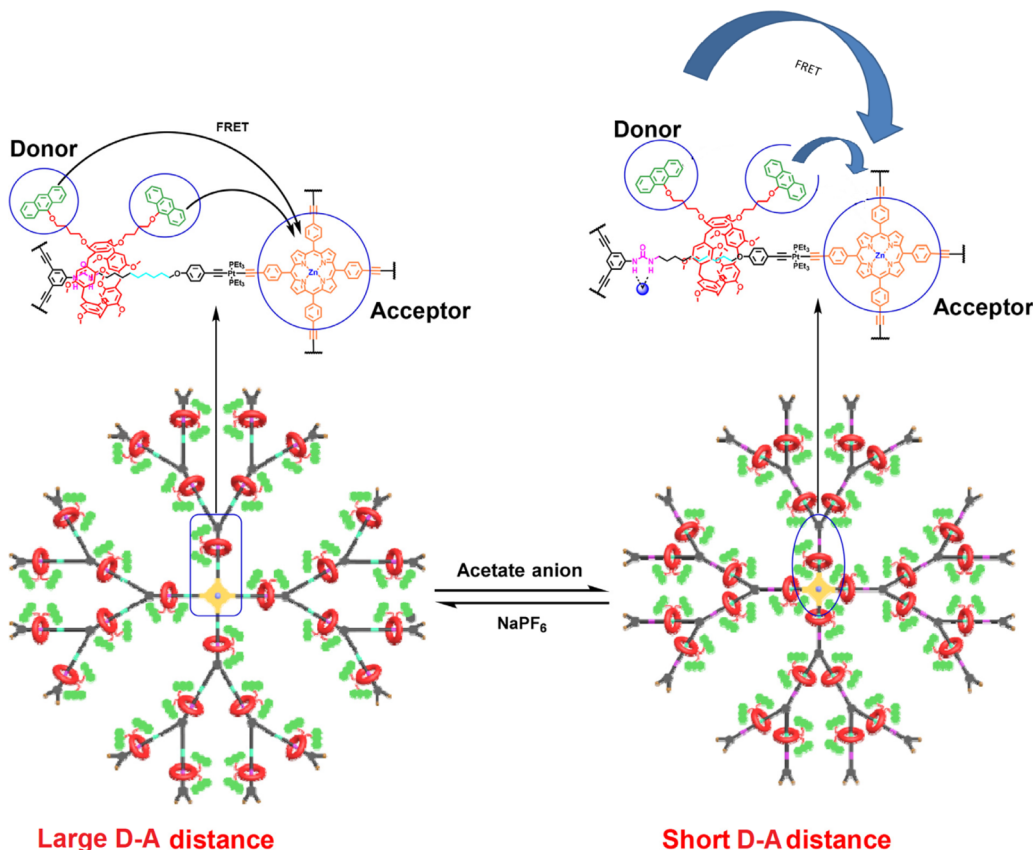


**Figure 96.** Illustration of the dynamic regulation of antenna effect in rotaxane dendrimer upon the addition or removal of external stimuli. The distance between D and A can be reversibly changed to control the energy transfer from the dendrimer antenna to the acceptor. Reprinted from ref 816 with permission from Elsevier. Copyright 2020 Elsevier.

Self-assembly and disintegration of supramolecular assemblies driven by light is another issue of supramolecular photochemistry. Examples include photoinduced fusion, disintegration, and rearrangement of azopyridine-containing diblock copolymeric vesicles,<sup>794</sup> the fusion of lipid vesicles through the use of a photosensitive surfactant containing an azobenzene moiety,<sup>795</sup> irradiation-induced fusion between giant vesicles and photoresponsive smaller vesicles containing malachite green derivative,<sup>796</sup> etc. Kundu et al. reported light-driven self-assembly of gold nanoparticles decorated with photoswitchable azobenzenes and dissolved in a nonpolar solvent of toluene.<sup>797</sup> The Z-isomer form of the molecules facilitated their aggregation due to the entropically favored release of the nonpolar solvent and opened polar groups of the Z-isomer, which resulted in ordered nanoparticle self-assembly; however, irradiation with blue light induced a ring-closing reaction that yielded less polar E-isomers, which led to spontaneous disassembly in the nonpolar solvent to form the initial individual nanoparticles.<sup>797</sup> This concept of successive light-induced self-assembly and disintegration of supramolecular compounds was realized in “click–photo–unclick” chemistry that gained important application in release of drugs or bioactive molecules driven in the tissue using low energy irradiation.<sup>798,799</sup>

Artificial “molecular assemblers” performing “mechanosynthesis” via photoexcitation were proposed as a new paradigm in chemistry and nanofabrication by Sell et al., who designed a simple nonproteinogenic machine-type molecule that drives an endergonic reaction triggered by light as the energy source resulting in condensation of vanadate to cyclic tetravanadate.<sup>800</sup>

The stages of this reaction include photoinduced *cis*–*trans* isomerization of the “molecular assembler”, followed by capture of monovanadate by the *trans*-isomer of the assembler and dimerization reaction (Figure 95). Subsequent irradiation with UV light leads to conversion of the ligands to the nonbinding *cis*-configuration with the product being released, which then hydrolyzes instantly to monovanadate.<sup>800</sup>

The term “analytical supramolecular chemistry” has been recently introduced in the field of photochemical sensors, where control of chemical sensing is realized using excited states of a supramolecular complex consisting of analyte, receptor, and reporter.<sup>801,802</sup> Colorimetric and fluorimetric chemosensors can utilize different properties of exciton dynamics, such as FRET, TADF, AIE, photon upconversion, photoinduced electron transfer, intramolecular and twisted intramolecular charge transfer, and ESIPT, which are useful to enhance sensitivity and selectivity of the sensor. In this concept, the sensing itself, that is, the formation of a supramolecular analyte–receptor complex, is accompanied by signaling through colorimetric changes or photon emission either directly by the receptor or by a reporter attached to the receptor.<sup>802</sup>

### 6.3. Light Harvesting and Photovoltaics

Manipulation with excitons for controlling light harvesting has been a subject of increasing interest in the last decades. Such a manipulation can be realized via directional transfer to the target donor–acceptor interface, multiple exciton generation, exciton energy upconversion, etc.

Multiplication of the exciton generation facilitates light harvesting and serves to improve efficiency of organic photo-

voltaic (OPV) cells. Different strategies are being undertaken in this direction; among them are the use of more effective acceptor absorbers, additional light absorbers, and luminescent concentrators. Effective acceptor absorbers in the form of non-fullerene acceptors (NFAs) recently replaced the fullerene-based ones in OPV cells. Compared to fullerene derivatives, NFAs show intense absorption in complementary spectral regions, that is, in the range of 400–810 nm, and have tunable energy levels, much higher absorption coefficient on the order of  $10^5 \text{ M}^{-1} \text{ cm}^{-1}$ ,<sup>803</sup> good morphological stability, and surprisingly long exciton diffusion lengths in the range of 20–47 nm.<sup>804</sup> Moreover, NFAs possess remarkably small exciton binding energies of 0.11–0.15 eV<sup>805</sup> and increased delocalization of electron wave functions at donor/acceptor interfaces that significantly reduce the Coulomb attraction between interfacial electron–hole pairs.<sup>806</sup> As a result, power conversion efficiency of NFA-based OPV cells recently reached the values over 18%,<sup>807–809</sup> and strategies to further boost it to over 20% have been developed.<sup>810</sup>

Strong broadband light absorption and scattering can be achieved due to addition of black phosphorus quantum dot (BPQD) absorbers to OPV cells. Liu et al. showed that addition of only 0.055 wt % BPQDs relative to the polymer donors in the OPV cell leads to dramatic improvement of device efficiencies by more than 10% compared to the control BPQD-free device. Here, the main contribution to the improvement was a strong broadband light absorption and scattering due to the BPQDs.<sup>811</sup>

Recently, luminescent solar concentrators have been applied to emerging solar cells, such as third-generation PV technologies and low-cost OPV cells.<sup>812</sup> An antenna concept was developed to obtain high light absorption without noticeable reabsorption or escape-cone losses.<sup>813</sup> In this approach, called funneling diffuse-light redirection (FunDiLight), an excess of randomly oriented pigments collects light from any direction while funneling it to the individual acceptors, which have identical orientations in a stretched polymer matrix and therefore emit ~90% of photons into angles suitable for total internal reflection, thus waveguiding the photons to the desired energy converters. The donor-pool energy funneling and donor–acceptor exciton transfer were found to occur within ~20 ps to hundreds of picoseconds, with emission quantum efficiencies of >80% and single-foil reabsorption <0.5%.<sup>813</sup>

One of the key issues in organic photovoltaics is exciton delivery to the donor/acceptor interface where it can dissociate and thus provide free charge carriers. In this direction, a supramolecular strategy has been proposed that aims at design of specific antennas for excitation of a small number of emitters by energy transfer from the large number of EET donors. This strategy combines functional assembly and molecular tailoring for easy tunability of spectral properties of the antenna. Functional assembly to provide both directional energy transfer and a decrease in energy dissipation can be designed by adopting a rigid dendritic backbone or choosing proper antenna chromophores, which sequentially provide an energy cascade.<sup>814,815</sup> Li et al. combined the strategy of supramolecular antenna collection of light and controlled energy transfer to the acceptor using the molecular machine mechanism.<sup>816</sup> The supramolecular antenna was constructed via synthesis of rotaxane dendrimers of three fractal generations containing up to 56 anthracene moieties (energy donor) on the wheels of the rotaxane units and one zinc(II) porphyrin moiety (energy acceptor) at the central core, where the addition and removal of acetate anions resulted in the directional and reversible motion

of rotaxane units on each axis, thus leading to the dynamic regulation of the antenna effect (Figure 96).

Another approach for directional energy transport in organic photovoltaic cells is application of interfacial passive exciton gates that intentionally bias energy transfer toward the D–A interface. In such a structure, the interface separates the materials that have either different band gaps or different density of molecular destination sites, thus creating either energetic asymmetry or asymmetry in hopping rates as hopping is proportional to the number of sites. Thus, an exciton from one side of the interface has an equal probability to move in either direction, while an exciton on the other side of the interface may only move away from the interface due to conservation of energy.<sup>817</sup> Since the gate interfaces work as diodes, large efficiencies of charge carrier collection can be reached without the need to increase the area of the dissociating interface.

Exciton multiplication in OPV cells can be obtained due to the singlet fission strategy, in which one singlet exciton is converted into two triplet excitons. The process of carrier multiplication via singlet fission can potentially exceed the Shockley–Queisser limit to increase the efficiency of single-junction photovoltaics. The singlet fission quantum yield is predicted to be close to the theoretical maximum of 200%; however, in OPV cells, this maximum is difficult to reach and the Shockley–Queisser limit most probably will not be broken in the near future.<sup>818</sup> Planar heterojunction organic solar cells based on pentacene with a peak external quantum efficiency of up to 126% in a limited region of the visible spectrum have been reported, demonstrating the ability to generate more than one electron per incident photon.<sup>819,820</sup> A more feasible trend is the application of singlet fission in an organic overlayer deposited on the surface of an inorganic PV cell like silicon for increasing efficiency of the latter.<sup>821</sup> The maximum combined yield of both SF in tetracene and the energy transfer to silicon was obtained at around 133%.<sup>822</sup> The additional excitons originating from singlet fission and transferred to silicon can increase the power conversion single-junction limit from 29% to as high as 35%.<sup>818</sup>

Exciton energy upconversion based on TTA is the opposite process to SF and can pick up photons from the low-energy region such as NIR to the visible one where most solar cells operate. However, no significant progress in OPV cells has been reached up to now due to the low-efficiency problem in organic triplet–triplet annihilation.<sup>823</sup> Again, a better outcome has been obtained when a molecular upconversion layer is combined with silicon, DSSCs, or intermediate band solar cells (IBSCs).<sup>824</sup> For example, in silicon-based solar cells an overall relative energy conversion efficiency increase of about 0.2% under 19 suns of noncoherent white excitation has been reported using tetrakisquinoxalinoporphyrin (PQ4Pd) and its derivative PQ4PdNA as sensitizers and rubrene as an annihilator/emitter moiety for NIR-to-vis upconversion.<sup>825</sup> In a DSSC based on a 5  $\mu\text{m}$  thick mesoporous  $\text{TiO}_2$  layer, the short-circuit photocurrent was enhanced by as much as 35% under one-sun light intensity when a model solar cell device was coupled with an organic TTA film and a reflector.<sup>826</sup> Recently, an IBSC based on an all-solid-state organic cell has been fabricated with the active layer composed of a blend of PtTPTBP and  $\alpha$ -sexithiophene ( $\alpha$ -6T) as the sensitizer and emitter, respectively, whereas the acceptor layer was diindenoperylene.<sup>827</sup> It was shown that this IBSC under subbandgap illumination intensity lower than 0.1 mW  $\text{cm}^{-2}$  has an increased photocurrent by 12% compared to the control  $\alpha$ -6T/ $\text{C}_{60}$  cell without the TTA layer.

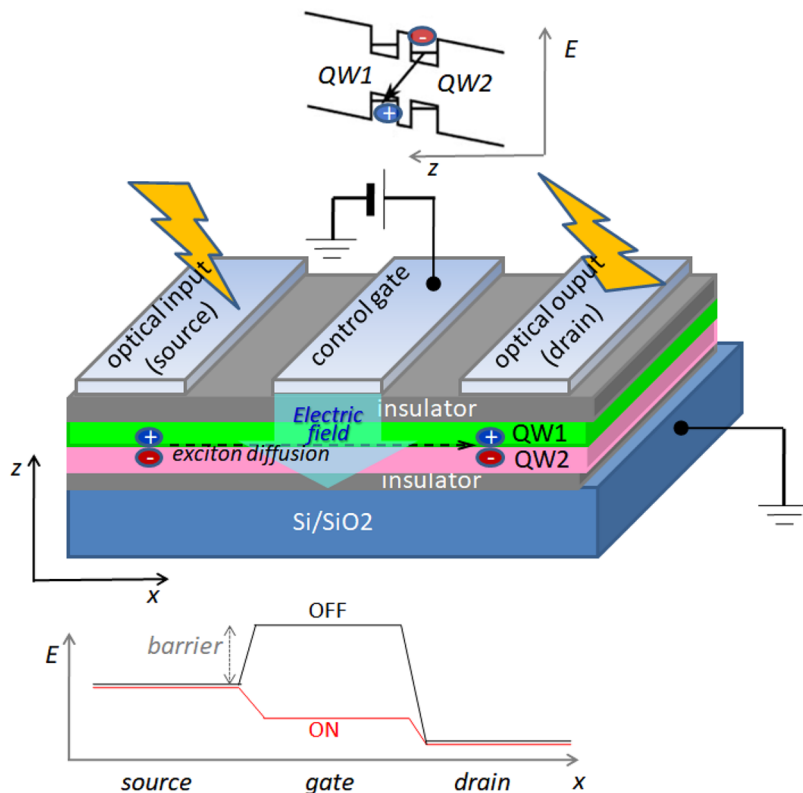


**Figure 97.** Schematic of an excitonic transistor. QW1 and QW2 designate quantum wells, for example, 2D transition-metal dichalcogenide layers. (top) Coupled quantum wells energy diagram. (bottom) Schematic of the exciton potential energy. The energy is freely transferred toward lower energy levels; however, the gate region can create a barrier for transport of excitons through increasing the exciton potential energy  $E$  by the voltage  $V_g$ .

#### 6.4. Supertransport of Excitons

Long-range and fast migration of excitons is of great importance for design of high-speed excitonic circuits, quantum computers, highly efficient solar cells, and light-emitting diodes. Coherence plays a crucial role in this issue as it assists in acceleration of exciton migration significantly. Recently, highly enhanced exciton diffusion coefficients have been measured for coherent exciton transport in quasi-1D molecular systems, such as nanofibers,<sup>828</sup> cylindrical bundles,<sup>829</sup> and nanotubes.<sup>830,831</sup> These coefficients ( $3\text{--}70\text{ cm}^2/\text{s}$ ) were significantly higher than the diffusion coefficients of incoherent excitons characteristic of other materials, that is,  $0.001\text{--}1\text{ cm}^2/\text{s}$  observed in conventional organic thin films and hybrid heterostructures,<sup>832,833</sup>  $0.01\text{--}14.5\text{ cm}^2/\text{s}$  in atomically thin transition metal dichalcogenides and phosphorene,<sup>834</sup> and  $0.1\text{--}10\text{ cm}^2/\text{s}$  in III-V semiconductor quantum wells.<sup>835</sup> Sharma et al. reported observation of a “supertransport” of excitons confined to an atomically thin two-dimensional organic semiconductor pentacene monolayer, with a measured high effective exciton diffusion coefficient of  $\sim 346.9\text{ cm}^2/\text{s}$  at room temperature. The obtained value, which is several orders of magnitude higher than the values reported for other organic molecular aggregates and low-dimensional inorganic materials was achieved by exciton transport between the coherent states at the 2D quantum limit. This effect was attributed to the enhanced exciton oscillator strength owing to the constructive dipole coupling in the J-aggregates in a pentacene monolayer, which forms an enhanced net optical dipole moment, which is very sensitive to the quantum confinement of the system.<sup>836</sup> The coherence in a pentacene monolayer was achieved due to exciton delocalization over  $\sim 135$  molecules; such a large exciton coherence length is

close to the theoretical estimates of the upper limit of the delocalization length.<sup>837</sup>

Another particularly promising advantage of 2D structures is that they can also provide a large cross-sectional area for light-matter interactions and possess enormous stretchability, providing potential applications in future excitonic devices. A method to tune the bandgap of suspended 2D semiconductors by applying a local strain gradient with a nanoscale tip has been proposed by Moon et al.<sup>838</sup> The strain allowed local and reversible shift of the exciton energy and steering of the exciton flux over micrometer-scale distances, thus providing dynamic control of the exciton flux.

Optical cavities have been shown to play a useful role in effective and ultralong exciton transport. Photons emitted by excitons in the quantum well can oscillate long enough within the cavity, where they can be reabsorbed, re-emitted again, and so on. The entangled exciton–photon eigenstates give rise to formation of cavity polaritons whose wave functions extend over distances much larger than the molecular scale. The strong coupling regime between exciton and photon supports exciton transport as well. Zhong et al. demonstrated nonradiative energy transfer well beyond the Förster limit for spatially separated donor and acceptor cyanine dyes strongly coupled to a cavity with energy transfer efficiency approaching 37% for donor–acceptor distances  $\geq 100\text{ nm}$ .<sup>839</sup> Zhong and coauthors discussed that the distance independent energy transfer process is consistent with the entangled and delocalized nature of the polaritonic states.

An ultralong-range energy transport in a disordered organic semiconductor at room temperature via coherent exciton–polariton propagation has been recently discovered.<sup>840,841</sup>

Exciton–polariton modes were generated due to coupling of a Bloch surface wave photon with molecular excitons mediated by optical microcavities containing a disordered excitonic material. The delocalized exciton–polariton was shown to possess a group velocity as high as  $3 \times 10^7 \text{ m s}^{-1}$  and a lifetime of 500 fs, leading to propagation distances of over 100  $\mu\text{m}$  from the excitation source. The exciton–polariton coherence length was determined to be as high as 20  $\mu\text{m}$  due to self-interference of the polariton mode. Wang et al. demonstrated the efficient channeling of excitation energy to a heterojunction interface consisting of energy or electron donor and acceptor materials coupled to the same cavity mode, where the rate of exciton harvesting was enhanced by 1 order of magnitude and the rate of energy transfer in the system was enhanced by 2–3 times.<sup>842</sup> The demonstration of fast and ultralong-range exciton–polariton transport at room temperature provides a great impact on development of new photonic and light harvesting systems, which operate through an energy transfer in disordered condensed matter systems.

## 6.5. Excitonic Circuits

The excitonic circuitry that is available in natural systems like photosynthesis inspired scientists toward development of a reasonable alternative to electronic circuits. One potential solution lies in excitonic devices that manipulate excitons instead of free carriers. In order to be applied in communication networks, such a device should be able to convert the optical signals that transmit data over long distances to the electrical signals used in data processing and vice versa. The key element of such devices is an excitonic transistor that is able to amplify the excitonic flux. The operation principle of the excitonic transistor is based on controlling the exciton flux by the gate voltage. Operational functionality of such a device can be achieved by meeting two crucial requirements. The first requirement is a sufficiently long exciton lifetime before recombination, which allows excitons to travel over large distances comparable to the device dimensions. This can be met by location of the bound electron and hole in different quantum wells. The second requirement is control of the exciton transport in a certain direction; this can be realized through the driving force acting on the exciton in a nonuniform electric field (see eq 22).

The details of the functioning of an excitonic transistor are illustrated in Figure 97. First, the photons are absorbed at the optical input (which represents a transparent transistor source electrode) and generate excitons in the semiconductor layer. Second, the excitons travel from the optical input to the optical output (which represents a transparent transistor drain electrode) due to the electrical field gradient created by the difference in the source voltage,  $V_s$ , and drain voltage,  $V_d$ . The exciton flux from source to drain is also controlled by a gate voltage,  $V_g$ , which separates the bound electron and hole at different energy levels of the quantum well in the region of the gate electrode. Third, photons are emitted at the optical output by exciton recombination. The exciton recombination rate is controlled electrically by the  $V_g$ ;<sup>843</sup> separation of electron and hole at an energetic barrier higher than  $k_B T$  by a relatively strong electric field causes the exciton diffusion to be impeded in the gate region, resulting in the suppression of light emission in the output region. In addition to electrical control, photonic control of the gate by a light beam can be introduced in all-optical excitonic transistors;<sup>844,845</sup> light induces variation in conductance and, therefore, the change in electric potential in the gate

region, and thus it lifts the barrier for transport of excitons created by the voltage,  $V_g$ .<sup>846</sup> It should be noted that the above transistor operates not as an amplifier but as an optical switch, in which a weak light beam or applied voltage can switch another beam on and off.

So far, excitonic transistors have been demonstrated using bulk inorganic semiconductors, which usually operate at low temperatures below  $-173^\circ\text{C}$ , because the excitons in inorganic bulk materials have low binding energy and dissociate at room temperatures.<sup>847</sup> However, recent works have suggested new solutions for development of excitonic transistors operating at room temperature. A prototype of such a device is based on two 2D-layer quantum wells as shown in Figure 97. Unuchek et al. used layers of two atomically thin transition-metal dichalcogenides, namely, molybdenum disulfide ( $\text{MoS}_2$ ) and tungsten diselenide ( $\text{WSe}_2$ ),<sup>848</sup> but such a prototype can in principle be constructed of organic semiconductor layers as well. One layer in the above heterostructure serves as electron donor and the other as electron acceptor, so light generates excitons that have CT character and are referred to as hybrid,<sup>849</sup> indirect,<sup>850</sup> or interlayer<sup>851</sup> excitons.

The benefit of the above system is that it provides a relatively large spatial separation between the electron and the hole, which increases the exciton lifetime by 2 orders of magnitude toward the nanosecond range compared to that in a single 2D material layer, which yields only about 10 ps.<sup>852</sup> The extended exciton lifetime allows for exciton diffusion over a scale of micrometers at room temperature. The other benefit is that the CT interlayer exciton in this two-layer structure has a built-in out-of-plane dipole moment, which can be manipulated and controlled by an applied electric field, which is not possible for excitons in a single 2D layer.

However, fabrication of even simple excitonic devices composed of assemblies of optically active molecules has been restricted so far by the limited amount of suitable molecular scale assembly technologies. A recent breakthrough demonstrated design and operational principles of a hybrid all-optical excitonic switch, which was assembled from donor/acceptor chromophores and photochromic nucleotide modulators with nanometer scale precision using DNA nanotechnology.<sup>853</sup> The excitonic device was based on molecular configuration changes occurring in the photochromic nucleotides based on diaryl-ethenes with the ring system in the CLOSED (absorbing) and OPEN (nonabsorbing) configurations, and it operated successfully in both liquid and solid phases. The device operated at speeds similar to current transistor technology and exhibited high ON/OFF switching contrast with no apparent cyclic fatigue through nearly 200 cycles.

Boulais et al. developed a synthetic strategy of strongly coupled excitonic circuits using spatially organized dye aggregates, which demonstrate tunable absorption spectra and strongly coupled exciton dynamics, and rigid DNA scaffolds to program the spatial organization of cyanine dye aggregates.<sup>854</sup> The programmed circuits exhibited excitonic transport properties with prominent circular dichroism, super-radiance, and fast delocalized exciton transfer.

Recently, Sawaya et al. proposed a novel design for an elementary excitonic transistor that is comprised of three molecules that play the roles of the collector (C), the gate (G), and the emitter (E), where multiplex excited states to control the flow of excitons in organic molecules are employed.<sup>855</sup> The operational principle of the device is based on the energy transfer among three molecules and particularly the excitation

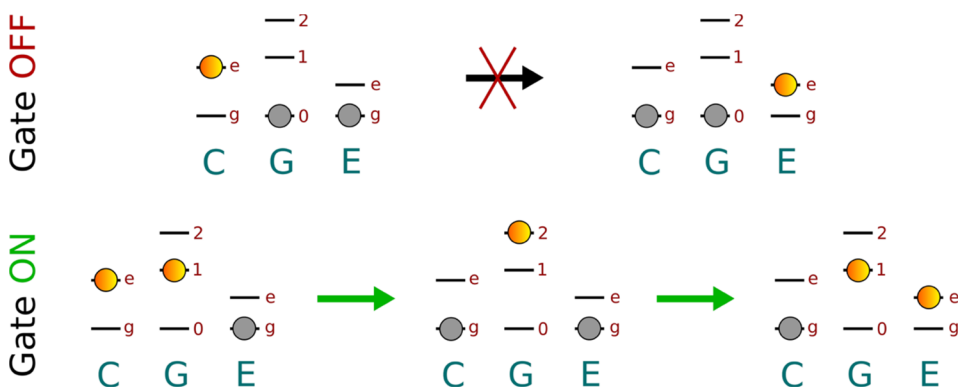


**Figure 98.** Schematic of a transistor-like excitonic device operating via the  $S_2$  exciton gate. The vertical direction denotes energy. C, G, and E denote collector, gate, and emitter organic molecules. States g and e correspond to electronic singlet ground and first excited states, respectively. States 0, 1, and 2 are the ground, first excited singlet, and second excited singlet states, respectively, of the gate molecule G. The exciton gate is OFF (top) when G is in its ground state G0. In this case, the energy levels forbid an exciton on C from migrating through G. Conversely, the exciton gate is ON (bottom) when G is in state G1. Because the energy gap  $\epsilon[G2] - \epsilon[G1]$  is less than or on resonance with  $\epsilon[C_e] - \epsilon[C_g]$ , energy can now flow through G via the G2 state. Reproduced from ref 855. Copyright 2018 American Chemical Society.

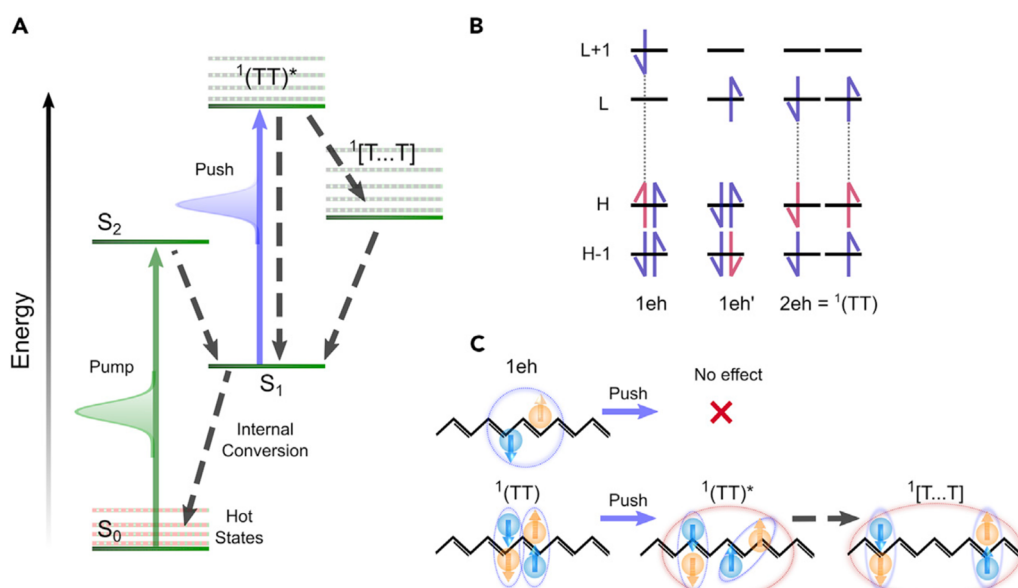


**Figure 99.** (A) Schematic of energy levels and dynamics measured in the pump–push–probe experiments (pump, green arrow; push, blue arrow). The  $S_1 ({}^1A_g^-)$  state can be tracked and selectively projected into the triplet-pair manifold by pushing the excited-state absorption transition  ${}^1(TT) - {}^1(TT)^*$ . The spatially separated triplet pairs ( ${}^1[T\dots T]$ ) appear from relaxation of  ${}^1(TT)^*$  (a  $B_u$  symmetry state). (B) Some possible electronic configurations of the frontier molecular orbitals that are superposed together by the configuration interaction into the low lying  $S_1 ({}^1A_g^-)$  wave function. Red arrows indicate the hole; electrons are shown in blue. 1eh indicates an electronic configuration containing one electron–hole pair in an excitonic spin-singlet state. The singlet  ${}^1(TT)$  configuration is a doubly excited configuration that can be seen as a pair of low energy triplet excitons with antialigned spins. (C) Illustrative sketch of some possible spatial wave functions of electrons and holes for the configurations shown in part B. The transition with the push pulse is derived from the transition of single, isolated triplets, that is, it represents an excitation of a single triplet component within the  ${}^1A_g^- / {}^1(TT)$  state (as opposed to an excitation of the entire multiexciton into a putative  $T^*T^*$  configuration). Furthermore, the push chiefly acts on the  ${}^1(TT)$  part of the wave function (bottom) and not the 1eh (or 1eh0) amplitudes (top). A mechanism is suggested for the push-induced separation of the triplet-pairs from  ${}^1(TT)^*$ , whereby one of the excited triplets is highly delocalized, promoting relaxation channels that separate the triplets far enough apart to behave as near-free particles. Reprinted from ref 858 with permission from Elsevier. Copyright 2020 Elsevier.

migration via a second excited singlet state ( $S_2$ ) of the gate molecule (Figure 98). It has certain benefits compared to the previous exciton switching schemes and particularly possesses a picosecond time scale of gate actuation, a lack of molecular rearrangement (while that is intrinsic to the isomerization switches), and availability of amplification or gain of excitonic flow by varying the intensity of incident light or an auxiliary flow of excitons. It is important that the latter functionality makes this single exciton device a true transistor that amplifies the signal.

Another design of optical transistors is based on the optical cavity. Zasedatelev et al. reported room-temperature operation of a polariton transistor based on a ladder-type polymer in an optical microcavity through vibron-mediated stimulated polariton relaxation and condensation of bosons in organic microcavities. Zasedatelev and coauthors obtained a net gain of  $\sim 10$  dB  $\mu\text{m}^{-1}$ , sub-picosecond switching time, cascaded amplification, and all-optical logic operation in ambient conditions.<sup>856</sup>

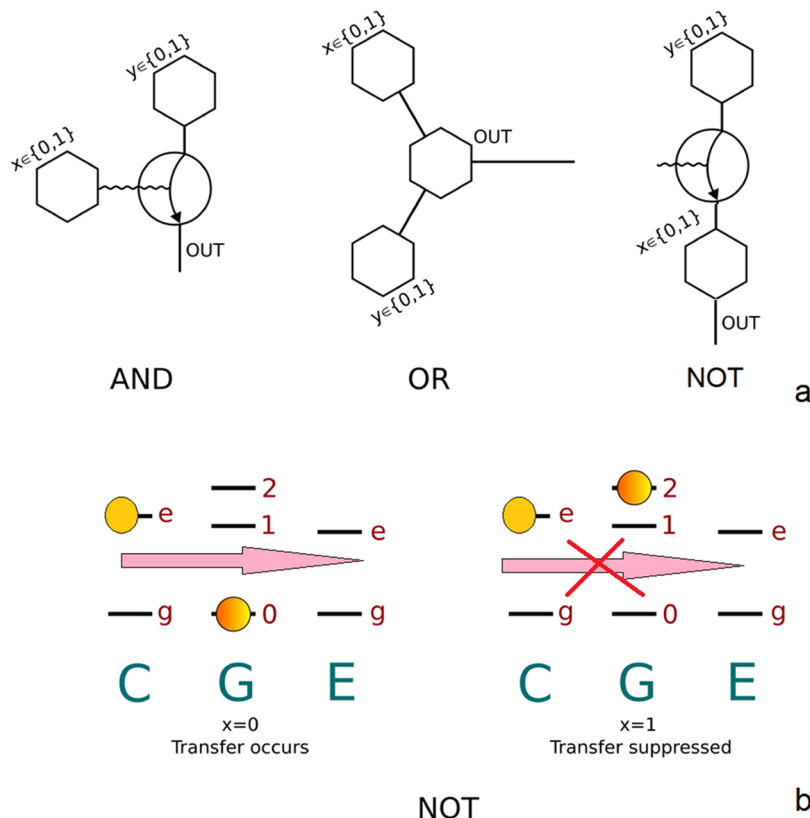


**Figure 100.** (a) Illustration of the exciton binary logic gates AND, OR, and NOT based on three molecules; the gate molecule is shown as a circle. (b) Operational principle for the NOT gate. The symbol meanings are the same as in Figure 99. Adapted from ref 855. Copyright 2018 American Chemical Society.

## 6.6. Quantum Computing

A quantum computer requires built-in sources of nonclassical states, such as squeezing, intermodal squeezing, antibunching, intermodal antibunching, and entanglement, which are needed for various quantum information processing tasks.<sup>857</sup> One of the key processes, the quantum entanglement, can be more easily realized in one-dimensional organic semiconductors compared to 3D inorganic semiconductors, as electrons in low-dimensional confined systems do not behave as quasi-independent particles. In molecules, not more than two electrons are available on each energy level, and the excited electron is tightly bound to its hole counterpart; therefore, each electron's state is critically dependent on the quantum states of the neighboring electron and hole, leading to correlations or entanglement between their quantum states, respectively. But such an entanglement is difficult to measure and control in organic nanostructures. Pandya et al. found experimental conditions using a sequence of ultrashort laser pulses that create pairs of entangled particles that carry spin information across the backbones of long polydiacetylene molecules and carotenoid aggregates, similar to the entangled photon pairs in the famous Einstein–Podolsky–Roden “paradox”.<sup>858</sup> Pandya and coauthors experimentally confirmed that an optically dark  $S_1$  ( $2^1\text{Ag}^-$ ) state is a superposition state with strong contributions from spin-entangled pairs of triplet  ${}^1(\text{TT})$  excitons and showed that optical manipulation of the  $S_1$  wave function allows selective projection of the  ${}^1(\text{TT})$  component into a manifold of spatially separated triplet pairs by pushing the excited-state absorption transition  ${}^1(\text{TT}) - {}^1(\text{TT})^*$  toward spatially separated triplet

pairs ( ${}^1[\text{T} \cdots \text{T}]$ ) with lifetimes enhanced by up to 1 order of magnitude (Figure 99).

Molecular qubit systems for quantum computing can use different operational principles. It was reported that the role of qubits can provide rotational<sup>859</sup> and vibrational<sup>860–862</sup> modes of polyatomic molecules, such as the two IR-active modes of acetylene, electric dipole moments of ultracold diatomic molecules,<sup>863,864</sup> and electron spin in molecular quantum dots, single-walled carbon nanotubes, and endohedral fullerenes.<sup>865,866</sup>

The role of excitons in quantum computing processes was elucidated decades ago. It was reported, for example, that manipulation of the strength and duration of the exciton states is necessary for producing highly entangled states and theoretical predictions suggested that several hundred single quantum bit rotations and controlled-NOT gates could be performed before decoherence of the excitonic states takes place.<sup>867</sup> The existence of a strong built-in electric field induced by the spontaneous polarization and by the piezoelectricity in GaN-based quantum dots was exploited to generate entangled few-exciton states without resorting to external fields.<sup>868</sup> Ghosh et al. showed that quantum tunneling and nonlinear interactions between the exciton–polariton condensates confined in a semiconductor micropillar and excited with a coherent laser allow SWAP, square-root SWAP, and controlled-NOT gate operations between the qubits.<sup>869</sup>

Recent studies demonstrate that exciton gate platforms can be used for implementation of a binary logic in molecular systems. Sawaya et al. showed how to create the AND, OR, and NOT gates, from which all other binary operators can be deduced.<sup>855</sup> The operational principles of these logic gates are based on

exciton transfer through the gate molecule, which functions as a valve that can be either open or closed. Here, the logic operation AND means that the exciton is transferred out only if both C and G molecules are activated, that is, they bear excitons (see Figure 98 (the case “gate on”) and Figure 100). The logic operation OR means that exciton is transferred out if any of the molecules connecting in parallel to the output gate bears an exciton (Figure 100a). The logic operation NOT prohibits exciton transfer through the gate molecule being in the state ON, that is, if it bears an  $S_2$  exciton, and allows this transfer if the gate molecule is OFF, that is, if it is in the ground state (Figure 100b). To connect the gates, the output exciton from one  $S_2$  exciton gate may be used as input to the next exciton gate. In this connection, one gate (G) molecule can serve as either the collector (C) or base (B) molecule of the next gate.

An even broader range of quantum operations has been proposed by Castellanos et al., who developed a strategy to determine the excitonic circuits of the four universal quantum logic gates: the one-qubit NOT, Hadamard, p/8 transformation, and entangling two-qubit CNOT transformation.<sup>870</sup> To encode a quantum transformation and construct these quantum logic gates, different geometric arrangements of excitonic dye molecules have been used, which can serve as an advanced step toward enabling quantum logic operations in excitonic systems.

These results provide surprising experimental schemes for future implementation of quantum processing in solid-state organics and elucidate some exciting ideas for manipulation with quantum information at the molecular level.

## 7. CONCLUSIONS

This work comprehensively reviewed all steps of the exciton journey during its variable lifetime, from birth to decay, and showed a broad palette of time scales within which the exciton realizes its dynamics. Specifically, these time scales cover many orders of magnitude, beginning from ultrafast processes on the sub-picosecond scale, such as localization–delocalization dynamics, self-trapping, and formation of charge-transfer states, to rather slow processes that occur on millisecond to second scales, such as intersystem crossing and phosphorescence. Such a great variety of rates, which span more than 10 orders of magnitude, provides fascinating incentives for excitonic pathways. These include excited-state chemical reactions, exciton-induced symmetry breaking and structural reorganization, energy upconversion and down-conversion, direct and reverse intersystem crossing, radiative and nonradiative decay, and so on. Of great importance is ultrafast energy funneling and long-range exciton transport, both coherent and incoherent, as these provide current and future applications of excitonic devices that fulfill light-driven mechanical motion at the nano- and microscale, conversion of excitation energy to electricity, high-speed operation of excitonic circuits, quantum computers, etc. Currently, the first molecular qubit systems, excitonic and phototransistors have been demonstrated, and the field is developing rapidly. Skilful molecular design allows one to progress well in constructing various artificial muscles and delivery means and optimization of OPV cells that have reached power conversion efficiency of over 18%. Quantum confinement of excitons and their coupling to cavity modes or plasmonic particles allows one to extend the exciton transport distances from nanometer to micrometer scales, leading to propagation distances of over 100  $\mu\text{m}$  from the excitation source.

The exciton transport is especially welcomed in organic materials, where the charge transport is limited by poor conductivity of the material and low mobility of charge carriers. In contrast, because charge carriers are tightly bound within the Frenkel exciton and because energy transfer in organic materials can be realized promptly, on the picosecond to nanosecond time scales, excitonic circuits based on conjugated molecules can be considered reasonable alternatives to electrical circuits. Therefore, the rich exciton dynamics in organic semiconductors promises great prospects for its application. Here, the hot topics include studies on quantum coherent exciton transport in natural photosynthetic systems and networks of biological proteins, which fuels ideas about how nature works and how our minds work. The exciting issues are ultrafast delivery of information through exciton supertransport, storage of light due to subradiant or delayed exciton decay, chirality transfer or transfer of stereoinformation as a result of photoisomerization, which can be used for photocontrol of enantioselectivity in asymmetric catalysis using catalysts built with molecular motor scaffolds, light-induced reversible covalent bond formation and scission, and light-controlled molecular machines, to mention just a few.

As there are many more excitonic states in organic chromophores that are bright rather than dark, such an inequality stimulates a thought that the research works in the field of exciton dynamics will have an equally bright future.

## ASSOCIATED CONTENT

### Supporting Information

The Supporting Information is available free of charge at <https://pubs.acs.org/doi/10.1021/acs.chemrev.1c00648>.

Extensive list of recent reviews and feature articles that are focused on specialized topics within the field of exciton dynamics in conjugated molecules and organic semiconductors ([PDF](#))

## AUTHOR INFORMATION

### Corresponding Author

Oleg P. Dimitriev – V. Lashkaryov Institute of Semiconductor Physics NAS of Ukraine, Kyiv 03028, Ukraine;  [orcid.org/0000-0002-6848-6401](https://orcid.org/0000-0002-6848-6401); Phone: +38 044 5255530; Email: [dimitr@isp.kiev.ua](mailto:dimitr@isp.kiev.ua)

Complete contact information is available at: <https://pubs.acs.org/10.1021/acs.chemrev.1c00648>

### Notes

The author declares no competing financial interest.

### Biography

Oleg Dimitriev began his education in Krasnoyarsk State University (Russia) and then in Taras Shevchenko Kyiv State University (Ukraine). He obtained his Ph.D. degree in solid state physics from Donetsk State University in 1992. Then he made his scientific career at V. Lashkaryov Institute of Semiconductor Physics, National Academy of Science of Ukraine, where he is now a Senior Research Fellow. Since 2004, he also serves as Assistant Professor at Igor Sikorsky Kyiv Polytechnic Institute, where he lectures a course in physics of disordered systems. He is a recipient of international awards from Swedish Institute, Fulbright Visiting Scholar Program, German Academic Exchange Service (DAAD), and Japan Society for the Promotion of Science (JSPS). His major research interests are focused

on photophysics of organic polymers and dyes but also include other issues such as material science of organic and hybrid heterostructures, energy conversion, and ecological thinking. He is the author of popular science books *Sensible Universe* and *What Does Your Clock Show?* (in Russian).

## ACKNOWLEDGMENTS

The author is indebted for Fulbright and DAAD scholarships within which the projects on ultrafast spectroscopy have been conducted. Separate thanks are extended to Swedish Institute and Linköping University library for help with the literature, to Dr. A. D. Kachkovskii for reading the manuscript and valuable notes, and to anonymous reviewers for the constructive critique.

## LIST OF ABBREVIATIONS

ADT	anthradithiophene	LED	organic light-emitting diode
AIE	aggregation-induced emission	LEGS	local exciton ground state
ASPL	anti-Stokes photoluminescence	LPPP	ladder-type poly( <i>para</i> -phenylene)
BLA	bond-length alternation	ME	multiexciton
BPQD	black phosphorus quantum dot	MEG	multiple exciton generation
CEP	cooperative energy pooling	MEH-PPV	poly[2-(2'-ethylhexyloxy)-5-methoxy-1,4-phenylene-nevinylene]
CR	charge recombination	MIR	mid-infrared
CS	charge separation	NFA	non-fullerene acceptor
CT	charge transfer	NIR	near-infrared
CQD	carbon quantum dot	NITZ	<i>N</i> -(2-(6-chloro-s-tetrazin-3-yloxy)ethyl)-naphthalimide
CRET	coherent resonance energy transfer	NW	nanowire
DE	doubly excited state	OBF	one bond flip
DHP	<i>N,N'</i> -disubstituted dihydrobenzo[ <i>a,c</i> ]phenazine	OLED	organic light-emitting diode
DOS	density of states	OPV	organic photovoltaic
DPA	9,10-diphenylanthracene	PL	photoluminescence
DPAC	9,14-diphenyl-9,14-dihydrodibenzo[ <i>a,c</i> ]phenazine	P3HT	poly(3-hexylthiophene)
DSSC	dye-sensitized solar cell	PANI	polyaniline
EB	emeraldine base	PANIMT	aniline-3-methylthiophene copolymer
EEA	exciton–exciton annihilation	PA	polyacetylene
EET	excitation energy transfer	PBI	perylene bisimide
EPer	ethynylene-perylene	PBTTF	poly(2,5-bis(3-alkylthiophen-2-yl) thiieno[3,2- <i>b</i> ]-thiophene)
ESA	excited state absorption	PDA	polydiacetylene
ESIPT	excited-state intramolecular proton transfer	PDI	peryleneediimide
ESPT	excited-state proton transfer	PDOT	poly(3-(2,5-diethylphenyl)thiophene)
ESSR	excited-state structural relaxation	PDPA	poly(diphenylacetylene)
ETU	energy transfer up-conversion	PE	phenylene ethynylene
EQE	external quantum efficiency	PF	polyfluorene
FC	free carrier	PMI	perylenemonoimide
FE	free exciton	PMMA	poly(methyl methacrylate)
FRET	Förster resonance energy transfer	PNB	pernigraniline
GO	graphene oxide	PIC	pseudoisocyanine
GSA	ground state absorption	PPG	photoremovable protecting groups
HBA	hot-band absorption	PPE	poly(phenylene ethynylene)
HCy2	heptamethine cyanine dye	PPP	poly( <i>p</i> -phenylene)
HH	head-to-head	PPV	poly( <i>para</i> -phenylene vinylene)
HT	head-to-tail	QD	quantum dot
HuT	hula-twist	QW	quantum well
IBSC	intermediate band solar cell	QY	quantum yield
IC	interconversion	RIC	reverse internal conversion
ICT	intramolecular charge transfer	RISC	reverse intersystem crossing
ISC	intersystem crossing	RR P3OT	regioregular poly(3-octylthiophene)
iSF	intramolecular singlet fission	PV	photovoltaic
IQE	internal quantum efficiency	SBCT	symmetry-breaking charge transfer
<i>J</i> <sub>SC</sub>	short-circuit current	SHG	second-harmonic generation
LB	leucoemeraldine base	SF	singlet fission
LDS	luminescent down-shifting	STE	self-trapped exciton
LE	local excitonic	SWCNT	single-wall carbon nanotube
		TADF	thermally activated delayed fluorescence
		TICT	twisted intramolecular charge-transfer
		2PA	two-photon absorption
		TPA	triphenylamine
		TTA	triplet–triplet annihilation
		TTET	triplet–triplet energy transfer
		UV	ultraviolet
		VIE	vibration-induced emission
		XB	halogen bond
		xSF	intermolecular singlet fission

## REFERENCES

- (1) Park, K. H.; Kim, W.; Yang, J.; Kim, D. Excited-State Structural Relaxation and Exciton Delocalization Dynamics in Linear and Cyclic n-Conjugated Oligothiophenes. *Chem. Soc. Rev.* **2018**, *47*, 4279–4294.
- (2) Deutsch, M.; Wirsing, S.; Kaiser, D.; Fink, R. F.; Tegeder, P.; Engels, B. Geometry Relaxation-Mediated Localization and Delocalization of Excitons in Organic Semiconductors: A Quantum Chemical Study. *J. Chem. Phys.* **2020**, *153*, 224104.
- (3) Lin, Y. L.; Fusella, M. A.; Rand, B. P. The Impact of Local Morphology on Organic Donor/Acceptor Charge Transfer States. *Adv. Energy Mater.* **2018**, *8*, 1702816.
- (4) Popp, W.; Polkehn, M.; Binder, R.; Burghardt, I. Coherent Charge Transfer Exciton Formation in Regioregular P3HT: A Quantum Dynamical Study. *J. Phys. Chem. Lett.* **2019**, *10*, 3326–3332.
- (5) Patalag, L. J.; Hoche, J.; Holzapfel, M.; Schmiedel, A.; Mitric, R.; Lambert, C.; Werz, D. Ultrafast Resonance Energy Transfer in Ethylene-Bridged BODIPY Heteroooligomers: From Frenkel to Förster Coupling Limit. *J. Am. Chem. Soc.* **2021**, *143* (19), 7414–7425.
- (6) Nagao, R.; Kagatani, K.; Ueno, Y.; Shen, J.-R.; Akimoto, S. Ultrafast Excitation Energy Dynamics in a Diatom Photosystem I-Antenna Complex: A Femtosecond Fluorescence Upconversion Study. *J. Phys. Chem. B* **2019**, *123* (12), 2673–2678.
- (7) Schlicke, B.; Belser, P.; De Cola, L.; Sabbioni, E.; Balzani, V. Photonic Wires of Nanometric Dimensions. Electronic Energy Transfer in Rigid Rodlike Ru(bpy)<sub>32+</sub>-(ph)n-Os(bpy)<sub>32+</sub> Compounds (ph = 1,4-Phenylene; n = 3, 5, 7). *J. Am. Chem. Soc.* **1999**, *121*, 4207–4214.
- (8) D'Aléo, A.; Welter, S.; Cecchetto, E.; De Cola, L. Electronic energy transfer in dinuclear metalcomplexes containing meta-substitutedphenylene units. *Pure Appl. Chem.* **2005**, *77*, 1035–1050.
- (9) Pun, A. B.; Asadpoordarvish, A.; Kumarasamy, E.; Tayebjee, M. J. Y.; Niesner, D.; McCamey, D. R.; Sanders, S. N.; Campos, L. M.; Sfeir, M. Y. Ultra-fast intramolecular singlet fission to persistent multiexcitons by molecular design. *Nat. Chem.* **2019**, *11*, 821–828.
- (10) Perego, J.; Pedrini, J.; Bezuidenhout, C. X.; Sozzani, P. E.; Meinardi, F.; Bracco, S.; Comotti, A.; Monguzzi, A. Engineering Porous Emitting Framework Nanoparticles with Integrated Sensitizers for Low-Power Photon Upconversion by Triplet Fusion. *Adv. Mater.* **2019**, *31*, 1903309.
- (11) Valiev, R. R.; Cherepanov, V. N.; Nasibullin, R. T.; Sundholm, D.; Kurten, T. Calculating Rate Constants for Intersystem Crossing and Internal Conversion in the Franck-Condon and Herzberg-Teller Approximations. *Phys. Chem. Chem. Phys.* **2019**, *21*, 18495–18500.
- (12) Noda, H.; Chen, X.-K.; Nakanotani, H.; Hosokai, T.; Miyajima, M.; Notsuka, N.; Kashima, Y.; Brédas, J.-L.; Adachi, C. Critical Role of Intermediate Electronic States for Spin-Flip Processes in Charge-Transfer-Type Organic Molecules with Multiple Donors and Acceptors. *Nat. Mater.* **2019**, *18*, 1084–1090.
- (13) Serdiuk, I. E.; Mońska, M.; Kozakiewicz, K.; Liberek, B.; Bojarski, P.; Park, S. Y. vibrationally Assisted Direct Intersystem Crossing between the Same Charge-Transfer States for Thermally Activated Delayed Fluorescence: Analysis by Marcus-Hush Theory Including Reorganization Energy. *J. Phys. Chem. B* **2021**, *125*, 2696–2706.
- (14) Zhao, J.; Chen, K.; Hou, Y.; Che, Y.; Liu, L.; Jia, D. Recent Progress in Heavy Atom-Free Organic Compounds Showing Unexpected Intersystem Crossing (ISC) Ability. *Org. Biomol. Chem.* **2018**, *16* (20), 3692–3701.
- (15) Lv, M.; Yu, Y.; Sandoval-Salinas, M. E.; Xu, J.; Lei, Z.; Casanova, D.; Yang, Y.; Chen, J. Engineering the Charge-Transfer State to Facilitate Spin-Orbit Charge Transfer Intersystem Crossing in Spirobis[Anthracene]Diones. *Angew. Chem., Int. Ed. Engl.* **2020**, *59*, 22179–22184.
- (16) Eng, J.; Thompson, S.; Goodwin, H.; Credgington, D.; Penfold, T. J. Competition between the Heavy Atom Effect and Vibronic Coupling in Donor-Bridge-Acceptor Organometallics. *Phys. Chem. Chem. Phys.* **2020**, *22*, 4659–4667.
- (17) Xiao, Y.-F.; Chen, J.-X.; Chen, W.-C.; Zheng, X.; Cao, C.; Tan, J.; Cui, X.; Yuan, Z.; Ji, S.; Lu, G.; Liu, W.; Wang, P.; Li, S.; Lee, C.-S. Achieving High Singlet-Oxygen Generation by Applying the Heavy-Atom Effect to Thermally Activated Delayed Fluorescent Materials. *Chem. Commun. (Camb.)* **2021**, *57*, 4902–4905.
- (18) Jin, F.; Ding, G.; Wang, Y.; Yuan, J.; Guo, W.; Yuan, H.; Sheng, C.; Ma, W.; Zhao, H. Thermal Annealing Effect on Ultrafast Charge Transfer in All-Polymer Solar Cells with a Non-Fullerene Acceptor N2200. *J. Phys. Chem. C* **2017**, *121*, 8804–8811.
- (19) Shi, T.; Zhang, Z.; Guo, X.; Liu, Z.; Wang, C.; Huang, S.; Jia, T.; Quan, C.; Xiong, Q.; Zhang, M.; Du, J.; Leng, Y. Ultrafast Charge Generation Enhancement in Nanoscale Polymer Solar Cells with DIO Additive. *Nanomaterials* **2020**, *10*, 2174.
- (20) Liu, Y.; Zuo, L.; Shi, X.; Jen, A. K.-Y.; Ginger, D. S. Unexpectedly Slow yet Efficient Picosecond to Nanosecond Photoinduced Hole-Transfer Occurs in a Polymer/Nonfullerene Acceptor Organic Photovoltaic Blend. *ACS Energy Lett.* **2018**, *3*, 2396–2403.
- (21) Braun, J. D.; Lozada, I. B.; Kolodziej, C.; Burda, C.; Newman, K. M. E.; van Lierop, J.; Davis, R. L.; Herbert, D. E. Iron(II) Coordination Complexes with Panchromatic Absorption and Nanosecond Charge-Transfer Excited State Lifetimes. *Nat. Chem.* **2019**, *11*, 1144–1150.
- (22) Boczar, B. P.; Mangle, E. A.; Schwartz, S. A.; Topp, M. R. Fluorescence Studies of Very Short-Lived Excited States of Aromatic Molecules. In *Applications of Picosecond Spectroscopy to Chemistry*; Eisenthal, K. B., Ed.; NATO ASI Series (Series C: Mathematical and Physical Sciences); Springer: Dordrecht, 1984; Vol. 127, pp 237–258.
- (23) Itoh, T. Fluorescence and Phosphorescence from Higher Excited States of Organic Molecules. *Chem. Rev.* **2012**, *112*, 4541–4568.
- (24) Chen, B.; Li, C.; Zhang, J.; Kan, J.; Jiang, T.; Zhou, J.; Ma, H. Sensing and Imaging of Mitochondrial Viscosity in Living Cells Using a Red Fluorescent Probe with a Long Lifetime. *Chem. Commun. (Camb.)* **2019**, *55*, 7410–7413.
- (25) Hu, W.; Guo, L.; Bai, L.; Miao, X.; Ni, Y.; Wang, Q.; Zhao, H.; Xie, M.; Li, L.; Lu, X.; Huang, W.; Fan, Q. Maximizing Aggregation of Organic Fluorophores to Prolong Fluorescence Lifetime for Two-Photon Fluorescence Lifetime Imaging. *Adv. Healthc. Mater.* **2018**, *7*, 1800299.
- (26) Lin, C.-W.; Bachilo, S. M.; Weisman, R. B. Delayed Fluorescence from Carbon Nanotubes through Singlet Oxygen-Sensitized Triplet Excitons. *J. Am. Chem. Soc.* **2020**, *142*, 21189–21196.
- (27) Cai, S.; Ma, H.; Shi, H.; Wang, H.; Wang, X.; Xiao, L.; Ye, W.; Huang, K.; Cao, X.; Gan, N.; Ma, C.; Gu, M.; Song, L.; Xu, H.; Tao, Y.; Zhang, C.; Yao, W.; An, Z.; Huang, W. Enabling Long-Lived Organic Room Temperature Phosphorescence in Polymers by Subunit Interlocking. *Nat. Commun.* **2019**, *10*, 4247.
- (28) Thomas, H.; Pastoetter, D. L.; Gmelch, M.; Achenbach, T.; Schlägl, A.; Louis, M.; Feng, X.; Reineke, S. Aromatic Phosphonates: A Novel Group of Emitters Showing Blue Ultralong Room Temperature Phosphorescence. *Adv. Mater.* **2020**, *32*, No. e2000880.
- (29) Ma, H.; Peng, Q.; An, Z.; Huang, W.; Shuai, Z. Efficient and Long-Lived Room-Temperature Organic Phosphorescence: Theoretical Descriptors for Molecular Designs. *J. Am. Chem. Soc.* **2019**, *141*, 1010–1015.
- (30) Li, Q.; Zhou, M.; Yang, M.; Yang, Q.; Zhang, Z.; Shi, J. Induction of Long-Lived Room Temperature Phosphorescence of Carbon Dots by Water in Hydrogen-Bonded Matrices. *Nat. Commun.* **2018**, *9*, 734.
- (31) Tian, S.; Ma, H.; Wang, X.; Lv, A.; Shi, H.; Geng, Y.; Li, J.; Liang, F.; Su, Z.-M.; An, Z.; Huang, W. Utilizing d-π Bonds for Ultralong Organic Phosphorescence. *Angew. Chem., Int. Ed. Engl.* **2019**, *58*, 6645–6649.
- (32) Pyshkin, S. *Excitons*; Pyshkin, S. L., Ed.; InTech: London, England, 2018.
- (33) Jang, S. *Dynamics of Molecular Excitons*, 1st ed.; Elsevier, 2020.
- (34) Kühn, O. Frenkel Exciton Dynamics: A Theoretical Perspective. In *Handbook of Organic Materials for Electronic and Photonic Devices*; Ostroverkhova, O., Ed.; Elsevier, 2019; pp 259–279.
- (35) Benedict, M. G.; Ermolaev, A. M.; Malyshev, V. A.; Sokolov, I. V.; Trifonov, E. D. In *Super-Radiance: Multiatom Coherent Emission*, 1st ed.; Benedict, M. G., Ed.; CRC Press: Boca Raton, FL, 2018.
- (36) Kilina, S. V.; Habenicht, B. F. In *Excitonic and Vibrational Dynamics in Nanotechnology: Quantum Dots vs. Nanotubes*, 1st ed.; Kilina, S., Habenicht, B. G., Eds.; Jenny Stanford Publishing, 2019.

- (37) Tang, Y.; Tang, B. Z. In *Principles and Applications of Aggregation-Induced Emission*, 1st ed.; Tang, Y., Tang, B. Z., Eds.; Springer International Publishing: Basel, Switzerland, 2018.
- (38) Abramavicius, D.; Palmieri, B.; Voronine, D. V.; Sanda, F.; Mukamel, S. Coherent Multidimensional Optical Spectroscopy of Excitons in Molecular Aggregates; Quasiparticle versus Supermolecule Perspectives. *Chem. Rev.* **2009**, *109*, 2350–2408.
- (39) Chuang, C.; Bennett, D. I. G.; Caram, J. R.; Aspuru-Guzik, A.; Bawendi, M. G.; Cao, J. Generalized Kasha's Model: T-Dependent Spectroscopy Reveals Short-Range Structures of 2D Excitonic Systems. *Chem.* **2019**, *5*, 3135–3150.
- (40) Gutiérrez-Meza, E.; Malatesta, R.; Li, H.; Bargigia, I.; Srimath Kandada, A. R.; Valverde-Chávez, D. A.; Kim, S.-M.; Li, H.; Stingelin, N.; Tretiak, S.; Bittner, E. R.; Silva-Acuña, C. Frenkel Biexcitons in Hybrid HJ Photophysical Aggregates. *Sci. Adv.* **2021**, *7*, No. eabi5197.
- (41) Jang, S. J.; Burghardt, I.; Hsu, C.-P.; Bardeen, C. J. Excitons: Energetics and Spatiotemporal Dynamics. *J. Chem. Phys.* **2021**, *155*, 200401.
- (42) Ostroverkhova, O. *Handbook of Organic Materials for Electronic and Photonic Devices*; Woodhead Publishing, 2019.
- (43) Rohatgi-Mukherjee, K. K. *Fundamentals of Photochemistry*; New Age International: New Dehli, India, 1978; 347 pp.
- (44) Wang, X.; Shi, H.; Ma, H.; Ye, W.; Song, L.; Zan, J.; Yao, X.; Ou, X.; Yang, G.; Zhao, Z.; Singh, M.; Lin, C.; Wang, H.; Jia, W.; Wang, Q.; Zhi, J.; Dong, C.; Jiang, X.; Tang, Y.; Xie, X.; Yang, Y.; Wang, J.; Chen, Q.; Wang, Y.; Yang, H.; Zhang, G.; An, Z.; Liu, X.; Huang, W. Organic Phosphors with Bright Triplet Excitons for Efficient X-Ray-Excited Luminescence. *Nat. Photonics* **2021**, *15*, 187–192.
- (45) Marian, C. M. Understanding and Controlling Intersystem Crossing in Molecules. *Annu. Rev. Phys. Chem.* **2021**, *72*, 617–640.
- (46) Luppi, B. T.; Majak, D.; Gupta, M.; Rivard, E.; Shankar, K. Triplet Excitons: Improving Exciton Diffusion Length For Enhanced Organic Photovoltaics. *J. Mater. Chem. A* **2019**, *7*, 2445–2463.
- (47) Ahmad, V.; Sobus, J.; Greenberg, M.; Shukla, A.; Philippa, B.; Pivrikas, A.; Vamvounis, G.; White, R.; Lo, S.-C.; Namdas, E. B. Charge and Exciton Dynamics of OLEDs under High Voltage Nanosecond Pulse: Towards Injection Lasing. *Nat. Commun.* **2020**, *11*, 4310.
- (48) Beljonne, D.; Cornil, J.; Friend, R. H.; Janssen, R. A. J.; Brédas, J. L. Influence of Chain Length and Derivatization on the Lowest Singlet and Triplet States and Intersystem Crossing in Oligothiophenes. *J. Am. Chem. Soc.* **1996**, *118*, 6453–6461.
- (49) Köhler, A.; Bässler, H. Triplet States in Organic Semiconductors. *Mater. Sci. Eng., R* **2009**, *66*, 71–109.
- (50) Vosskötter, S.; Konieczny, P.; Marian, C. M.; Weinkauf, R. Towards an Understanding of the Singlet-Triplet Splittings in Conjugated Hydrocarbons: Azulene Investigated By Anion Photoelectron Spectroscopy and Theoretical Calculations. *Phys. Chem. Chem. Phys.* **2015**, *17*, 23573–23581.
- (51) Pollice, R.; Friederich, P.; Lavigne, C.; dos Passos Gomes, G.; Aspuru-Guzik, A. Organic Molecules With Inverted Gaps Between First Excited Singlet and Triplet States and Appreciable Fluorescence Rates. *Matter* **2021**, *4*, 1654–1682.
- (52) Ueta, M.; Kanzaki, H.; Kobayashi, K.; Toyozawa, Y.; Hanamura, E. *Excitonic Processes in Solids*; Springer Series in Solid State Sciences, Springer: Berlin, Heidelberg, 1986; Vol. 60, pp 203–284.
- (53) Song, K. S.; Williams, R. T. Introduction. In: *Self-Trapped Excitons*; Springer Berlin Heidelberg: Berlin, Heidelberg, 1996; pp 1–31.
- (54) Furukawa, M.; Mizuno, K.-I.; Matsui, A.; Tamai, N.; Yamazaki, I. Branching of Exciton Relaxation to the Free and Self-Trapped Exciton States. *Chem. Phys.* **1989**, *138*, 423–432.
- (55) Bässler, H. Charge Transport in Disordered Organic Semiconductors a Monte Carlo Simulation Study. *Phys. Status Solidi B* **1993**, *175*, 15–56.
- (56) Richards, T.; Bird, M.; Sirringhaus, H. A Quantitative Analytical Model for Static Dipolar Disorder Broadening of the Density of States at Organic Heterointerfaces. *J. Chem. Phys.* **2008**, *128*, 234905.
- (57) Zheng, Z.; Tummala, N. R.; Wang, T.; Coropceanu, V.; Brédas, J.-L. Charge-Transfer States at Organic-Organic Interfaces: Impact of Static and Dynamic Disorders. *Adv. Energy Mater.* **2019**, *9*, 1803926.
- (58) Reiser, P.; Konrad, M.; Fedai, A.; Léon, S.; Wenzel, W.; Friederich, P. Analyzing Dynamical Disorder for Charge Transport in Organic Semiconductors via Machine Learning. *J. Chem. Theory Comput.* **2021**, *17*, 3750–3759.
- (59) Li, C.; Gao, K.; Meng, R.; Yang, L.; Zhang, M. Effect of Intrachain Configuration Disorder on the Exciton Delocalization in -Conjugated Polymers. *Org. Electron.* **2017**, *48*, 342–347.
- (60) Gross, M.; Haroche, S. Superradiance: An Essay on the Theory of Collective Spontaneous Emission. *Phys. Rep.* **1982**, *93*, 301–396.
- (61) Kira, M.; Koch, S. W. Many-Body Correlations and Excitonic Effects in Semiconductor Spectroscopy. *Prog. Quantum Electron.* **2006**, *30*, 155–296.
- (62) Kira, M.; Koch, S. W. *Semiconductor Quantum Optics*; Cambridge University Press: Cambridge, England, 2011; pp 550–571.
- (63) Moody, G.; Kavir Dass, C.; Hao, K.; Chen, C.-H.; Li, L.-J.; Singh, A.; Tran, K.; Clark, G.; Xu, X.; Berghäuser, G.; Malic, E.; Knorr, A.; Li, X. Intrinsic Homogeneous Linewidth And Broadening Mechanisms Of Excitons In Monolayer Transition Metal Dichalcogenides. *Nat. Commun.* **2015**, *6*, 8315.
- (64) Zerah Harush, E.; Dubi, Y. Do Photosynthetic Complexes Use Quantum Coherence to Increase Their Efficiency? Probably Not. *Sci. Adv.* **2021**, *7*, No. eabc4631.
- (65) Keren, N.; Paltiel, Y. Photosynthetic Energy Transfer at the Quantum/Classical Border. *Trends Plant Sci.* **2018**, *23*, 497–506.
- (66) Cao, J.; Cogdell, R. J.; Coker, D. F.; Duan, H.-G.; Hauer, J.; Kleinekathofer, U.; Jansen, T. L.; Mančal, T.; Miller, R. D.; Ogilvie, J. P.; et al. Quantum Biology Revisited. *Sci. Adv.* **2020**, *6*, No. eaaz4888.
- (67) Yang, P.-Y.; Cao, J. Steady-State Analysis of Light-Harvesting Energy Transfer Driven by Incoherent Light: From Dimers to Networks. *J. Phys. Chem. Lett.* **2020**, *11*, 7204–7211.
- (68) Bourne Worster, S.; Stross, C.; Vaughan, F. M.; Linden, N.; Manby, F. R. Structure and Efficiency in Bacterial Photosynthetic Light Harvesting. *J. Phys. Chem. Lett.* **2019**, *10*, 7383–7390.
- (69) Kafle, T. R.; Kattel, B.; Wang, T.; Chan, W.-L. The Relationship Between the Coherent Size, Binding Energy and Dissociation Dynamics of Charge Transfer Excitons at Organic Interfaces. *J. Phys.: Condens. Matter.* **2018**, *30*, 454001.
- (70) Tretiak, S.; Saxena, A.; Martin, R. L.; Bishop, A. R. Conformational Dynamics of Photoexcited Conjugated Molecules. *Phys. Rev. Lett.* **2002**, *89*, 097402.
- (71) Demchenko, A. P.; Tomin, V. I.; Chou, P.-T. Breaking the Kasha Rule for More Efficient Photochemistry. *Chem. Rev.* **2017**, *117*, 13353–13381.
- (72) Xu, Y.; Xu, P.; Hu, D.; Ma, Y. Recent Progress in Hot Exciton Materials for Organic Light-Emitting Diodes. *Chem. Soc. Rev.* **2021**, *50*, 1030–1069.
- (73) Ishii, K.; Takeuchi, S.; Tahara, T. Pronounced Non-Condon Effect as the Origin of the Quantum Beat Observed in the Time-Resolved Absorption Signal from Excited-State cis-Stilbene. *J. Phys. Chem. A* **2008**, *112*, 2219–2227.
- (74) Kraner, S.; Scholz, R.; Plasser, F.; Koerner, C.; Leo, K. Exciton Size and Binding Energy Limitations in One-Dimensional Organic Materials. *J. Chem. Phys.* **2015**, *143*, 244905.
- (75) Zhu, X.-Y.; Yang, Q.; Muntwiler, M. Charge-Transfer Excitons at Organic Semiconductor Surfaces and Interfaces. *Acc. Chem. Res.* **2009**, *42*, 1779–1787.
- (76) Imahori, H.; Kobori, Y.; Kaji, H. Manipulation of Charge-Transfer States by Molecular Design: Perspective from "Dynamic Exciton". *Acc. Mater. Res.* **2021**, *2*, 501–514.
- (77) Varella, M. T. do N.; Stojanović, L.; Vuong, V. Q.; Irle, S.; Niehaus, T. A.; Barbatti, M. How the Size and Density of Charge-Transfer Excitons Depend on Heterojunction's Architecture. *J. Phys. Chem. C Nanomater. Interfaces* **2021**, *125*, 5458–5474.
- (78) Feierabend, M.; Brem, S.; Malic, E. Optical Fingerprint of Bright and Dark Localized Excitonic States in Atomically Thin 2D Materials. *Phys. Chem. Chem. Phys.* **2019**, *21*, 26077–26083.

- (79) Schmidgall, E. R.; Schwartz, I.; Cogan, D.; Gantz, L.; Don, Y.; Gershoni, D. Coherent Control of Dark Excitons in Semiconductor Quantum Dots. In *Quantum Dots for Quantum Information Technologies*; Springer International Publishing: Cham, 2017; pp 123–164.
- (80) Le Reste, L.; Hohlbein, J.; Gryte, K.; Kapanidis, A. N. Characterization of Dark Quencher Chromophores as Nonfluorescent Acceptors for Single-Molecule FRET. *Biophys. J.* **2012**, *102*, 2658–2668.
- (81) He, X. F. Excitons in Anisotropic Solids: The Model of Fractional-Dimensional Space. *Phys. Rev. B* **1991**, *43*, 2063–2068.
- (82) Zhang, Y. Applications of Huang-Rhys Theory in Semiconductor Optical Spectroscopy. *J. Semiconduct.* **2019**, *40*, 091102.
- (83) Brédas, J.-L.; Beljonne, D.; Coropceanu, V.; Cornil, J. Charge-Transfer and Energy-Transfer Processes in Pi-Conjugated Oligomers and Polymers: A Molecular Picture. *Chem. Rev.* **2004**, *104*, 4971–5004.
- (84) Cornil, J.; Beljonne, D.; Heller, C. M.; Campbell, I. H.; Laurich, B. K.; Smith, D. L.; Bradley, D. D. C.; Müllen, K.; Brédas, J. L. Photoluminescence Spectra of Oligo-Paraphenylenevinylenes: A Joint Theoretical and Experimental Characterization. *Chem. Phys. Lett.* **1997**, *278*, 139–145.
- (85) Kanemoto, K.; Sudo, T.; Akai, I.; Hashimoto, H.; Karasawa, T.; Aso, Y.; Otsubo, T. Intrachain Photoluminescence Properties of Conjugated Polymers as Revealed by Long Oligothiophenes and Polythiophenes Diluted in an Inactive Solid Matrix. *Phys. Rev. B* **2006**, *73*, 235203.
- (86) Devos, A.; Lannoo, M. Electron-Phonon Coupling for Aromatic Molecular Crystals: Possible Consequences for Their Superconductivity. *Phys. Rev. B Condens. Matter* **1998**, *58*, 8236–8239.
- (87) Alberga, D.; Perrier, A.; Ciofini, I.; Mangiatordi, G. F.; Lattanzi, G.; Adamo, C. Morphological and Charge Transport Properties of Amorphous and Crystalline P3HT and PBTTT: Insights from Theory. *Phys. Chem. Chem. Phys.* **2015**, *17*, 18742–18750.
- (88) Williams, R. T.; Song, K. S. The Self-Trapped Exciton. *J. Phys. Chem. Solids* **1990**, *51*, 679–716.
- (89) Katrich, G. S.; Kemnitz, K.; Malyukin, Y. V.; Ratner, A. M. Distinctive Features of Exciton Self-Trapping in Quasi-One-Dimensional Molecular Chains (J-Aggregates). *J. Lumin.* **2000**, *90*, 55–71.
- (90) Rashba, E. I. Theory of Strong Interactions of Electron Excitations with Lattice Vibrations in Molecular Crystals. 2. *Optika i Spektroskopiya* **1957**, *2*, 88–98.
- (91) Toyozawa, Y. Self-Trapping of an Electron by the Acoustical Mode of Lattice Vibration. I. *Prog. Theor. Phys.* **1961**, *26*, 29–44.
- (92) Ruseckas, A.; Samuel, I. D. W. Exciton Self-Trapping in MEH-PPV Films Studied by Ultrafast Emission Depolarization. *Phys. Status Solidi* **2006**, *3*, 263–266.
- (93) Banerji, N.; Cowan, S.; Vauthey, E.; Heeger, A. J. Ultrafast Relaxation of the Poly(3-Hexylthiophene) Emission Spectrum. *J. Phys. Chem. C Nanomater. Interfaces* **2011**, *115*, 9726–9739.
- (94) Binder, R.; Lauvergnat, D.; Burghardt, I. Conformational Dynamics Guides Coherent Exciton Migration in Conjugated Polymer Materials: First-Principles Quantum Dynamical Study. *Phys. Rev. Lett.* **2018**, *120*, 227401.
- (95) Ness, H.; Shevlin, S. A.; Fisher, A. J. Coherent Electron-Phonon Coupling and Polaron-Like Transport in Molecular Wires. *Phys. Rev. B* **2001**, *63*, 125422.
- (96) Wells, N. P.; Blank, D. A. Correlated Exciton Relaxation in Poly(3-Hexylthiophene). *Phys. Rev. Lett.* **2008**, *100*, 086403.
- (97) Busby, E.; Carroll, E. C.; Chinn, E. M.; Chang, L.; Moulé, A. J.; Larsen, D. S. Excited-State Self-Trapping and Ground-State Relaxation Dynamics in Poly(3-Hexylthiophene) Resolved with Broadband Pump-Dump-Probe Spectroscopy. *J. Phys. Chem. Lett.* **2011**, *2*, 2764–2769.
- (98) Lenderink, E.; Duppen, K.; Wiersma, D. A. Femtosecond Twisting and Coherent Vibrational Motion in the Excited State of Tetraphenylethylene. *J. Phys. Chem.* **1995**, *99*, 8972–8977.
- (99) Chang, M.-H.; Hoffmann, M.; Anderson, H. L.; Herz, L. M. Dynamics of Excited-State Conformational Relaxation and Electronic Delocalization in Conjugated Porphyrin Oligomers. *J. Am. Chem. Soc.* **2008**, *130*, 10171–10178.
- (100) Roy, P.; Jha, A.; Yasrapudi, V. B.; Ram, T.; Puttaraju, B.; Patil, S.; Dasgupta, J. Ultrafast Bridge Planarization in Donor-n-Acceptor Copolymers Drives Intramolecular Charge Transfer. *Nature Commun.* **2017**, *8*, 1716.
- (101) Hintschich, S. I.; Dias, F. B.; Monkman, A. P. Dynamics of Conformational Relaxation in Photoexcited Oligofluorenes and Polyfluorene. *Phys. Rev. B* **2006**, *74*, 045210.
- (102) Clark, J.; Nelson, T.; Tretiak, S.; Cirmi, G.; Lanzani, G. Femtosecond torsional relaxation. *Nat. Phys.* **2012**, *8*, 225–231.
- (103) Lauchlan, L.; Etemad, S.; Chung, T. C.; Heeger, A. J.; MacDiarmid, A. G. Photoexcitations in Polyacetylene. *Phys. Rev. B* **1981**, *24*, 3701.
- (104) Bloor, D. Electrical Conductivity. In *Comprehensive Polymer Science and Supplements*; Booth, C., Price, C., Eds.; Pergamon Press: Oxford, 1989; Vol. 2, pp 687–705.
- (105) Leng, J. M.; McCall, R. P.; Cromack, K. R.; Sun, Y.; Manohar, S. K.; MacDiarmid, A. G.; Epstein, A. J. Photoexcited Solitons and Polarons in Pernigraniline-Based Polymers. *Phys. Rev. B Condens. Matter* **1993**, *48*, 15719–15731.
- (106) Nechtschein, M.; Devreux, F.; Greene, R. L.; Clarke, T. C.; Street, G. B. One-Dimensional Spin Diffusion in Polyacetylene, (CH)x. *Phys. Rev. Lett.* **1980**, *44*, 356–359.
- (107) Yamabe, T.; Tanaka, K.; Yamanaka, S.; Koike, T.; Fukui, K. Intersoliton Hopping in Lightly Doped Polyacetylene: Assistance by Vibrational Motion of the Dopant. *J. Chem. Phys.* **1985**, *82*, 5737–5741.
- (108) Korovyanko, O. J.; Gontia, I. I.; Vardeny, Z. V.; Masuda, T.; Yoshino, K. Ultrafast Dynamics of Excitons and Solitons in Disubstituted Polyacetylene. *Phys. Rev. B* **2003**, *67*, 035114.
- (109) Bishop, A. R.; Campbell, D. K.; Lomdahl, P. S.; Horovitz, B.; Phillipot, S. R. Non-Linear Dynamics, Breathers and Photoinduced Absorption in Polyacetylene. *Synth. Met.* **1984**, *9*, 223–239.
- (110) Bishop, A. R.; Campbell, D. K.; Lomdahl, P. S.; Horovitz, B.; Phillipot, S. R. Breathers and Photoinduced Absorption in Polyacetylene. *Phys. Rev. Lett.* **1984**, *52*, 671.
- (111) Takimoto, J.-I.; Sasai, M. Excited States and Their Relaxation Dynamics in *Trans*-Polyacetylene. *Phys. Rev. B* **1989**, *39*, 8511.
- (112) Wang, C. L.; Martino, F. Photogenerated Exciton-Breather State in *Trans*-Polyacetylene. *Phys. Rev. B* **1986**, *34*, 5540.
- (113) Tretiak, S.; Saxena, A.; Martin, R. L.; Bishop, A. R. Photoexcited Breathers in Conjugated Polyenes: An Excited-State Molecular Dynamics Study. *Proc. Natl. Acad. Sci. U. S. A.* **2003**, *100*, 2185–2190.
- (114) Hidayat, R.; Tatsuhara, S.; Kim, D. W.; Ozaki, M.; Yoshino, K.; Teraguchi, M.; Masuda, T. Time-Resolved Study of Luminescence in Highly Luminescent Disubstituted Polyacetylene and Its Blend with Poorly Luminescent Monosubstituted Polyacetylene. *Phys. Rev. B Condens. Matter* **2000**, *61*, 10167–10173.
- (115) Zhu, Z.; Crochet, J.; Arnold, M. S.; Hersam, M. C.; Ulbricht, H.; Resasco, D.; Hertel, T. Pump-Probe Spectroscopy of Exciton Dynamics in (6,5) Carbon Nanotubes. *J. Phys. Chem. C Nanomater. Interfaces* **2007**, *111*, 3831–3835.
- (116) Styers-Barnett, D. J.; Ellison, S. P.; Mehl, B. P.; Westlake, B. C.; House, R. L.; Park, C.; Wise, K. E.; Papanikolas, J. M. Exciton Dynamics and Biexciton Formation in Single-Walled Carbon Nanotubes Studied with Femtosecond Transient Absorption Spectroscopy. *J. Phys. Chem. C Nanomater. Interfaces* **2008**, *112*, 4507–4516.
- (117) Knupfer, M.; Fink, J.; Zojer, E.; Leising, G.; Scherf, U.; Müllen, K. Localized and Delocalized Singlet Excitons in Ladder-Type Poly(Paraphenylenene). *Phys. Rev. B Condens. Matter* **1998**, *57*, R4202–R4205.
- (118) Kraabel, B.; Joffre, M.; Lapersonne-Meyer, C.; Schott, M. Singlet Exciton Relaxation in Isolated Polydiacetylene Chains Studied by Subpicosecond Pump-Probe Experiments. *Phys. Rev. B Condens. Matter* **1998**, *58*, 15777–15788.
- (119) Kobayashi, T.; Yoshizawa, M.; Stamm, U.; Taiji, M.; Hasegawa, M. Relaxation Dynamics of Photoexcitations in Polydiacetylenes and Polythiophene. *J. Opt. Soc. Am. B* **1990**, *7*, 1558.

- (120) Haacke, S.; Berréhar, J.; Lapersonne-Meyer, C.; Schott, M. Dynamics of Singlet Excitons in 1D Conjugated Polydiacetylene Chains: A Femtosecond Fluorescence Study. *Chem. Phys. Lett.* **1999**, *308*, 363–368.
- (121) Léguiller, R.; Berréhar, J.; Ganière, J. D.; Lapersonne-Meyer, C.; Lavallard, P.; Schott, M. Fluorescence yield and lifetime of isolated polydiacetylene chains: Evidence for a one-dimensional exciton band in a conjugated polymer. *Phys. Rev. B* **2002**, *66*, 125205.
- (122) Ondarse-Alvarez, D.; Nelson, T.; Lupton, J. M.; Tretiak, S.; Fernandez-Alberti, S. Let Digons Be Bygones: The Fate of Excitons in Curved  $\pi$ -Systems. *J. Phys. Chem. Lett.* **2018**, *9*, 7123–7129.
- (123) Thiessen, A.; Würsch, D.; Jester, S.-S.; Aggarwal, A. V.; Idelson, A.; Bange, S.; Vogelsang, J.; Höger, S.; Lupton, J. M. Exciton Localization in Extended  $\pi$ -Electron Systems: Comparison of Linear and Cyclic Structures. *J. Phys. Chem. B* **2015**, *119*, 9949–9958.
- (124) Scholes, G. D.; Rumbles, G. Excitons in Nanoscale Systems. *Nat. Mater.* **2006**, *5*, 683–696.
- (125) Davydov, A. S. *Theory of Molecular Excitons*; Springer: New York, 2013; p 319.
- (126) Spano, F. C.; Kuklinski, J. R.; Mukamel, S. Cooperative Radiative Dynamics in Molecular Aggregates. *J. Chem. Phys.* **1991**, *94*, 7534–7544.
- (127) Kasha, M. Characterization of Electronic Transitions in Complex Molecules. *Discuss. Faraday Soc.* **1950**, *9*, 14–19.
- (128) Hestand, N. J.; Spano, F. C. Molecular Aggregate Photophysics beyond the Kasha Model: Novel Design Principles for Organic Materials. *Acc. Chem. Res.* **2017**, *50*, 341–350.
- (129) Beenken, W. J. D.; Dahlbom, M.; Kjellberg, P.; Pullerits, T. Potential Surfaces and Delocalization of Excitons In Dimers. *J. Chem. Phys.* **2002**, *117*, 5810–5820.
- (130) Malyukin, Yu Coexistence of Free and Self-Trapped Excitons in Disordered J-Aggregates. *Phys. Stat. Solidi C* **2006**, *3*, 3386–3393.
- (131) Sorokin, A. V.; Pereverzev, N. V.; Grankina, I. I.; Yefimova, S. L.; Malyukin, Y. V. Evidence of Exciton Self-Trapping in Pseudoisocyanine J-Aggregates Formed in Layered Polymer Films. *J. Phys. Chem. C Nanomater. Interfaces* **2015**, *119*, 27865–27873.
- (132) Malyukin, Y. V.; Sorokin, A. V.; Semynozhenko, V. P. Features of Exciton Dynamics in Molecular Nanoclusters (J-Aggregates): Exciton Self-Trapping (Review Article). *Low Temp. Phys.* **2016**, *42*, 429–440.
- (133) Spano, F. C.; Silva, C. H- and J-Aggregate Behavior in Polymeric Semiconductors. *Annu. Rev. Phys. Chem.* **2014**, *65*, 477–500.
- (134) Spano, F. C. The Spectral Signatures of Frenkel Polarons in H- and J-aggregates. *Acc. Chem. Res.* **2010**, *43*, 429–439.
- (135) Spano, F. C.; Yamagata, H. Vibronic Coupling in J-Aggregates and Beyond: A Direct Means of Determining the Exciton Coherence Length from the Photoluminescence Spectrum. *J. Phys. Chem. B* **2011**, *115*, 5133–5143.
- (136) Spano, F. C.; Clark, J.; Silva, C.; Friend, R. H. Determining Exciton Coherence from the Photoluminescence Spectral Line Shape in Poly(3-Hexylthiophene) Thin Films. *J. Chem. Phys.* **2009**, *130*, 074904.
- (137) De Rossi, U.; Dähne, S.; Gomez, U.; Port, H. Evidence for Incoherent Energy Transfer Processes in J-Aggregates with Davydov Splitting. *Chem. Phys. Lett.* **1998**, *287*, 395–402.
- (138) Kobayashi, T. *J-Aggregates*; Kobayashi, T., Ed.; World Scientific Publishing: Singapore, Singapore, 2012; Vol. 2.
- (139) Eisfeld, A.; Vlaming, S. M.; Malyshev, V. A.; Knoester, J. Excitons in Molecular Aggregates with Lévy-Type Disorder: Anomalous Localization and Exchange Broadening of Optical Spectra. *Phys. Rev. Lett.* **2010**, *105*, 137402.
- (140) Matsui, A. H. Excitonic Processes in Aromatic Molecular Crystals of Strong Exciton-Phonon Coupling. *Pure Appl. Chem.* **1995**, *67*, 429–436.
- (141) Hoche, J.; Schmitt, H.-C.; Humeniuk, A.; Fischer, I.; Mitríć, R.; Röhr, M. I. S. The Mechanism of Excimer Formation: An Experimental and Theoretical Study on the Pyrene Dimer. *Phys. Chem. Chem. Phys.* **2017**, *19*, 25002–25015.
- (142) Pensack, R. D.; Ashmore, R. J.; Paoletta, A. L.; Scholes, G. D. The Nature of Excimer Formation in Crystalline Pyrene Nanoparticles. *J. Phys. Chem. C Nanomater. Interfaces* **2018**, *122*, 21004–21017.
- (143) Birks, J. B. *Excimers. Rep. Prog. Phys.* **1975**, *38*, 903–974.
- (144) Han, G.; Kim, D.; Park, Y.; Bouffard, J.; Kim, Y. Excimers Beyond Pyrene: A Far-Red Optical Proximity Reporter and its Application to the Label-Free Detection of DNA. *Angew. Chem., Int. Ed.* **2015**, *54*, 3912–3916.
- (145) Winnik, F. M. Photophysics of Preassociated Pyrenes in Aqueous Polymer Solutions and in Other Organized Media. *Chem. Rev.* **1993**, *93*, 587–614.
- (146) Sung, J.; Kim, P.; Fimmel, B.; Würthner, F.; Kim, D. Direct Observation of Ultrafast Coherent Exciton Dynamics in Helical  $\pi$ -Stacks of Self-Assembled Perylene Bisimides. *Nat. Commun.* **2015**, *6*, 8646.
- (147) Kaufmann, C.; Kim, W.; Nowak-Król, A.; Hong, Y.; Kim, D.; Würthner, F. Ultrafast Exciton Delocalization, Localization, and Excimer Formation Dynamics in a Highly Defined Perylene Bisimide Quadruple  $\pi$ -Stack. *J. Am. Chem. Soc.* **2018**, *140*, 4253–4258.
- (148) Dimitriev, O. P.; Piryatinski, Yu.P.; Slominskii, Yu.L. Excimer Emission in J-Aggregates. *J. Phys. Chem. Lett.* **2018**, *9*, 2138–2143.
- (149) Bredas, J.-L.; Silbey, R.; Boudreux, D. S.; Chance, R. R. Chain-Length Dependence of Electronic and Electrochemical Properties of Conjugated Systems: Polyacetylene, Polyphenylene, Polythiophene, and Polypyrrole. *J. Am. Chem. Soc.* **1983**, *105*, 6555.
- (150) Tolmachev, A. I.; Slominsky, Yu.L.; Ishchenko, A. A. In *Near-Infrared Dyes for High Technology Applications*; Dahne, S., Resh-Genge, U., Wolfbeis, U., Eds.; Kluwer Academic Publishers: New York, 1998; pp 384–515.
- (151) Hunig, S.; Linhart, F. 2-Step Redox Systems. 19. UV-Vis Spectroscopy of Vinylogous and Azavinylogous Redox Systems. *Justus Liebigs Ann. Chem.* **1975**, *1975*, 2116–2129.
- (152) Kuhn, C. Step Potential Model for Non-Linear Optical Properties of Polyenes, Push-Pull Polyenes and Cyanines and the Motion of Solitons in Long-Chain Cyanines. *Synth. Met.* **1991**, *43*, 3681–3688.
- (153) Tolbert, L. M.; Zhao, X. Beyond the Cyanine Limit: Peierls Distortion and Symmetry Collapse in a Polymethine Dye. *J. Am. Chem. Soc.* **1997**, *119*, 3253–3258.
- (154) Lepkowicz, R. S.; Przhonska, O. V.; Hales, J. M.; Fu, J.; Hagan, D. J.; Van Stryland, E. W.; Bondar, M. V.; Slominsky, Y. L.; Kachkovski, A. D. Nature of the Electronic Transitions in Thiacarbocyanines with a Long Polymethine Chain. *Chem. Phys.* **2004**, *305*, 259–270.
- (155) Callahan, R. W.; Keene, F. R.; Meyer, T. J.; Salmon, D. J. Intervalence Transfer and Electron Transfer in the Mixed-Valence Ion [(bpy)<sub>2</sub>ClRu(pyz)RuCl(bpy)<sub>2</sub>]<sup>3+</sup>. *J. Am. Chem. Soc.* **1977**, *99*, 1064.
- (156) Kachkovski, O. D.; Tolmachov, O. I.; Slominskii, Y. L.; Kudinova, M. O.; Derevyanko, N. O.; Zhukova, O. O. Electronic Properties of Polymethine Systems 7: Soliton Symmetry Breaking and Spectral Features of Dyes with a Long Polymethine Chain. *Dyes Pigm.* **2005**, *64*, 207–216.
- (157) Eskandari, M.; Roldao, J. C.; Cerezo, J.; Milian-Medina, B.; Gierschner, J. Counterion-Mediated Crossing of the Cyanine Limit in Crystals and Fluid Solution: Bond Length Alternation and Spectral Broadening Unveiled by Quantum Chemistry. *J. Am. Chem. Soc.* **2020**, *142*, 2835–2843.
- (158) Schwartz, B. J. Conjugated Polymers as Molecular Materials: How Chain Conformation and Film Morphology Influence Energy Transfer and Interchain Interactions. *Annu. Rev. Phys. Chem.* **2003**, *54*, 141–172.
- (159) Menšík, M.; Rais, D.; Pfleger, J. Time Resolved Excitation Dynamics in Emeraldine Base. *Chem. Phys.* **2015**, *456*, 79–84.
- (160) Dimitriev, O. P.; Lavrik, N. V. Protonation and Charge Transfer in Polyaniline: An Optical Absorption Study of The Mixed Solutions. *Synth. Met.* **1997**, *90*, 1–4.
- (161) Dimitriev, O. P.; Ogurtsov, N. A.; Pud, A. A.; Smertenko, P. S.; Piryatinski, Yu.P.; Noskov, Yu.V.; Kutsenko, A. S.; Shapoval, G. S. Probing of Charge and Energy Transfer in Hybrid Systems Of Aniline-

- 3-Methylthiophene Copolymer with CdS and CdSe Nanoparticles. *J. Phys. Chem. C* **2008**, *112*, 14745–14753.
- (162) Zhao, J.; Zheng, Y. Exploring and Elaborating Excited-State Intramolecular Double-Proton Transfer Mechanisms. *Hydrogen-Bonding Research in Photochemistry, Photobiology, and Optoelectronic Materials*; World Scientific (Europe), 2019; pp 409–432.
- (163) Zhao, J.; Yao, H.; Liu, J.; Hoffmann, M. R. New Excited-State Proton Transfer Mechanisms for 1,8-Dihydroxydibenzo[*a,h*]phenazine. *J. Phys. Chem. A* **2015**, *119*, 681–688.
- (164) Tseng, H.-W.; Shen, J.-Y.; Kuo, T.-Y.; Tu, T.-S.; Chen, Y.-A.; Demchenko, A. P.; Chou, P.-T. Excited-State Intramolecular Proton-Transfer Reaction Demonstrating Anti-Kasha Behavior. *Chem. Sci.* **2016**, *7*, 655–665.
- (165) Cui, Y.; Zhao, H.; Jiang, L.; Li, P.; Ding, Y.; Song, P.; Xia, L. Solvation Effect on the Excited-State Intramolecular Proton Transfer Mechanism of 1-Morpholinylmethyl-2-Naphthol. *Comput. Theor. Chem.* **2015**, *1074*, 125–130.
- (166) Zhao, J.; Song, P.; Ma, F. A New Excited-State Intramolecular Proton Transfer Mechanism for C2 Symmetry of 10-hydroxybenzoquinoline. *Commun. Comput. Chem.* **2018**, *2*, 117–130.
- (167) Huang, J.-D. Straightforward Stepwise Excited State Dual Proton Transfer Mechanism for 9-10-HBQ System. *Commun. Comput. Chem.* **2018**, *5*, 27–36.
- (168) Driscoll, E.; Sorenson, S.; Dawlaty, J. M. Ultrafast Intramolecular Electron and Proton Transfer in Bis(imino)isoindole Derivatives. *J. Phys. Chem. A* **2015**, *119*, 5618–5625.
- (169) Paul, S.; Paul, T. K.; Taraphder, S. Reaction Coordinate, Free Energy, and Rate of Intramolecular Proton Transfer in Human Carbonic Anhydrase II. *J. Phys. Chem. B* **2018**, *122*, 2851–2866.
- (170) Demchenko, A. P.; Tang, K.-C.; Chou, P.-T. Excited-State Proton Coupled Charge Transfer Modulated By Molecular Structure And Media Polarization. *Chem. Soc. Rev.* **2013**, *42*, 1379–1408.
- (171) Chen, C.-L.; Chen, Y.-T.; Demchenko, A. P.; Chou, P.-T. Amino Proton Donors in Excited-State Intramolecular Proton-Transfer Reactions. *Nat. Rev. Chem.* **2018**, *2*, 131–143.
- (172) Welsch, R.; Driscoll, E.; Dawlaty, J. M.; Miller, T. F., III Molecular Seesaw: How Increased Hydrogen Bonding Can Hinder Excited-State Proton Transfer. *J. Phys. Chem. Lett.* **2016**, *7*, 3616–3620.
- (173) Guo, Y.; Dahal, D.; Kuang, Z.; Wang, X.; Song, H.; Guo, Q.; Pang, Y.; Xia, A. Ultrafast Excited State Intramolecular Proton/Charge Transfers in Novel NIR-Emitting Molecules. *AIP Adv.* **2019**, *9*, 015229.
- (174) Zhao, L.; Wildman, A.; Pavošević, F.; Tully, J. C.; Hammes-Schiffer, S.; Li, X. Excited State Intramolecular Proton Transfer with Nuclear-Electronic Orbital Ehrenfest Dynamics. *J. Phys. Chem. Lett.* **2021**, *12*, 3497–3502.
- (175) Yoneda, Y.; Sotome, H.; Mathew, R.; Lakshmann, Y. A.; Miyasaka, H. Non-Condon Effect on Ultrafast Excited-State Intramolecular Proton Transfer. *J. Phys. Chem. A* **2020**, *124*, 265–271.
- (176) Tolbert, L. M.; Solntsev, K. M. Excited-State Proton Transfer: From Constrained Systems to “Super” Photoacids to Superfast Proton Transfer. *Acc. Chem. Res.* **2002**, *35*, 19–27.
- (177) Vander Donckt, E. *Progress in Reaction Kinetics*; Porter, G., Ed.; Pergamon Press: Oxford, 1970; Vol. 5, p 273.
- (178) Weller, A. Quantitative Untersuchungen der Fluoreszenzumwandlung bei Naphthalen. *Z. Elektrochem.* **1952**, *56*, 662–668.
- (179) Cotter, L. F.; Brown, P. J.; Nelson, R. C.; Takematsu, K. Divergent Hammett Plots of the Ground- and Excited-State Proton Transfer Reactions of 7-Substituted-2-Naphthol Compounds. *J. Phys. Chem. B* **2019**, *123*, 4301–4310.
- (180) Zhou, P.; Han, K. Unraveling the Detailed Mechanism of Excited-State Proton Transfer. *Acc. Chem. Res.* **2018**, *51*, 1681–1690.
- (181) Pines, E.; Pines, D.; Gajst, O.; Huppert, D. Reversible Intermolecular-Coupled-Intramolecular (RICI) Proton Transfer Occuring on the Reaction-Radius *a* of 2-Naphthol-6,8-Disulfonate Photoacid. *J. Chem. Phys.* **2020**, *152*, 074205.
- (182) Gajst, O.; Pinto da Silva, L.; Esteves da Silva, J. C. G.; Huppert, D. Excited-State Proton Transfer from the Photoacid 2-Naphthol-8-sulfonate to Acetonitrile/Water Mixtures. *J. Phys. Chem. A* **2018**, *122*, 6166–6175.
- (183) Agmon, N. Elementary Steps in Excited-State Proton Transfer. *J. Phys. Chem. A* **2005**, *109*, 13–35.
- (184) Moreira, P. F.; Giestas, L.; Yihwa, C.; Vautier-Giongo, C.; Quina, F. H.; Maçanita, A. L.; Lima, J. C. Ground- and Excited-State Proton Transfer in Anthocyanins: From Weak Acids to Superphotoacids. *J. Phys. Chem. A* **2003**, *107*, 4203–4210.
- (185) Dereka, B.; Rosspeintner, A.; Li, Z.; Liska, R.; Vauthey, E. Direct Visualization of Excited-State Symmetry Breaking Using Ultrafast Time-Resolved Infrared Spectroscopy. *J. Am. Chem. Soc.* **2016**, *138*, 4643–4649.
- (186) Dereka, B.; Rosspeintner, A.; Stęzycki, R.; Ruckebusch, C.; Gryko, D. T.; Vauthey, E. Excited-State Symmetry Breaking in a Quadrupolar Molecule Visualized in Time and Space. *J. Phys. Chem. Lett.* **2017**, *8*, 6029–6034.
- (187) Ivanov, A. I.; Dereka, B.; Vauthey, E. A Simple Model of Solvent-Induced Symmetry-Breaking Charge Transfer in Excited Quadrupolar Molecules. *J. Chem. Phys.* **2017**, *146*, 164306.
- (188) Dereka, B.; Rosspeintner, A.; Krzeszewski, M.; Gryko, D. T.; Vauthey, E. Symmetry-Breaking Charge Transfer and Hydrogen Bonding: Toward Asymmetrical Photochemistry. *Angew. Chem., Int. Ed.* **2016**, *55*, 15624–15628.
- (189) Eswaramoorthi, S.; Thamaraiselvi, P.; Duraimurugan, K.; Beneto, A. J.; Siva, A.; Nair, B. U. Charge Instability of Symmetry Broken Dipolar States in Quadrupolar and Octupolar Triphenylamine Derivatives. *Chem. Commun. (Camb.)* **2014**, *50*, 6902–6905.
- (190) Stahl, R.; Lambert, C.; Kaiser, C.; Wortmann, R.; Jakober, R. Triarylboranes: Symmetry Breaking in Ground and Excited State. *Chem.—Eur. J.* **2006**, *12*, 2358–2370.
- (191) Piet, J. J.; Schuddeboom, W.; Wegewijs, B. R.; Grozema, F. C.; Warman, J. M. Symmetry Breaking in the Relaxed S1 Excited State of Bianthryl Derivatives in Weakly Polar Solvents. *J. Am. Chem. Soc.* **2001**, *123*, 5337–5347.
- (192) Ma, Y.; Sette, F.; Meigs, G.; Modesti, S.; Chen, C. T. Breaking of Ground-State Symmetry in Core-Excited Ethylene and Benzene. *Phys. Rev. Lett.* **1989**, *63*, 2044–2047.
- (193) Schalk, O.; Boguslavskiy, A. E.; Stolow, A.; Schuurman, M. S. Through-Bond Interactions and the Localization of Excited-State Dynamics. *J. Am. Chem. Soc.* **2011**, *133*, 16451–16458.
- (194) Bleger, D.; Yu, Z.; Hecht, S. Toward Optomechanics: Maximizing the Photodeformation of Individual Molecules. *Chem. Commun.* **2011**, *47*, 12260–12266.
- (195) Yao, H.-H.; Cheng, H.-H.; Cheng, C.-H.; Lin, C.-K.; Yang, J.-S.; Chen, I. C. Charge-Transfer and Isomerization Reactions of Trans-4-(N-Arylamino)Stilbenes. *Phys. Chem. Chem. Phys.* **2016**, *18*, 28164–28174.
- (196) Karlsson, J. K. G.; Laude, A.; Hall, M. J.; Harriman, A. Photo-Isomerization of the Cyanine Dye Alexa-Fluor 647 (AF-647) in the Context of DSTORM Super-Resolution Microscopy. *Chemistry* **2019**, *25*, 14983–14998.
- (197) Yu, X.; Wang, Z.; Buchholz, M.; Füllgrabe, N.; Grosjean, S.; Bebensee, F.; Bräse, S.; Wöll, C.; Heinke, L. Cis-to-Trans Isomerization of Azobenzene Investigated by Using Thin Films of Metal Organic Frameworks. *Phys. Chem. Chem. Phys.* **2015**, *17*, 22721–22725.
- (198) Kwasniewski, S. P.; Claes, L.; Francois, J.-P.; Deleuze, M. S. High Level Theoretical Study of the Structure and Rotational Barriers of Trans-Stilbene. *J. Chem. Phys.* **2003**, *118*, 7823–7836.
- (199) Dou, Y.; Allen, R. E. Detailed Dynamics of a Complex Photochemical Reaction: Cis-Trans Photoisomerization of Stilbene. *J. Chem. Phys.* **2003**, *119*, 10658–10666.
- (200) Kovalenko, S. A.; Dobryakov, A. L.; Ioffe, I.; Ernsting, N. P. Evidence for the Phantom State in Photoinduced Cis-Trans Isomerization of Stilbene. *Chem. Phys. Lett.* **2010**, *493*, 255–258.
- (201) Pronkin, P.; Tatikolov, A. Isomerization and Properties of Isomers of Carbocyanine Dyes. *Sci.* **2019**, *1*, 19.
- (202) Krishnamoorthy, G.; Asato, A. E.; Liu, R. S. H. Conformational Isomerizations of Symmetrically Substituted Styrenes. No-Reaction Photoreactions by Hula-Twist. *Chem. Commun.* **2003**, 2170–2171.

- (203) Liu, R. S. H.; Hammond, G. S. The Case of Medium-Dependent Dual Mechanisms For Photoisomerization: One-Bond-Flip and Hula-Twist. *Proc. Natl. Acad. Sci. U.S.A.* **2000**, *97*, 11153–11158.
- (204) Liu, R. S. H.; Hammond, G. S. Examples of Hula-Twist in Photochemical *cis-trans* Isomerization. *Chem.—Eur. J.* **2001**, *7*, 4536–4545.
- (205) Budyka, M. F. Diarylethene Photoisomerization and Photocyclization Mechanisms. *Russ. Chem. Rev.* **2012**, *81*, 477–493.
- (206) Gerwien, A.; Schildhauer, M.; Thumser, S.; Mayer, P.; Dube, H. Direct evidence for hula twist and single-bond rotation photoproducts. *Nat. Commun.* **2018**, *9*, 2510.
- (207) Yang, L.-Y.; Harigai, M.; Imamoto, Y.; Kataoka, M.; Ho, T.-I.; Andrioukhina, E.; Federova, O.; Shevyakov, S.; Liu, R. S. H. Stilbene Analogs in Hula-Twist Photoisomerization. *Photochem. Photobiol. Sci.* **2006**, *5*, 874–882.
- (208) Sajadi, M.; Dobryakov, A. L.; Garbin, E.; Ernsting, N. P.; Kovalenko, S. A. Time-Resolved Fluorescence Spectra of Cis-Stilbene in Hexane and Acetonitrile. *Chem. Phys. Lett.* **2010**, *489*, 44–47.
- (209) Adamska, L.; Nayyar, I.; Chen, H.; Swan, A. K.; Oldani, N.; Fernandez-Alberti, S.; Golder, M. R.; Jasti, M. R.; Doorn, S. K.; Tretiak, S. Self-Trapping of Excitons, Violation of Condon Approximation, and Efficient Fluorescence in Conjugated Cycloparaphenylenes. *Nano Lett.* **2014**, *14*, 6539–6546.
- (210) Condon, E. U. Nuclear Motions Associated with Electron Transitions in Diatomic Molecules. *Phys. Rev.* **1928**, *32*, 858–872.
- (211) Jo, W.-K.; Tayade, R. J. Recent Developments in Photocatalytic Dye Degradation Upon Irradiation With Energy-Efficient Light Emitting Diodes. *Chin. J. Catal.* **2014**, *35*, 1781–1792.
- (212) Moses, B.; You, Y. Emerging Strategies For Controlling Drug Release by Using Visible/Near IR Light. *Med. Chem.* **2013**, *3*, 192–198.
- (213) Ashfold, M. N. R.; Cronin, B.; Devine, A. L.; Dixon, R. N.; Nix, M. G. D. The Role of  $\pi\sigma^*$  Excited States in the Photodissociation of Heteroaromatic Molecules. *Science* **2006**, *312*, 1637–1640.
- (214) Huang, J. B.; Zeng, G. S.; Li, X. S.; Cheng, X. C.; Tong, H. Theoretical Studies on Bond Dissociation Enthalpies for Model Compounds of Typical Plastic Polymers. *IOP Conf. Ser.: Earth Environ. Sci.* **2018**, *167*, 012029.
- (215) Kuzina, S. I.; Bol'shakov, A. I.; Kulikov, A. V.; Mikhailov, A. I. Low-Temperature Photolysis of Benzoyl Peroxide. *Russ. J. Phys. Chem.* **2020**, *94*, 189–195.
- (216) Peterson, J. A.; Wijesooriya, C.; Gehrmann, E. J.; Mahoney, K. M.; Goswami, P. P.; Albright, T. R.; Syed, A.; Dutton, A. S.; Smith, E. A.; Winter, A. H. Family of BODIPY Photocages Cleaved by Single Photons of Visible/near-Infrared Light. *J. Am. Chem. Soc.* **2018**, *140*, 7343–7346.
- (217) Erbas-Cakmak, S.; Akkaya, E. U. Cascading of Molecular Logic Gates for Advanced Functions: A Self Reporting, Activatable Photosensitizer. *Angew. Chem., Int. Ed.* **2013**, *52*, 11364–11368.
- (218) Erbas-Cakmak, S.; Akkaya, E. U. Toward Singlet Oxygen Delivery at a Measured Rate: A Self Reporting Photosensitizer. *Org. Lett.* **2014**, *16*, 2946–2949.
- (219) Lv, W.; Li, Y.; Li, F.; Lan, X.; Zhang, Y.; Du, L.; Zhao, Q.; Phillips, D. L.; Wang, W. Upconversion-like Photolysis of BODIPY-Based Prodrugs via a One-Photon Process. *J. Am. Chem. Soc.* **2019**, *141*, 17482–17486.
- (220) Arian, D.; Kovbasyuk, L.; Mokhir, A. 1,9-Dialkoxyanthracene as a  $1\text{O}_2$ -Sensitive Linker. *J. Am. Chem. Soc.* **2011**, *133*, 3972–3980.
- (221) Offenbartl-Stiegert, D.; Clarke, T. M.; Bronstein, H.; Nguyen, H. P.; Howorka, S. Solvent-Dependent Photophysics of a Red-Shifted, Biocompatible Coumarin Photocage. *Org. Biomol. Chem.* **2019**, *17*, 6178–6183.
- (222) Yamaji, M.; Horimoto, A.; Marciak, B. Laser Photolysis Studies of  $\omega$ -Bond Dissociation In Aromatic Carbonyls With a C-C Triple Bond Stimulated by Triplet Sensitization. *Phys. Chem. Chem. Phys.* **2017**, *19*, 17028–17035.
- (223) Khudyakov, I. V.; Turro, N. J. Laser Flash Photolysis of Photoinitiators: ESR, Optical, and IR Spectroscopy Detection of Transients. In *Carbon-Centered Free Radicals and Radical Cations*; Forbes, M. D. E., Ed.; John Wiley & Sons, 2010; pp 249–279.
- (224) Qian, T.; Chen, F.; Chen, Y.; Wang, Y.-X.; Hu, W. Photolysis of Polymeric Self-Assembly Controlled by Donor-Acceptor Interaction. *Chem. Commun.* **2017**, *53*, 11822–11825.
- (225) Vorob'ev, A. Y.; Dranova, T. Y.; Moskalensky, A. E. Photolysis of Dimethoxynitrobenzyl-“Caged” Acids Yields Fluorescent Products. *Sci. Rep.* **2019**, *9*, 13421.
- (226) Lin, Q.; Yang, L.; Wang, Z.; Hua, Y.; Zhang, D.; Bao, B.; Bao, C.; Gong, X.; Zhu, L. Coumarin Photocaging Groups Modified with an Electron-Rich Styryl Moiety at the 3-Position: Long-Wavelength Excitation, Rapid Photolysis, and Photobleaching. *Angew. Chem., Int. Ed. Engl.* **2018**, *57*, 3722–3726.
- (227) Jönsson, E. S.; Lee, T. Y.; Viswanathan, K.; Hoyle, C. E.; Roper, T. M.; Guymon, C. A.; Nason, C.; Khudyakov, I. V. Photoinduced Free Radical Polymerization Using Self-Initiating Monomers. *Prog. Org. Coat.* **2005**, *52*, 63–72.
- (228) Zhang, X.; Xi, W.; Huang, S.; Long, K.; Bowman, C. N. Wavelength-Selective Sequential Polymer Network Formation Controlled with a Two-Color Responsive Initiation System. *Macromolecules* **2017**, *50*, 5652–5660.
- (229) Huang, C.; Zheng, M.; Xu, J.; Zhang, Y. Photo-Induced Cycloaddition Reactions of  $\alpha$ -Diketones and Transformations of the Photocycloadducts. *Molecules* **2013**, *18*, 2942–2966.
- (230) Liu, Q.; Wang, J.; Li, D.; Yang, C.; Xia, W. Photoinduced Intermolecular [4 + 2] Cycloaddition Reaction for Construction of Benzobicyclo[2.2.2]octane Skeletons. *J. Org. Chem.* **2017**, *82*, 1389–1402.
- (231) Junkers, T. [2 + 2] Photo-Cycloadditions for Polymer Modification and Surface Decoration. *Eur. Polym. J.* **2015**, *62*, 273–280.
- (232) Kaur, G.; Singh, G.; Singh, J. Photochemical Tuning Of Materials: A Click Chemistry Perspective. *Mater. Today Chem.* **2018**, *8*, 56–84.
- (233) Blasco, E.; Wegener, M.; Barner-Kowollik, C. Photochemically Driven Polymeric Network Formation: Synthesis and Applications. *Adv. Mater.* **2017**, *29*, 1604005.
- (234) Fairbanks, B. D.; Macdougall, L. J.; Mavila, S.; Sinha, J.; Kirkpatrick, B. E.; Anseth, K. S.; Bowman, C. N. Photoclick Chemistry: A Bright Idea. *Chem. Rev.* **2021**, *121*, 6915–6990.
- (235) Armaroli, N.; Balzani, V.; Collin, J.-P.; Gaviña, P.; Sauvage, J.-P.; Ventura, B. Rotaxanes Incorporating Two Different Coordinating Units in Their Thread: Synthesis and Electrochemically and Photochemically Induced Molecular Motions. *J. Am. Chem. Soc.* **1999**, *121*, 4397–4408.
- (236) Saracini, C.; Fukuzumi, S.; Lee, Y.-M.; Nam, W. Photoexcited State Chemistry of Metal-Oxygen Complexes. *Dalton Trans.* **2018**, *47*, 16019–16026.
- (237) Loutfy, R. O.; De Mayo, P. Primary Bond Formation in the Addition of Cyclopentenone to Chloroethylenes. *Can. J. Chem.* **1972**, *50*, 3465.
- (238) Frisch, H.; Marschner, D. E.; Goldmann, A. S.; Barner-Kowollik, C. Wavelength-Gated Dynamic Covalent Chemistry. *Angew. Chem., Int. Ed.* **2018**, *57*, 2036.
- (239) Saracini, C.; Malik, D. D.; Sankaralingam, M.; Lee, Y.-M.; Nam, W.; Fukuzumi, S. Enhanced Electron-Transfer Reactivity of a Long-Lived Photoexcited State of a Cobalt-Oxygen Complex. *Inorg. Chem.* **2018**, *57*, 10945–10952.
- (240) Menon, A.; Slominskii, Y. L.; Joseph, J.; Dimitriev, O. P.; Guldi, D. M. Reversible Charge Transfer with Single-Walled Carbon Nanotubes Upon Harvesting the Low Energy Part of the Solar Spectrum. *Small* **2020**, *16*, 1906745.
- (241) Atilgan, A.; Ecik, E. T.; Guliyev, R.; Uyar, T. B.; Erbas-Cakmak, S.; Akkaya, E. U. Near-IR-Triggered, Remote-Controlled Release of Metal Ions: A Novel Strategy for Caged Ions. *Angew. Chem., Int. Ed.* **2014**, *53*, 10678–10681.
- (242) Pina, F.; Melo, M. J.; Maestri, M.; Passaniti, P.; Balzani, V. Artificial Chemical Systems Capable of Mimicking Some Elementary Properties of Neurons. *J. Am. Chem. Soc.* **2000**, *122*, 4496–4498.
- (243) Collin, J.-P.; Laemmel, A.-C.; Sauvage, J.-P. Photochemical Expulsion of a Ru(Phen)<sub>2</sub> Unit From a Macroyclic Receptor and its Thermal Reco-Ordination. *New J. Chem.* **2001**, *25*, 22–24.

- (244) Balzani, V.; Credi, A.; Venturi, M. *Molecular Devices and Machines. Concepts and Perspectives for the Nanoworld*; Wiley: Weinheim, 2008; Chapter 2, pp 23–46.
- (245) Martin, M. M.; Plaza, P.; Dai Hung, N.; Meyer, Y. H.; Bourson, J.; Valeur, B. Photoejection of Cations from Complexes with a Crown-Ether-Linked Merocyanine Evidenced by Ultrafast Spectroscopy. *Chem. Phys. Lett.* **1993**, *202*, 425–430.
- (246) Conceição, R.; Hungerford, G.; Costa, S. P. G.; Gonçalves, M. S. T. Photolytic Release of Bioactive Carboxylic Acids from Fused Pyran Conjugates. *Dyes Pigm.* **2018**, *148*, 368–379.
- (247) Holland, J. P.; Gut, M.; Klingler, S.; Fay, R.; Guillou, A. Photochemical Reactions in the Synthesis of Protein-Drug Conjugates. *Chem.—Eur. J.* **2020**, *26*, 33–48.
- (248) Wong, P. T.; Roberts, E. W.; Tang, S.; Mukherjee, J.; Cannon, J.; Nip, A. J.; Corbin, K.; Krummel, M. F.; Choi, S. K. Control of an Unusual Photo-Claisen Rearrangement in Coumarin Caged Tamoxifen through an Extended Spacer. *ACS Chem. Biol.* **2017**, *12*, 1001–1010.
- (249) Ballister, E. R.; Aonbangkhen, C.; Mayo, A. M.; Lampson, M. A.; Chenoweth, D. M. Localized Light-Induced Protein Dimerization in Living Cells Using a Photocaged Dimerizer. *Nat. Commun.* **2014**, *5*, 5475.
- (250) Bini, D.; Russo, L.; Battocchio, C.; Natalello, A.; Polzonetti, G.; Doglia, S. M.; Nicotra, F.; Cipolla, L. Dendron Synthesis and Carbohydrate Immobilization on a Biomaterial Surface by a Double-Click Reaction. *Org. Lett.* **2014**, *16*, 1298–1301.
- (251) Yu, Z. G.; Smith, D. L.; Saxena, A.; Martin, R. L.; Bishop, A. R. Molecular Geometry Fluctuations and Field-Dependent Mobility in Conjugated Polymers. *Phys. Rev. B* **2001**, *63*, 085202.
- (252) Kurti, J.; Surjan, P. R. Quinoid vs Aromatic Structure of Polyisothianaphthene. *J. Chem. Phys.* **1990**, *92*, 3247–3248.
- (253) Nayak, K.; Marynick, D. S. The Interplay Between Geometric And Electronic Structures In Polyisothianaphthene, Polyisonaphtho-thiophene, Polythieno(3,4–6)Pyrazine, and Polythieno(3,4–6)-quinoxaline. *Macromolecules* **1990**, *23*, 2237–2245.
- (254) Krieger, Ju. H. Structural Instability of One-Dimensional Systems as a Physical Principle Underlying the Functioning of Molecular Electronic Devices. *J. Struct. Chem.* **1999**, *40*, 594–619.
- (255) Westenhoff, S.; Beenken, W. J. D.; Friend, R. H.; Greenham, N. C.; Yartsev, A.; Sundström, V. Anomalous Energy Transfer Dynamics due to Torsional Relaxation in a Conjugated Polymer. *Phys. Rev. Lett.* **2006**, *97*, 166804.
- (256) Binder, R.; Wahl, J.; Römer, S.; Burghardt, I. Coherent Exciton Transport Driven by Torsional Dynamics: A Quantum Dynamical Study of Phenylene-Vinylene Type Conjugated Systems. *Faraday Discuss.* **2013**, *163*, 205–222.
- (257) Barford, W.; Lidzey, D. G.; Makhov, D. V.; Meijer, A. J. H. Exciton Localization in Disordered Poly(3-hexylthiophene). *J. Chem. Phys.* **2010**, *133*, 044504.
- (258) Milad, R.; Shi, J.; Aguirre, A.; Cardone, A.; Milián-Medina, B.; Farinola, G. M.; Abderrabba, M.; Gierschner, J. Effective Conjugation in Conjugated Polymers with Strongly Twisted Backbones: A Case Study on Fluorinated MEHPPV. *J. Mater. Chem. C Mater. Opt. Electron. Devices* **2016**, *4*, 6900–6906.
- (259) Vaschetto, M. E.; Monkman, A. P.; Springborg, M. First-Principles Studies of Some Conducting Polymers: PPP, PPy, PPV, PPyV, and PANI. *THEOCHEM* **1999**, *468*, 181–191.
- (260) Pollard, T. D., Earnshaw, W. C., Lippincott-Schwartz, J., Johnson, G. T., Eds.; Biophysical Principles. *Cell Biology*, 3rd ed.; Elsevier, 2017; pp 53–62.
- (261) Coleman, A. C.; Beierle, J. M.; Stuart, M. C. A.; Maciá, B.; Caroli, G.; Mika, J. T.; van Dijken, D. J.; Chen, J.; Browne, W. R.; Feringa, B. L. Light-Induced Disassembly of Self-Assembled Vesicle-Capped Nanotubes Observed in Real Time. *Nat. Nanotechnol.* **2011**, *6*, 547–552.
- (262) Goodwin, A. P.; Mynar, J. L.; Ma, Y.; Fleming, G. R.; Fréchet, J. M. J. Synthetic Micelle Sensitive to IR Light via a Two-Photon Process. *J. Am. Chem. Soc.* **2005**, *127*, 9952–9953.
- (263) Bogdanov, A. V.; Vorobiev, A. Kh Direct Microscopic Observation of Domain Rearrangement Mechanism of Photo-Orientation Process in Azobenzene-Containing Materials. *J. Phys. Chem. Lett.* **2018**, *9*, 1372–1376.
- (264) Li, Z.; Wang, H.; Chu, M.; Guan, P.; Zhao, Y.; Zhao, Y.; Wang, J. Photo-Isomerization and Light-Modulated Aggregation Behavior of Azobenzene-Based Ionic Liquids in Aqueous Solutions. *RSC Adv.* **2017**, *7*, 44688–44695.
- (265) Wu, A.; Lu, F.; Sun, P.; Gao, X.; Shi, L.; Zheng, L. Photoresponsive Self-Assembly of Surface Active Ionic Liquid. *Langmuir* **2016**, *32*, 8163–8170.
- (266) Shi, S.; Yin, T.; Tao, X.; Shen, W. Light Induced Micelle to Vesicle Transition in an Aqueous Solution of a Surface Active Ionic Liquid. *RSC Adv.* **2015**, *5*, 75806–75809.
- (267) Pawlicka, A.; Sabadini, R. C.; Nunzi, J.-M. Reversible Light-Induced Solubility of Disperse Red 1 Dye in a 2 Hydroxypropyl cellulose Matrix. *Cellulose* **2018**, *25*, 2083–2090.
- (268) Dohno, C.; Uno, S.; Sakai, S.; Oku, M.; Nakatani, K. The Effect of Linker Length on Binding Affinity of a Photoswitchable Molecular Glue for DNA. *Bioorg. Med. Chem.* **2009**, *17*, 2536–2543.
- (269) Brieke, C.; Rohrbach, F.; Gottschalk, A.; Mayer, G.; Heckel, A. Light-Controlled Tools. *Angew. Chem., Int. Ed.* **2012**, *S1*, 8446–8476.
- (270) Nishioka, H.; Liang, X.; Kato, T.; Asanuma, H. A Photon-Fueled DNA Nanodevice that Contains Two Different Photoswitches. *Angew. Chem., Int. Ed.* **2012**, *S1*, 1165–1168.
- (271) Petrenko, V. Yu.; Dimitriev, O. P. Light-Induced Self-Assembly and Decay of J-Aggregates of Thiamonomethinecyanine Dyes. *ChemPhysChem* **2014**, *15*, 3938–3943.
- (272) Herrmann-Westendorf, F.; Sachse, T.; Schulz, M.; Kaufmann, M.; Sivakov, V.; Beckert, R.; Martínez, T.; Dietzek, B.; Presselt, M. Photoannealing of Merocyanine Aggregates. *J. Phys. Chem. A* **2018**, *122*, 9821–9832.
- (273) Zhen, S. J.; Zhang, Z. Y.; Li, N.; Zhang, Z. D.; Wang, J.; Li, C. M.; Zhan, L.; Zhuang, H. L.; Huang, C. Z. UV Light-Induced Self-Assembly of Gold Nanocrystals into Chains and Networks in a Solution of Silver Nitrate. *Nanotechnol.* **2013**, *24*, 055601.
- (274) Shapiro, B. I. Block Building of Polymethine Dye Aggregates. *Nanotechnol. Russ.* **2008**, *3*, 139–150.
- (275) Karl, F. A Free Energy Principle for Biological Systems. *Entropy* **2012**, *14*, 2100–2121.
- (276) Harigaya, K. Long-Range Excitons in Conjugated Polymers With Ring Torsions. *Chem. Phys. Lett.* **1997**, *281*, 319–324.
- (277) Dykstra, T. E.; Hennebicq, E.; Beljonnie, D.; Gierschner, J.; Claudio, G.; Bittner, E. R.; Knoester, J.; Scholes, G. D. Conformational Disorder and Ultrafast Exciton Relaxation in PPV-Family Conjugated Polymers. *J. Phys. Chem. B* **2009**, *113*, 656–667.
- (278) Barford, W.; Lidzey, D. G.; Makhov, D. V.; Meijer, A. J. H. Exciton Localization in Disordered Poly(3-Hexylthiophene). *J. Chem. Phys.* **2010**, *133*, 044504.
- (279) Barford, W.; Trembath, D. Exciton Localization in Polymers with Static Disorder. *Phys. Rev. B* **2009**, *80*, 165418.
- (280) Barford, W.; Boczarow, I.; Wharram, T. Ultrafast Dynamical Localization of Photoexcited States in Conformationally Disordered Poly(p-phenylenevinylene). *J. Phys. Chem. A* **2011**, *115*, 9111–9119.
- (281) Xu, B.; Holdcroft, S. Molecular Control of Luminescence from Poly(3-Hexylthiophenes). *Macromolecules* **1993**, *26*, 4457–4460.
- (282) Dimitriev, O. P. Origin of the Exciton Transition Shift in Thin Films of Polyaniline. *Synth. Met.* **2001**, *125*, 359–363.
- (283) Dimitriev, O. P. Suppression of the Emeraldine Base-To-Emeraldine Salt Transition in Ultra-Thin Films of Polyaniline. *Synth. Met.* **2001**, *122*, 315–319.
- (284) Dimitriev, O. P.; Kopylov, O. N.; Tracz, A. Mechanisms of Polyaniline Film Formation Via Solution Casting: Intra-Chain Contraction Versus Inter-Chain Association. *Eur. Polym. J.* **2015**, *66*, 119–128.
- (285) Fernandez-Alberti, S.; Kleiman, V. D.; Tretiak, S.; Roitberg, A. E. Unidirectional Energy Transfer in Conjugated Molecules: The Crucial Role of High-Frequency C C Bonds. *J. Phys. Chem. Lett.* **2010**, *1*, 2699–2704.
- (286) Galindo, J. F.; Atas, E.; Altan, A.; Kuroda, D. G.; Fernandez-Alberti, S.; Tretiak, S.; Roitberg, A. E.; Kleiman, V. D. Dynamics of

- Energy Transfer in a Conjugated Dendrimer Driven by Ultrafast Localization of Excitations. *J. Am. Chem. Soc.* **2015**, *137*, 11637–11644.
- (287) Aguilera, M. C.; Roitberg, A. E.; Kleiman, V. D.; Fernandez-Alberti, S.; Galindo, J. F. Unraveling Direct and Indirect Energy Transfer Pathways in a Light-Harvesting Dendrimer. *J. Phys. Chem. C* **2020**, *124*, 22383–22391.
- (288) Nelson, T.; Fernandez-Alberti, S.; Roitberg, A. E.; Tretiak, S. Electronic Delocalization, Vibrational Dynamics, and Energy Transfer in Organic Chromophores. *J. Phys. Chem. Lett.* **2017**, *8*, 3020–3031.
- (289) Lakowicz, J. R. *Principles of Fluorescence Spectroscopy*; Plenum Press: New York, 1999; pp 291–319.
- (290) Yan, Y.; Kühn, O. Laser Control of Dissipative Two-Exciton Dynamics in Molecular Aggregates. *New J. Phys.* **2012**, *14*, 105004.
- (291) Schröter, M.; Ivanov, S. D.; Schulze, J.; Polyutov, S. P.; Yan, Y.; Pullerits, T.; Kühn, O. Exciton-Vibrational Coupling in the Dynamics and Spectroscopy of Frenkel Excitons in Molecular Aggregates. *Phys. Rep.* **2015**, *567*, 1–78.
- (292) Agranovich, V. M.; Galanin, M. D. *Electronic Excitation Energy Transfer in Condensed Matter*; North-Holland: Amsterdam, NY, 1983; pp 189–244.
- (293) Chin, A.; Prior, J.; Rosenbach, R.; Caycedo-Soler, F.; Huelga, S. F.; Plenio, M. B. The Role of Non-Equilibrium Vibrational Structures in Electronic Coherence and Recoherence in Pigment-Protein Complexes. *Nat. Phys.* **2013**, *9*, 113.
- (294) Lim, J.; Paleček, D.; Caycedo-Soler, F.; Lincoln, C. N.; Prior, J.; von Berlepsch, H.; Huelga, S. F.; Plenio, M. B.; Zigmantas, D.; Hauer, J. Vibronic Origin of Long-Lived Coherence in an Artificial Molecular Light Harvester. *Nat. Commun.* **2015**, *6*, 8755.
- (295) Freixas, V. M.; Tretiak, S.; Makhov, D. V.; Shalashilin, D. V.; Fernandez-Alberti, S. Vibronic Quantum Beating between Electronic Excited States in a Heterodimer. *J. Phys. Chem. B* **2020**, *124*, 3992–4001.
- (296) Fassoli, F.; Dinshaw, R.; Arpin, P. C.; Scholes, G. D. Photosynthetic Light Harvesting: Excitons and Coherence. *J. R. Soc., Interface* **2014**, *11*, 20130901.
- (297) Kakitani, T.; Kimura, A.; Sumi, H. Theory of Excitation Transfer in the Intermediate Coupling Case. *J. Phys. Chem. B* **1999**, *103*, 3720–3726.
- (298) Kimura, A.; Kakitani, T.; Yamato, T. Theory of Excitation Energy Transfer in the Intermediate Coupling Case. II. Criterion for Intermediate Coupling Excitation Energy Transfer Mechanism and Application to the Photosynthetic Antenna System. *J. Phys. Chem. B* **2000**, *104*, 9276–9287.
- (299) Kimura, A.; Kakitani, T. Advanced Theory of Excitation Energy Transfer in Dimers. *J. Phys. Chem. A* **2007**, *111*, 12042–12048.
- (300) Ishizaki, A.; Fleming, G. R. Unified Treatment of Quantum Coherent and Incoherent Hopping Dynamics In Electronic Energy Transfer: Reduced Hierarchy Equation Approach. *J. Chem. Phys.* **2009**, *130*, 234111.
- (301) Ishizaki, A.; Fleming, G. R. On the Interpretation of Quantum Coherent Beats Observed in Two-Dimensional Electronic Spectra of Photosynthetic Light Harvesting Complexes. *J. Phys. Chem. B* **2011**, *115*, 6227–6233.
- (302) Scholes, G. D. Coherence from Light Harvesting to Chemistry. *J. Phys. Chem. Lett.* **2018**, *9*, 1568–1572.
- (303) Alvertis, A. M.; Barford, W.; Bourne Worster, S.; Burghardt, I.; Datta, A.; Dijkstra, A.; Fay, T.; Ghosh, S.; Grünbaum, T.; Habershon, S.; et al. Quantum Coherence in Complex Environments: General Discussion. *Faraday Discuss.* **2020**, *221*, 168–201.
- (304) Collini, E.; Scholes, G. D. Electronic and Vibrational Coherences in Resonance Energy Transfer along MEH-PPV Chains at Room Temperature. *J. Phys. Chem. A* **2009**, *113*, 4223–4241.
- (305) Förster, T. Zwischenmolekulare Energiewanderung und Fluoreszenz. *Ann. Physik* **1948**, *437*, 55–75.
- (306) Jang, S. J. Effects of Donor-Acceptor Quantum Coherence and Non-Markovian Bath on the Distance Dependence of Resonance Energy Transfer. *J. Phys. Chem. C* **2019**, *123*, 5767–5775.
- (307) Nelson, T. R.; Ondarse-Alvarez, D.; Oldani, N.; Rodriguez-Hernandez, B.; Alfonso-Hernandez, L.; Galindo, J. F.; Kleiman, V. D.; Fernandez-Alberti, S.; Roitberg, A. E.; Tretiak, S. Coherent Exciton-Vibrational Dynamics and Energy Transfer in Conjugated Organics. *Nat. Commun.* **2018**, *9*, 2316.
- (308) Wang, T.; Chan, W.-L. Dynamical Localization Limiting the Coherent Transport Range of Excitons in Organic Crystals. *J. Phys. Chem. Lett.* **2014**, *5*, 1812–1818.
- (309) Brédas, J.-L.; Sargent, E. H.; Scholes, G. D. Photovoltaic Concepts Inspired by Coherence Effects in Photosynthetic Systems. *Nat. Mater.* **2017**, *16*, 35–44.
- (310) Brédas, J.-L.; Silbey, R. Excitons Surf Along Conjugated Polymer Chains. *Science* **2009**, *323*, 348–349.
- (311) Cannon, B. L.; Kellis, D. L.; Patten, L. K.; Davis, P. H.; Lee, J.; Graugnard, E.; Yurke, B.; Knowlton, W. B. Coherent Exciton Delocalization in a Two-State DNA-Templated Dye Aggregate System. *J. Phys. Chem. A* **2017**, *121*, 6905–6916.
- (312) Dahlbom, M.; Pullerits, T.; Mukamel, S.; Sundström, V. Exciton Delocalization in the B850 Light-Harvesting Complex: Comparison of Different Measures. *J. Phys. Chem. B* **2001**, *105*, 5515–5524.
- (313) Dubin, F.; Melet, R.; Barisien, T.; Grousson, R.; Legrand, L.; Schott, M.; Voliotis, V. Macroscopic Coherence of a Single Exciton State in an Organic Quantum Wire. *Nat. Phys.* **2006**, *2*, 32–35.
- (314) Shepherd, W. E. B.; Platt, A. D.; Kendrick, M. J.; Loth, M. A.; Anthony, J. E.; Ostroverkhova, O. Energy Transfer and Exciplex Formation and Their Impact on Exciton and Charge Carrier Dynamics in Organic Films. *J. Phys. Chem. Lett.* **2011**, *2*, 362–366.
- (315) Dimitriev, O. P.; Piryatinski, Yu. P.; Slominskii, Yu. L. Abnormal Emission in the Heterogeneous J-Aggregate System. *J. Phys. Chem. C* **2019**, *123*, 28611–28619.
- (316) Dimitriev, O. P.; Mazarchuk, I. A.; Morozovska, V. Y.; Trischuk, L. I. Antenna Size Effect: The Influence on Energy Transfer in the CdTe-Pseudoisocyanine Nanocomposite System. *Chem. Phys. Lett.* **2012**, *554*, 168–171.
- (317) Singh, V.; Zoric, M. R.; Hargenrader, G. N.; Valentine, A. J. S.; Zivojinovic, O.; Milic, D. R.; Li, X.; Glusac, K. D. Exciton Coherence Length and Dynamics in Graphene Quantum Dot Assemblies. *J. Phys. Chem. Lett.* **2020**, *11*, 210–216.
- (318) Zhang, Y. L.; Liu, X. J.; Sun, Z.; An, Z. Dynamics of Exciton Transfer in Coupled Polymer Chains. *J. Chem. Phys.* **2013**, *138*, 174906.
- (319) Herz, L. M.; Silva, C.; Grimsdale, A. C.; Müllen, K.; Phillips, R. T. Time-Dependent Energy Transfer Rates in a Conjugated Polymer Guest-Host System. *Phys. Rev. B* **2004**, *70*, 165207.
- (320) Pope, M.; Swenberg, C. E. *Electronic Processes in Organic Crystals and Polymers*, 2nd ed.; Oxford University Press, 1999; 1350 p.
- (321) Baer, R.; Rabani, E. Theory of Resonance Energy Transfer Involving Nanocrystals: The Role of High Multipoles. *J. Chem. Phys.* **2008**, *128*, 184710.
- (322) Mikhnenko, O. V.; Blom, P. W. M.; Nguyen, T.-Q. Exciton Diffusion in Organic Semiconductors. *Energy Environ. Sci.* **2015**, *8*, 1867–1888.
- (323) Dexter, D. L.; Knox, R. S.; Förster, T. The Radiationless Transfer of Energy of Electronic Excitation Between Impurity Molecules in Crystals. *Phys. Status Solidi B Basic Res.* **1969**, *34*, K159–K162.
- (324) Scholes, G. D. Long-Range Resonance Energy Transfer in Molecular Systems. *Annu. Rev. Phys. Chem.* **2003**, *54*, 57–87.
- (325) Baranovskii, S.; Rubel, O. Charge Transport in Disordered Materials. In *Springer Handbook of Electronic and Photonic Materials*; Kasap, S., Capper, P., Eds. Springer: Cham, 2017; pp 161–186.
- (326) Beenken, W. J. D.; Pullerits, T. Spectroscopic Units in Conjugated Polymers: A Quantum Chemically Founded Concept? *J. Phys. Chem. B* **2004**, *108*, 6164–6169.
- (327) Lupton, J. M. Chromophores in Conjugated Polymers—All Straight? *ChemPhysChem* **2012**, *13*, 901–907.
- (328) Wang, C. I.; Hsu, C. H.; Hua, C. C. The Correspondence Between The Conformational and Chromophoric Properties of Amorphous Conjugated Polymers in Mesoscale Condensed Systems. *Phys. Chem. Chem. Phys.* **2017**, *19*, 20818–20828.
- (329) Barford, W.; Marcus, M. Perspective: Optical Spectroscopy in PPPPPP-Conjugated Polymers and How It Can Be Used To

- Determine Multiscale Polymer Structures. *J. Chem. Phys.* **2017**, *146*, 130902.
- (330) Kanemoto, K.; Sudo, T.; Akai, I.; Hashimoto, H.; Karasawa, T.; Aso, Y.; Otsubo, T. Intrachain Photoluminescence Properties of Conjugated Polymers as Revealed by Long Oligothiophenes and Polythiophenes Diluted in an Inactive Solid Matrix. *Phys. Rev. B* **2006**, *73*, 235203.
- (331) Barford, W.; Bittner, E. R.; Ward, A. Exciton Dynamics in Disordered Poly(p-phenylenevinylene). 2. Exciton Diffusion. *J. Phys. Chem. A* **2012**, *116*, 10319–10327.
- (332) Madigan, C.; Bulovic, V. Modeling of Exciton Diffusion in Amorphous Organic Thin Films. *Phys. Rev. Lett.* **2006**, *96*, 046404.
- (333) Mikhnenko, O. V.; Cordella, F.; Sieval, A. B.; Hummelen, J. C.; Blom, P. W. M.; Loi, M. A. Temperature Dependence of Exciton Diffusion in Conjugated Polymers. *J. Phys. Chem. B* **2008**, *112*, 11601–11604.
- (334) Lin, J. D. A.; Mikhnenko, O. V.; van der Poll, T. S.; Bazan, G. C.; Nguyen, T.-Q. Temperature Dependence of Exciton Diffusion in a Small Molecule Organic Semiconductor Processed With and Without Additive. *Adv. Mater.* **2015**, *27*, 2528–2532.
- (335) Rai, D.; Holmes, R. J. Measurement of the Triplet Exciton Diffusion Length in Organic Semiconductors. *J. Mater. Chem. C* **2019**, *7*, 5695–5701.
- (336) Narushima, K.; Kiyota, Y.; Mori, T.; Hirata, S.; Vacha, M. Suppressed Triplet Exciton Diffusion Due to Small Orbital Overlap as a Key Design Factor for Ultralong-Lived Room-Temperature Phosphorescence in Molecular Crystals. *Adv. Mater.* **2019**, *31*, 1807268.
- (337) Rai, D.; Bangsund, J. S.; Barriocanal, J. G.; Holmes, R. J. Impact of Molecular Structure on Singlet and Triplet Exciton Diffusion in Phenanthroline Derivatives. *J. Mater. Chem. C* **2020**, *8*, 6118–6123.
- (338) Tamura, H.; Azumaya, K.; Ishikita, H. Long-Range Exciton Diffusion via Singlet Revival Mechanism. *J. Phys. Chem. Lett.* **2019**, *10*, 7623–7628.
- (339) Yeboah, D.; Singh, J. Dependence of Exciton Diffusion Length and Diffusion Coefficient on Photophysical Parameters in Bulk Heterojunction Organic Solar Cells. *J. Electron. Mater.* **2017**, *46*, 6451–6460.
- (340) Markov, D. E.; Tanase, C.; Blom, P. W. M.; Wildeman, J. Simultaneous Enhancement of Charge Transport and Exciton Diffusion in Poly(Phenylene Vinylene) Derivatives. *Phys. Rev. B* **2005**, *72*, 045217.
- (341) Menke, S. M.; Holmes, R. J. Exciton Diffusion in Organic Photovoltaic Cells. *Energy Environ. Sci.* **2014**, *7*, 499–512.
- (342) Athanasopoulos, S.; Hoffmann, S. T.; Bässler, H.; Köhler, A.; Beljonnie, D. To Hop or Not to Hop? Understanding the Temperature Dependence of Spectral Diffusion in Organic Semiconductors. *J. Phys. Chem. Lett.* **2013**, *4*, 1694–1700.
- (343) Bjorgaard, J. A.; Köse, M. E. Simulations of Singlet Exciton Diffusion in Organic Semiconductors: A Review. *RSC Adv.* **2015**, *5*, 8432–8445.
- (344) Grage, M. M.-L.; Pullerits, T.; Ruseckas, A.; Theander, M.; Inganäs, O.; Sundström, V. Conformational Disorder of a Substituted Polythiophene in Solution Revealed by Excitation Transfer. *Chem. Phys. Lett.* **2001**, *339*, 96–102.
- (345) Ferreira, B.; da Silva, P. F.; de Melo, J. S. S.; Pina, J.; Maçanita, A. Excited-State Dynamics and Self-Organization of Poly(3-hexylthiophene) (P3HT) in Solution and Thin Films. *J. Phys. Chem. B* **2012**, *116*, 2347–2355.
- (346) Anantharaman, S. B.; Stöferle, T.; Nüesch, F. A.; Mahrt, R. F.; Heier, J. Exciton Dynamics and Effects of Structural Order in Morphology-Controlled J-Aggregate Assemblies. *Adv. Funct. Mater.* **2019**, *29*, 1806997.
- (347) Kelbauskas, L.; Bagdonas, S.; Dietel, W.; Rotomskis, R. Excitation Relaxation and Structure of TPPS4 J-Aggregates. *J. Lumin.* **2003**, *101*, 253–262.
- (348) Yang, F.; Meng, R.; Zhang, G.; Gao, K.; Xie, S. Migration of an Exciton in Organic Polymers Driven by a Nonuniform Internal Electric Field. *Org. Electron.* **2016**, *30*, 171–175.
- (349) Meng, R.; Li, Y.; Gao, K.; Qin, W.; Wang, L. Ultrafast Exciton Migration and Dissociation in  $\pi$ -Conjugated Polymers Driven by Local Nonuniform Electric Fields. *J. Phys. Chem. C* **2017**, *121*, 20546–20552.
- (350) Meng, R.; Li, Y.; Li, C.; Gao, K.; Yin, S.; Wang, L. Exciton Transport in  $\pi$ -Conjugated Polymers with Conjugation Defects. *Phys. Chem. Chem. Phys.* **2017**, *19*, 24971–24978.
- (351) Golubov, S. I.; Konobeev, Y. V. Effects of Diffusion on Energy Transfer by Resonance in Solids. *Phys. Stat. Sol. b* **1973**, *56*, 69–77.
- (352) Saini, S.; Srinivas, G.; Bagchi, B. Distance and Orientation Dependence of Excitation Energy Transfer: From Molecular Systems to Metal Nanoparticles. *J. Phys. Chem. B* **2009**, *113*, 1817–1832.
- (353) Di Maiolo, F.; Painelli, A. Dynamical Disorder and Resonance Energy Transfer: A Novel Quantum-Classical Approach. *Phys. Chem. Chem. Phys.* **2020**, *22*, 1061–1068.
- (354) Prodhan, S.; Giannini, S.; Wang, L.; Beljonnie, D. Long-Range Interactions Boost Singlet Exciton Diffusion in Nanofibers of  $\pi$ -Extended Polymer Chains. *J. Phys. Chem. Lett.* **2021**, *12*, 8188–8193.
- (355) Sneyd, A. J.; Fukui, T.; Palecek, D.; Prodhan, S.; Wagner, I.; Zhang, Y.; Sung, J.; Collins, S. M.; Slater, T. J. A.; Andaji-Garmaroudi, Z.; et al. Efficient Energy Transport in an Organic Semiconductor Mediated by Transient Exciton Delocalization. *Sci. Adv.* **2021**, *7*, No. eabh4232.
- (356) Wittmann, B.; Wenzel, F. A.; Wiesneth, S.; Haedler, A. T.; Drechsler, M.; Kreger, K.; Köhler, J.; Meijer, E. W.; Schmidt, H.-W.; Hildner, R. Enhancing Long-Range Energy Transport in Supramolecular Architectures by Tailoring Coherence Properties. *J. Am. Chem. Soc.* **2020**, *142*, 8323–8330.
- (357) Li, X.; Buda, F.; de Groot, H. J. M.; Sevink, G. J. A. Dynamic Disorder Drives Exciton Transfer in Tubular Chlorosomal Assemblies. *J. Phys. Chem. B* **2020**, *124*, 4026–4035.
- (358) Lee, H.; Cheng, Y.-C.; Fleming, G. R. Coherence Dynamics in Photosynthesis: Protein Protection of Excitonic Coherence. *Science* **2007**, *316*, 1462–1465.
- (359) Collini, E.; Scholes, G. D. Coherent Intrachain Energy Migration in a Conjugated Polymer at Room Temperature. *Science* **2009**, *323*, 369.
- (360) Yang, X.; Dykstra, T. E.; Scholes, G. D. Photon-Echo Studies of Collective Absorption and Dynamic Localization of Excitation in Conjugated Polymers and Oligomers. *Phys. Rev. B* **2005**, *71*, 045203.
- (361) Tiwari, V.; Peters, W. K.; Jonas, D. M. Electronic Resonance with Anticorrelated Pigment Vibrations Drives Photosynthetic Energy Transfer Outside the Adiabatic Framework. *Proc. Natl. Acad. Sci.* **2013**, *110*, 1203–1208.
- (362) Paleček, D.; Edlund, P.; Westenhoff, S.; Zigmantas, D. Quantum Coherence as a Witness of Vibronically Hot Energy Transfer in Bacterial Reaction Center. *Sci. Adv.* **2017**, *3*, No. e1603141.
- (363) Engel, G. S.; Calhoun, T. R.; Read, E. L.; Ahn, T.-K.; Mančal, T.; Cheng, Y.-C.; Blankenship, R. E.; Fleming, G. R. Evidence for Wavelike Energy Transfer Through Quantum Coherence In Photosynthetic Systems. *Nature* **2007**, *446*, 782–786.
- (364) Scholes, G. D. Quantum-Coherent Electronic Energy Transfer: Did Nature Think Of It First? *J. Phys. Chem. Lett.* **2010**, *1*, 2–8.
- (365) Christansson, N.; Kauffmann, H. F.; Pullerits, T.; Mančal, T. Origin of Long-Lived Coherences in Light-Harvesting Complexes. *J. Phys. Chem. B* **2012**, *116*, 7449–7454.
- (366) Thyrhaug, E.; Žídek, K.; Dostál, J.; Bína, D.; Zigmantas, D. Exciton Structure and Energy Transfer in the Fenna-Matthews-Olson Complex. *J. Phys. Chem. Lett.* **2016**, *7*, 1653–1660.
- (367) Duan, H.-G.; Prokhorenko, V. I.; Cogdell, R. J.; Ashraf, K.; Stevens, A. L.; Thorwart, M.; Miller, R. J. D. Nature Does Not Rely On Long-Lived Electronic Quantum Coherence For Photosynthetic Energy Transfer. *Proc. Natl. Acad. Sci. U.S.A.* **2017**, *114*, 8493–8498.
- (368) Panitchayangkoon, G.; Hayes, D.; Fransted, K. A.; Caram, J. R.; Harel, E.; Wen, J.; Blankenship, R. E.; Engel, G. S. Long-Lived Quantum Coherence in Photosynthetic Complexes at Physiological Temperature. *Proc. Natl. Acad. Sci. U. S. A.* **2010**, *107*, 12766–12770.
- (369) Ishizaki, A.; Fleming, G. R. Quantum Coherence in Photosynthetic Light Harvesting. *Annu. Rev. Condens. Matter Phys.* **2012**, *3*, 333–361.

- (370) Scholes, G. D.; Fleming, G. R.; Chen, L. X.; Aspuru-Guzik, A.; Buchleitner, A.; Coker, D. F.; Engel, G. S.; van Grondelle, R.; Ishizaki, A.; Jonas, D. M.; et al. Using Coherence to Enhance Function in Chemical and Biophysical Systems. *Nature* **2017**, *543*, 647–656.
- (371) Rafiq, S.; Scholes, G. D. From Fundamental Theories to Quantum Coherences in Electron Transfer. *J. Am. Chem. Soc.* **2019**, *141*, 708–722.
- (372) Ishizaki, A.; Fleming, G. R. Theoretical Examination of Quantum Coherence in a Photosynthetic System at Physiological Temperature. *Proc. Natl. Acad. Sci. U. S. A.* **2009**, *106*, 17255–17260.
- (373) Sarovar, M.; Ishizaki, A.; Fleming, G. R.; Whaley, K. B. Quantum Entanglement in Photosynthetic Light-Harvesting Complexes. *Nat. Phys.* **2010**, *6*, 462–467.
- (374) Ishizaki, A.; Calhoun, T. R.; Schlau-Cohen, G. S.; Fleming, G. R. Quantum Coherence and Its Interplay with Protein Environments in Photosynthetic Electronic Energy Transfer. *Phys. Chem. Chem. Phys.* **2010**, *12*, 7319–7337.
- (375) Ghosh, S.; Bishop, M. M.; Roscioli, J. D.; LaFountain, A. M.; Frank, H. A.; Beck, W. F. Excitation Energy Transfer by Coherent and Incoherent Mechanisms in the Peridinin-Chlorophyll *a* Protein. *J. Phys. Chem. Lett.* **2017**, *8*, 463–469.
- (376) Hu, Z.; Engel, G. S.; Alharbi, F. H.; Kais, S. Dark States and Delocalization: Competing Effects of Quantum Coherence on the Efficiency of Light Harvesting Systems. *J. Chem. Phys.* **2018**, *148*, 064304.
- (377) Singh, D. Coherent Speedup of Excitation Energy Transfer in PC645. *J. Phys. Chem. B* **2021**, *125*, 557–561.
- (378) Bennett, D. I. G.; Maly, P.; Kreisbeck, C.; van Grondelle, R.; Aspuru-Guzik, A. Mechanistic Regimes of Vibronic Transport in a Heterodimer and the Design Principle of Incoherent Vibronic Transport in Phycobiliproteins. *J. Phys. Chem. Lett.* **2018**, *9*, 2665–2670.
- (379) Cho, K. H.; Rhee, Y. M. Computational Elucidations on the Role of Vibrations in Energy Transfer Processes of Photosynthetic Complexes. *Phys. Chem. Chem. Phys.* **2021**, *23*, 26623–26639.
- (380) Cui, X. Y.; Yan, Y. J.; Wei, J. H. Theoretical Study on the Effect of Environment on Excitation Energy Transfer in Photosynthetic Light-Harvesting Systems. *J. Phys. Chem. B* **2020**, *124*, 2354–2362.
- (381) Arsenault, E. A.; Yoneda, Y.; Iwai, M.; Niyogi, K. K.; Fleming, G. R. Vibronic Mixing Enables Ultrafast Energy Flow in Light-Harvesting Complex II. *Nat. Commun.* **2020**, *11*, 1460.
- (382) Lambrev, P. H.; Akhtar, P.; Tan, H.-S. Insights into the Mechanisms and Dynamics of Energy Transfer in Plant Light-Harvesting Complexes From Two-Dimensional Electronic Spectroscopy. *Biochim. Biophys. Acta - Bioenerg.* **2020**, *1861*, 148050.
- (383) Roscioli, J. D.; Ghosh, S.; LaFountain, A. M.; Frank, H. A.; Beck, W. F. Quantum Coherent Excitation Energy Transfer by Carotenoids in Photosynthetic Light Harvesting. *J. Phys. Chem. Lett.* **2017**, *8*, 5141–5147.
- (384) Roscioli, J. D.; Ghosh, S.; LaFountain, A. M.; Frank, H. A.; Beck, W. F. Structural Tuning of Quantum Decoherence and Coherent Energy Transfer in Photosynthetic Light Harvesting. *J. Phys. Chem. Lett.* **2018**, *9*, 5071–5077.
- (385) Higgins, J. S.; Lloyd, L. T.; Sohail, S. H.; Allodi, M. A.; Otto, J. P.; Saer, R. G.; Wood, R. E.; Massey, S. C.; Ting, P.-C.; Blankenship, R. E.; Engel, G. S. Photosynthesis Tunes Quantum-Mechanical Mixing of Electronic and Vibrational States to Steer Exciton Energy Transfer. *Proc. Natl. Acad. Sci. U. S. A.* **2021**, *118*, No. e2018240118.
- (386) Penrose, R. *Shadows of the Mind: a Search for the Missing Science of Consciousness*; Oxford University Press: Oxford, 1994; 477 p.
- (387) Beck, F.; Eccles, J. Quantum processes in the brain: A scientific basis for consciousness. In *Neural Basis of Consciousness*; Osaka, N., Ed.; John Benjamins Publ.: Philadelphia, PA, 2003; pp 141–166.
- (388) Reimers, J. R.; McKemmish, L. K.; McKenzie, R. H.; Mark, A. E.; Hush, N. S. Weak, Strong, and Coherent Regimes of Fröhlich Condensation and Their Applications to Terahertz Medicine And Quantum Consciousness. *Proc. Natl. Acad. Sci. U. S. A.* **2009**, *106*, 4219–4224.
- (389) Vaziri, A.; Plenio, M. Quantum Coherence in Ion Channels: Resonances, Transport and Verification. *New J. Phys.* **2010**, *12*, 085001.
- (390) Mensky, M. B. *Consciousness and quantum mechanics: life in parallel worlds: miracles of consciousness from quantum reality*; World Scientific: New Jersey, 2010; 246 p.
- (391) Loewenstein, W. R., Ed. *Physics in Mind: A Quantum View of the Brain*; Basic Books: New York, 2013.
- (392) Fisher, M. P. A. Quantum Cognition: The Possibility of Processing With Nuclear Spins in the Brain. *Ann. Phys.* **2015**, *362*, 593–602.
- (393) Jedlicka, P. Revisiting the Quantum Brain Hypothesis: Toward Quantum (Neuro) biology? *Front. Mol. Neurosci.* **2017**, *10*, 366.
- (394) Craddock, T. J.; Priel, A.; Tuszyński, J. A. Keeping Time: Could Quantum Beating In Microtubules Be The Basis For The Neural Synchrony Related To Consciousness? *J. Integr. Neurosci.* **2014**, *13*, 293–311.
- (395) Uhlhaas, P. J.; Pipa, G.; Lima, B.; Melloni, L.; Neuenschwander, S.; Nikolic, D.; Singer, W. Neural Synchrony in Cortical Networks: History, Concept and Current Status. *Front. Integr. Neurosci.* **2009**, *3*, 17.
- (396) Hameroff, S.; Nip, A.; Porter, M.; Tuszyński, J. Conduction Pathways in Microtubules, Biological Quantum Computation, and Consciousness. *Biosystems* **2002**, *64*, 149–168.
- (397) Craddock, T. J. A.; Friesen, D.; Mane, J.; Hameroff, S.; Tuszyński, J. A. The Feasibility of Coherent Energy Transfer in Microtubules. *J. R. Soc. Interface* **2014**, *11*, 20140677.
- (398) Tory Toole, J.; Kurian, P.; Craddock, T. J. A. Coherent Energy Transfer and the Potential Implications for Consciousness. *J. Cogn. Sci.* **2018**, *19*, 115–124.
- (399) Hidayat, R.; Tatsuhara, S.; Kim, D. W.; Ozaki, M.; Yoshino, K.; et al. Time-Resolved Study of Luminescence in Highly Luminescent Disubstituted Polyacetylene and its Blend with Poorly Luminescent Monosubstituted Polyacetylene. *Phys. Rev. B* **2000**, *61*, 10167–10173.
- (400) Hayes, G. R.; Samuel, I. D. W.; Phillips, R. T. Exciton Dynamics in Electroluminescent Polymers Studied by Femtosecond Time-Resolved Photoluminescence Spectroscopy. *Phys. Rev. B* **1995**, *52*, R11569.
- (401) Kranzelbinder, G.; Byrne, H. J.; Hallstein, S.; Roth, S.; Leising, G.; Scherf, U. Picosecond Spectroscopy and Hyperlinear Photoluminescence in Poly(Para-Phenylen)-Type Ladder Polymers. *Phys. Rev. B* **1997**, *56*, 1632–1636.
- (402) Dimitriev, O. P.; Blank, D. A.; Ganser, C.; Teichert, C. Effect of the Polymer Chain Arrangement on Exciton and Polaron Dynamics in P3HT and P3HT:PCBM Films. *J. Phys. Chem. C* **2018**, *122*, 17096–17109.
- (403) Jin, Y.-J.; Kwak, G. Unusual, Highly Efficient Fluorescence Emission Enhancement of Conjugated Polymers with an Intramolecular Stack Structure Through Thermal Annealing at High Temperature. *Macromolecules* **2017**, *50*, 9846–9851.
- (404) Schwartz, B. J.; Nguyen, T.-Q.; Wu, J.; Tolbert, S. H. Interchain and Intrachain Exciton Transport in Conjugated Polymers: Ultrafast Studies of Energy Migration in Aligned MEH-PPV/Mesoporous Silica Composites. *Synth. Met.* **2001**, *116*, 35–40.
- (405) Nguyen, T.-Q.; Wu, J.; Doan, V.; Schwartz, B. J.; Tolbert, S. H. Control of Energy Transfer in Oriented Conjugated Polymer-Mesoporous Silica Composites. *Science* **2000**, *288*, 652–656.
- (406) Beljonne, D.; Pourtois, G.; Silva, C.; Hennebicq, E.; Herz, L. M.; Friend, R. H.; Scholes, G. D.; Setayesh, S.; Mullen, K.; Bredas, J. L. Interchain vs. Intrachain Energy Transfer in Acceptor-Capped Conjugated Polymers. *Proc. Natl. Acad. Sci. U. S. A.* **2002**, *99*, 10982–10987.
- (407) Nguyen, T.-Q.; Wu, J.; Tolbert, S. H.; Schwartz, B. J. Control of Energy Transport in Conjugated Polymers Using an Ordered Mesoporous Silica Matrix. *Adv. Mater.* **2001**, *13*, 609–611.
- (408) Yamagata, H.; Spano, F. C. Interplay between Intrachain and Interchain Interactions in Semiconducting Polymer Assemblies: The HJ-Aggregate Model. *J. Chem. Phys.* **2012**, *136*, 184901.

- (409) Binder, R.; Polkeln, M.; Ma, T.; Burghardt, I. Ultrafast Exciton Migration in an HJ-Aggregate: Potential Surfaces and Quantum Dynamics. *Chem. Phys.* **2017**, *482*, 16–26.
- (410) Peteanu, L. A.; Chowdhury, S.; Wildeman, J.; Sfeir, M. Y. Exciton–Exciton Annihilation as a Probe of Interchain Interactions in PPV-Oligomer Aggregates. *J. Phys. Chem. B* **2017**, *121*, 1707–1714.
- (411) Tapping, P. C.; Clafon, S. N.; Schwarz, K. N.; Kee, T. W.; Huang, D. M. Molecular-Level Details of Morphology-Dependent Exciton Migration in Poly(3-hexylthiophene) Nanostructures. *J. Phys. Chem. C* **2015**, *119*, 7047–7059.
- (412) Ghosh, A.; Jana, B.; Chakraborty, S.; Maiti, S.; Jana, B.; Ghosh, H. N.; Patra, A. Exciton Dynamics and Formation Mechanism of MEH-PPV Polymer Based Nanostructures. *J. Phys. Chem. C* **2017**, *121*, 21062–21072.
- (413) Jin, X.-H.; Price, M. B.; Finnegan, J. R.; Boot, C. E.; Richter, J. M.; Rao, A.; Menke, S. M.; Friend, R. H.; Whittell, G. R.; Manners, I. Long-Range Exciton Transport in Conjugated Polymer Nanofibers Prepared by Seeded Growth. *Science* **2018**, *360*, 897–900.
- (414) Barford, W.; Duffy, C. D. P. Role of Quantum Coherence and Energetic Disorder in Exciton Transport in Polymer Films. *Phys. Rev. B* **2006**, *74*, 075207.
- (415) Meng, R.; Gao, K.; Zhang, G.; Han, S.; Yang, F.; Li, Y.; Xie, S. Exciton Intrachain Transport Induced by Interchain Packing Configurations in Conjugated Polymers. *Phys. Chem. Chem. Phys.* **2015**, *17*, 18600–18605.
- (416) Hu, D.; Yu, J.; Padmanaban, G.; Ramakrishnan, S.; Barbara, P. F. Spatial Confinement of Exciton Transfer and the Role of Conformational Order in Organic Nanoparticles. *Nano Lett.* **2002**, *2*, 1121–1124.
- (417) Dykstra, T. E.; Kovalevskij, V.; Yang, X.; Scholes, G. D. Excited State Dynamics of a Conformationally Disordered Conjugated Polymer: A Comparison of Solutions and Film. *Chem. Phys.* **2005**, *318*, 21–32.
- (418) Beenken, W. J. D. Excitons in Conjugated Polymers: Do We Need a Paradigm Change? *Phys. Stat. Solidi A* **2009**, *206*, 2750–2756.
- (419) Bolinger, J. C.; Traub, M. C.; Brazard, J.; Adachi, T.; Barbara, P. F.; Vanden Bout, D. A. Conformation and Energy Transfer in Single Conjugated Polymers. *Acc. Chem. Res.* **2012**, *45*, 1992–2001.
- (420) Kwon, Y.; Kaufman, L. J. Nearly Isotropic Conjugated Polymer Aggregates with Efficient Local Exciton Diffusion. *J. Phys. Chem. C* **2019**, *123*, 29418–29426.
- (421) Adachi, T.; Lakhwani, G.; Traub, M. C.; Ono, R. J.; Bielawski, C. W.; Barbara, P. F.; Vanden Bout, D. A. Conformational Effect on Energy Transfer in Single Polythiophene Chains. *J. Phys. Chem. B* **2012**, *116*, 9866–9872.
- (422) Hu, Z.; Adachi, T.; Haws, R.; Shuang, B.; Ono, R. J.; Bielawski, C. W.; Landes, C. F.; Rossky, P. J.; Vanden Bout, D. A. Excitonic Energy Migration in Conjugated Polymers: The Critical Role of Interchain Morphology. *J. Am. Chem. Soc.* **2014**, *136*, 16023–16031.
- (423) Thiessen, A.; Vogelsang, J.; Adachi, T.; Steiner, F.; Vanden Bout, D.; Lupton, J. M. Unraveling the Chromophoric Disorder Of Poly(3-Hexylthiophene). *Proc. Natl. Acad. Sci. U. S. A.* **2013**, *110*, E3550–E3556.
- (424) Benniston, A. C.; Harriman, A.; Li, P.; Patel, P. V.; Sams, C. A. The Effect of Torsion Angle on the Rate of Intramolecular Triplet Energy Transfer. *Phys. Chem. Chem. Phys.* **2005**, *7*, 3677–3679.
- (425) Van Averbeke, B.; Beljonne, D. Conformational Effects on Excitation Transport along Conjugated Polymer Chains. *J. Phys. Chem. A* **2009**, *113*, 2677–2682.
- (426) Westenhoff, S.; Abrusci, A.; Feast, W. J.; Henze, O.; Kilbinger, A. F. M.; Schenning, A. P. H. J.; Silva, C. Supramolecular Electronic Coupling in Chiral Oligothiophene Nanostructures. *Adv. Mater.* **2006**, *18*, 1281–1285.
- (427) Nesterov, E. E.; Zhu, Z.; Swager, T. M. Conjugation Enhancement of Intramolecular Exciton Migration in Poly(*p*-phenylene ethynylene)s. *J. Am. Chem. Soc.* **2005**, *127*, 10083–10088.
- (428) Andrew, T. L.; Swager, T. M. Structure-Property Relationships for Exciton Transfer in Conjugated Polymers. *J. Polym. Sci. B Polym. Phys.* **2011**, *49*, 476–498.
- (429) Shreve, A. P.; Trautman, J. K.; Frank, H. A.; Owens, T. G.; Albrecht, A. C. Femtosecond Energy-Transfer Processes in the B800–850 Light-Harvesting Complex of Rhodobacter sphaeroides 2.4.1. *Biochim. Biophys. Acta* **1991**, *1058*, 280–288.
- (430) Jimenez, R.; Dikshit, S. N.; Bradforth, S. E.; Fleming, G. R. Electronic Excitation Transfer in The LH2 Complex of Rhodobacter Sphaeroides. *J. Phys. Chem.* **1996**, *100*, 6825–6834.
- (431) Sumi, H. Theory on Rates of Excitation-Energy Transfer Between Molecular Aggregates Through Distributed Transition Dipoles With Application To The Antenna System In Bacterial Photosynthesis. *J. Phys. Chem. B* **1999**, *103*, 252–260.
- (432) Mukai, K.; Abe, S.; Sumi, H. Theory of Rapid Excitation-Energy Transfer from B800 to Optically-Forbidden Exciton States of B850 in the Antenna System LH2 Of Photosynthetic Purple Bacteria. *J. Phys. Chem. B* **1999**, *103*, 6096–6102.
- (433) Walla, P. J.; Linden, P. A.; Hsu, C. P.; Scholes, G. D.; Fleming, G. R. Femtosecond Dynamics of The Forbidden Carotenoid S1 State in Light-Harvesting Complexes of Purple Bacteria Observed after Two-Photon Excitation. *Proc. Natl. Acad. Sci. U.S.A.* **2000**, *97*, 10808–10813.
- (434) Jang, S.; Newton, M. D.; Silbey, R. J. Multichromophoric Förster Resonance Energy Transfer From B800 to B850 in the Light Harvesting Complex 2: Evidence for Subtle Energetic Optimization by Purple Bacteria. *J. Phys. Chem. B* **2007**, *111*, 6807–6814.
- (435) Didraga, C.; Malyshev, V. A.; Knoester, J. Excitation Energy Transfer Between Closely Spaced Multichromophoric Systems: Effects of Band Mixing and Intraband Relaxation. *J. Phys. Chem. B* **2006**, *110*, 18818–18827.
- (436) Abasto, D. F.; Mohseni, M.; Lloyd, S.; Zanardi, P. Exciton Diffusion Length in Complex Quantum Systems: The Effects of Disorder and Environmental Fluctuations On Symmetry-Enhanced Supertransfer. *Philos. Trans. R. Soc. A* **2012**, *370*, 3750–3770.
- (437) Chuang, C.; Knoester, J.; Cao, J. Scaling Relations and Optimization of Excitonic Energy Transfer Rates Between One-Dimensional Molecular Aggregates. *J. Phys. Chem. B* **2014**, *118*, 7827–7834.
- (438) Saini, S.; Singh, H.; Bagchi, B. Fluorescence Resonance Energy Transfer (FRET) in Chemistry and Biology: Non-Förster Distance Dependence of the FRET rate. *J. Chem. Sci.* **2006**, *118*, 23–35.
- (439) Barford, W. Beyond Förster Resonance Energy Transfer in Linear Nanoscale Systems. *J. Phys. Chem. A* **2010**, *114*, 11842–11843.
- (440) Rogach, A. L.; Klar, T. A.; Lupton, J. M.; Meijerink, A.; Feldmann, J. Energy Transfer With Semiconductor Nanocrystals. *J. Mater. Chem.* **2009**, *19*, 1208–1221.
- (441) Weeraddana, D.; Premaratne, M.; Andrews, D. L. Direct and Third-Body Mediated Resonance Energy Transfer in Dimensionally Constrained Nanostructures. *Phys. Rev. B* **2015**, *92*, 035128.
- (442) Krueger, B. P.; Scholes, G. D.; Fleming, G. R. Calculation of Couplings and Energy-Transfer Pathways Between the Pigments of LH2 by the Ab Initio Transition Density Cube Method. *J. Phys. Chem. B* **1998**, *102*, 5378–5386.
- (443) Beenken, W. J. D.; Pullerits, T. Excitonic Coupling in Polythiophenes: Comparison of Different Calculation Methods. *J. Chem. Phys.* **2004**, *120*, 2490–2495.
- (444) Wong, K. F.; Bagchi, B.; Rossky, P. J. Distance and Orientation Dependence of Excitation Transfer Rates in Conjugated Systems: Beyond the Förster Theory. *J. Phys. Chem. A* **2004**, *108*, 5752–5763.
- (445) Beljonne, D.; Curutchet, C.; Scholes, G. D.; Silbey, R. J. Beyond Förster Resonance Energy Transfer in Biological and Nanoscale Systems. *J. Phys. Chem. B* **2009**, *113*, 6583–6599.
- (446) Dong, H.; Xu, D.-Z.; Huang, J. F.; Sun, C.-P. Coherent Excitation Transfer via the Dark-State Channel in a Bionic System. *Light Sci. Appl.* **2012**, *1*, No. e2.
- (447) Bondarenko, A. S.; Knoester, J.; Jansen, T. L. C. Comparison of Methods to Study Excitation Energy Transfer in Molecular Multichromophoric Systems. *Chem. Phys.* **2020**, *529*, 110478.
- (448) Kobayashi, T.; Taneichi, T.; Takasaka, S. Exciton Energy Transfer Between Optically Forbidden States of Molecular Aggregates. *J. Chem. Phys.* **2007**, *126*, 194705.

- (449) Dimitriev, O. P.; Zirzlmeier, J.; Menon, A.; Slominskii, Yu; Guldi, D. M. Exciton Dynamics in *J*- and *H*-Aggregates of a Tricarbocyanine Near-Infrared Dye. *J. Phys. Chem. C* **2021**, *125*, 9855–9865.
- (450) Sissa, C.; Manna, A. K.; Terenziani, F.; Painelli, A.; Pati, S. K. Beyond the Förster Formulation for Resonance Energy Transfer: The Role of Dark States. *Phys. Chem. Chem. Phys.* **2011**, *13*, 12734–12744.
- (451) Eckardt, A. Colloquium: Atomic Quantum Gases in Periodically Driven Optical Lattices. *Rev. Mod. Phys.* **2017**, *89*, 011004.
- (452) Bukov, M.; D'Alessio, L.; Polkovnikov, A. Universal High-Frequency Behavior of Periodically Driven Systems: From Dynamical Stabilization to Floquet Engineering. *Adv. Phys.* **2015**, *64*, 139–226.
- (453) Holthaus, M. Floquet Engineering with Quasienergy Bands of Periodically Driven Optical Lattices. *J. Phys. B: At., Mol. Opt. Phys.* **2016**, *49*, 013001.
- (454) Kohler, S.; Lehmann, J.; Hägggi, P. Driven Quantum Transport on The Nanoscale. *Phys. Rep.* **2005**, *406*, 379–443.
- (455) Thanh Phuc, N.; Ishizaki, A. Control of Excitation Energy Transfer in Condensed Phase Molecular Systems by Floquet Engineering. *J. Phys. Chem. Lett.* **2018**, *9*, 1243–1248.
- (456) Schwennicke, K.; Yuen-Zhou, J. Optical Activity from the Exciton Aharonov-Bohm Effect: A Floquet Engineering Approach. *J. Phys. Chem. C* **2020**, *124*, 4206–4214.
- (457) Jones, G. A.; Bradshaw, D. S. Resonance Energy Transfer: From Fundamental Theory to Recent Applications. *Front. Phys.* **2019**, *7*, 100.
- (458) Salam, A. The Unified Theory of Resonance Energy Transfer According to Molecular Quantum Electrodynamics. *Atoms* **2018**, *6*, 56.
- (459) Andrews, D. L.; Ford, J. S. Resonance Energy Transfer: Influence of Neighboring Matter Absorbing in the Wavelength Region of the Acceptor. *J. Chem. Phys.* **2013**, *139*, 014107.
- (460) Salam, A. Mediation of Resonance Energy Transfer by a Third Molecule. *J. Chem. Phys.* **2012**, *136*, 014509.
- (461) Ford, J. S.; Andrews, D. L. Geometrical Effects on Resonance Energy Transfer Between Orthogonally-Oriented Chromophores, Mediated by a Nearby Polarisable Molecule. *Chem. Phys. Lett.* **2014**, *591*, 88–92.
- (462) Salam, A. Near-Zone Mediation of RET by One and Two Proximal Particles. *J. Phys. Chem. A* **2019**, *123*, 2853–2860.
- (463) Wang, Y. Local Field Effect in Small Semiconductor Clusters and Particles. *J. Phys. Chem.* **1991**, *95*, 1119–1124.
- (464) Hsu, L.-Y.; Ding, W.; Schatz, G. C. Plasmon-Coupled Resonance Energy Transfer. *J. Phys. Chem. Lett.* **2017**, *8*, 2357–2367.
- (465) An, K. H.; Shtein, M.; Pipe, K. P. Surface Plasmon Mediated Energy Transfer of Electrically-Pumped Excitons. *Opt. Express* **2010**, *18*, 4041–4048.
- (466) Yang, K. Y.; Choi, K. C.; Ahn, C. W. Surface Plasmon-Enhanced Energy Transfer in an Organic Light-Emitting Device Structure. *Opt. Express* **2009**, *17*, 11495–11504.
- (467) El-Sayed, M. A. Effect of Spin Orbit Interactions on the Dipolar Nature of the Radiative Microwave Zero-Field Transitions in Aromatic Molecules. *J. Chem. Phys.* **1974**, *60*, 4502–4507.
- (468) Baranes, L. Unexpected Intersystem Crossing. *Nat. Chem.* **2019**, *11*, 103–108.
- (469) Lefebvre-Brion, H.; Field, R. W. *The Spectra and Dynamics of Diatomic Molecules*; Elsevier Inc., 2004; pp 621–739.
- (470) McGlynn, S. P.; Azumi, T.; Kinoshita, M. *Molecular Spectroscopy of the Triplet State*; Prentice-Hall: Hoboken, 1969; 434 p.
- (471) Bixon, M.; Jortner, J. Intramolecular Radiationless Transitions. *J. Chem. Phys.* **1968**, *48*, 715–726.
- (472) Turro, N. J.; Ramamurthy, V.; Scaiano, J. C. *Principles of Molecular Photochemistry: An Introduction*; University Science Books: Sausalito, CA, 2009; Chapter 3; pp 109–168.
- (473) Gibbons, D. J.; Farawar, A.; Mazzella, P.; Leroy-Lhez, S.; Williams, R. M. Making Triplets from Photo-Generated Charges: Observations, Mechanisms and Theory. *Photochem. Photobiol. Sci.* **2020**, *19*, 136–158.
- (474) Zhao, J.; Chen, K.; Hou, Y.; Che, Y.; Liu, L.; Jia, D. Recent Progress in Heavy Atom-Free Organic Compounds Showing Unexpected Intersystem Crossing (ISC) Ability. *Org. Biomol. Chem.* **2018**, *16*, 3692–3701.
- (475) Lv, M.; Yu, Y.; Sandoval-Salinas, M. E.; Xu, J.; Lei, Z.; Casanova, D.; Yang, Y.; Chen, J. Engineering the Charge-Transfer State to Facilitate Spin-Orbit Charge Transfer Intersystem Crossing in Spirobis[anthracene]diones. *Angew. Chem., Int. Ed.* **2020**, *59*, 22179–22184.
- (476) Colvin, M. T.; Ricks, A. B.; Scott, A. M.; Co, D. T.; Wasielewski, M. R. Intersystem Crossing Involving Strongly Spin Exchange-Coupled Radical Ion Pairs in Donor-bridge-Acceptor Molecules. *J. Phys. Chem. A* **2012**, *116*, 1923–1930.
- (477) Wang, X.; Martínez-Fernández, L.; Zhang, Y.; Zhang, K.; Improta, R.; Kohler, B.; Xu, J.; Chen, J. Solvent-Dependent Stabilization of a Charge Transfer State Is the Key to Ultrafast Triplet State Formation in an Epigenetic DNA Nucleoside. *Chemistry* **2021**, *27*, 10932–10940.
- (478) Pensack, R. D.; Song, Y.; McCormick, T. M.; Jahnke, A. A.; Hollinger, J.; Seferos, D. S.; Scholes, G. D. Evidence for the Rapid Conversion of Primary Photoexcitations to Triplet States in Seleno- and Telluro-Analogues of Poly(3-hexylthiophene). *J. Phys. Chem. B* **2014**, *118*, 2589–2597.
- (479) Ompong, D.; Singh, J. Study of Intersystem Crossing Mechanism in Organic Materials. *Phys. Status Solidi C* **2016**, *13*, 89–92.
- (480) Auböck, G.; Chergui, M. Sub-50-fs Photoinduced Spin Crossover in [Fe(bpy)<sub>3</sub>]<sup>2+</sup>. *Nat. Chem.* **2015**, *7*, 629–633.
- (481) Baryshnikov, G.; Minaev, B.; Ågren, H. Theory and Calculation of the Phosphorescence Phenomenon. *Chem. Rev.* **2017**, *117*, 6500–6537.
- (482) Cekli, S.; Winkel, R. W.; Alarousu, E.; Mohammed, O. F.; Schanze, K. S. Triplet Excited State Properties in Variable Gap Pconjugated Donor-Acceptor-Donor Chromophores. *Chem. Sci.* **2016**, *7*, 3621–3631.
- (483) Ang, S. J.; Chwee, T. S.; Wong, M. W. Does Halogen Bonding Promote Intersystem Crossing and Phosphorescence in Benzaldehyde? *J. Phys. Chem. C* **2018**, *122*, 12441–12447.
- (484) Minns, R. S.; Parker, D. S. N.; Penfold, T. J.; Worth, G. A.; Fielding, H. H. Competing Ultrafast Intersystem Crossing and Internal Conversion in The ‘Channel 3’ Region of Benzene. *Phys. Chem. Chem. Phys.* **2010**, *12*, 15607–15615.
- (485) Stephansen, A. B.; Sølling, T. I. Distortion Dependent Intersystem Crossing: A Femtosecond Time-Resolved Photoelectron Spectroscopy Study of Benzene, Toluene, and p-Xylene. *Struct. Dyn.* **2017**, *4*, 044008.
- (486) Martínez-Fernández, L.; Corral, I.; Granucci, G.; Persico, M. Competing Ultrafast Intersystem Crossing and Internal Conversion: A Time Resolved Picture for the Deactivation of 6-Thioguanine. *Chem. Sci.* **2014**, *5*, 1336–1347.
- (487) Reichardt, C.; Vogt, R. A.; Crespo-Hernández, C. E. On the Origin of Ultrafast Nonradiative Transitions in Nitro-Polycyclic Aromatic Hydrocarbons: Excited State Dynamics in 1-Nitronaphthalene. *J. Chem. Phys.* **2009**, *131*, 224518.
- (488) Vogt, R. A.; Reichardt, C.; Crespo-Hernández, C. E. Excited-State Dynamics in Nitro-Naphthalene Derivatives: Intersystem Crossing to the Triplet Manifold in Hundreds of Femtoseconds. *J. Phys. Chem. A* **2013**, *117*, 6580–6588.
- (489) Penfold, T. J.; Gindensperger, E.; Daniel, C.; Marian, C. M. Spin-Vibronic Mechanism for Intersystem Crossing. *Chem. Rev.* **2018**, *118*, 6975–7025.
- (490) Baba, M. Intersystem Crossing in the  $1\pi\pi^*$  and  $1\pi\pi^*$  States. *J. Phys. Chem. A* **2011**, *115*, 9514–9519.
- (491) Okada, T.; Karaki, I.; Matsuzawa, E.; Mataga, N.; Sakata, Y.; Misumi, S. Ultrafast Intersystem Crossing in Some Intramolecular Heteroexcimers. *J. Phys. Chem.* **1981**, *85*, 3957–3960.
- (492) Williams, R. M.; Zwier, J. M.; Verhoeven, J. W. Photoinduced Intramolecular Electron Transfer in a Bridged C<sub>60</sub> (Acceptor)-Aniline (Donor) System: Photophysical Properties of the First “Active” Fullerene Diad. *J. Am. Chem. Soc.* **1995**, *117*, 4093–4099.
- (493) Hou, Y.; Zhang, X.; Chen, K.; Liu, D.; Wang, Z.; Liu, Q.; Zhao, J.; Barbon, A. Charge Separation, Charge Recombination, Long-Lived

- Charge Transfer State Formation and Intersystem Crossing in Organic Electron Donor/Acceptor Dyads. *J. Mater. Chem. C Mater. Opt. Electron. Devices* **2019**, *7*, 12048–12074.
- (494) Roest, M. R.; Oliver, A. M.; Paddon-Row, M. N.; Verhoeven, J. W. Distance Dependence of Singlet and Triplet Charge Recombination Pathways in a Series of Rigid Bichromophoric Systems. *J. Phys. Chem. A* **1997**, *101*, 4867–4871.
- (495) Buck, J. T.; Boudreau, A. M.; DeCarmine, A.; Wilson, R. W.; Hampsey, J.; Mani, T. Spin-Allowed Transitions Control the Formation of Triplet Excited States in Orthogonal Donor-Acceptor Dyads. *Chem.* **2019**, *5*, 138–155.
- (496) Filatov, M. A.; Karuthedath, S.; Polestshuk, P. M.; Savoie, H.; Flanagan, K. J.; Sy, C.; Sitte, E.; Telitchko, M.; Laquai, F.; Boyle, R. W.; Senge, M. O. Generation of Triplet Excited States via Photoinduced Electron Transfer in meso-antra-BODIPY: Fluorogenic Response toward Singlet Oxygen in Solution and in Vitro. *J. Am. Chem. Soc.* **2017**, *139*, 6282–6285.
- (497) Wang, Z.; Zhao, J. BODIPY-Anthracene Dyads as Triplet Photosensitizers: Effect of Chromophore Orientation on Triplet-State Formation Efficiency and Application in Triplet-Triplet Annihilation Upconversion. *Org. Lett.* **2017**, *19*, 4492–4495.
- (498) Filatov, M. A.; Karuthedath, S.; Polestshuk, P. M.; Callaghan, S.; Flanagan, K. J.; Wiesner, T.; Laquai, F.; Senge, M. O. BODIPY-Pyrene and Perylene Dyads as Heavy-Atom-Free Singlet Oxygen Sensitizers. *ChemPhotoChem* **2018**, *2*, 606–615.
- (499) Golden, J. H.; Estergreen, L.; Porter, T.; Tadle, A. C.; Sylvinson, M. R., D.; Facendola, J. W.; Kubiak, C. P.; Bradforth, S. E.; Thompson, M. E. Symmetry-Breaking Charge Transfer in Boron Dipyridylmethene (DIPYR) Dimers. *ACS Appl. Energy Mater.* **2018**, *1*, 1083–1095.
- (500) Hou, Y.; Biskup, T.; Rein, S.; Wang, Z.; Bussotti, L.; Russo, N.; Foggi, P.; Zhao, J.; Di Donato, M.; Mazzone, G.; Weber, S. Spin-Orbit Charge Recombination Intersystem Crossing in Phenothiazine-Anthracene Compact Dyads: Effect of Molecular Conformation on Electronic Coupling, Electronic Transitions, and Electron Spin Polarizations of the Triplet States. *J. Phys. Chem. C* **2018**, *122*, 27850–27865.
- (501) Dong, Y.; Sukhanov, A. A.; Zhao, J.; Elmali, A.; Li, X.; Dick, B.; Karatay, A.; Voronkova, V. K. Spin-Orbit Charge-Transfer Intersystem Crossing (SOCT-ISC) in Bodipy-Phenoxazine Dyads: Effect of Chromophore Orientation and Conformation Restriction on the Photophysical Properties. *J. Phys. Chem. C* **2019**, *123*, 22793–22811.
- (502) Liu, Y.; Zhao, J.; Iagatti, A.; Bussotti, L.; Foggi, P.; Castellucci, E.; Di Donato, M.; Han, K.-L. A Revisit to the Orthogonal Bodipy Dimers: Experimental Evidence for the Symmetry Breaking Charge Transfer-Induced Intersystem Crossing. *J. Phys. Chem. C* **2018**, *122*, 2502–2511.
- (503) Etinski, M.; Rai-Constapel, V.; Marian, C. M. Time-Dependent Approach to Spin-Vibronic Coupling: Implementation and Assessment. *J. Chem. Phys.* **2014**, *140*, 114104.
- (504) Ohmori, N.; Suzuki, T.; Ito, M. Why Does Intersystem Crossing Occur in Isolated Molecules of Benzaldehyde, Acetophenone, and Benzophenone? *J. Phys. Chem.* **1988**, *92*, 1086–1093.
- (505) Ou, Q.; Subotnik, J. E. Electronic Relaxation in Benzaldehyde Evaluated via TD-DFT and Localized Diabatization: Intersystem Crossings, Conical Intersections, and Phosphorescence. *J. Phys. Chem. C* **2013**, *117*, 19839–19849.
- (506) Datko, B. D.; Livshits, M.; Zhang, Z.; Qin, Y.; Jakubikova, E.; Rack, J. J.; Grey, J. K. Large Excited State Conformational Displacements Expedite Triplet Formation in a Small Conjugated Oligomer. *J. Phys. Chem. Lett.* **2019**, *10*, 1259–1263.
- (507) Nagarajan, K.; Mallia, A. R.; Muraleedharan, K.; Hariharan, M. Enhanced Intersystem Crossing in Core-Twisted Aromatics. *Chem. Sci.* **2017**, *8*, 1776–1782.
- (508) Parker, D. S. N.; Minns, R. S.; Penfold, T. J.; Worth, G. A.; Fielding, H. H. Ultrafast Dynamics of the S1 Excited State of Benzene. *Chem. Phys. Lett.* **2009**, *469*, 43–47.
- (509) Penfold, T. J.; Worth, G. A. The Effect of Molecular Distortions on Spin-Orbit Coupling in Simple Hydrocarbons. *Chem. Phys.* **2010**, *375*, 58–66.
- (510) Perun, S.; Tatchen, J.; Marian, C. M. Singlet and Triplet Excited States and Intersystem Crossing in Free-Base Porphyrin: TDDFT and DFT/MRCI Study. *ChemPhysChem* **2008**, *9*, 282–292.
- (511) Lyskov, I.; Marian, C. M. Climbing up the Ladder: Intermediate Triplet States Promote the Reverse Intersystem Crossing in the Efficient TADF Emitter ACRSA. *J. Phys. Chem. C* **2017**, *121*, 21145–21153.
- (512) Penfold, T. J.; Dias, F. B.; Monkman, A. P. The Theory of Thermally Activated Delayed Fluorescence For Organic Light Emitting Diodes. *Chem. Commun.* **2018**, *54*, 3926–3935.
- (513) Aizawa, N.; Harabuchi, Y.; Maeda, S.; Pu, Y.-J. Kinetic Prediction of Reverse Intersystem Crossing in Organic Donor-Acceptor Molecules. *Nature Commun.* **2020**, *11*, 3909.
- (514) Dias, F. B.; Bourdakos, K. N.; Jankus, V.; Moss, K. C.; Kamtekar, K. T.; Bhalla, V.; Santos, J.; Bryce, M. R.; Monkman, A. P. Triplet Harvesting with 100% Efficiency by Way of Thermally Activated Delayed Fluorescence in Charge Transfer OLED Emitters. *Adv. Mater.* **2013**, *25*, 3707–3714.
- (515) Cai, X.; Li, X.; Xie, G.; He, Z.; Gao, K.; Liu, K.; Chen, D.; Cao, Y.; Su, S.-J. Rate-Limited Effect” Of Reverse Intersystem Crossing Process: The Key For Tuning Thermally Activated Delayed Fluorescence Lifetime And Efficiency Roll-Off Of Organic Light Emitting Diodes. *Chem. Sci.* **2016**, *7*, 4264–4275.
- (516) Delorme, R.; Perrin, F. Duration of the Fluorescence of Solid Uranyl Salts and Their Solution. *J. Phys. Rad. Ser.* **1929**, *10*, 177–186.
- (517) Uoyama, H.; Goushi, K.; Shizu, K.; Nomura, H.; Adachi, C. Highly Efficient Organic Light-Emitting Diodes From Delayed Fluorescence. *Nature* **2012**, *492*, 234–238.
- (518) Tsutsui, T.; Adachi, C.; Saito, S. In *Photochemical Processes in Organized Molecular Systems*; Honda, K., Ed.; Elsevier, 1991; pp 437–450.
- (519) Segal, M.; Baldo, M. A.; Holmes, R. J.; Forrest, S. R.; Soos, Z. G. Excitonic Singlet-Triplet Ratios In Molecular And Polymeric Organic Materials. *Phys. Rev. B* **2003**, *68*, 075211.
- (520) Liu, Y.; Li, C.; Ren, Z.; Yan, S.; Bryce, M. R. All-Organic Thermally Activated Delayed Fluorescence Materials For Organic Light-Emitting Diodes. *Nat. Rev. Mater.* **2018**, *3*, 18020.
- (521) Gibson, J.; Penfold, T. J. Nonadiabatic Coupling Reduces the Activation Energy in Thermally Activated Delayed Fluorescence. *Phys. Chem. Chem. Phys.* **2017**, *19*, 8428–8434.
- (522) Samanta, P. K.; Kim, D.; Coropeceanu, V.; Bredas, J.-L. Up-Conversion Intersystem Crossing Rates in Organic Emitters for Thermally Activated Delayed Fluorescence (TADF): Impact of the Nature of Singlet vs. Triplet Excited States. *J. Am. Chem. Soc.* **2017**, *139*, 4042–4051.
- (523) Lv, L.; Yuan, K.; Wang, Y. Theoretical Studying of Basic Photophysical Processes in a Thermally Activated Delayed Fluorescence Copper (I) Complex: Determination of Reverse Intersystem Crossing and Radiative Rate Constants. *Org. Electron.* **2017**, *51*, 207–219.
- (524) Albrecht, K.; Matsuoka, K.; Yokoyama, D.; Sakai, Y.; Nakayama, A.; Fujita, K.; Yamamoto, K. Thermally Activated Delayed Fluorescence OLEDs with Fully Solution Processed Organic Layers Exhibiting Nearly 10% External Quantum Efficiency. *Chem. Commun. (Camb.)* **2017**, *53*, 2439–2442.
- (525) Huang, T.; Jiang, W.; Duan, L. Recent Progress in Solution Processable TADF Materials for Organic Light-Emitting Diodes. *J. Mater. Chem. C* **2018**, *6*, 5577–5596.
- (526) Etherington, M. K.; Gibson, J.; Higginbotham, H. F.; Penfold, T. J.; Monkman, A. P. Revealing the Spin-Vibronic Coupling Mechanism of Thermally Activated Delayed Fluorescence. *Nat. Commun.* **2016**, *7*, 13680.
- (527) Natali, M.; Campagna, S.; Scandola, F. Photoinduced Electron Transfer Across Molecular Bridges. Electron- and Hole-Transfer Superexchange Pathways. *Chem. Soc. Rev.* **2014**, *43*, 4005–4018.
- (528) Huang, Z.; Ji, D.; Xia, A.; Koberling, F.; Patting, M.; Erdmann, R. Direct Observation of Delayed Fluorescence from a Remarkable Back-Isomerization in Cy5. *J. Am. Chem. Soc.* **2005**, *127*, 8064–8066.

- (529) Shpaisman, H.; Niitsoo, O.; Lubomirsky, I.; Cahen, D. Can Up-and Down-Conversion and Multi-Exciton Generation Improve Photovoltaics? *Sol. Energy Mater. Sol. Cells* **2008**, *92*, 1541–1546.
- (530) Manmohan, A.; Prasad, A.; Dharavath, R.; Karthikeyan, S. P.; Raglend, I. J. Up and Down Conversion of Photons with Modified Perturb and Observe MPPT Technique for Efficient Solar Energy Generation. *Energy Procedia* **2017**, *117*, 786–793.
- (531) Hasegawa, Y.; Kitagawa, Y.; Nakanishi, T. Effective Photosensitized, Electrosensitized, and Mechanosensitized Luminescence of Lanthanide Complexes. *NPG Asia Mater.* **2018**, *10*, 52–70.
- (532) Ye, H.; Bogdanov, V.; Liu, S.; Vajandar, S.; Osipowicz, T.; Hernández, I.; Xiong, Q. Bright Photon Upconversion on Composite Organic Lanthanide Molecules through Localized Thermal Radiation. *J. Phys. Chem. Lett.* **2017**, *8*, 5695–5699.
- (533) Rieder, G. *Photonik*; Springer Verlag: Wien, 1997.
- (534) Auzel, F. Upconversion and Anti-Stokes Processes with *f* and *d* Ions in Solids. *Chem. Rev.* **2004**, *104*, 139–174.
- (535) Dimitriev, O. P. Harvesting of the Infrared Energy: Direct Collection, Up-conversion, and Storage. *Semicond. Phys. Quantum Electron. Optoelectron.* **2019**, *22*, 457–469.
- (536) Drobizhev, M.; Makarov, N. S.; Tillo, S. E.; Hughes, T. E.; Rebane, A. Two-Photon Absorption Properties of Fluorescent Proteins. *Nat. Methods* **2011**, *8*, 393–399.
- (537) He, G. S.; Tan, L.-S.; Zheng, Q.; Prasad, P. N. Multiphoton Absorbing Materials: Molecular Designs, Characterizations, and Applications. *Chem. Rev.* **2008**, *108*, 1245–1330.
- (538) Cole, J. M. Organic Materials for Second-Harmonic Generation: Advances in Relating Structure to Function. *Philos. Trans. R. Soc. A* **2003**, *361*, 2751–2770.
- (539) LaCount, M. D.; Weingarten, D.; Hu, N.; Shaheen, S. E.; van de Lagemaat, J.; Rumbles, G.; Walba, D. M.; Lusk, M. T. Energy Pooling Upconversion in Organic Molecular Systems. *J. Phys. Chem. A* **2015**, *119*, 4009–4016.
- (540) Weingarten, D. H.; LaCount, M. D.; van de Lagemaat, J.; Rumbles, G.; Lusk, M. T.; Shaheen, S. E. Experimental Demonstration of Photon Upconversion via Cooperative Energy Pooling. *Nat. Commun.* **2017**, *8*, 14808.
- (541) Merrifield, R. E. Diffusion and Mutual Annihilation of Triplet Excitons in Organic Crystals. *Acc. Chem. Res.* **1968**, *1*, 129–135.
- (542) Bharmoria, P.; Bildirir, H.; Moth-Poulsen, K. Triplet-Triplet Annihilation Based near Infrared to Visible Molecular Photon Upconversion. *Chem. Soc. Rev.* **2020**, *49*, 6529–6554.
- (543) Huang, L.; Kakadiaris, E.; Vanekova, T.; Huang, K.; Vaculovicova, M.; Han, G. Designing next Generation of Photon Upconversion: Recent Advances in Organic Triplet-Triplet Annihilation Upconversion Nanoparticles. *Biomaterials* **2019**, *201*, 77–86.
- (544) Mahr, H. Two-Photon Absorption Spectroscopy. In *Quantum Electronics: A Treatise*; Rabin, H., Tang, C. L., Eds.; Nonlinear Optics, Part A; Academic Press: New York, 2012; Vol. 1, pp 286–363.
- (545) Ye, C.; Zhou, L.; Wang, X.; Liang, Z. Photon Upconversion: From Two-Photon Absorption (TPA) to Triplet-Triplet Annihilation (TTA). *Phys. Chem. Chem. Phys.* **2016**, *18*, 10818–10835.
- (546) Yang, W.; Zhao, J.; Sonn, Ch.; Escudero, D.; Karatay, A.; Yaglioglu, H. G.; Küçüköz, B.; Hayvali, M.; Li, C.; Jacquemin, D. Efficient Inter-System Crossing in Heavy-Atom-Free Perylene-Bisimide Derivatives. *J. Phys. Chem. C* **2016**, *120*, 10162–10175.
- (547) Svagan, A. J.; Busko, D.; Avlasevich, Yu.; Glasser, G.; Baluschev, S.; Landfester, K. Photon Energy Upconverting Nanopaper: A Bioinspired Oxygen Protection Strategy. *ACS Nano* **2014**, *8*, 8198–8207.
- (548) Yakutkin, V.; Aleshchenkov, S.; Chernov, S.; Miteva, T.; Nelles, G.; Cheprakov, A.; Baluschev, S. Towards the IR Limit of the Triplet-Triplet Annihilation-Supported Upconversion: Tetraanthra-Porphyrin. *Chem.—Eur. J.* **2008**, *14*, 9846–9850.
- (549) Kiseleva, N.; Nazari, P.; Dee, C.; Busko, D.; Richards, B. S.; Seitz, M.; Howard, I. A.; Turshatov, A. Lanthanide Sensitizers for Large Anti-Stokes Shift near-Infrared-to-Visible Triplet-Triplet Annihilation Photon Upconversion. *J. Phys. Chem. Lett.* **2020**, *11*, 2477–2481.
- (550) Nishimura, N.; Gray, V.; Allardice, J. R.; Zhang, Z.; Pershin, A.; Beljonne, D.; Rao, A. Photon Upconversion from Near-Infrared to Blue Light with TIPS-Anthracene as an Efficient Triplet-Triplet Annihilator. *ACS Materials Lett.* **2019**, *1*, 660–664.
- (551) MacDougall, S. K. W.; Ivaturi, A.; Marques-Hueso, J.; Krämer, K. W.; Richards, B. S. Ultra-High Photoluminescent Quantum Yield of  $\beta$ -NaYF<sub>4</sub>:10% Er<sup>3+</sup> via Broadband Excitation of Upconversion for Photovoltaic Devices. *Opt. Express* **2012**, *20* (6), A879–87.
- (552) Radiunas, E.; Raišys, S.; Juršėnas, S.; Jozeliūnaitė, A.; Javorkis, T.; Šinkevičiūtė, U.; Orentas, E.; Kazlauskas, K. Understanding the Limitations of NIR-to-Visible Photon Upconversion in Phthalocyanine-Sensitized Rubrene Systems. *J. Mater. Chem. C Mater. Opt. Electron. Devices* **2020**, *8*, 5525–5534.
- (553) Huang, L.; Wu, W.; Li, Y.; Huang, K.; Zeng, L.; Lin, W.; Han, G. Highly Effective Near-Infrared Activating Triplet-Triplet Annihilation Upconversion for Photoredox Catalysis. *J. Am. Chem. Soc.* **2020**, *142*, 18460–18470.
- (554) Fan, C.; Wei, L.; Niu, T.; Rao, M.; Cheng, G.; Chruma, J. J.; Wu, W.; Yang, C. Efficient Triplet-Triplet Annihilation Upconversion with an Anti-Stokes Shift of 1.08 eV by Chemically Tuning Sensitizers. *J. Am. Chem. Soc.* **2019**, *141*, 15070–15077.
- (555) Mizukuro, T.; Abulikemu, A.; Suzuki, K.; Sakagami, Y.; Nishii, R.; Jin, T.; Kamada, K. Triplet-Triplet Annihilation Upconversion Through Triplet Energy Transfer at a Nanoporous Solid-Liquid Interface. *Phys. Chem. Chem. Phys.* **2020**, *22*, 17807–17813.
- (556) Nishimura, N.; Allardice, J. R.; Xiao, J.; Gu, Q.; Gray, V.; Rao, A. Photon Upconversion Utilizing Energy Beyond The Band Gap Of Crystalline Silicon With A Hybrid TES-ADT/Pbs Quantum Dots System. *Chem. Sci.* **2019**, *10*, 4750–4760.
- (557) Huang, Z.; Xu, Z.; Mahboub, M.; Li, X.; Taylor, J. W.; Harman, W. H.; Lian, T.; Tang, M. L. PbS/CdS Core-Shell Quantum Dots Suppress Charge Transfer and Enhance Triplet Transfer. *Angew. Chem., Int. Ed.* **2017**, *56*, 16583–16587.
- (558) Li, X.; Fast, A.; Huang, Z.; Fishman, D. A.; Tang, M. L. Complementary Lock-and-Key Ligand Binding of a Triplet Transmitter to a Nanocrystal Photosensitizer. *Angew. Chem., Int. Ed.* **2017**, *56*, 5598–5602.
- (559) Gray, V.; Xia, P.; Huang, Z.; Moses, E.; Fast, A.; Fishman, D. A.; Vullev, V. I.; Abrahamsson, M.; Moth-Poulsen, K.; Lee Tang, M. CdS/ZnS Core-Shell Nanocrystal Photosensitizers for Visible to UV Upconversion. *Chem. Sci.* **2017**, *8*, 5488–5496.
- (560) Jenkins, R. D.; Andrews, D. L. Three-Center Systems for Energy Pooling: Quantum Electrodynamical Theory. *J. Phys. Chem. A* **1998**, *102*, 10834–10842.
- (561) Wen, S.; Zhou, J.; Zheng, K.; Bednarkiewicz, A.; Liu, X.; Jin, D. Advances in Highly Doped Upconversion Nanoparticles. *Nat. Commun.* **2018**, *9*, 2415.
- (562) Zhu, X.; Su, Q.; Feng, W.; Li, F. Anti-Stokes Shift Luminescent Materials for Bio-Applications. *Chem. Soc. Rev.* **2017**, *46*, 1025–1039.
- (563) Ha, S. T.; Shen, C.; Zhang, J.; Xiong, Q. Laser Cooling Of Organic-Inorganic Lead Halide Perovskites. *Nat. Photonics* **2016**, *10*, 115–121.
- (564) Seletskiy, D. V.; Epstein, R.; Sheik-Bahae, M. Laser Cooling in Solids: Advances and Prospects. *Rep. Prog. Phys.* **2016**, *79*, 096401.
- (565) Sheik-Bahae, M.; Epstein, R. I. Can Laser Light Cool Semiconductors? *Phys. Rev. Lett.* **2004**, *92*, 247403.
- (566) Zhang, J.; Li, D.; Chen, R.; Xiong, Q. Laser Cooling of a Semiconductor by 40 K. *Nature* **2013**, *493*, 504–508.
- (567) Goldschmidt, J. C.; Fischer, S. Upconversion for Photovoltaics - A Review of Materials, Devices and Concepts for Performance Enhancement. *Adv. Opt. Mater.* **2015**, *3*, 510–535.
- (568) Duan, C.; Liang, L.; Li, L.; Zhang, R.; Xu, Z. P. Recent Progress in Upconversion Luminescence Nanomaterials for Biomedical Applications. *J. Mater. Chem. B Mater. Biol. Med.* **2018**, *6*, 192–209.
- (569) Yamamoto, K.; Togawa, R.; Fujimura, R.; Kajikawa, K. Local Temperature Variation Measurement Bby Anti-Stokes Luminescence in Attenuated Total Reflection Geometry. *Opt. Express* **2016**, *24*, 19026–19031.

- (570) Kachynski, A. V.; Kuzmin, A. N.; Pudavar, H. E.; Prasad, P. N. Three-Dimensional Confocal Thermal Imaging Using Anti-Stokes Luminescence. *Appl. Phys. Lett.* **2005**, *87*, 023901.
- (571) Zhu, L.; Ye, C.; Dai, G.; Wang, X.; Yu, X.; Liu, T.; Tao, X. Highly-Efficient Upconversion via Direct One-Photon Absorption of Xanthene-Based Chromophores. *Dyes Pigm.* **2020**, *172*, 107853.
- (572) Gajdos, T.; Hopp, B.; Erdélyi, M. Hot-Band Anti-Stokes Fluorescence Properties of Alexa Fluor 568. *J. Fluoresc.* **2020**, *30*, 437–443.
- (573) Drobizhev, M.; Karotki, A.; Kruk, M.; Krivokapic, A.; Anderson, H. L.; Rebane, A. Photon Energy Upconversion in Porphyrins: One-Photon Hot-Band Absorption versus Two-Photon Absorption. *Chem. Phys. Lett.* **2003**, *370*, 690–699.
- (574) Chen, T.-H.; Zhang, S.; Jaishi, M.; Adhikari, R.; Bi, J.; Fang, M.; Xia, S.; Zhang, Y.; Luck, R. L.; Pati, R.; Lee, H.-M.; Luo, F.-T.; Tiwari, A.; Liu, H. New Near-Infrared Fluorescent Probes with Single-Photon Anti-Stokes-Shift Fluorescence for Sensitive Determination of PH Variances in Lysosomes with a Double-Checked Capability. *ACS Appl. Bio Mater.* **2018**, *1*, 549–560.
- (575) Meshalkin, Y. P.; Svetlichnyi, V. A.; Lapin, I. N. Anti-Stokes Fluorescence of Polymethine Dyes Excited by a Titanium-Sapphire Laser. *Russ. Phys. J.* **2007**, *50*, 267–274.
- (576) Dimitriev, O.; Fedoryak, A.; Slominskii, Y.; Smirnova, A.; Yoshida, T. Phonon-Assisted Anti-Stokes Luminescence of Tricarbocyanine Near-Infrared Dye. *Chem. Phys. Lett.* **2020**, *738*, 136905.
- (577) Han, J.; Zhang, J.; Zhao, T.; Liu, M.; Duan, P. Photoswitchable Photon Upconversion from Turn-on Mode Fluorescent Diarylethenes. *CCS Chem.* **2021**, *3*, 665–674.
- (578) Liu, M. Optical Properties of Carbon Dots: A Review. *Nanoarchitectonics* **2020**, *1*, 1–12.
- (579) Li, D.; Liang, C.; Ushakova, E. V.; Sun, M.; Huang, X.; Zhang, X.; Jing, P.; Yoo, S. J.; Kim, J.-G.; Liu, E.; Zhang, W.; Jing, L.; Xing, G.; Zheng, W.; Tang, Z.; Qu, S.; Rogach, A. L. Thermally Activated Upconversion Near-Infrared Photoluminescence from Carbon Dots Synthesized via Microwave Assisted Exfoliation. *Small* **2019**, *15*, No. e1905050.
- (580) Sharanov, I.; Slominskii, Y.; Ishchenko, A.; Fedoryak, A.; Dimitriev, O. Single-Photon Upconversion Via Hot-Band Absorption and Assessment of the Laser Cooling Effect of Tricarbocyanine Dyes. *Chem. Phys. Impact* **2021**, *2*, 100026.
- (581) Ma, X.; Pan, F.; Li, H.; Shen, P.; Ma, C.; Zhang, L.; Niu, H.; Zhu, Y.; Xu, S.; Ye, H. Mechanism of Single-Photon Upconversion Photoluminescence in All-Inorganic Perovskite Nanocrystals: The Role of Self-Trapped Excitons. *J. Phys. Chem. Lett.* **2019**, *10*, 5989–5996.
- (582) Shen, J.; Zhu, Y.; Chen, C.; Yang, X.; Li, C. Facile Preparation and Upconversion Luminescence of Graphene Quantum Dots. *Chem. Commun.* **2011**, *47*, 2580–2582.
- (583) Nagai, K.; Uchida, K.; Yoshikawa, N.; Endo, T.; Miyata, Y.; Tanaka, K. Dynamical Symmetry of Strongly Light-Driven Electronic System in Crystalline Solids. *Commun. Phys.* **2020**, *3*, 137.
- (584) Grage, M. M.-L.; Wood, P. W.; Ruseckas, A.; Pullerits, T.; Mitchell, W.; Burn, P. L.; Samuel, I. D. W.; Sundström, V. Conformational Disorder and Energy Migration in MEH-PPV with Partially Broken Conjugation. *J. Chem. Phys.* **2003**, *118*, 7644.
- (585) Matsuo, K.; Yasuda, T. Blue Thermally Activated Delayed Fluorescence Emitters Incorporating Acridan Analogues with Heavy Group 14 Elements for High-Efficiency Doped and Non-Doped OLEDs. *Chem. Sci.* **2019**, *10*, 10687–10697.
- (586) Li, H.; Han, J.; Zhao, H.; Liu, X.; Luo, Y.; Shi, Y.; Liu, C.; Jin, M.; Ding, D. Lighting up the Invisible Twisted Intramolecular Charge Transfer State by High Pressure. *J. Phys. Chem. Lett.* **2019**, *10*, 748–753.
- (587) Todorova, M.; Bakalska, R.; Kolev, T. Synthesis, Crystal Structure, and Spectroscopic Properties of New Stilbazolium Salt with Enlarged i-Conjugated System. *Spectrochim. Acta A Mol. Biomol. Spectrosc.* **2013**, *108*, 211–222.
- (588) Kundu, A.; Karthikeyan, S.; Sagara, Y.; Moon, D.; Anthony, S. P. Temperature-Controlled Locally Excited and Twisted Intramolecular Charge-Transfer State-Dependent Fluorescence Switching in Triphenylamine-Benzothiazole Derivatives. *ACS Omega* **2019**, *4*, 5147–5154.
- (589) Sissa, C.; Painelli, A.; Terenziani, F.; Trotta, M.; Ragni, R. About the Origin of the Large Stokes Shift in Aminoalkyl Substituted Heptamethine Cyanine Dyes. *Phys. Chem. Chem. Phys.* **2020**, *22*, 129–135.
- (590) Ourahmoun, O.; Trigaud, T.; Ratier, B.; Belkaid, M. S.; Galmiche, L.; Audebert, P. An Efficient Tetrazine Photoluminescent Layer Used for Organic Solar Cells down Shifting. *Synth. Met.* **2017**, *234*, 106–110.
- (591) Qing, Z.; Audebert, P.; Clavier, G.; Méallet-Renault, R.; Miomandre, F.; Tang, J. Bright Fluorescence through Activation of a Low Absorption Fluorophore: The Case of a Unique Naphthalimide-Tetrazine Dyad. *New J. Chem.* **2011**, *35*, 1678.
- (592) Clavier, G.; Audebert, P. s-Tetrazines as Building Blocks For New Functional Molecules and Molecular Materials. *Chem. Rev.* **2010**, *110*, 3299–3314.
- (593) Plugge, M.; Alain-Rizzo, V.; Audebert, P.; Brouwer, A. M. Excited State Dynamics of 3,6-Diaryl-1,2,4,5-Tetrazines. Experimental and Theoretical Studies. *J. Photochem. Photobiol. A: Chem.* **2012**, *234*, 12–20.
- (594) Zhang, Z.; Song, W.; Su, J.; Tian, H. Vibration-Induced Emission (VIE) of N, N'-Disubstituted-Dihydribenzo[a, c]phenazines: Fundamental Understanding and Emerging Applications. *Adv. Funct. Mater.* **2020**, *30*, 1902803.
- (595) Zhang, Z.; Wu, Y.-S.; Tang, K.-C.; Chen, C.-L.; Ho, J.-W.; Su, J.; Tian, H.; Chou, P.-T. Excited-State Conformational/Electronic Responses of Saddle-Shaped N,N'-Disubstituted-Dihydribenzo-[a,c]phenazines: Wide-Tuning Emission from Red to Deep Blue and White Light Combination. *J. Am. Chem. Soc.* **2015**, *137*, 8509–8520.
- (596) Chen, W.; Chen, C.-L.; Zhang, Z.; Chen, Y.-A.; Chao, W.-C.; Su, J.; Tian, H.; Chou, P.-T. Snapshotting the Excited-State Planarization of Chemically Locked N,N'-Disubstituted Dihydribenzo[a,c]phenazines. *J. Am. Chem. Soc.* **2017**, *139*, 1636–1644.
- (597) Ren, J.; Sun, J.; Sun, X.; Song, R.; Xie, Z.; Zhou, S. Precisely Controlled Up/Down-Conversion Liquid and Solid State Photoluminescence of Carbon Dots. *Adv. Opt. Mater.* **2018**, *6*, 1800115.
- (598) Xia, J.; Chen, S.; Zou, G. Y.; Yu, Y. L.; Wang, J. H. Synthesis of Highly Stable Red-Emissive Carbon Polymer Dots By Modulated Polymerization: From the Mechanism to Application in Intracellular pH Imaging. *Nanoscale* **2018**, *10*, 22484–22492.
- (599) Ding, L.; Zhang, Z.; Li, X.; Su, J. Highly Sensitive Determination of Low-Level Water Content in Organic Solvents Using Novel Solvatochromic Dyes Based on Thioxanthone. *Chem. Commun.* **2013**, *49*, 7319.
- (600) Dhenadhayalan, N.; Lin, K. C.; Suresh, R.; Ramamurthy, P. Unravelling the Multiple Emissive States in Citric-Acid-Derived Carbon Dots. *J. Phys. Chem. C* **2016**, *120*, 1252–1261.
- (601) Ma, G.-F.; Xie, H.-J.; Cheng, P.-P.; Li, Y.-Q.; Tang, J.-X. Performance Enhancement of Polymer Solar Cells with Luminescent Down-Shifting Sensitizer. *Appl. Phys. Lett.* **2013**, *103*, 043302.
- (602) Gheno, A.; Trigaud, T.; Bouclé, J.; Audebert, P.; Ratier, B.; Vedraire, S. Stability Assessments on Luminescent Down-Shifting Molecules for UV-Protection of Perovskite Solar Cells. *Opt. Mater. (Amst.)* **2018**, *75*, 781–786.
- (603) Yang, D.; Zhou, X.; Wang, Y.; Vadim, A.; Alshehri, S. M.; Ahamed, T.; Ma, D. Deep Ultraviolet-To-NIR Broad Spectral Response Organic Photodetectors with Large Gain. *J. Mater. Chem. C* **2016**, *4*, 2160–2164.
- (604) Pintossi, D.; Iannaccone, G.; Colombo, A.; Bella, F.; Välimäki, M.; Väistönen, K.-L.; Hast, J.; Levi, M.; Gerbaldo, C.; Dragonetti, C.; Turri, S.; Griffini, G. Luminescent Downshifting by Photo-Induced Sol-Gel Hybrid Coatings: Accessing Multifunctionality on Flexible Organic Photovoltaics via Ambient Temperature Material Processing. *Adv. Electron. Mater.* **2016**, *2*, 1600288.
- (605) Engmann, S.; Machalek, M.; Turkovic, V.; Rösch, R.; Rädlein, E.; Gobsch, G.; Hoppe, H. Photon Recycling across a Ultraviolet-

- Blocking Layer by Luminescence in Polymer Solar Cells. *J. Appl. Phys.* **2012**, *112*, 034517.
- (606) Smith, M. B.; Michl, J. Singlet Fission. *Chem. Rev.* **2010**, *110*, 6891–936.
- (607) Chan, W. L.; Ligges, M.; Jailaubekov, A.; Kaake, L.; Miaja-Avila, L.; Zhu, X. Y. Observing the Multiexciton State in Singlet Fission and Ensuing Ultrafast Multielectron Transfer. *Science* **2011**, *334*, 1541–1545.
- (608) Wilson, M. W.; Rao, A.; Clark, J.; Kumar, R. S.; Brida, D.; Cerullo, G.; Friend, R. H. Ultrafast Dynamics of Exciton Fission in Polycrystalline Pentacene. *J. Am. Chem. Soc.* **2011**, *133*, 11830–11833.
- (609) Sakuma, T.; Sakai, H.; Araki, Y.; Mori, T.; Wada, T.; Tkachenko, N. V.; Hasobe, T. Long-Lived Triplet Excited States Of Bent-Shaped Pentacene Dimers by Intramolecular Singlet Fission. *J. Phys. Chem. A* **2016**, *120*, 1867–1875.
- (610) Bardeen, C. J. The Structure and Dynamics of Molecular Excitons. *Annu. Rev. Phys. Chem.* **2014**, *65*, 127–148.
- (611) Smith, M. B.; Michl, J. Recent Advances in Singlet Fission. *Annu. Rev. Phys. Chem.* **2013**, *64*, 361–386.
- (612) Xia, J.; Sanders, S. N.; Cheng, W.; Low, J. Z.; Liu, J.; Campos, L. M.; Sun, T. Singlet Fission: Progress and Prospects in Solar Cells. *Adv. Mater.* **2017**, *29*, 1601652.
- (613) Thompson, N. J.; Congreve, D. N.; Goldberg, D.; Menon, V. M.; Baldo, M. A. Slow Light Enhanced Singlet Exciton Fission Solar Cells with a 126% Yield of Electrons per Photon. *Appl. Phys. Lett.* **2013**, *103*, 263302.
- (614) Tabachnyk, M.; Karani, A. H.; Broch, K.; Pazos-Outón, L. M.; Xiao, J.; Jellico, T. C.; Novák, J.; Harkin, D.; Pearson, A. J.; Rao, A.; Greenham, N. C.; Böhm, M. L.; Friend, R. H. Efficient Singlet Exciton Fission in Pentacene Prepared from a Soluble Precursor. *APL Mater.* **2016**, *4*, 116112.
- (615) Sanders, S. N.; Pun, A. B.; Parenti, K. R.; Kumarasamy, E.; Yablon, L. M.; Sfeir, M. Y.; Campos, L. M. Understanding the Bound Triplet-Pair State in Singlet Fission. *Chem.* **2019**, *5*, 1988–2005.
- (616) Lee, T. S.; Lin, Y. L.; Kim, H.; Pensack, R. D.; Rand, B. P.; Scholes, G. D. Triplet Energy Transfer Governs the Dissociation of the Correlated Triplet Pair in Exothermic Singlet Fission. *J. Phys. Chem. Lett.* **2018**, *9*, 4087–4095.
- (617) Miyata, K.; Conrad-Burton, F. S.; Geyer, F. L.; Zhu, X. Y. Triplet Pair States in Singlet Fission. *Chem. Rev.* **2019**, *119*, 4261–4292.
- (618) Tayebjee, M. J. Y.; Sanders, S. N.; Kumarasamy, E.; Campos, L. M.; Sfeir, M. Y.; McCamey, D. R. Quintet Multiexciton Dynamics in Singlet Fission. *Nat. Phys.* **2017**, *13*, 182–188.
- (619) Pensack, R. D.; Ostroumov, E. E.; Tilley, A. J.; Mazza, S.; Grieco, C.; Thorley, K. J.; Asbury, J. B.; Seferos, D. S.; Anthony, J. E.; Scholes, G. D. Observation of Two Triplet-Pair Intermediates in Singlet Exciton Fission. *J. Phys. Chem. Lett.* **2016**, *7*, 2370–2375.
- (620) Wang, Z.; Zhang, C.; Wang, R.; Wang, G.; Wang, X.; Xiao, M. Weakly Coupled Triplet Pair States Probed by Quantum Beating in Delayed Fluorescence in Tetracene Crystals. *J. Chem. Phys.* **2019**, *151*, 134309.
- (621) Wan, Y.; Wiederrecht, G. P.; Schaller, R. D.; Johnson, J. C.; Huang, L. Transport of Spin-Entangled Triplet Excitons Generated by Singlet Fission. *J. Phys. Chem. Lett.* **2018**, *9*, 6731–6738.
- (622) Berkelbach, T. C.; Hybertsen, M. S.; Reichman, D. R. Microscopic Theory of Singlet Exciton Fission. II. Application to Pentacene Dimers and the Role of Superexchange. *J. Chem. Phys.* **2013**, *138*, 114103.
- (623) Greyson, E. C.; Vura-Weis, J.; Michl, J.; Ratner, M. A. Maximizing Singlet Fission in Organic Dimers: Theoretical Investigation of Triplet Yield in the Regime of Localized Excitation and Fast Coherent Electron Transfer. *J. Phys. Chem. B* **2010**, *114*, 14168–14177.
- (624) Teichen, P. E.; Eaves, J. D. A Microscopic Model of Singlet Fission. *J. Phys. Chem. B* **2012**, *116*, 11473–11481.
- (625) Ito, S.; Nagami, T.; Nakano, M. Molecular Design for Efficient Singlet Fission. *J. Photochem. Photobiol. C* **2018**, *34*, 85–120.
- (626) Felter, K. M.; Grozema, F. C. Singlet Fission in Crystalline Organic Materials: Recent Insights and Future Directions. *J. Phys. Chem. Lett.* **2019**, *10*, 7208–7214.
- (627) Renaud, N.; Grozema, F. C. Intermolecular Vibrational Modes Speed up Singlet Fission in Perylenediimide Crystals. *J. Phys. Chem. Lett.* **2015**, *6*, 360–365.
- (628) Xie, X.; Santana-Bonilla, A.; Fang, W.; Liu, C.; Troisi, A.; Ma, H. Exciton-Phonon Interaction Model for Singlet Fission in Prototypical Molecular Crystals. *J. Chem. Theory Comput.* **2019**, *15*, 3721–3729.
- (629) Wilson, M. W. B.; Rao, A.; Ehrler, B.; Friend, R. H. Singlet Exciton Fission in Polycrystalline Pentacene: From Photophysics toward Devices. *Acc. Chem. Res.* **2013**, *46*, 1330–1338.
- (630) Monahan, N. R.; Sun, D.; Tamura, H.; Williams, K. W.; Xu, B.; Zhong, Y.; Kumar, B.; Nuckolls, C.; Harutyunyan, A. R.; Chen, G.; et al. Dynamics of the Triplet-Pair State Reveals the Likely Coexistence of Coherent and Incoherent Singlet Fission in Crystalline Hexacene. *Nat. Chem.* **2017**, *9*, 341.
- (631) Tempelaar, R.; Reichman, D. R. Vibronic Exciton Theory of Singlet Fission. III. How Vibronic Coupling and Thermodynamics Promote Rapid Triplet Generation in Pentacene Crystals. *J. Chem. Phys.* **2018**, *148*, 244701.
- (632) Musser, A. J.; Al-Hashimi, M.; Maiuri, M.; Brida, D.; Heeney, M.; Cerullo, G.; Friend, R. H.; Clark, J. Activated Singlet Exciton Fission in a Semiconducting Polymer. *J. Am. Chem. Soc.* **2013**, *135*, 12747–12754.
- (633) Sanders, S. N.; Kumarasamy, E.; Pun, A. B.; Steigerwald, M. L.; Sfeir, M. Y.; Campos, L. M. Singlet Fission in Poly(pentacene). *Chem.* **2016**, *1*, 505–511.
- (634) Zirzlmeier, J.; Lehnher, D.; Coto, P. B.; Chernick, E. T.; Casillas, R.; Basel, B. S.; Thoss, M.; Tykwiński, R. R.; Guldi, D. M. Singlet Fission in Pentacene Dimers. *Proc. Natl. Acad. Sci. U. S. A.* **2015**, *112*, 5325–5330.
- (635) Khan, S.; Mazumdar, S. Diagrammatic Exciton Basis Theory of the Photophysics of Pentacene Dimers. *J. Phys. Chem. Lett.* **2017**, *8*, 4468–4478.
- (636) Huang, H.; He, G.; Xu, K.; Wu, Q.; Wu, D.; Sfeir, M. Y.; Xia, J. Achieving Long-Lived Triplet States in Intramolecular SF Films through Molecular Engineering. *Chem.* **2019**, *5*, 2405–2417.
- (637) Fuemmeler, E. G.; Sanders, S. N.; Pun, A. B.; Kumarasamy, E.; Zeng, T.; Miyata, K.; Steigerwald, M. L.; Zhu, X.-Y.; Sfeir, M. Y.; Campos, L. M.; Ananth, N. A Direct Mechanism of Ultrafast Intramolecular Singlet Fission in Pentacene Dimers. *ACS Cent. Sci.* **2016**, *2*, 316–324.
- (638) Basel, B. S.; Zirzlmeier, J.; Hetzer, C.; Reddy, S. R.; Phelan, B. T.; Krzyaniak, M. D.; Volland, M. K.; Coto, P. B.; Young, R. M.; Clark, T.; Thoss, M.; Tykwiński, R. R.; Wasielewski, M. R.; Guldi, D. M. Evidence for Charge-Transfer Mediation in the Primary Events of Singlet Fission in a Weakly Coupled Pentacene Dimer. *Chem.* **2018**, *4*, 1092–1111.
- (639) Sanders, S. N.; Kumarasamy, E.; Pun, A. B.; Trinh, M. T.; Choi, B.; Xia, J.; Taffet, E. J.; Low, J. Z.; Miller, J. R.; Roy, X.; Zhu, X. Y.; Steigerwald, M. L.; Sfeir, M. Y.; Campos, L. M. Quantitative Intramolecular Singlet Fission in Bipentacenes. *J. Am. Chem. Soc.* **2015**, *137*, 8965–8972.
- (640) Sanders, S. N.; Kumarasamy, E.; Pun, A. B.; Appavoo, K.; Steigerwald, M. L.; Campos, L. M.; Sfeir, M. Y. Exciton Correlations in Intramolecular Singlet Fission. *J. Am. Chem. Soc.* **2016**, *138*, 7289–7297.
- (641) Poletayev, A. D.; Clark, J.; Wilson, M. W. B.; Rao, A.; Makino, Y.; Hotta, S.; Friend, R. H. Triplet Dynamics in Pentacene Crystals: Applications to Fission-Sensitized Photovoltaics. *Adv. Mater.* **2014**, *26*, 919–924.
- (642) Wan, Y.; Guo, Z.; Zhu, T.; Yan, S.; Johnson, J.; Huang, L. Cooperative Singlet And Triplet Exciton Transport In Tetracene Crystals Visualized By Ultrafast Microscopy. *Nat. Chem.* **2015**, *7*, 785–792.
- (643) Nozik, A. J.; Beard, M. C.; Luther, J. M.; Law, M. M.; Ellingson, R. J.; Johnson, J. C. Semiconductor Quantum Dots and Quantum Dot Arrays and Applications of Multiple Exciton Generation to 3rd Generation PV Solar Cells. *Chem. Rev.* **2010**, *110*, 6873–6890.
- (644) Beard, M. C.; Luther, J. M.; Semonin, O.; Nozik, A. J. Third Generation Photovoltaics Based on Multiple Exciton Generation in

- Quantum Confined Semiconductors. *Acc. Chem. Res.* **2013**, *46*, 1252–1260.
- (645) Beard, M. C.; Johnson, J. C.; Luther, J. M.; Nozik, A. J. Multiple Exciton Generation in Quantum Dots versus Singlet Fission in Molecular Chromophores for Solar Photon Conversion. *Philos. Trans. A Math. Phys. Eng. Sci.* **2015**, *373*, 20140412.
- (646) Schaller, R.; Klimov, V. High Efficiency Carrier Multiplication in PbSe Nanocrystals: Implications for Solar Energy Conversion. *Phys. Rev. Lett.* **2004**, *92*, 186601.
- (647) Beard, M. C.; Knutson, K. P.; Yu, P.; Luther, J. M.; Song, Q.; Metzger, W. K.; Ellingson, R. J.; Nozik, A. J. Multiple Exciton Generation in Colloidal Silicon Nanocrystals. *Nano Lett.* **2007**, *7*, 2506–2512.
- (648) Stubbs, S. K.; Hardman, S. J. O.; Graham, D. M.; Spencer, B. F.; Flavell, W. R.; Glarvey, P.; Masala, O.; Pickett, N. L.; Binks, D. J. Efficient Carrier Multiplication in InP Nanoparticles. *Phys. Rev. B* **2010**, *81*, 081303.
- (649) Wang, S.; Khafizov, M.; Tu, X.; Zheng, M.; Krauss, T. D. Multiple Exciton Generation in Single-Walled Carbon Nanotubes. *Nano Letters.* **2010**, *10*, 2381–2386.
- (650) Konabe, S.; Okada, S. Multiple Exciton Generation by a Single Photon in Single-Walled Carbon Nanotubes. *Phys. Rev. Lett.* **2012**, *108*, 227401.
- (651) Kryjevski, A.; Mihaylov, D.; Kilina, S.; Kilin, D. Multiple Exciton Generation in Chiral Carbon Nanotubes: Density Functional Theory Based Computation. *J. Chem. Phys.* **2017**, *147*, 154106.
- (652) Kryjevski, A. Comprehensive Study of Multiple Exciton Generation in Chiral Carbon Nanotubes Using Many-Body Perturbation Theory Based on Density Functional Theory Simulations. In *ACS Symposium Series*; American Chemical Society: Washington, DC, 2019; pp 157–179.
- (653) Kanemitsu, Y. Multiple Exciton Generation and Recombination in Carbon Nanotubes and Nanocrystals. *Acc. Chem. Res.* **2013**, *46*, 1358–1366.
- (654) Matsunaga, R.; Matsuda, K.; Kanemitsu, Y. Observation of Charged Excitons in Hole-Doped Carbon Nanotubes Using Photoluminescence and Absorption Spectroscopy. *Phys. Rev. Lett.* **2011**, *106*, 037404.
- (655) Gabor, N. M. Exciton Multiplication in Graphene. *Acc. Chem. Res.* **2013**, *46*, 1348–1357.
- (656) McClain, J.; Schrier, J. Multiple Exciton Generation in Graphene Nanostructures. *J. Phys. Chem. C* **2010**, *114*, 14332–14338.
- (657) Teymourinia, H.; Salavati-Niasari, M.; Amiri, O.; Farangi, M. Facile Synthesis of Graphene Quantum Dots from Corn Powder and Their Application as Down Conversion Effect in Quantum Dot-Dye-Sensitized Solar Cell. *J. Mol. Liq.* **2018**, *251*, 267–272.
- (658) Wu, F.; Rocca, D.; Ping, Y. Dimensionality and Anisotropicity Dependence of Radiative Recombination in Nanostructured Phosphorene. *J. Mater. Chem. C* **2019**, *7*, 12891–12897.
- (659) Dowgiallo, A.-M.; Mistry, K. S.; Johnson, J. C.; Reid, O. G.; Blackburn, J. L. Probing Exciton Diffusion and Dissociation in Single-Walled Carbon Nanotube-C<sub>60</sub> Heterojunctions. *J. Phys. Chem. Lett.* **2016**, *7*, 1794–1799.
- (660) Sension, R. J.; Phillips, C. M.; Szarka, A. Z.; Romanow, W. J.; McGhie, A. R.; McCauley, J. P.; Smith, A. B.; Hochstrasser, R. M. Transient Absorption Studies of Carbon (C<sub>60</sub>) in Solution. *J. Phys. Chem.* **1991**, *95*, 6075–6078.
- (661) Benatto, L.; Marchiori, C. F. N.; Araujo, C. M.; Koehler, M. Molecular Origin of Efficient Hole Transfer From Non-Fullerene Acceptors: Insights from First-Principles Calculations. *J. Mater. Chem. C* **2019**, *7*, 12180–12193.
- (662) Selig, M.; Berghäuser, G.; Raja, A.; Nagler, P.; Schüller, C.; Heinz, T. F.; Korn, T.; Chernikov, A.; Malic, E.; Knorr, A. Excitonic Linewidth and Coherence Lifetime in Monolayer Transition Metal Dichalcogenides. *Nat. Commun.* **2016**, *7*, 13279.
- (663) Spataru, C. D.; Ismail-Beigi, S.; Capaz, R. B.; Louie, S. G. Theory and *Ab Initio* Calculation of Radiative Lifetime of Excitons in Semiconducting Carbon Nanotubes. *Phys. Rev. Lett.* **2005**, *95*, 247402.
- (664) Hofmann, M. S.; Glückert, J. T.; Noé, J.; Bourjau, C.; Dehmel, R.; Högele, A. Bright, Long-Lived and Coherent Excitons in Carbon Nanotube Quantum Dots. *Nat. Nanotechnol.* **2013**, *8*, 502–505.
- (665) Wang, F.; Dukovic, G.; Brus, L. E.; Heinz, T. F. Time-Resolved Fluorescence of Carbon Nanotubes and Its Implication for Radiative Lifetimes. *Phys. Rev. Lett.* **2004**, *92*, 177401.
- (666) Maultzsch, J.; Pomraenke, R.; Reich, S.; Chang, E.; Prezzi, D.; Ruini, A.; Molinari, E.; Strano, M. S.; Thomsen, C.; Lienau, C. Exciton Binding Energies in Carbon Nanotubes from Two-Photon Photoluminescence. *Phys. Rev. B* **2005**, *72*, No. 241402.
- (667) DeCapua, M. C.; Wu, Y.-C.; Taniguchi, T.; Watanabe, K.; Yan, J. Probing the Bright Exciton State in Twisted Bilayer Graphene via Resonant Raman Scattering. *Appl. Phys. Lett.* **2021**, *119*, 013103.
- (668) Tries, A.; Osella, S.; Zhang, P.; Xu, F.; Ramanan, C.; Kläui, M.; Mai, Y.; Beljonne, D.; Wang, H. I. Experimental Observation of Strong Exciton Effects in Graphene Nanoribbons. *Nano Lett.* **2020**, *20*, 2993–3002.
- (669) Feng, S.-W. Radiative Recombination Lifetime and Exciton Dimension in Zinc Blende Al<sub>x</sub>Ga<sub>1-x</sub>N/AlN Quantum Boxes. *Jpn. J. Appl. Phys.* **2009**, *48*, 051001.
- (670) Chen, H.-Y.; Jhalani, V. A.; Palummo, M.; Bernardi, M. Ab Initio Calculations of Exciton Radiative Lifetimes in Bulk Crystals, Nanostructures, and Molecules. *Phys. Rev. B* **2019**, *100*, 075135.
- (671) He, Z.; Ke, C.; Tang, B. Z. Journey of Aggregation-Induced Emission Research. *ACS Omega* **2018**, *3*, 3267–3277.
- (672) Jimenez, E. R.; Rodriguez, H. Aggregation-Induced Emission: A Review of Promising Cyano-Functionalized AIEgens. *J. Mater. Sci.* **2020**, *55*, 1366–1387.
- (673) Ghosh, R.; Nandi, A.; Kushwaha, A.; Das, D. Ultrafast Conformational Relaxation Dynamics in Anthryl-9-Benzothiazole: Dynamic Planarization Driven Delocalization and Protonation-Induced Twisting Dynamics. *J. Phys. Chem. B* **2019**, *123*, 5307–5315.
- (674) Hollingsworth, W. R.; Lee, J.; Fang, L.; Ayzner, A. L. Exciton Relaxation in Highly Rigid Conjugated Polymers: Correlating Radiative Dynamics with Structural Heterogeneity and Wavefunction Delocalization. *ACS Energy Lett.* **2017**, *2*, 2096–2102.
- (675) Dimitriev, O. P. Effect of Confinement on Photophysical Properties of P3HT Chains in PMMA Matrix. *Nanoscale Res. Lett.* **2017**, *12*, 510.
- (676) Sahoo, D.; Tian, Y.; Sforazzini, G.; Anderson, H. L.; Scheblykin, I. G. Photo-Induced Fluorescence Quenching in Conjugated Polymers Dispersed in Solid Matrices at Low Concentration. *J. Mater. Chem. C* **2014**, *2*, 6601–6608.
- (677) Hestand, N. J.; Spano, F. C. The Effect of Chain Bending on the Photophysical Properties of Conjugated Polymers. *J. Phys. Chem. B* **2014**, *118*, 8352–8363.
- (678) Spano, F. C. The Fundamental Photophysics of Conjugated Oligomer Herringbone Aggregates. *J. Chem. Phys.* **2003**, *118*, 981–994.
- (679) Parkinson, P.; Kondratuk, D. V.; Menelaou, C.; Gong, J. Q.; Anderson, H. L.; Herz, L. M. Chromophores in Molecular Nanorings: When Is a Ring a Ring? *J. Phys. Chem. Lett.* **2014**, *5*, 4356–4361.
- (680) Fidder, H. Absorption and Emission Studies on Pure and Mixed J-Aggregates of Pseudoisocyanine. *Chem. Phys.* **2007**, *341*, 158.
- (681) Grad, J.; Hernandez, G.; Mukamel, S. Radiative Decay and Energy Transfer in Molecular Aggregates: The Role of Intermolecular Dephasing. *Phys. Rev. A* **1988**, *37*, 3835–3846.
- (682) Adachi, T.; Vogelsang, J.; Lupton, J. M. Chromophore Bending Controls Fluorescence Lifetime in Single Conjugated Polymer Chains. *J. Phys. Chem. Lett.* **2014**, *5*, 2165–2170.
- (683) Rörich, I.; Mikhnenco, O. V.; Gehrig, D.; Blom, P. W. M.; Crăciun, N. I. Influence of Energetic Disorder on Exciton Lifetime and Photoluminescence Efficiency in Conjugated Polymers. *J. Phys. Chem. B* **2017**, *121*, 1405–1412.
- (684) Wagner, N. L.; Greco, J. A.; Enriquez, M. M.; Frank, H. A.; Birge, R. R. The Nature of the Intramolecular Charge Transfer State in Peridinin. *Biophys. J.* **2013**, *104*, 1314–1325.
- (685) Gierschner, J.; Shi, J.; Milián-Medina, B.; Roca-Sanjuán, D.; Varghese, S.; Park, S. Y. Luminescence in Crystalline Organic Materials:

- From Molecules to Molecular Solids. *Adv. Opt. Mater.* **2021**, *9*, 2002251.
- (686) Oelkrug, D.; Tompert, A.; Egelhaaf, H.-J.; Hanack, H.-J.; Steinhuber, E.; Hohloch, M.; Meier, H.; Stalmach, U. Towards Highly Luminescent Phenylene Vinylene Films. *Synth. Met.* **1996**, *83*, 231.
- (687) Mataga, N.; Chosrowjan, H.; Taniguchi, S.; Tanaka, F.; Kitamura, M.; Kido, N. Femtosecond Fluorescence Dynamics of Flavoproteins: Comparative Studies on Flavodoxin, Its Site-Directed Mutants, and Riboflavin Binding Protein Regarding Ultrafast Electron Transfer in Protein Nanospaces. *J. Phys. Chem. B* **2002**, *106*, 8917–8920.
- (688) Bjorklund, T. G.; Lim, S.-H.; Bardeen, C. J. Use of Picosecond Fluorescence Dynamics as an Indicator of Exciton Motion in Conjugated Polymers: Dependence on Chemical Structure and Temperature. *J. Phys. Chem. B* **2001**, *105*, 11970.
- (689) Parkinson, P.; Muller, C.; Stingelin, N.; Johnston, M. B.; Herz, L. M. Role of Ultrafast Torsional Relaxation in the Emission from Polythiophene Aggregates. *J. Phys. Chem. Lett.* **2010**, *1*, 2788.
- (690) Rhodes, W. Nonradiative Relaxation and Quantum Beats in the Radiative Decay Dynamics of Large Molecules. *J. Phys. Chem.* **1983**, *87*, 30–40.
- (691) Baranov, V. I.; Gribov, L. A.; Zavalii, M. V. Simulation of the Processes of Isomerization of Complex Molecules and of Their Spectra With Time Resolution. *J. Appl. Spectrosc.* **2004**, *71*, 320.
- (692) Morozov, V. A. A Mathematical Simulation of Intramolecular Proton Phototransfer. *Russ. J. Phys. Chem. B* **2009**, *3*, 699–706.
- (693) Bagryansky, V. A.; Borovkov, V. I.; Molin, Yu. N. Quantum Beats in Radical Pairs. *Russ. Chem. Rev.* **2007**, *76*, 493–506.
- (694) Gejo, T.; Bitto, H.; Huber, J. R. Quantum Beats in the S1 Dynamics of Acetaldehyde. *Chem. Phys. Lett.* **1996**, *261*, 443–449.
- (695) Franco, I.; Rubio, A.; Brumer, P. Long-Lived Oscillatory Incoherent Electron Dynamics in Molecules: Trans-Polyacetylene Oligomers. *New J. Phys.* **2013**, *15*, 043004.
- (696) Wang, R.; Zhang, C.; Zhang, B.; Liu, Y.; Wang, X.; Xiao, M. Magnetic Dipolar Interaction between Correlated Triplets Created by Singlet Fission in Tetracene Crystals. *Nat. Commun.* **2015**, *6*, 8602.
- (697) Wolf, E. A.; Finton, D. M.; Zoutenbier, V.; Biaggio, I. Quantum Beats of a Multiexciton State in Rubrene Single Crystals. *Appl. Phys. Lett.* **2018**, *112*, 083301.
- (698) Burdett, J. J.; Bardeen, C. J. Quantum Beats in Crystalline Tetracene Delayed Fluorescence Due to Triplet Pair Coherences Produced by Direct Singlet Fission. *J. Am. Chem. Soc.* **2012**, *134*, 8597–8607.
- (699) Burdett, J. J.; Piland, J. B.; Bardeen, C. J. Magnetic Field Effects and the Role of Spin States in Singlet Fission. *Chem. Phys. Lett.* **2013**, *585*, 1–10.
- (700) Jaffe, H. H.; Miller, A. L. The Fates of Electronic Excitation Energy. *J. Chem. Educ.* **1966**, *43*, 469–473.
- (701) Ma, W. L.; Li, S.-S. Multiphonon Effects on the Optical Emission Spectra of the Nitrogen-Vacancy Center in Diamond at Different Temperatures. *J. Appl. Phys.* **2012**, *111*, 063519.
- (702) Huang, K. Statistical Distribution of Phonons Emitted in Multiphonon Transitions. *J. Lumin.* **1984**, *31–32*, 738–743.
- (703) de Jong, M.; Seijo, L.; Meijerink, A.; Rabouw, F. T. Resolving the Ambiguity in the Relation between Stokes Shift and Huang-Rhys Parameter. *Phys. Chem. Chem. Phys.* **2015**, *17*, 16959–16969.
- (704) Englman, R.; Jortner, J. The Energy Gap Law for Radiationless Transitions in Large Molecules. *Mol. Phys.* **1970**, *18*, 145–164.
- (705) He, S.-J.; Wang, D.-K.; Jiang, N.; Lu, Z.-H. Nonradiative Charge-Transfer Exciton Recombination at Organic Heterojunctions. *J. Phys. Chem. C Nanomater. Interfaces* **2016**, *120*, 21325–21329.
- (706) Turro, N. J. *Modern Molecular Photochemistry*; University Science Books: Sausalito, CA, 1991.
- (707) Jackson, C. T.; Jeong, S.; Dorliac, G. F.; Landry, M. P. Advances in Engineering Near-Infrared Luminescent Materials. *iScience* **2021**, *24*, 102156.
- (708) Dimitrov, S. D.; Schroeder, B. C.; Nielsen, C. B.; Bronstein, H.; Fei, Z.; McCulloch, I.; Heeney, M.; Durrant, J. R. Singlet Exciton Lifetimes in Conjugated Polymer Films for Organic Solar Cells. *Polymers* **2016**, *8*, 14.
- (709) Wei, Y.-C.; Wang, S. F.; Hu, Y.; Liao, L.-S.; Chen, D.-G.; Chang, K.-H.; Wang, C.-W.; Liu, S.-H.; Chan, W.-H.; Liao, J.-L.; et al. Overcoming the Energy Gap Law in Near-Infrared OLEDs by Exciton-Vibration Decoupling. *Nat. Photonics* **2020**, *14*, 570–577.
- (710) Chen, W.-C.; Chou, P.-T.; Cheng, Y.-C. Low Internal Reorganization Energy of the Metal-Metal-to-Ligand Charge Transfer Emission in Dimeric Pt(II) Complexes. *J. Phys. Chem. C Nanomater. Interfaces* **2019**, *123*, 10225–10236.
- (711) May, V. Kinetic Theory of Exciton-Exciton Annihilation. *J. Chem. Phys.* **2014**, *140*, 054103.
- (712) Wolter, S.; Aizezers, J.; Fennel, F.; Seidel, M.; Würthner, F.; Kühn, O.; Lochbrunner, S. Size-Dependent Exciton Dynamics in One-Dimensional Perylene Bisimide Aggregates. *New J. Phys.* **2012**, *14*, 105027.
- (713) Tamai, Y.; Ohkita, H.; Benten, H.; Ito, S. Exciton Diffusion in Conjugated Polymers: From Fundamental Understanding to Improvement in Photovoltaic Conversion Efficiency. *J. Phys. Chem. Lett.* **2015**, *6*, 3417–3428.
- (714) Chmeliov, J.; Narkeliunas, J.; Graham, M. W.; Fleming, G. R.; Valkunas, L. Exciton-Exciton Annihilation and Relaxation Pathways in Semiconducting Carbon Nanotubes. *Nanoscale* **2016**, *8*, 1618–1626.
- (715) Soavi, G.; Dal Conte, S.; Manzoni, C.; Viola, D.; Narita, A.; Hu, Y.; Feng, X.; Hohenester, U. A.; Molinari, E.; Prezzi, D.; et al. Exciton-Exciton Annihilation and Biexciton Stimulated Emission in Graphene Nanoribbons. *Nat. Commun.* **2016**, *7*, 11010.
- (716) Ma, F. Dynamics and Coherent Control of Exciton-Exciton Annihilation in Aqueous J-Aggregate. *J. Phys. Chem. B* **2018**, *122*, 10746–10753.
- (717) Martini, I. B.; Smith, A. D.; Schwartz, B. J. Exciton-Exciton Annihilation and the Production of Interchain Species in Conjugated Polymer Films: Comparing the Ultrafast Stimulated Emission and Photoluminescence Dynamics of MEH-PPV. *Phys. Rev. B* **2004**, *69*, 035204.
- (718) Tempelaar, R.; Jansen, T. L. C.; Knoester, J. Exciton-Exciton Annihilation Is Coherently Suppressed in H-Aggregates, but Not in J-Aggregates. *J. Phys. Chem. Lett.* **2017**, *8*, 6113–6117.
- (719) Benatto, L.; Marchiori, C. F. N.; Araujo, C. M.; Koehler, M. Molecular Origin of Efficient Hole Transfer from Non-Fullerene Acceptors: Insights from First-Principles Calculations. *J. Mater. Chem. C* **2019**, *7*, 12180–12193.
- (720) Gregg, B. A. Entropy of Charge Separation in Organic Photovoltaic Cells: The Benefit of Higher Dimensionality. *J. Phys. Chem. Lett.* **2011**, *2*, 3013–3015.
- (721) Yu, Y.; Chien, S.-C.; Sun, J.; Hettiaratchy, E. C.; Myers, R. C.; Lin, L.-C.; Wu, Y. Excimer-Mediated Intermolecular Charge Transfer in Self-Assembled Donor-Acceptor Dyes on Metal Oxides. *J. Am. Chem. Soc.* **2019**, *141*, 8727–8731.
- (722) Brabec, C. J.; Zerza, G.; Cerullo, G.; De Silvestri, S.; Luzzati, S.; Hummelen, J. C.; Sariciftci, S. *Chem. Phys. Lett.* **2001**, *340*, 232.
- (723) Guo, J.; Ohkita, H.; Benten, H.; Ito, S. Charge Generation and Recombination Dynamics in Poly(3-hexylthiophene)/Fullerene Blend Films with Different Regioregularities and Morphologies. *J. Am. Chem. Soc.* **2010**, *132*, 6154–6164.
- (724) Andersson, M.; Davidsson, J.; Hammarström, L.; Korppi-Tommola, J.; Peltola, T. Photoinduced Electron Transfer Reactions in a Porphyrin-Viologen Complex: Observation of S2 to S1 Relaxation and Electron Transfer from the S2 State. *J. Phys. Chem. B* **1999**, *103*, 3258–3262.
- (725) LeGourrierec, D.; Andersson, M.; Davidsson, J.; Mukhtar, E.; Sun, L.; Hammarstrom, L. Photoinduced Electron Transfer from a Higher Excited State of a Porphyrin in a Zinc Porphyrin-Ruthenium(II) tris-Bipyridine Dyad. *J. Phys. Chem. A* **1999**, *103*, 557–559.
- (726) Giaimo, J. M.; Gusev, A. V.; Wasielewski, M. R. Excited-State Symmetry Breaking in Cofacial and Linear Dimers of a Green Perylenediimide Chlorophyll Analogue Leading to Ultrafast Charge Separation. *J. Am. Chem. Soc.* **2002**, *124*, 8530–8531.

- (727) Villegas, C.; Krokos, E.; Bouit, P.-A.; Delgado, J. L.; Guldi, D. M.; Martin, N. Efficient Light Harvesting Anionic Heptamethine Cyanine-[60] and [70]Fullerene Hybrids. *Energy Environ. Sci.* **2011**, *4*, 679–684.
- (728) Balzani, V.; Credi, A.; Venturi, M. *Molecular Devices and Machines. Concepts and Perspectives for the Nanoworld*; Wiley: Weinheim, 2008; Chapter 4; pp 69–106.
- (729) Lederer, M.; Ince, M.; Martinez-Diaz, M. V.; Torres, T.; Guldi, D. M. Photoinduced Electron Transfer in a Zinc Phthalocyanine–Fullerene Conjugate Connected by a Long Flexible Spacer. *ChemPlusChem.* **2016**, *81*, 941–946.
- (730) Suneesh, C. V.; Gopidas, K. R. Long-Lived Photoinduced Charge Separation Due to the Inverted Region Effect in 1,6-Bis(phenylethynyl)pyrene-Phenothiazine Dyad. *J. Phys. Chem. C* **2010**, *114*, 18725–18734.
- (731) Kleverlaan, C. J.; Indelli, M. T.; Bignozzi, C. A.; Pavanin, L.; Scandola, F.; Hasselman, G. M.; Meyer, G. J. Stepwise Charge Separation in Heterotriads. Binuclear Ru(II)–Rh(III) Complexes on Nanocrystalline Titanium Dioxide. *J. Am. Chem. Soc.* **2000**, *122*, 2840.
- (732) Han, Y.; Dobbeck, L.; Gong, A.; Meng, F.; Spangler, C. W.; Spangler, L. H. Millisecond long-lived charge separated state at room temperature in a flexibly linked diphenylaminopolyene-C60 dyad. *Chem. Commun.* **2005**, 1067.
- (733) Flamigni, L.; Baranoff, E.; Collin, J.-P.; Sauvage, J.-P. A Triad Based on an Iridium(III) Bisterpyridine Complex Leading to a Charge-Separated State with a 120- $\mu$ s Lifetime at Room Temperature. *Chem. Eur. J.* **2006**, *12* (12), 6592–6606.
- (734) Albrecht, U.; Bässler, H. Yield of Geminant Pair Dissociation in an Energetically Random Hopping System. *Chem. Phys. Lett.* **1995**, *235*, 389–393.
- (735) Berlin, Y. A.; Grozema, F. C.; Siebbeles, L. D. A.; Ratner, M. A. Charge Transfer in Donor-Bridge-Acceptor Systems: Static Disorder, Dynamic Fluctuations, and Complex Kinetics. *J. Phys. Chem. C* **2008**, *112*, 10988–11000.
- (736) Nayak, P. K.; Narasimhan, K. L.; Cahen, D. Separating Charges at Organic Interfaces: Effects of Disorder, Hot States, and Electric Field. *J. Phys. Chem. Lett.* **2013**, *4*, 1707–1717.
- (737) Bittner, E. R.; Lankevich, V.; Gélinas, S.; Rao, A.; Ginger, D. A.; Friend, R. H. How Disorder Controls the Kinetics of Triplet Charge Recombination in Semiconducting Organic Polymer Photovoltaics. *Phys. Chem. Chem. Phys.* **2014**, *16*, 20321–20328.
- (738) Sun, Z.; Stafström, S. Dynamics of Charge Separation at an Organic Donor-Acceptor Interface. *Phys. Rev. B* **2014**, *90*, 115420.
- (739) Hood, S. N.; Kassal, I. Entropy and Disorder Enable Charge Separation in Organic Solar Cells. *J. Phys. Chem. Lett.* **2016**, *7*, 4495–4500.
- (740) Kästner, C.; Vandewal, K.; Egbe, D. A. M.; Hoppe, H. Revelation of Interfacial Energetics in Organic Multiheterojunctions. *Adv. Sci.* **2017**, *4*, 1600331.
- (741) Li, C.; Li, Y.; Zhang, M.; Xu, L.; Qin, W.; Gao, K. Ultrafast Charge Separation from a “Cold” Charge-Transfer State Driven by Nonuniform Packing of Polymers at Donor/Acceptor Interfaces. *J. Phys. Chem. C* **2019**, *123*, 2746–2754.
- (742) Hou, Y.; Zhang, X.; Chen, K.; Liu, D.; Wang, Z.; Liu, Q.; Zhao, J.; Barbon, A. Charge Separation, Charge Recombination, Long-Lived Charge Transfer State and Intersystem Crossing in Organic Electron Donor/Acceptor Dyads. *J. Mater. Chem. C* **2019**, *7*, 12048–12074.
- (743) Garcia, N. A.; Kowalczyk, T. Extension of Intramolecular Charge-Transfer State Lifetime by Encapsulation in Porous Frameworks. *J. Phys. Chem. C* **2017**, *121*, 20673–20679.
- (744) Marcus, R. A.; Sutin, N. Electron Transfers in Chemistry and Biology. *Biochem. Biophys. Acta* **1985**, *811*, 265–322.
- (745) Closs, G. L.; Calcaterra, L. T.; Green, N. J.; Penfield, K. W.; Miller, J. R. Distance, Stereoelectronic Effects, and the Marcus Inverted Region in Intramolecular Electron Transfer in Organic Radical Anions. *J. Phys. Chem.* **1986**, *90*, 3673–3683.
- (746) Yonemoto, E. H.; Riley, R. L.; Kim, Y. I.; Atherton, S. J.; Schmehl, R. H.; Mallouk, T. E. Photoinduced Electron Transfer in Covalently Linked Ruthenium Tris(bipyridyl 1)-Viologen Molecules: Observation of Back Electron Transfer in the Marcus Inverted Region. *J. Am. Chem. Soc.* **1992**, *114*, 8081–8087.
- (747) Schuster, D. I.; Cheng, P.; Jarowski, P. D.; Guldi, D. M.; Luo, C.; Echegoyen, L.; Pyo, S.; Holzwarth, A. R.; Braslavsky, S. E.; Williams, R. M.; Klihm, G. Design, Synthesis, and Photophysical Studies of a Porphyrin-Fullerene Dyad with Parachute Topology; Charge Recombination in the Marcus Inverted Region. *J. Am. Chem. Soc.* **2004**, *126*, 7257.
- (748) Saini, R. K.; Kuchlyan, J.; Sarkar, N. Effect of Viscosity on Photoinduced Electron Transfer Reaction: An Observation of the Marcus Inverted Region in Homogeneous Solvents. *Chem. Phys. Lett.* **2016**, *660*, 81–86.
- (749) Makita, H.; Hastings, G. Inverted-Region Electron Transfer As a Mechanism for Enhancing Photosynthetic Solar Energy Conversion Efficiency. *Proc. Natl. Acad. Sci. U. S. A.* **2017**, *114*, 9267–9272.
- (750) Verhoeven, J. W.; van Ramesdonk, H. J.; Groeneveld, M. M.; Benniston, A. C.; Harriman, A. Long-Lived Charge-Transfer States in Compact Donor-Acceptor Dyads. *Chemphyschem.* **2005**, *6*, 2251–2260.
- (751) Hvilsted, L.; Bouwman, W. G.; Padden-Row, M. N.; van Ramesdonk, H. J.; Verhoeven, J. W.; Brouwer, A. M. Spin Control of The Lifetime of an Intramolecular Charge-Transfer Excited State. *Photochem. Photobiol. Sci.* **2003**, *2*, 995–1001.
- (752) Yang, Q.; Li, X.; Tang, H.; Li, Y.; Fu, Y.; Li, Z.; Xie, Z. Ultrafast Spectroscopic Investigation of the Effect of Solvent Additives on Charge Photogeneration and Recombination Dynamics in Non-Fullerene Organic Photovoltaic Blends. *J. Mater. Chem. C Mater. Opt. Electron. Devices* **2020**, *8*, 6724–6733.
- (753) Zheng, Z.; Tummala, N. R.; Fu, Y.-T.; Coropceanu, V.; Brédas, J.-L. Charge-Transfer States in Organic Solar Cells: Understanding the Impact of Polarization, Delocalization, and Disorder. *ACS Appl. Mater. Interfaces* **2017**, *9*, 18095–18102.
- (754) Paquin, F.; Latini, G.; Sakowicz, M.; Karsenti, P.-L.; Wang, L.; Beljonne, D.; Stingelin, N.; Silva, C. Charge Separation in Semicrystalline Polymeric Semiconductors by Photoexcitation: Is the Mechanism Intrinsic or Extrinsic? *Phys. Rev. Lett.* **2011**, *106*, 197401.
- (755) Dimitriev, O.; Smertenko, P.; Slominskii, Y. Photoinduced Charge Transport in Films of Near-Infrared Dye Assisted by Nanoscale Inhomogeneity of Dye Aggregates. *ECS J. Solid State Sci. Technol.* **2022**, *11*, 034004.
- (756) Glowe, J.-F.; Perrin, M.; Beljonne, D.; Hayes, S. C.; Gardeben, F.; Silva, C. Charge-Transfer Excitons in Strongly Coupled Organic Semiconductors. *Phys. Rev. B* **2010**, *81*, No. 041201.
- (757) Vandewal, K. Interfacial Charge Transfer States in Condensed Phase Systems. *Annu. Rev. Phys. Chem.* **2016**, *67*, 113–133.
- (758) Cardenas, G.; Nogueira, J. J. Stacking Effects on Anthraquinone/DNA Charge-Transfer Electronically Excited States. *Molecules* **2020**, *25*, 5927.
- (759) Hu, Z.; Willard, A. P.; Ono, R. J.; Bielawski, C. W.; Rossky, P. J.; Vanden Bout, D. A. An Insight into Non-Emissive Excited States Inconjugated Polymers. *Nat. Commun.* **2015**, *6*, 8246.
- (760) Tuna, D.; Sobolewski, A. L.; Domcke, W. Mechanisms of Ultrafast Excited-State Deactivation in Adenosine. *J. Phys. Chem. A* **2014**, *118*, 122–127.
- (761) Lee, J.; Vandewal, K.; Yost, S. R.; Bahlke, M. E.; Goris, L.; Baldo, M. A.; Manca, J. V.; Van Voorhis, T. Charge Transfer State Versus Hot Exciton Dissociation in Polymer-Fullerene Blended Solar Cells. *J. Am. Chem. Soc.* **2010**, *132*, 11878–11880.
- (762) Benko, G.; Kallioinen, J.; Korppi-Tommola, J. E. I.; Yartsev, A. P.; Sundstrom, V. Photoinduced Ultrafast Dye-to-Semiconductor Electron Injection from Nonthermalized and Thermalized Donor States. *J. Am. Chem. Soc.* **2002**, *124*, 489–493.
- (763) Tamura, H.; Burghardt, I. Ultrafast Charge Separation in Organic Photovoltaics Enhanced by Charge Delocalization and Vibronically Hot Exciton Dissociation. *J. Am. Chem. Soc.* **2013**, *135*, 16364–16367.
- (764) Jailaubekov, A. E.; Willard, A. P.; Tritsch, J. R.; Chan, W.-L.; Sai, N.; Gearba, R.; Kaake, L. G.; Williams, K. J.; Leung, K.; Rossky, P. J.; Zhu, X.-Y. Hot Charge-Transfer Excitons Set the Time Limit for

- Charge Separation at Donor/Acceptor Interfaces in Organic Photovoltaics. *Nat. Mater.* **2013**, *12*, 66–73.
- (765) Kassem, S.; van Leeuwen, T.; Lubbe, A. S.; Wilson, M. R.; Feringa, B. L.; Leigh, D. A. Artificial Molecular Motors. *Chem. Soc. Rev.* **2017**, *46*, 2592–2621.
- (766) Groppi, J.; Baroncini, M.; Venturi, M.; Silvi, S.; Credi, A. Design of Photo-Activated Molecular Machines: Highlights from the Past Ten Years. *Chem. Commun. (Camb.)* **2019**, *55*, 12595–12602.
- (767) Astumian, R. D. How Molecular Motors Work - Insights from the Molecular Machinist's Toolbox: The Nobel Prize in Chemistry 2016. *Chem. Sci.* **2017**, *8*, 840–845.
- (768) van Leeuwen, T.; Lubbe, A.; Stacko, P.; Wezenberg, S. J.; Feringa, B. L. Dynamic Control of Function by Light-Driven Molecular Motors. *Nat. Rev. Chem.* **2017**, *1*, 0096.
- (769) Jurissek, C.; Berger, F.; Eisenreich, F.; Kathan, M.; Hecht, S. External Reversal of Chirality Transfer in Photoswitches. *Angew. Chem., Int. Ed.* **2019**, *58*, 1945.
- (770) Pijper, D.; Feringa, B. L. Molecular Transmission: Controlling the Twist Sense of a Helical Polymer With a Single Light-Driven Molecular Motor. *Angew. Chem., Int. Ed.* **2007**, *46*, 3693–3696.
- (771) Noji, H.; Yasuda, R.; Yoshida, M.; Kinoshita, K., Jr. Direct Observation of the Rotation of F1-ATPase. *Nature* **1997**, *386*, 299–302.
- (772) Chen, J.; Vachon, J.; Feringa, B. L. Design, Synthesis, and Isomerization Studies of Light-Driven Molecular Motors for Single Molecular Imaging. *J. Org. Chem.* **2018**, *83*, 6025–6034.
- (773) Roke, D.; Wezenberg, S. J.; Feringa, B. L. Molecular Rotary Motors: Unidirectional Motion around Double Bonds. *Proc. Natl. Acad. Sci. U.S.A.* **2018**, *115*, 9423–9431.
- (774) Filatov, M.; Paolino, M.; Min, S. K.; Kim, K. S. Fulgides as Light Driven Molecular Rotary Motors: Computational Design of a Prototype Compound. *J. Phys. Chem. Lett.* **2018**, *9*, 4995–5001.
- (775) van Leeuwen, T.; Danowski, W.; Pizzolato, S. F.; Stacko, P.; Wezenberg, S. J.; Feringa, B. L. Braking of a Light-Driven Molecular Rotary Motor by Chemical Stimuli. *Chem.—Eur. J.* **2018**, *24*, 81–84.
- (776) Berrocal, J. A.; Pfeifer, L.; Heijnen, D.; Feringa, B. L. Synthesis of Core-Modified Third-Generation Light-Driven Molecular Motors. *J. Org. Chem.* **2020**, *85*, 10670–10680.
- (777) Kistemaker, J. C. M.; Stacko, P.; Roke, D.; Wolters, A. T.; Heideman, G. H.; Chang, M.-C.; Van Der Meulen, P.; Visser, J.; Otten, E.; Feringa, B. L. Third-Generation Light-Driven Symmetric Molecular Motors. *J. Am. Chem. Soc.* **2017**, *139*, 9650–9661.
- (778) Kudernac, T.; Ruangsrapiphat, N.; Parschau, M.; Maciá, B.; Katsonis, N.; Harutyunyan, S. R.; Ernst, K.-H.; Feringa, B. L. Electrically Driven Directional Motion of a Four-Wheeled Molecule on a Metal Surface. *Nature* **2011**, *479*, 208–211.
- (779) Hou, J.; Mondal, A.; Long, G.; de Haan, L.; Zhao, W.; Zhou, G.; Liu, D.; Broer, D. J.; Chen, J.; Feringa, B. L. Photo-responsive Helical Motion by Light-Driven Molecular Motors in a Liquid-Crystal Network. *Angew. Chem., Int. Ed.* **2021**, *60*, 8251–8257.
- (780) Yang, X.; Li, J.; Jiang, S.; Xie, P.; Liu, G.; Zheng, X.; Cao, Z.; Zheng, X.; Zou, D.; Wu, Y.; An, W. Light Driven Molecular Lock Comprises a Ru(Bpy)<sub>2</sub>(Hpip) Complex and Cucurbit[8]Uril. *RSC Adv.* **2021**, *11*, 8444–8449.
- (781) Li, H.; Cheng, C.; McGonigal, P. R.; Fahrenbach, A. C.; Frasconi, M.; Liu, W.-G.; Zhu, Z.; Zhao, Y.; Ke, C.; Lei, J.; et al. Relative Unidirectional Translation in an Artificial Molecular Assembly Fueled by Light. *J. Am. Chem. Soc.* **2013**, *135*, 18609–18620.
- (782) Ragazzon, G.; Baroncini, M.; Silvi, S.; Venturi, M.; Credi, A. Light-Powered, Artificial Molecular Pumps: A Minimalistic Approach. *Beilstein J. Nanotechnol.* **2015**, *6*, 2096–2104.
- (783) Casimiro, L.; Groppi, J.; Baroncini, M.; La Rosa, M.; Credi, A.; Silvi, S. Photochemical Investigation of Cyanoazobenzene Derivatives as Components of Artificial Supramolecular Pumps. *Photochem. Photobiol. Sci.* **2018**, *17*, 734–740.
- (784) Suda, M.; Thatthong, Y.; Promarak, V.; Kojima, H.; Nakamura, M.; Shiraogawa, T.; Ehara, M.; Yamamoto, H. M. Light-Driven Molecular Switch for Reconfigurable Spin Filters. *Nat. Commun.* **2019**, *10*, 2455.
- (785) Hall, C. R.; Conyard, J.; Heisler, I. A.; Jones, G.; Frost, J.; Browne, W. R.; Feringa, B. L.; Meech, S. R. Ultrafast Dynamics in Light Driven Molecular Rotary Motors Probed by Femtosecond Stimulated Raman Scattering. *J. Am. Chem. Soc.* **2017**, *139*, 7408–7414.
- (786) Wang, Y.; Tian, Y.; Chen, Y.-Z.; Niu, L.-Y.; Wu, L.-Z.; Tung, C.-H.; Yang, Q.-Z.; Boulatov, R. A Light-Driven Molecular Machine Based on Stiff Stilbene. *Chem. Commun.* **2018**, *54*, 7991–7994.
- (787) Armaroli, N. From Metal Complexes to Fullerene Arrays: Exploring the Exciting World of Supramolecular Photochemistry Fifteen Years after Its Birth. *Photochem. Photobiol. Sci.* **2003**, *2*, 73–87.
- (788) Ramamurthy, V.; Sivaguru, J. Supramolecular Photochemistry as a Potential Synthetic Tool: Photocycloaddition. *Chem. Rev.* **2016**, *116*, 9914–9993.
- (789) Kathan, M.; Hecht, S. Photoswitchable Molecules as Key Ingredients to Drive Systems Away from the Global Thermodynamic Minimum. *Chem. Soc. Rev.* **2017**, *46*, 5536–5550.
- (790) Kathan, M.; Eisenreich, F.; Jurissek, C.; Dallmann, A.; Gurke, J.; Hecht, S. Light-Driven Molecular Trap Enables Bidirectional Manipulation of Dynamic Covalent Systems. *Nat. Chem.* **2018**, *10*, 1031–1036.
- (791) Barrell, M. J.; Campana, A. G.; von Delius, M.; Geertsema, E. M.; Leigh, D. A. Light-Driven Transport of a Molecular Walker in Either Direction along a Molecular Track. *Angew. Chem., Int. Ed.* **2011**, *50*, 285–290.
- (792) Li, P.; Xie, G.; Liu, P.; Kong, X.-Y.; Song, Y.; Wen, L.; Jiang, L. Light-Driven ATP Transmembrane Transport Controlled by DNA Nanomachines. *J. Am. Chem. Soc.* **2018**, *140*, 16048–16052.
- (793) Wang, L.; Wen, Q.; Jia, P.; Jia, M.; Lu, D.; Sun, X.; Jiang, L.; Guo, W. Light-Driven Active Proton Transport through Photoacid- and Photobase-Doped Janus Graphene Oxide Membranes. *Adv. Mater.* **2019**, *31*, 1903029.
- (794) Lin, L.; Yan, Z.; Gu, J.; Zhang, Y.; Feng, Z.; Yu, Y. UV-Responsive Behavior of Azopyridine-Containing Diblock Copolymeric Vesicles: Photoinduced Fusion, Disintegration and Rearrangement. *Macromol. Rapid Commun.* **2009**, *30*, 1089–1093.
- (795) Suzuki, Y.; Nagai, K. H.; Zinchenko, A.; Hamada, T. Photoinduced Fusion of Lipid Bilayer Membranes. *Langmuir* **2017**, *33*, 2671–2676.
- (796) Uda, R. M.; Yoshikawa, Y.; Kitaba, M.; Nishimoto, N. Irradiation-Induced Fusion Between Giant Vesicles Andphotoresponsive Large Unilamellar Vesicles Containing Malachite Green Derivative. *Colloids Surf. B Biointerfaces* **2018**, *167*, 544–549.
- (797) Kundu, P. K.; Samanta, D.; Leizrowice, R.; Margulis, B.; Zhao, H.; Börner, M.; Udayabhaskararao, T.; Manna, D.; Klajn, R. Light-Controlled Self-Assembly of Non-Photoresponsive Nanoparticles. *Nat. Chem.* **2015**, *7*, 646–652.
- (798) Bio, M.; Nkepang, G.; You, Y. Click and Photo-Unclick Chemistry of Aminoacrylate for Visible Light-Triggered Drug Release. *Chem. Commun.* **2012**, *48*, 6517–6519.
- (799) Yuan, Z.; Zhang, L. Photoinduced Controlled-Release Drug Delivery Systems for Applications in Nanomedicine. *Curr. Org. Chem.* **2016**, *20*, 1768–1785.
- (800) Sell, H.; Gehl, A.; Plaul, D.; Sönnichsen, F. D.; Schütt, C.; Köhler, F.; Steinborn, K.; Herges, R. Towards a Light Driven Molecular Assembler. *Commun. Chem.* **2019**, *2*, 62.
- (801) You, L.; Zha, D.; Anslyn, E. V. Recent Advances in Supramolecular Analytical Chemistry Using Optical Sensing. *Chem. Rev.* **2015**, *115*, 7840–7892.
- (802) Fukuhara, G. Analytical Supramolecular Chemistry: Colorimetric and Fluorimetric Chemosensors. *J. Photochem. Photobiol. C Photochem. Rev.* **2020**, *42*, 100340.
- (803) Li, S.; Liu, W.; Li, C.-Z.; Shi, M.; Chen, H. Efficient Organic Solar Cells with Non-Fullerene Acceptors. *Small* **2017**, *13*, 1701120.
- (804) Firdaus, Y.; Le Corre, V. M.; Karuthedath, S.; Liu, W.; Markina, A.; Huang, W.; Chattopadhyay, S.; Nahid, M. M.; Nugraha, M. I.; Lin, I.; et al. Long-Range Exciton Diffusion in Molecular Non-Fullerene Acceptors. *Nat. Commun.* **2020**, *11*, 5220.
- (805) Zhu, L.; Zhang, J.; Guo, Y.; Yang, C.; Yi, Y.; Wei, Z. Small Exciton Binding Energies Enabling Direct Charge Photogeneration

- Towards Low-Driving-Force Organic Solar Cells. *Angew. Chem., Int. Ed.* **2021**, *60*, 15348–15353.
- (806) Zhang, G.; Chen, X. K.; Xiao, J.; C. Y.; Chow, P. C. Y.; Ren, M.; Kupgan, G.; Jiao, X.; Chan, C. C. S.; Du, X.; Xia, R.; et al. Delocalization of Exciton and Electron Wavefunction in Non-Fullerene Acceptor Molecules Enables Efficient Organic Solar Cells. *Nat. Commun.* **2020**, *11*, 3943.
- (807) Liu, Q.; Jiang, Y.; Jin, K.; Qin, J.; Xu, J.; Li, W.; Xiong, J.; Liu, J.; Xiao, Z.; Sun, K.; et al. 18% Efficiency organic solar cells. *Sci. Bull.* **2020**, *65*, 272–275.
- (808) Li, C.; Zhou, J.; Song, J.; Xu, J.; Zhang, H.; Zhang, X.; Guo, J.; Zhu, L.; Wei, D.; Han, G.; et al. Non-Fullerene Acceptors With Branched Side Chains and Improved Molecular Packing to Exceed 18% Efficiency in Organic Solar Cells. *Nat. Energy* **2021**, *6*, 605–613.
- (809) Chen, S.; Feng, L.; Jia, T.; Jing, J.; Hu, Z.; Zhang, K.; Huang, F. High-Performance Polymer Solar Cells With Efficiency Over 18% Enabled By Asymmetric Side Chain Engineering of Non-Fullerene Acceptors. *Sci. China Chem.* **2021**, *64*, 1192–1199.
- (810) Firdaus, Y.; Le Corre, V. M.; Khan, J. I.; Kan, Z.; Laquai, F.; Beaujuge, P. M.; Anthopoulos, T. D. Key Parameters Requirements for Non-Fullerene-Based Organic Solar Cells with Power Conversion Efficiency > 20%. *Adv. Sci.* **2019**, *6*, 1802028.
- (811) Liu, S.; Lin, S.; You, P.; Surya, C.; Lau, S. P.; Yan, F. Black Phosphorus Quantum Dots Used for Boosting Light Harvesting in Organic Photovoltaics. *Angew. Chem., Int. Ed.* **2017**, *56*, 13717–13721.
- (812) Mateen, F.; Saeed, M. A.; Shim, J. W.; Hong, S.-K. Indoor/Outdoor Light-Harvesting by Coupling Low-Cost Organic Solar Cell with a Luminescent Solar Concentrator. *Sol. Energy* **2020**, *207*, 379–387.
- (813) Pieper, A.; Hohgardt, M.; Willich, M.; Gacek, D. A.; Hafi, N.; Pfennig, D.; Albrecht, A.; Walla, P. J. Biomimetic Light-Harvesting Funnels for Re-Directioning of Diffuse Light. *Nat. Commun.* **2018**, *9*, 666.
- (814) Zeng, Y.; Chen, J.; Yu, T.; Yang, G.; Li, Y. Molecular-Supramolecular Light Harvesting for Photochemical Energy Conversion: Making Every Photon Count. *ACS Energy Lett.* **2017**, *2*, 357–363.
- (815) Aguilera, M. C.; Roitberg, A. E.; Kleiman, V. D.; Fernandez-Alberti, S.; Galindo, J. F. Unraveling Direct and Indirect Energy Transfer Pathways in a Light-Harvesting Dendrimer. *J. Phys. Chem. C* **2020**, *124*, 22383–22391.
- (816) Li, W.-J.; Wang, X.-Q.; Wang, W.; Hu, Z.; Ke, Y.; Jiang, H.; He, C.; Wang, X.; Hu, Y.-X.; Jia, P.-P.; Yin, P.; Chen, J.; Sun, H.; Sun, Z.; Xu, L.; Yang, H.-B. Dynamic Artificial Light-Harvesting Systems Based on Rotaxane Dendrimers. *Giant* **2020**, *2*, 100020.
- (817) Menke, S. M.; Mullenbach, T. K.; Holmes, R. J. Directing Energy Transport in Organic Photovoltaic Cells Using Interfacial Exciton Gates. *ACS Nano* **2015**, *9*, 4543–4552.
- (818) Rao, A.; Friend, R. H. Harnessing Singlet Exciton Fission to Break the Shockley-Queisser Limit. *Nature Rev. Mater.* **2017**, *2*, 17063.
- (819) Congreve, D. N.; Lee, J.; Thompson, N. J.; Hontz, E.; Yost, S. R.; Reusswig, P. D.; Bahlke, M. E.; Reineke, S.; van Voorhis, T.; Baldo, M. A. External Quantum Efficiency Above 100% in a Singlet-Exciton-Fission-Based Organic Photovoltaic Cell. *Science* **2013**, *340*, 334–337.
- (820) Thompson, N. J.; Congreve, D. N.; Goldberg, D.; Menon, V. M.; Baldo, M. A. Slow Light Enhanced Singlet Exciton Fission Solar Cells with a 126% Yield of Electrons per Photon. *Appl. Phys. Lett.* **2013**, *103*, 263302.
- (821) Futscher, M. H.; Rao, A.; Ehrler, B. The Potential of Singlet Fission Photon Multipliers as an Alternative to Silicon-Based Tandem Solar Cells. *ACS Energy Lett.* **2018**, *3*, 2587–2592.
- (822) Einzinger, M.; Wu, T.; Komppala, J. F.; Smith, H. L.; Perkinson, C. F.; Nienhaus, L.; Wieghold, S.; Congreve, D. N.; Kahn, A.; Bawendi, M. G.; Baldo, M. A. Sensitization of Silicon by Singlet Exciton Fission in Tetracene. *Nature* **2019**, *571*, 90–94.
- (823) Gray, V.; Moth-Poulsen, K.; Albinsson, B.; Abrahamsson, M. Towards Efficient Solid-State Triplet-Triplet Annihilation Based Photon Upconversion: Supramolecular, Macromolecular and Self-Assembled Systems. *Coord. Chem. Rev.* **2018**, *362*, 54–71.
- (824) Pedrini, J.; Monguzzi, A. Recent Advances in the Application Triplet-Triplet Annihilation-Based Photon Upconversion Systems to Solar Technologies. *J. Photon. Energy* **2018**, *8*, 022005.
- (825) Schulze, T. F.; Czolk, J.; Cheng, Y.-Y.; Fückel, B.; MacQueen, R. W.; Khouri, T.; Crossley, M. J.; Stannowski, B.; Lips, K.; Lemmer, U.; et al. Efficiency Enhancement of Organic and Thin-Film Silicon Solar Cells With Photochemical Upconversion. *J. Phys. Chem. C* **2012**, *116*, 22794–22801.
- (826) Li, C.; Koenigsmann, C.; Deng, F.; Hagstrom, A.; Schmuttenmaer, C. A.; Kim, J.-H. Photocurrent Enhancement From Solid-State Triplet-Triplet Annihilation Upconversion of Low-Intensity, Low-Energy Photons. *ACS Photonics* **2016**, *3*, 784–790.
- (827) Lin, Y. L.; Koch, M.; Brigeman, A. N.; Freeman, D. M. E.; Zhao, L.; Bronstein, H.; Giebink, N. C.; Scholes, G. D.; Rand, B. P. Enhanced Sub-Bandgap Efficiency of a Solid-State Organic Intermediate Band Solar Cell Using Triplet-Triplet Annihilation. *Energy Environ. Sci.* **2017**, *10*, 1465–1475.
- (828) Haedler, A. T.; Kreger, K.; Issac, A.; Wittmann, B.; Kivala, M.; Hammer, N.; Köhler, J.; Schmidt, H. W.; Hildner, R. Long-Range Energy Transport in Single Supramolecular Nanofibres at Room Temperature. *Nature* **2015**, *523*, 196–199.
- (829) Caram, J. R.; Doria, S.; Eisele, D. M.; Freyria, F. S.; Sinclair, T. S.; Rebentrost, P.; Lloyd, S.; Bawendi, M. G. Room-Temperature Micron-Scale Exciton Migration in a Stabilized Emissive Molecular Aggregate. *Nano Lett.* **2016**, *16*, 6808–6815.
- (830) Clark, K. A.; Krueger, E. L.; Vanden Bout, D. A. Direct Measurement of Energy Migration in Supramolecular Carbocyanine Dye Nanotubes. *J. Phys. Chem. Lett.* **2014**, *5*, 2274–2282.
- (831) Wan, Y.; Stradomska, A.; Knoester, J.; Huang, L. Direct Imaging of Exciton Transport in Tubular Porphyrin Aggregates by Ultrafast Microscopy. *J. Am. Chem. Soc.* **2017**, *139*, 7287–7293.
- (832) Sajjad, M. T.; Zhang, Y.; Geraghty, P. B.; Mitchell, V. D.; Ruseckas, A.; Blaszczyk, O.; Jones, D. J.; Samuel, I. D. W. Tailoring Exciton Diffusion and Domain Size in Photovoltaic Small Molecules by Annealing. *J. Mater. Chem. C* **2019**, *7*, 7922–7928.
- (833) Zhu, T.; Yuan, L.; Zhao, Y.; Zhou, M.; Wan, Y.; Mei, J.; Huang, L. Highly Mobile Charge-Transfer Excitons in Two-Dimensional WS<sub>2</sub>/Tetracene Heterostructures. *Sci. Adv.* **2018**, *4*, No. eaao3104.
- (834) Sun, D. Z.; Rao, Y.; Reider, G. A.; Chen, G.; You, Y.; Brézin, L.; Harutyunyan, A. R.; Heinz, T. F. Observation of Rapid Exciton-Exciton Annihilation in Monolayer Molybdenum Disulfide. *Nano Lett.* **2014**, *14*, 5625–5629.
- (835) Vörös, Z.; Balili, R.; Snoke, D. W.; Pfeiffer, L.; West, K. Long-Distance Diffusion of Excitons in Double Quantum Well Structures. *Phys. Rev. Lett.* **2005**, *94*, 226401.
- (836) Sharma, A.; Zhang, L.; Tollerud, J. O.; Dong, M.; Zhu, Y.; Halbich, R.; Vogl, T.; Liang, K.; Nguyen, H. T.; Wang, F.; Sanwlani, S.; Earl, S. K.; Macdonald, D.; Lam, P. K.; Davis, J. A.; Lu, Y. Supertransport of Excitons in Atomically Thin Organic Semiconductors at the 2D Quantum Limit. *Light Sci. Appl.* **2020**, *9*, 116.
- (837) Scholes, G. D. Limits of Exciton Delocalization in Molecular Aggregates. *Faraday Discuss.* **2020**, *221*, 265–280.
- (838) Moon, H.; Gross, G.; Chakraborty, C.; Peng, C.; Taniguchi, T.; Watanabe, K.; Englund, D. Dynamic Exciton Funneling by Local Strain Control in a Monolayer Semiconductor. *Nano Lett.* **2020**, *20*, 6791–6797.
- (839) Zhong, X.; Chervy, T.; Zhang, L.; Thomas, A.; George, J.; Genet, C.; Hutchison, J. A.; Ebbesen, T. W. Energy Transfer between Spatially Separated Entangled Molecules. *Angew. Chem., Int. Ed.* **2017**, *56*, 9034.
- (840) Rozenman, G. G.; Akulov, K.; Golombek, A.; Schwartz, T. Long-Range Transport of Organic Exciton-Polaritons Revealed by Ultrafast Microscopy. *ACS Photonics* **2018**, *5*, 105–110.
- (841) Hou, S.; Khatoniar, M.; Ding, K.; Qu, Y.; Napolov, A.; Menon, V. M.; Forrest, S. R. Ultralong-Range Energy Transport in a Disordered Organic Semiconductor at Room Temperature via Coherent Exciton-Polariton Propagation. *Adv. Mater.* **2020**, *32*, 2002127.

- (842) Wang, M.; Hertzog, M.; Börjesson, K. Polariton-Assisted Excitation Energy Channeling in Organic Heterojunctions. *Nat. Commun.* **2021**, *12*, 1874.
- (843) High, A. A.; Hammack, A. T.; Butov, L. V.; Hanson, M.; Gossard, A. C. Exciton Optoelectronic Transistor. *Opt. Lett.* **2007**, *32*, 2466–2468.
- (844) Kuznetsova, Y. Y.; Remeika, M.; High, A. A.; Hammack, A. T.; Butov, L. V.; Hanson, M.; Gossard, A. C. All-Optical Excitonic Transistor. *Opt. Lett.* **2010**, *35*, 1587–1589.
- (845) Andreakou, P.; Poltavtsev, S. V.; Leonard, J. R.; Calman, E. V.; Remeika, M.; Kuznetsova, Y. Y.; Butov, L. V.; Wilkes, J.; Hanson, M.; Gossard, A. C. Optically Controlled Excitonic Transistor. *Appl. Phys. Lett.* **2014**, *104*, 091101.
- (846) Matys, M.; Domanowska, A.; Michalewicz, A.; Adamowicz, B.; Kachi, T. All-Optical Transistor Using Deep-Level Defects in Nitride Semiconductors for Room Temperature Optical Computing. *AIP Advances* **2020**, *10*, 105232.
- (847) Butov, L. V. Excitonic Devices. *Superlattices Microstruct.* **2017**, *108*, 2–26.
- (848) Unuchek, D.; Ciarrocchi, A.; Avsar, A.; et al. Room-Temperature Electrical Control of Exciton Flux in a Van Der Waals Heterostructure. *Nature* **2018**, *560*, 340–344.
- (849) Zhang, H.; Abhiraman, B.; Zhang, Q.; Miao, J.; Jo, K.; Roccasecca, S.; Knight, M. W.; Davoyan, A. R.; Jariwala, D. Hybrid Exciton-Plasmon-Polaritons in van Der Waals Semiconductor Gratings. *Nat. Commun.* **2020**, *11*, 3552.
- (850) Butov, L. V. Condensation and Pattern Formation in Cold Exciton Gases in Coupled Quantum Wells. *J. Phys.: Condens. Matter* **2004**, *16*, R1577.
- (851) Lin, K.-Q. A Roadmap for Interlayer Excitons. *Light Sci. Appl.* **2021**, *10*, 99.
- (852) Robert, C.; Lagarde, D.; Cadiz, F.; Wang, G.; Lassagne, B.; Amand, T.; Balocchi, A.; Renucci, P.; Tongay, S.; Urbaszek, B.; Marie, X. Exciton Radiative Lifetime in Transition Metal Dichalcogenide Monolayers. *Phys. Rev. B* **2016**, *93*, 205423.
- (853) Kellis, D. L.; Sarter, C.; Cannon, B. L.; Davis, P. H.; Graugnard, E.; Lee, J.; Pensack, R. D.; Kolmar, T.; Jaschke, A.; Yurke, B.; Knowlton, W. B. An All-Optical Excitonic Switch Operated in the Liquid and Solid Phases. *ACS Nano* **2019**, *13*, 2986–2994.
- (854) Boulais, É.; Sawaya, N. P. D.; Veneziano, R.; Andreoni, A.; Banal, J. L.; Kondo, T.; Mandal, S.; Lin, S.; Schlau-Cohen, G. S.; Woodbury, N. W.; Yan, H.; Aspuru-Guzik, A.; Bathe, M. Programmed Coherent Coupling in a Synthetic DNA-Based Excitonic Circuit. *Nat. Mater.* **2018**, *17*, 159–166.
- (855) Sawaya, N. P. D.; Rappoport, D.; Tabor, D. P.; Aspuru-Guzik, A. Excitonics: A Set of Gates for Molecular Exciton Processing and Signaling. *ACS Nano* **2018**, *12*, 6410–6420.
- (856) Zasedatelev, A. V.; Baranikov, A. V.; Urbonas, D.; Scafirimuto, F.; Scherf, U.; Stöferle, T.; Mahrt, R. F.; Lagoudakis, P. G. A Room-Temperature Organic Polariton Transistor. *Nat. Photonics* **2019**, *13*, 378–383.
- (857) Mukhopadhyay, A.; Sen, B.; Thapliyal, K.; Mandal, S.; Pathak, A. Interaction of Light and Semiconductor Can Generate Quantum States Required for Solid-State Quantum Computing: Entangled, Steered and Other Nonclassical States. *Quantum Inf. Process.* **2019**, *18*, 234.
- (858) Pandya, R.; Gu, Q.; Cheminal, A.; Chen, R. Y.S.; Booker, E. P.; Soucek, R.; Schott, M.; Legrand, L.; Mathevret, F.; Greenham, N. C.; et al. Optical Projection and Spatial Separation of Spin-Entangled Triplet Pairs from the S1 (21 Ag-) State of Pi-Conjugated Systems. *Chem.* **2020**, *6*, 2826–2851.
- (859) Mishima, K.; Yamashita, K. Quantum Computing Using Rotational Modes of Two Polar Molecules. *Chem. Phys.* **2009**, *361*, 106–117.
- (860) Tesch, C. M.; de Vivie-Riedle, R. Vibrational Molecular Quantum Computing: Basis Set Independence and Theoretical Realization of the Deutsch-Jozsa Algorithm. *J. Chem. Phys.* **2004**, *121*, 12158.
- (861) Babikov, D. Accuracy of Gates in a Quantum Computer Based on Vibrational Eigenstates. *J. Chem. Phys.* **2004**, *121*, 7577.
- (862) Shyshlov, D.; Berrios, E.; Gruebele, M.; Babikov, D. On Readout of Vibrational Qubits Using Quantum Beats. *J. Chem. Phys.* **2014**, *141*, 224306.
- (863) DeMille, D. Quantum Computation with Trapped Polar Molecules. *Phys. Rev. Lett.* **2002**, *88*, 067901.
- (864) Yelin, S. F.; Kirby, K.; Côté, R. Schemes for Robust Quantum Computation with Polar Molecules. *Phys. Rev. A* **2006**, *74*, No. 050301.
- (865) Liu, R.-B.; Yao, W.; Sham, L. J. Quantum Computing by Optical Control of Electron Spins. *Adv. Phys.* **2010**, *59*, 703–802.
- (866) Ardavan, A.; Austwick, M.; Benjamin, S. C.; Briggs, G. A. D.; Dennis, T. J. S.; Ferguson, A.; Hasko, D. G.; Kanai, M.; Khlobystov, A. N.; Lovett, B. W.; et al. Nanoscale Solid-State Quantum Computing. *Philos. Trans. R. Soc. A* **2003**, *361*, 1473–1485.
- (867) Reina, J. H.; Quiroga, L.; Johnson, N. F. Quantum Entanglement and Information Processing via Excitons in Optically Driven Quantum Dots. *Phys. Rev. A* **2000**, *62*, 012305.
- (868) De Rinaldis, S.; D'Amico, I.; Biolatti, E.; Rinaldi, R.; Cingolani, R.; Rossi, F. Intrinsic Exciton-Exciton Coupling in Gan-Based Quantum Dots: Application to Solid-State Quantum Computing. *Phys. Rev. B* **2002**, *65*, No. 081309.
- (869) Ghosh, S.; Liew, T. C. H. Quantum Computing with Exciton-Polariton Condensates. *npj Quantum Inf.* **2020**, *6*, 16.
- (870) Castellanos, M. A.; Dodin, A.; Willard, A. P. On the Design of Molecular Excitonic Circuits for Quantum Computing: The Universal Quantum Gates. *Phys. Chem. Chem. Phys.* **2020**, *22*, 3048–3057.

## □ Recommended by ACS

### Anti-Kasha Fluorescence in Molecular Entities: Central Role of Electron-Vibrational Coupling

Koen Veys and Daniel Escudero

SEPTEMBER 01, 2022

ACCOUNTS OF CHEMICAL RESEARCH

READ ▶

### Predicting the Second-Order Nonlinear Optical Responses of Organic Materials: The Role of Dynamics

Frédéric Castet, Benoît Champagne, et al.

DECEMBER 05, 2022

ACCOUNTS OF CHEMICAL RESEARCH

READ ▶

### Nonadiabatic Excited State Dynamics of Organic Chromophores: Take-Home Messages

Pratip Chakraborty, Spiridoula Matsika, et al.

SEPTEMBER 07, 2022

THE JOURNAL OF PHYSICAL CHEMISTRY A

READ ▶

### Uncovering Transport Mechanisms in Perovskite Materials and Devices with Recombination-Induced Action Spectroscopies

Meredith G. McNamee, Andrew M. Moran, et al.

FEBRUARY 02, 2023

THE JOURNAL OF PHYSICAL CHEMISTRY C

READ ▶

Get More Suggestions >